Interactions of ozone and acetic acid with natural Gobi dust

Xianjie Wang

Sorbonne Université

École doctorale Physique en Île-de-France

Laboratoire de Physique des Plasmas

Sciences de l'Atmosphère et Génie de l'Environnement

Interactions of ozone and acetic acid with natural Gobi dust

Par Xianjie WANG

Thèse de doctorat de Physique

Dirigée par Antoine ROUSSEAU et Frédéric THEVENET

Présentée et soutenue publiquement le 10/09/2019

Devant un jury composé de :

DUTEN Xavier	Professeur, LSPM, Université Paris 13	Rapporteur
ASSADI Aymen	Maître de conférences, ENSC, École nationale Supérieure de Chimie de Rennes	Rapporteur
CASSAIGNON Sophie	Professeure, CNRS, LCMCP, Collège de France, Sorbonne Université	Examinatrice
VERBRUGGEN Sammy	Assistant professor, University of Antwerp	Examinateur
BATIOT-DUPEYRAT Catherine	Professeure, ENSIP, Université de Poitiers	Examinatrice
ROUSSEAU Antoine	Directeur de recherche CNRS, LPP, École Polytechnique, Sorbonne Université	Directeur de thèse
THEVENET Frédéric	Professeur, SAGE, IMT Lille Douai	Co-directeur de thèse
ROMANIAS Emmanouil	Maître de conférences, SAGE, IMT Lille Douai	Co-encadrant

To my family

Acknowledgements

I would first like to thank China Scholarship Council (CSC) for granting my 3-year PhD.

My most sincere gratitude is expressed to my PhD directors, Professor Antoine Rousseau from LPP of Ecole polytechnique Sorbonne University and Professor Frederic Thevenet from SAGE department of IMT Lille-Douai as my tremendous mentors. Thank you for turoring me, supporting my research, providing me with maximum flexibility and autonmy in my work, trusting, understanding and truly caring about me, for being my tutors, colleagues and friends. The 3-year PhD life with you is my fortune for life.

I would like to give my special appreciation to my supervisor, Dr. Emmanouil Romanias, for providing me with countless guidiance on my research, priceless advice on my redaction, and encouragement during the tough time.

I would also like to address my sincere thanks to Dr. Zixian Jia, for being a great tutor for me at the beginning of my PhD.

My gratitude is expressed to my colleagues at LPP, Dr. Bruno Honnorat, Constance Duchesne, Bo Liu, not only for helping me and supporting me through my research but also for being my good friends, our friendship and comradeship will last for a lifetime. I would also like to thank Dr. Nadira Frescaline and Dr. Jaime Arancibia of LPP for being such good colleagues.

My gratitude is also sent to Dr. Jerome Lasne, Dr. Mohamad Zeineddine, and Dr. Frederic Batault from SAGE department, for the aid and support on my research.

I also want to thank my temporary colleagues in LPP such as Huan Xu, Hang Yang, Chenyang Ding, Zhehao Pei, and Zhicheng Wu, for the great time spent with you. To all the staff in LPP, especially Philippe Auvray, Edouard Bouchet, Cherifa Ighoud, Catherine Jegu, Marilyne Bazin, Stephane Ravenel, I also want to thank you, for all the administrative and technical support and aid that you provided.

A big thank to my committee members, Professor Xavier Duten, professor Aymen Assadi, Professor Sophie Cassaignon, Professor Sammy Verbruggen, and Professor Catherine Batiot-Dupeyrat. Thank you for the brilliant comments and suggestions on my work, and also thank you for making my defense such a wonderful and enjoyable moment.

Thank you, Tony, for being an incredible friend and my personal medical consultant.

Thank you, Sevag, for always being there for me.

Finally, I thank my family. Without your love and support, I wouldn't have made it this far.

Table of contents

General introduction

Administrative context

This thesis has been conducted in collaboration between LPP (*Laboratoire de Physique des Plasmas*)[1] and SAGE Research Unit (Unité de Recherche / *Sciences de l'Atmosphère et Génie de l'Environnement*) at *Institut Mines Télécom Lille Douai* (*IMT Lille Douai*)[2]. The research motivations of SAGE are based on both fundamental and applied researches in atmospheric sciences and aim at a better understanding of the physical and chemical processes of generation and transformation of gaseous and particulate pollutants. The research axes of LPP focus on the fundamental and applied researches of plasmas, covering high temperature plasma, thermal plasma, and non-thermal plasma. The collaboration of both laboratories benefits from their backgrounds in heterogeneous chemistry and physics as well as a significant experimental expertise.

The three-year PhD grant has been provided by the China Scholarship Council (CSC). This work directly contributes to the research activities of the Labex CaPPA (Excellence Laboratory / Chemistry and Physics of Aerosols in the Atmosphere), project funded by the ANR through the PIA under contract ANR-11-LABX-0005-01, the "Hauts de France" Regional Council and the European Regional Development Fund (ERDF). This study is part of the Work Package 2 "WP2". Aerosol microphysical, chemical and optical properties from fundamental heterogeneous processes to remote sensing" of the Labex CaPPA.

Scientific context

Natural mineral dusts, as geo-materials, have recently drawn the attention of the scientific community. This consideration is primarily motivated by the concerns for atmosphere in the context of severe climate change. Meanwhile, mineral dust attracted the attention of media as well. One of the first sparks leading to a special focus on mineral dusts was caused by Eyjafjallajokul volcano eruption in 2010 inducing a total shut down of flights over North Atlantic Ocean and most of Western Europe. The intense, but localized, nature of dust emission from volcanoes should not hide the fact that more than 3 billion tons of mineral dusts are annually emitted into the atmosphere mainly from arid or semi-arid areas on Earth [1]. Beyond Eyjafjallajokul, fluxes of mineral dusts from Earth's ground and crust to the atmosphere are tremendous, making atmosphere a gigantic heterogeneous reactor.

Due to the global transportation by winds, suspended mineral dusts can travel overseas, cross continents and contribute to various environmental compartments connected by atmosphere [2-12]. Along their worldwide travels, mineral dusts get involved in key biogeochemical cycles [3, 13, 14]. In parallel, they

[1] LPP, CNRS, Ecole Polytechnique, Sorbonne Université, Université Paris-Sud, Observatoire de Paris, Université Pairs-Saclay, F-91128 Palaiseau, France.
[2] SAGE, IMT Lille Douai, Université de Lille, F-59500 Douai, France

significantly impact climate from a physical point a view, acting as a key solar scattering media and as could and ice condensation nuclei [15-19]. At ground level, mineral dust may severely impact human health and life through direct effects by decreasing air quality, or indirect effects such as damaging crops [20-22]. The investigation of the interactions between atmospheric gases and the surface of mineral dusts remains one of the less explored aspects. For instance, the impact of heterogeneous atmospheric chemistry involving mineral dusts on the budget of atmospheric trace gases is still questioned [23-26]. Similarly, the impact of gases on the surface chemistry of natural mineral dust, i.e. ageing, is unclear as well. The surface properties of these geo-materials definitely need to be addressed.

Several studies examined the uptake properties of mineral dust towards water vapor [27-29], ozone [30-33], NO_x [34-36], SO_2 [34, 35, 37, 38], HO° radicals [39, 40] as well as volatile organic compounds (VOCs) [41-44]. However, natural mineral dusts exhibit highly contrasted surface properties depending on their origins. Indeed, as a crustal material, the composition of mineral dust is directly related to the geological and environmental phenomena resulting in their formations and emissions. Among the studies focusing on the investigation of gas uptake onto mineral dusts, one approach consists in trying to provide a wide screening of numerous dusts with different origins and compositions. Such studies generally try to identify correlations between surface properties and dust compositions. In spite of the diversity of mineral dusts on Earth, some trends are typified. For instance, the Al/Si ratio is notably proposed as one descriptor of the surface properties of dust [44]. But this descriptor should be balanced by other kinds of surface characteristics such as the exact nature of mineral phases and corresponding surface chemistry, the hygroscopicity or the specific surface and more generally the morphology. Among investigated natural mineral dusts, the dust from Gobi Desert in Asia, characterized by one of the highest Al/Si ratio and basic surface properties, can be pointed out as a material of interest.

Since the 2000s, the synergetic effect reported about plasma and material association coupling has been explored to understand the physics and chemistry underlying this positive interaction. Beyond the impact of the material on the physics of the discharge [45-49], the material composition, its morphology and more precisely its surface properties have been evidenced as the driving parameters of the synergy observed for the removal of pollutants [47, 50, 51] since it controls the ability of the coupling material to make the most of plasma generated species and to interact with target pollutants. Along the last ten years, the role of heterogeneous phenomena, especially sorptive processes and active surface sites present onto the material inserted in the discharge have been explored using *in-situ* or *post-situ* coupling configurations [52, 53] and screening the composition of the coupling materials [53-67]. It should be noted that the most synergetic and efficient coupling materials are metal oxides, combing sustainability inside the discharge zone with sorptive and reactive properties. Plasma-catalysis is now clearly identified as a heterogeneous process set at the crossroad of (i) plasma technology, (ii) catalysis and (iii) surface science.

In first approach, the question of mineral dust in the atmosphere poorly overlaps with plasma-catalysis. However, when detailing the key issues of these two domains, meeting points arise. Both are heterogeneous processes, driven by the physics and chemistry of gas-surface interactions. Atmospheric chemistry, whether homogeneous or heterogeneous, involves oxidants and volatile organic compounds. Among oxidants, ozone plays a major role in the oxidative capacity of the atmosphere and subsequently in the fate of VOCs. These aspects are clearly shared with plasma-catalysis, where the abilities of the coupling material (i) to interact with plasma generated ozone and (ii) to adsorb targeted VOCs are crucial. Investigating geo-materials, whether in a context of mineral dust suspended in the atmosphere or catalytic coupling bed in a plasma discharge, requires: (i) the understanding of ozone uptake and decomposition on the material surface, (ii) the exploration of the VOC uptake and the detailed description of the corresponding surface processes, and (iii) the investigation of the dual VOC and ozone exposure of the geo-material to address further the surface oxidation process. In both cases, fundamental investigations are currently needed to provide a better description of the driving factors in gas-surface interactions.

Structure of the PhD thesis

The manuscript is divided in four chapters and a general conclusion.

Chapter 1 reviews the scientific context of this study. In this chapter, a general introduction on natural mineral dusts in the atmosphere, the essential background knowledge of uptake and adsorption theories related to this study, bibliographic reviews regarding the interactions of ozone and VOCs with minerals, and the potential application related to the current study, i.e., NTP-catalysis for indoor VOC abatement are presented. At the end of this chapter, the objectives and the structure of this study are presented.

Chapter 2 introduces the materials and methods used in this study. In this chapter, the characterizations of Gobi dust sample, as well as the gas species and the synthetic materials used are presented. Then, the experimental setups and protocols developed and used to address the heterogeneous interactions of ozone and acetic acid with Gobi dust are described.

Chapter 3 and chapter 4 present the results and discussions related to the investigations of the interactions of ozone with Gobi dust and the interactions of acetic acid with Gobi dust respectively under different experimental conditions. The former chapter is aiming to study the performance of the geomaterial towards ozone decomposition and to describe the mechanism. While Chapter 4 is dedicated to the investigation of the uptake properties of the surface regarding acetic acid and understanding the uptake processes on the surface of the geomaterial. Together, these two chapter is expected to provide comprehensive evaluations of the surface properties of Gobi dust towards ozone and acetic acid.

Finally, the general conclusion summarizes the main outcomes of this thesis.

References of general introduction

[1] P. Ginoux, M. Chin, I. Tegen, J.M. Prospero, B. Holben, O. Dubovik, S.J. Lin, Sources and distributions of dust aerosols simulated with the GOCART model, Journal of Geophysical Research: Atmospheres, 106 (2001) 20255-20273.

[2] C.R. Usher, A.E. Michel, V.H. Grassian, Reactions on mineral dust, Chemical reviews, 103 (2003) 4883-4940.

[3] S. Guerzoni, R. Chester, The impact of desert dust across the Mediterranean, Springer Science & Business Media1996.

[4] J.M. Prospero, Long-range transport of mineral dust in the global atmosphere: Impact of African dust on the environment of the southeastern United States, Proceedings of the National Academy of Sciences, 96 (1999) 3396-3403.

[5] K.D. Perry, T.A. Cahill, R.A. Eldred, D.D. Dutcher, T.E. Gill, Long-range transport of North African dust to the eastern United States, Journal of Geophysical Research: Atmospheres, 102 (1997) 11225-11238.

[6] P. Formenti, M. Andreae, L. Lange, G. Roberts, J. Cafmeyer, I. Rajta, W. Maenhaut, B. Holben, P. Artaxo, J. Lelieveld, Saharan dust in Brazil and Suriname during the Large-Scale Biosphere-Atmosphere Experiment in Amazonia (LBA)-Cooperative LBA Regional Experiment (CLAIRE) in March 1998, Journal of Geophysical Research: Atmospheres, 106 (2001) 14919-14934.

[7] J. Prospero, R. Glaccum, R. Nees, Atmospheric transport of soil dust from Africa to South America, Nature, 289 (1981) 570.

[8] R. Talbot, M. Andreae, H. Berresheim, P. Artaxo, M. Garstang, R. Harriss, K. Beecher, S. Li, Aerosol chemistry during the wet season in central Amazonia: The influence of long-range transport, Journal of Geophysical Research: Atmospheres, 95 (1990) 16955-16969.

[9] L.G. Franzén, M. Hjelmroos, P. Kållberg, E. Brorström-Lunden, S. Juntto, A.-L. Savolainen, The 'yellow snowepisode'of northern Fennoscandia, march 1991—A case study of long-distance transport of soil, pollen and stable organic compounds, Atmospheric environment, 28 (1994) 3587-3604.

[10] L.G. Franzén, M. Hjelmroos, P. Kållberg, A. Rapp, J.O. Mattsson, E. Brorström-Lundén, The Saharan dust episode of south and central Europe, and northern Scandinavia, March 1991, Weather, 50 (1995) 313-318.

[11] E. Ganor, H. Foner, S. Brenner, E. Neeman, N. Lavi, The chemical composition of aerosols settling in Israel following dust storms, Atmospheric Environment. Part A. General Topics, 25 (1991) 2665-2670.

[12] P. Alpert, E. Ganor, Sahara mineral dust measurements from TOMS: Comparison to surface observations over the Middle East for the extreme dust storm, March 14–17, 1998, Journal of Geophysical Research: Atmospheres, 106 (2001) 18275-18286.

[13] G. Zhuang, R.A. Duce, D.R. Kester, The dissolution of atmospheric iron in surface seawater of the open ocean, Journal of Geophysical Research: Oceans, 95 (1990) 16207-16216.

[14] X. Zhu, J.M. Prospero, D.L. Savoie, F.J. Millero, R.G. Zika, E.S. Saltzman, Photoreduction of iron (III) in marine mineral aerosol solutions, Journal of Geophysical Research: Atmospheres, 98 (1993) 9039-9046.

[15] A.L. Quijano, I.N. Sokolik, O.B. Toon, Radiative heating rates and direct radiative forcing by mineral dust in cloudy atmospheric conditions, Journal of Geophysical Research: Atmospheres, 105 (2000) 12207-12219.

[16] D. Rosenfeld, R. Lahav, A. Khain, M. Pinsky, The role of sea spray in cleansing air pollution over ocean via cloud processes, Science, 297 (2002) 1667-1670.

[17] Y. Yin, S. Wurzler, Z. Levin, T.G. Reisin, Interactions of mineral dust particles and clouds: Effects on precipitation and cloud optical properties, Journal of Geophysical Research: Atmospheres, 107 (2002) AAC 19-11-AAC 19-14.

[18] P.J. DeMott, D.C. Rogers, S.M. Kreidenweis, The susceptibility of ice formation in upper tropospheric clouds to insoluble aerosol components, Journal of Geophysical Research: Atmospheres, 102 (1997) 19575-19584.

[19] H.-M. Hung, A. Malinowski, S.T. Martin, Kinetics of heterogeneous ice nucleation on the surfaces of mineral dust cores inserted into aqueous ammonium sulfate particles, The Journal of Physical Chemistry A, 107 (2003) 1296-1306.

[20] G.D. Clayton, F.E. Clayton, Patty's industrial hygiene and toxicology. Vol. 2A. Toxicology, John Wiley & Sons, Inc., Baffins Lane, Chichester, Sussex PO19 1DU1981.

[21] A. Parker, J.E. Rae, Environmental interactions of clays: clays and the environment, Springer Science & Business Media1998.

[22] R. Stefanski, M. Sivakumar, Impacts of sand and dust storms on agriculture and potential agricultural applications of a SDSWS, IOP Conference Series: Earth and Environmental Science, IOP Publishing, 2009, pp. 012016.

[23] S. Liu, M. Trainer, M. Carroll, G. Hübler, D. Montzka, R. Norton, B. Ridley, J. Walega, E. Atlas, B. Heikes, A study of the photochemistry and ozone budget during the Mauna Loa Observatory Photochemistry Experiment, Journal of Geophysical Research: Atmospheres, 97 (1992) 10463-10471.

[24] R.B. Chatfield, Anomalous HNO3/NOx ratio of remote tropospheric air: Conversion of nitric acid to formic acid and NOx?, Geophysical Research Letters, 21 (1994) 2705-2708.

[25] S.M. Fan, D.J. Jacob, D. Mauzerall, J. Bradshaw, S. Sandholm, D. Blake, H. Singh, R. Talbot, G. Gregory, G. Sachse, Origin of tropospheric NO x over subarctic eastern Canada in summer, Journal of Geophysical Research: Atmospheres, 99 (1994) 16867-16877.

[26] H. Singh, D. Herlth, R. Kolyer, L. Salas, J. Bradshaw, S. Sandholm, D. Davis, J. Crawford, Y. Kondo, M. Koike, Reactive nitrogen and ozone over the western Pacific: Distribution, partitioning, and sources, Journal of Geophysical Research: Atmospheres, 101 (1996) 1793-1808.

[27] M. Tang, D.J. Cziczo, V.H. Grassian, Interactions of water with mineral dust aerosol: water adsorption, hygroscopicity, cloud condensation, and ice nucleation, Chemical reviews, 116 (2016) 4205-4259.

[28] N. Joshi, M.N. Romanias, V. Riffault, F. Thevenet, Investigating water adsorption onto natural mineral dust particles: Linking DRIFTS experiments and BET theory, Aeolian Research, 27 (2017) 35-45.

[29] S. Ibrahim, M.N. Romanias, L.Y. Alleman, M.N. Zeineddine, G.K. Angeli, P.N. Trikalitis, F. Thevenet, Water Interaction with Mineral Dust Aerosol: Particle Size and Hygroscopic Properties of Dust, ACS Earth and Space Chemistry, 2 (2018) 376-386.

[30] C. Usher, A. Michel, D. Stec, V. Grassian, Laboratory studies of ozone uptake on processed mineral dust, Atmospheric Environment, 37 (2003) 5337-5347.

[31] F. Karagulian, M.J.J.I.j.o.c.k. Rossi, The heterogeneous decomposition of ozone on atmospheric mineral dust surrogates at ambient temperature, 38 (2006) 407-419.

[32] T.D. Fairlie, D.J. Jacob, J.E. Dibb, B. Alexander, M.A. Avery, A.v. Donkelaar, L. Zhang, Impact of mineral dust on nitrate, sulfate, and ozone in transpacific Asian pollution plumes, Atmospheric Chemistry and Physics, 10 (2010) 3999-4012.

[33] X. Wang, M.N. Romanias, F. Thévenet, A.J.C. Rousseau, Geocatalytic Uptake of Ozone onto Natural Mineral Dust, 8 (2018) 263.

[34] M. Ullerstam, M.S. Johnson, R. Vogt, E. Ljungström, DRIFTS and Knudsen cell study of the heterogeneous reactivity of SO 2 and NO 2 on mineral dust, Atmospheric Chemistry and Physics, 3 (2003) 2043-2051.

[35] H. He, Y. Wang, Q. Ma, J. Ma, B. Chu, D. Ji, G. Tang, C. Liu, H. Zhang, J. Hao, Mineral dust and NOx promote the conversion of SO 2 to sulfate in heavy pollution days, Scientific reports, 4 (2014) 4172.

[36] M. Ndour, B. D'Anna, C. George, O. Ka, Y. Balkanski, J. Kleffmann, K. Stemmler, M. Ammann, Photoenhanced uptake of NO2 on mineral dust: Laboratory experiments and model simulations, Geophysical Research Letters, 35 (2008).

[37] Y. Dupart, S.M. King, B. Nekat, A. Nowak, A. Wiedensohler, H. Herrmann, G. David, B. Thomas, A. Miffre, P. Rairoux, Mineral dust photochemistry induces nucleation events in the presence of SO2, Proceedings of the National Academy of Sciences, 109 (2012) 20842-20847.

[38] C. Usher, H. Al-Hosney, S. Carlos-Cuellar, V. Grassian, A laboratory study of the heterogeneous uptake and oxidation of sulfur dioxide on mineral dust particles, Journal of Geophysical Research: Atmospheres, 107 (2002) ACH 16-11-ACH 16-19.

[39] Y. Bedjanian, M.N. Romanias, A.J.T.J.o.P.C.A. El Zein, Interaction of OH radicals with Arizona test dust: uptake and products, 117 (2013) 393-400.

[40] Y. Bedjanian, M. Romanias, A.E. Zein, Uptake of HO 2 radicals on arizona test dust, Atmospheric Chemistry and Physics, 13 (2013) 6461-6471.

[41] M.N. Zeineddine, M.N. Romanias, V. Gaudion, V.r. Riffault, F.d.r. Thévenet, Heterogeneous Interaction of Isoprene with Natural Gobi Dust, ACS Earth and Space Chemistry, 1 (2017) 236-243.

[42] M.N. Romanias, H. Ourrad, F. Thevenet, V. Riffault, Investigating the Heterogeneous Interaction of VOCs with Natural Atmospheric Particles: Adsorption of Limonene and Toluene on Saharan Mineral Dusts, Journal of Physical Chemistry A, 120 (2016) 1197-1212.

[43] M.N. Romanias, M.N. Zeineddine, V. Gaudion, X. Lun, F. Thevenet, V. Riffault, Heterogeneous Interaction of Isopropanol with Natural Gobi Dust, Environmental science & technology, 50 (2016) 11714-11722.

[44] M.N. Zeineddine, M.N. Romanias, V. Riffault, F. Thévenet, Heterogeneous Interaction of Various Natural Dust Samples with Isopropanol as a Probe VOC, The Journal of Physical Chemistry A, (2018).

[45] H.L. Chen, H.M. Lee, S.H. Chen, M.B. Chang, Review of packed-bed plasma reactor for ozone generation and air pollution control, Industrial & Engineering Chemistry Research, 47 (2008) 2122-2130.

[46] H.L. Chen, H.M. Lee, S.H. Chen, M.B. Chang, S.J. Yu, S.N. Li, Removal of volatile organic compounds by single-stage and two-stage plasma catalysis systems: a review of the performance enhancement mechanisms, current status, and suitable applications, Environmental science & technology, 43 (2009) 2216-2227.

[47] J. Van Durme, J. Dewulf, C. Leys, H. Van Langenhove, Combining non-thermal plasma with heterogeneous catalysis in waste gas treatment: A review, Applied Catalysis B: Environmental, 78 (2008) 324-333.

[48] A.M. Vandenbroucke, R. Morent, N. De Geyter, C. Leys, Non-thermal plasmas for non-catalytic and catalytic VOC abatement, Journal of hazardous materials, 195 (2011) 30-54.

[49] A. Mizuno, H. Ito, Basic performance of an electrostatically augmented filter consisting of a packed ferroelectric pellet layer, Journal of electrostatics, 25 (1990) 97-107.

[50] A.M. Vandenbroucke, R. Morent, N. De Geyter, C. Leys, Decomposition of Toluene with Plasma-catalysis: A Review, Journal of Advanced Oxidation Technologies, 15 (2012) 232-241.

[51] F. Thevenet, L. Sivachandiran, O. Guaitella, C. Barakat, A. Rousseau, Plasma-catalyst coupling for volatile organic compound removal and indoor air treatment: a review, Journal of Physics D-Applied Physics, 47 (2014).

[52] L. Sivachandiran, F. Thevenet, A. Rousseau, Isopropanol removal using MnXOY packed bed non-thermal plasma reactor: Comparison between continuous treatment and sequential sorption/regeneration, Chemical Engineering Journal, 270 (2015) 327-335.

[53] C. Barakat, P. Gravejat, O. Guaitella, F. Thevenet, A. Rousseau, Oxidation of isopropanol and acetone adsorbed on TiO2 under plasma generated ozone flow: Gas phase and adsorbed species monitoring, Applied Catalysis B-Environmental, 147 (2014) 302-313.

[54] A.M. Harling, V. Demidyuk, S.J. Fischer, J.C. Whitehead, Plasma-catalysis destruction of aromatics for environmental clean-up: Effect of temperature and configuration, Applied Catalysis B: Environmental, 82 (2008) 180-189.

[55] F. Holzer, U. Roland, F.-D. Kopinke, Combination of non-thermal plasma and heterogeneous catalysis for oxidation of volatile organic compounds: Part 1. Accessibility of the intra-particle volume, Applied Catalysis B: Environmental, 38 (2002) 163-181.

[56] H. Einaga, T. Ibusuki, S. Futamura, Performance evaluation of a hybrid system comprising silent discharge plasma and manganese oxide catalysts for benzene decomposition, Ieee Transactions on Industry Applications, 37 (2001) 1476-1482.

[57] V. Demidiouk, S.I. Moon, J.O. Chae, D.Y. Lee, Application of a plasma-catalytic system for decomposition of volatile organic compounds, Journal of the Korean Physical Society, 42 (2003) S966-S970.

[58] B. Lu, X. Zhang, X. Yu, T. Feng, S. Yao, Catalytic oxidation of benzene using DBD corona discharges, Journal of Hazardous Materials, 137 (2006) 633-637.

[59] K. Krawczyk, M. Mlotek, Combined plasma-catalytic processing of nitrous oxide, Applied Catalysis B-Environmental, 30 (2001) 233-245.

[60] J.L. Wu, Y.X. Huang, Q.B. Xia, Z. Li, Decomposition of Toluene in a Plasma Catalysis System with NiO, MnO2, CeO2, Fe2O3, and CuO Catalysts, Plasma Chemistry and Plasma Processing, 33 (2013) 1073-1082.

[61] S. Futamura, H. Einaga, H. Kabashima, L.Y. Hwan, Synergistic effect of silent discharge plasma and catalysts on benzene decomposition, Catalysis Today, 89 (2004) 89-95.

[62] S. Futamura, A. Gurusamy, Synergy of nonthermal plasma and catalysts in the decomposition of fluorinated hydrocarbons, Journal of Electrostatics, 63 (2005) 949-954.

[63] M. Sugasawa, S. Futamura, Ieee, Synergistic Effect of Nonthermal Plasma and Catalysts on the Decomposition of VOCs, Conference Record of the 2007 Ieee Industry Applications Conference Forty-Second Ias Annual Meeting, Vols. 1-52007, pp. 1485-1488.

[64] L. Sivachandiran, F. Thevenet, A. Rousseau, Non-Thermal Plasma Assisted Regeneration of Acetone Adsorbed TiO2 Surface, Plasma Chemistry and Plasma Processing, 33 (2013) 855-871.

[65] T. Zhang, Q.R. Li, Y. Liu, Y.L. Duan, W.Y. Zhang, Equilibrium and kinetics studies of fluoride ions adsorption on CeO2/Al2O3 composites pretreated with non-thermal plasma, Chemical Engineering Journal, 168 (2011) 665-671.

[66] X.B. Zhu, X. Tu, D.H. Mei, C.H. Zheng, J.S. Zhou, X. Gao, Z.Y. Luo, M.J. Ni, K.F. Cen, Investigation of hybrid plasma-catalytic removal of acetone over CuO/gamma-Al2O3 catalysts using response surface method, Chemosphere, 155 (2016) 9-17.

[67] C. Norsic, J.M. Tatibouet, C. Batiot-Dupeyrat, E. Fourre, Non thermal plasma assisted catalysis of methanol oxidation on Mn, Ce and Cu oxides supported on gamma-Al2O3, Chemical Engineering Journal, 304 (2016) 563-572.

Chapter I. State of the art and objectives

Table of contents

Table of figures

In this chapter, background and basic knowledge is provided to understand the reactivity of natural dust towards ozone and VOC presented in this manuscript are introduced. It will start with the introduction of natural mineral dust, followed by the basic knowledge of uptake and adsorption theories. Then a targeted but detailed literature review will be given concerning the interaction of minerals with ozone and VOCs. At the end, the objectives of applications of this study will be illustrated.

1 Natural mineral dust

Among the aerosols in the atmosphere, natural mineral dusts are one of the most important aerosols in the atmosphere, contributing more than 50% of the total annual aerosol emission on the earth among other aerosols such as marine sea salts, volcanic ashes, and sulfates [1]. Natural mineral dust refers to the small eroded soil particles of the earth which are mobilized and entrained into atmosphere by wind power [2].

1.1 Sources and transport of natural mineral dust

Sources. Averagely speaking, for each year from 1×10^9 to 3×10^9 tons of mineral dust are emitted into the atmosphere from the arid or semiarid areas on the earth or due to human activities [3]. Human activities, such as improper agricultural and grazing practices also contribute to the loading of the mineral dust in the atmospheric, accounting from 10% to 50% based on the intensity and the frequency of these activities [4, 5]. The massive emissions of natural mineral dust are mostly related to the sandstorms in desert. Among these emissions, Saharan Desert is the largest global emission source of natural mineral dust which accounts for almost half of all the aeolian materials, according to A.S. Goudie and N. J. Middleton [6]. Gobi Desert in North China is the second most important source of mineral dust in the atmosphere in a global scale which contributes to more than 11 % to the global dust emissions [7-9].

Transport. One of the important features of natural mineral dust events is the global transportation for long distance and in wide areas [2]. For example, the dust from Saharan Desert (Saharan dust) can be transported to North America [10-12], South America [13-15], northern Europe [16, 17], and through the Middle East into Central Asia [10, 18, 19]. Meanwhile, the dust from Gobi Desert (Gobi dust) in northern Asia significantly affects eastern Asia [7-9] and western North America [20-22]. Figure I-1 is a moderate resolution imaging spectroradiometer (MODIS) image made by Jacques Descloitres in MODIS Rapid Response Team of NASA/GSFC where a graceful arc of Saharan dust is streaming off the coast of northwest Africa and sweeping out over the Atlantic Ocean and the Canary Islands, on February 18, 2004 [23].

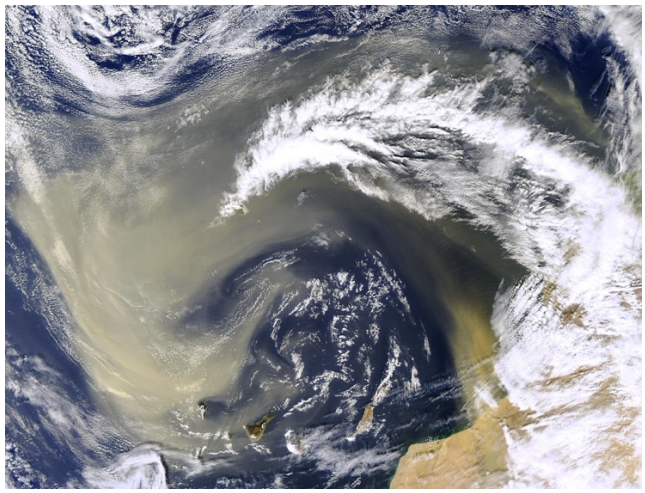

Figure I-1 Image by Jacques Descloitres, MODIS Rapid Response Team, NASA/GSFC [23]. (This image is used following the Terms of Use of Visible Earth https://visibleearth.nasa.gov.)

Size distribution. The size distribution of the mineral dusts determines the specific way, by which the mineral dust particles will be transported. For example, the particles of mineral dust which are suspended into the atmosphere and transported for long distance, i.e. thousands kilometers, the size range is normally below 100 μm [24, 25] since within these particle range, the mineral dust particles are easy to be suspended and carried by wind. For other grain sizes, the mechanism of transport might be different. Generally speaking, for particles whose size $> 500\ \mu m$, the transport way is called creep, which means the rolling or sliding of particles along the ground surface [24]. For particles whose size $70 - 500\ \mu m$, the main transport way is saltation, meaning that the particles can be suspended to a certain height, i.e. ~1 m, and then settle to the surface due to gravity resistance [2, 26]. Moreover, some physical properties and chemical compositions of mineral dust can depend on the size distribution of the particles [2, 26]. For wind-transported aerosol with a given size distribution, typically the coarser particles are found to consist of feldspars, carbonates and quartz while the finer particles often consist of micas or clays [2]. The finer particles which are transported longer and further, are more enriched by clays during the transport processes, while the coarser particles have shorter transport process due to gravitational settling [2]. It has been also reported that the mineral dust with low particle size fraction is usually characterized by low SiO_2 contents [27]. Moreover, the specific surface area of the mineral dust with low particle size fraction is always higher, compared to the coarser particles, according to the studies by C. Bueno-Ferrer et al. [28].

1.2 Composition of natural mineral dust

Since the natural mineral dusts are eroded particles of crustal rocks, their chemical compositions should be similar, if not identical, to what of the crustal rock. According to K. Hans Wedepohl [29], the major elements of the upper continental crust are Si (30.3%), Al (7.7%), Fe (3.1%), Ca (3.0%), Na (2.6%), Mg (1.4%), K (2.9%), Ti (0.3%), Ba (0.06%), Mn (0.05%). These elements consisting the upper continental

crust exist mostly as oxides: SiO_2 (61.5%), Al_2O_3 (15.1%), Fe_2O_3 (6.28%), CaO (5.5%), Na_2O (3.2%), MgO (3.7%), K_2O (2.4%), TiO_2 (0.68%), BaO (0.06%) and MnO (0.1%).

As a result, natural mineral dust is supposed to share the same major elemental compositions of continental crust and be a mixture of metal oxides found in earth crust. Indeed, the main elemental compositions of natural mineral dust have been reported to be Si, Al, Ca, Fe, K, based on the investigation of mineral dust from different emission sources such as northern Sahara, Central Asia, southwestern U.S. with sedimentary rocks as reference minerals [30-33]. Figure I-2 displays the relative elemental concentrations of mineral dusts from different emission sources L. Gomes and D. A. Gilette [31].

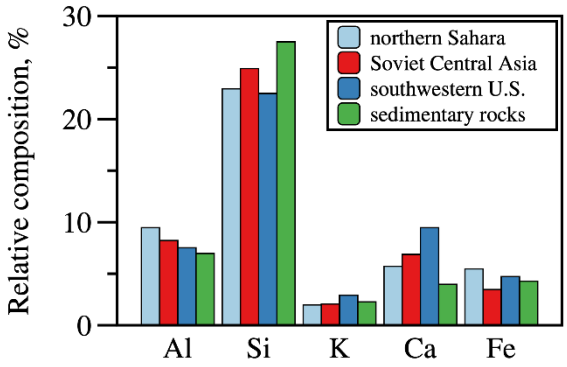

Figure I-2 Relative concentrations of major elements in mineral dust with different emission sources. (The data is retrieved from Gomes L, Gillette D A [31].)

Regarding mineral phase present in dusts, it is generally reported that a natural mineral dust is approximately 60% of SiO_2, 10 – 15% Al_2O_3, as well as some other metal oxides such as Fe_2O_3, MgO, CaO and etc. based on the investigations on mineral dust collected from different locations overall the world [2, 7, 18, 34, 35]. However, the exact mineralogical composition can significantly vary from one source to another. Indeed, Table I-1 displays the relative abundances in percentage of the oxides in mineral dust for various sources. The names of the location refer to the collection place of the natural mineral dust samples.

Table I-1 confirms the fact that natural mineral dust is a mixture of oxides, especially metal oxides dominated by Si and Al oxides [35]. It also evidences that the chemical compositions from one mineral dust from another are different depending on their source locations. The mineral phase of the dust originating from Africa is dominated by SiO_2 and Al_2O_3 which might suggest the significance of quartz in the wind-transported dust. The dust from Asia, according to Table I-1, have lower SiO_2 content compared with most of the dusts from Africa. Even when the chemical compositions of mineral dust from different sources are similar, the mineralogy, such as the chemical formulas and crystal structures, of the dust particles can still vary [24, 38] because different minerals might share similar chemical

compositions, such as kaolinite ($Al_2Si_2O_5(OH)_4$) and Muscovite ($KAl_3Si_3O_{10}(OH)_2$), according to Table I-1.

Table I-1 Relative abundances (in %) of mineral phases in different natural mineral dusts from various origins.

Dust sample	Gobi	Harmattan [6]	Mbour [35]	Nefta [35]	Rawdat [35]	Touggourt [36]	N'Goussa [36]	Bordj [36]	Arizona [36, 37]
Origin	Asia	Africa	Africa	Africa	Asia	Africa	Africa	Africa	North America
SiO_2	33	60.95	95.0	82.0	61.0	79	82	88	76
Al_2O_3	-	11.02	1.2	0.3	4.4	0.30	3.0	4.4	8.8
$CaCO_3$	8.7	-	1.5	11.0	21.0	11	3.4	2.1	-
$NaAlSi_3O_8$	8.6	-	-	-	10.0	-	-	-	-
$KAl_3Si_3O_{10}(OH)_2$	25.8	-	-	-	-	-	-	-	-
Fe_2O_3	-	4.5	0.5	0.2	-	0.50	0.50	0.6	2.0
Fe_3O_4	-	-	-	-	1.3	-	-	-	-
TiO_2	4.4	0.82	0.3	1.5	0.2	1.2	0.60	0.15	0.30
CaO	-	2.31	-	-	-	-	-	-	2.5
MgO	-	0.76	-	-	-	-	-	-	0.80
$Al_2Si_2O_5(OH)_4$	8.9	-	-	-	-	-	-	-	-
$Mg_3Al_2(SiO_4)_3$	4.1	-	-	-	-	-	-	-	-
K_2O	-	2.81	-	-	2.0	-	-	-	2.4
MnO	-	0.09	-	-	-	-	-	-	-
Na_2O	-	1.39	-	-	-	-	-	-	1.9
P_2O_5	-	0.20	-	-	-	-	-	-	-
$CaHPO_4•2H_2O$				5.0		12.4	6.6	-	-
$CaMg(CO_3)_2$	-	-	-	-	-	1.7	-	-	-
$CaTiO_3$	-	-	-	-	-	1.0	1.0	-	-
Others	6.5	-	1.5	0	0.1	-	-	-	5.3

1.3 Impacts of natural mineral dust on climate, public health, biogeochemical cycle and atmospheric chemistry

With the huge flux of mineral dust into the atmosphere, i.e. 1×10^9 to 3×10^9 tons each year, and global-scale transport, research shows that mineral dusts can interact with atmospheric systems, oceanic systems as well as terrestrial systems [11, 39-42]. A brief description of the impacts of natural mineral dust are presented hereby in four aspects: climate, public health, biogeochemical cycle and atmospheric chemistry.

1.3.1 Climate

It has been widely reported in the literature that mineral dust in the atmosphere, as well as other kinds of aerosols, has significant influence on the local or global radiative budget through absorption and scattering of solar radiation, resulting in warming or cooling effect on Earth's surface [5, 43-47]. Besides, the mineral particles suspended in the atmosphere can act as ice condensation nuclei (ICN) and cloud condensation nuclei (CCN), thus influencing local precipitation [48-52] through cloud formation.

1.3.2 Public health

It becomes more and more concerning nowadays that mineral dust in the low atmosphere brings up health issues on public health. The most dangerous and well-known impact of mineral dust on public health is the harm of inhaling mineral particles in human respiratory system [53]. It has been reported that continuous exposure to silica dust as well as some other fine mineral fibers can cause pulmonary disorders [54]. If the exposure lasts long and the inhalation becomes serious, it could finally lead to silicosis [55]. Fine and fibrous mineral dust such as palygorskite can be lodged in lung tissue of human beings [56]. To this concern, the U.S. Environmental Protection Agency established the "PM (Particulate Matter 2.5)" standard to emphasize the significant impact on public health of the aerosols which have diameters inferior to 2.5 micrometers in 1997. Additionally to the health issues abovementioned, the mineral dust suspended in air may also act as the carrier of organisms or chemicals which causes infectious diseases or allergies [2].

1.3.3 Biogeochemical cycle

At the same time when mineral dust with different sources has been transported by wind power and deposited thousands of kilometers away, it carries biomaterials such as bacteria, virus or other microorganism that can cause diseases from one place to another, thus influencing the native species in the local system where it is deposited. Mineral dust itself also enrich the nutrients in the soil, which are somehow not present the native soil. For example, the dust from Asia which has high silica content caused the deposition and accumulation of quartz in Hawaiian Island where the dust contains little quartz [57]. Not only for soil, this impact of mineral dust also increases the nutrition and mineral contents of the upper ocean [10, 58, 59]. It needs to mention that mineral dust has been reported to cause sudden increases of soluble iron and other micronutrients to biological species to the ocean [58, 60], sometimes resulting in the growth of *Gymnodinium breve*, which is a toxic dinoflagellate responsible for fish death, shellfish poisoning, sea water discoloration, respiratory diseases for people living near the shore, and economic losses caused by the reduced tourism on affected beaches [61, 62].

1.3.4 Atmospheric chemistry.

Mineral dust in the atmosphere could participate into chemical reactions with atmospheric trace gases. Different from gas-gas interactions, i.e., homogeneous interactions between the trace gases, mineral dust provides surfaces for solid-gas interactions, i.e., heterogeneous interactions, with atmospheric trace gases. And these heterogeneous interactions on the surface of mineral dust help explaining some atmospheric reaction pathways which cannot be explained only by homogeneous interactions within gas phase [63-66]. Research also shows that particles of mineral dust can act as sinks, or sources in other cases, for different atmospheric chemical species, thus influencing the chemical budget in the atmosphere. As a result, research groups have focused on the interactions of mineral dust with different

atmospheric gas species such as water vapor [1, 67, 68], ozone [41, 69-71], NO_x [72-74], SO_2 [72, 73, 75, 76], HO° radicals [77, 78] as well as volatile organic compounds (VOCs) [35, 36, 79, 80].

1.4 Summary and the implementation in atmospheric chemistry study

In this section, a general introduction of natural mineral dusts in atmosphere is presented, describing the sources, transport, compositions as well as the global impacts of this geomaterials. The global impacts of mineral dusts are highlighted due to environmental concerns and summarized by Figure I-3.

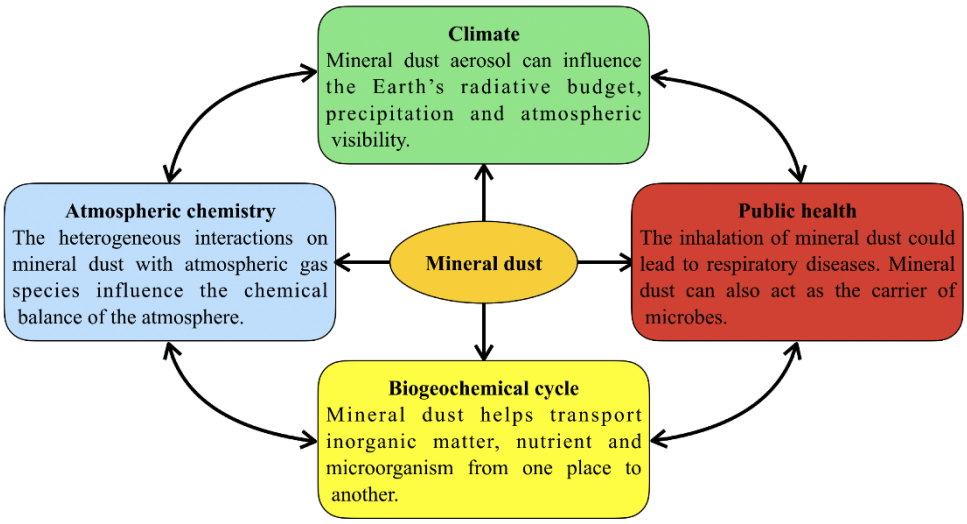

Figure I-3 Overall impacts of natural mineral dust on global processes.

The impacts that mineral dusts have on atmospheric chemistry are closely related to the subject of this thesis: the reactivity of natural mineral dusts towards gas phase species. Studying the reactivity of mineral dust particles towards gas phase species could help evaluate the role that mineral particles play in atmospheric chemistry.

To conduct atmospheric chemistry studies, field measurement and observation, modeling, and laboratory research are the three key approaches, which provide data and understanding from different aspects and support each other.

Field measurements can provide direct information related to the evolutions of local atmospheric trace gas concentrations due to mineral dust. However, it has several obvious limitations in space and time: local measurement versus the scale of the atmosphere, low sampling rate and limited sampling time scale versus the long-term atmosphere evolution, limitations from the detecting equipment and etc.

Modeling is another approach to understand atmospheric chemistry [3, 74, 81]. Take the study by F. J. Dentener et al [82] as an example where they used a global three-dimensional model of the troposphere to simulate the sources, transports, and the removal of the mineral dust aerosols and their impacts on the

budges of SO_2, HO_x, NO_y, and ozone. Authors succeeded to illustrate the significant impact of the mineral dust on the atmospheric chemistry by their modeling: For SO_2, authors showed that more than 10% of sulfate is associated with the mineral dust from east Asia to Pacific Ocean center, into southern Indian Ocean, spanning from central Africa to the northeastern South America; For gas phase nitric acid, authors showed that there is a vast area where at least 40% of total nitrate is found on the mineral aerosol; For the heterogeneous interaction with N_2O_5, HO_2 radicals and ozone, authors suggested that mineral dust have significant impacts on the photochemical oxidant cycle thus causing up to 10% of ozone concentration drop near by the dust emission area. Their simulations and suggestions are supported and confirmed by filed measurements [83, 84] as well as laboratory studies [85, 86].

Laboratory study provides fundamental understanding and the parameters for atmospheric chemistry. A well-working model for atmospheric chemistry needs to be built up on correct mechanism of reactions with proper data. This is the primary goal of my study.

As a result, this study of the reactivity of natural mineral towards ozone and VOCs, will provide data experimental determined related to the reactivity of mineral dust towards gas species, and also provide accurate and comprehensive understanding for the mechanism of the heterogeneous interactions. To understand the study presented, necessary knowledge of uptake and adsorption theories, and related literature reviews will be introduced in the following sections.

2 Uptake and adsorption theory of gases on solid surface

2.1 Uptake of gases on solid surface

Uptake of a gas phase species on the surface of a solid describes a process at the interface where the gas species is lost from gas phase onto the surface. Uptake doesn't define the nature of the gas lose: it could be physically adsorption, absorption or reactive decomposition and etc.

2.1.1 Uptake coefficient γ

Uptake process of a gas species on solid surface is characterized by uptake coefficient γ. The uptake coefficient γ of a gas phase species X on surface is defined as the probability of the loss of a molecule X from gas phase upon a collision with the surface. According to its definition, uptake coefficient of X equals the ratio between the net loss of X molecules from the gas phase to the surface per second and the total number of gas-surface collisions per second. It is widely used to characterize the kinetics of heterogeneous interactions, especially in atmospheric chemistry studies as mentioned previously [87-90].

For a system consisting of gas X and a solid surface, the loss of X from gas phase at the interface can be described as a first-order process by equation (I-1):

$$\mathrm{d}\{X\}/\mathrm{d}t = -\gamma\frac{c}{4}A[X] \quad \text{(I-1)}$$

Thus, uptake coefficient γ can be derived with Equation (I-2):

$$\gamma = \frac{4|\mathrm{d}\{X\}/\mathrm{d}t|}{cA[X]} \quad \text{(I-2)}$$

where {X} is the number of X molecules, [X] denotes the concentration of X in gas phase (molecules cm^{-3}), A is the specific area of the surface in cm^2, c is the mean molecular speed of X molecules in gas phase in cm s^{-1}.

The uptake coefficient depends on several factors. In the latest evaluation of the International Union of Pure and Applied Chemistry (IUPAC) [88], it has been clearly pointed out that uptake coefficients strongly depend on the following experimental conditions:

(i) The gas phase concentration of the molecule (uptake decreases as the concentration of the gas increases).

(ii) The total pressure, and the temperature applied to carry out the experiment.

(iii) The determination of the uptake coefficient may also be affected by the experimental protocol: The temporal resolution of the instrument applied to monitor the gas concentration of the reactor outlet.

(iv) The residence time of the molecule in the reactor.

Finally, the uptake coefficient of a given species on a surface may vary during the exposure time and its initial value generally differs from its steady-state value [88]. As a result, the comparison of uptake coefficients should be made with same/similar condition.

2.1.2 Heterogeneous life time, τ_{het}

Based on uptake coefficient, the life-time τ_{het} of the species X, related to surface uptake, can be calculated via equation (I-3).

$$\tau_{het} = \frac{4}{\gamma cD} \quad \text{(I-3)}$$

where γ is the uptake coefficient of the gas phase species X onto solid particles, c is the mean molecular speed cm s^{-1}, and D is the surface area density (cm^2 cm^{-3}) of the solid particles.

τ_{het} describes the time for the concentration of X to fall to 1/e of the initial value, thus allowing to determine if the heterogeneous interaction is important or negligible in the whole atmospheric chemistry activities involved X.

2.2 Fundamentals of adsorption of gases on solid surface

Adsorption of a gas species on a solid surface refers to the adhesion of the gas species to the surface and generally results in the formation of adsorbed species on the surface. The solid is defined as adsorbent.

Adsorption may be caused by the Van Der Waals interactions or chemical reactions: the former is known as physical adsorption (or physisorption) and the latter is chemical adsorption (or chemisorption). For clarity, the important points of physical adsorption and chemical adsorption are listed:

- *Physisorption.* The main interaction between the adsorbate and the adsorbent is the Van Der Waals interaction or hydrogen bonding. The gas species molecule remains in its main molecular structure. The physical adsorption process can result in several layers of adsorbate on the surface. The enthalpy of physisorption is generally around -40 to -5 kJ mol^{-1} [91].
- *Chemisorption.* Chemical adsorption occurs with the formation of chemical bonds between adsorbate molecules and the surface sites whether by sharing or exchanging electrons. As a result, chemical adsorption can only occur as a monolayer [92] and it stops when all the surface sites are occupied. Since the interaction of chemical adsorption is much stronger than physical adsorption, the enthalpy of the whole system is correspondingly higher than that of physical adsorption system, i.e., -800 to -40 kJ mol^{-1} [93].

Adsorption is an exothermic process [91] indicating that the enthalpy of adsorption is negative. The absolute value of adsorption enthalpy of an adsorption process is higher, the adsorbed species formed on the surface is more stable. Physisorption is generally weaker than chemisorption. Also, when the temperature of the system increases (or the pressure of the gas phase decreases), the physically adsorbed molecules on the surface can be released into the gas phase, this is the process of desorption.

2.3 Adsorption isotherm

Adsorption isotherm is essential for describing adsorption process. Generally for a given adsorption process, when it reaches equilibrium between the adsorbate on the adsorbed phase and gas molecules in gas phase, this equilibrium can be described as a function of the gas phase partial pressure P and the temperature T [94]. In practice, the working temperature is normally a constant value, T_0, so the adsorption equilibrium can be described as an isotherm, and only depends on the partial pressure of gas phase, as described in equation (I-4):

$$\frac{x}{m} = f(P)\ at\ T_0 \quad \text{(I-4)}$$

where is x is the total amount of the adsorbate in g or mol, m is the total mass of the adsorbent in g.

The interpretation of an experimental adsorption isotherm by mathematical equations can help extract the most important characteristics of the adsorption system, [95]. Along the history of the development of the adsorption theories, there are two important adsorption isotherms which are particularly important for the studies presented in this thesis: Langmuir adsorption isotherm and BET adsorption isotherm.

2.3.1 Langmuir adsorption isotherm

Derived from kinetic studies and based on some assumptions, Irving Langmuir developed a adsorption model to describe the adsorption process [96]. The assumptions are listed:

Following are the assumptions:

- The adsorbing gas adsorbs into an immobile state.
- All sites on the surface are equivalent.
- Each site can hold at most one molecule of adsorbate (mono-layer coverage only).
- There are no interactions between adsorbate molecules on adjacent sites.
- The number of adsorbed molecules does not influence the adsorption energy.

Langmuir adsorption theory provided a clear concept of monolayer adsorption for the first time [93, 97]. Within the restriction of the assumptions mentioned above, it can be applied to physisorption and chemisorption. A brief kinetic derivation of the Langmuir adsorption isotherm is given.

With the assumptions, adsorption process can be described by equation (I-5) with the equilibrium constant K_{eq}:

$$X_g + S \rightleftharpoons XS \quad \text{(I-5)}$$

where X_g is the gas phase molecule, S is the free surface sites on the surface, XS is the adsorbed species formed by X and S on the surface. The rate of adsorption r_{ad} and the rate of desorption r_d can be calculated from Equation (I-6) and Equation (I-7):

$$r_{ad} = k_{ad}\, P_{X_g}\, [S] \quad \text{(I-6)}$$

$$r_d = k_d\, [XS] \quad \text{(I-7)}$$

P_{X_g} is the partial pressure of molecule A over the surface, [S] is the concentration of the free sites in number/m^2, [XS] is the surface concentration of X in molecules/m^2, and k_{ad} and k_d are the constants of adsorption process and desorption process during equation (I-5).

The surface coverage θ (varying from 0 to 1) is defined as the fractional occupancy of the surface sites as in Equation (I-8):

$$\theta = \frac{[XS]}{[XS] + [S]} \tag{I-8}$$

When the system is at equilibrium, the rate of adsorption equals the rate of desorption. The equilibrium constant K_{eq} can be expressed in equation (I-9):

$$K_{eq} = \frac{k_{ad}}{k_d} = \frac{[XS]}{P_{X_g}\,[S]} \tag{I-9}$$

As a result, θ can be described as equation (I-10):

$$\theta = \frac{K_{eq}\,P_{X_g}}{K_{eq}\,P_{X_g} + 1} \tag{I-10}$$

However, when it comes to the adsorption where adsorption of gas molecules onto solid surface ends up in multilayer, Langmuir adsorption isotherm is not applicable. BET adsorption theory, is needed in this case.

2.3.2 BET adsorption isotherm

BET adsorption theory [98, 99] successfully extends the concept of Langmuir adsorption theory from monolayer to multilayer, where the former monolayer acts as a substrate for the latter adsorption. It was built up also with some assumptions [100]:

- The adsorbing gas adsorbs into an immobile state.
- Gas species is regarded ideal.
- All sites on the surface are equivalent.
- Each site can hold multiple molecule of adsorbate.
- Adsorbed molecules produce new sites for other gas molecules.
- There are no interactions between adsorbate molecules on adjacent sites.

With the assumptions, the BET isotherm can be presented in equation (I-11):

$$\frac{1}{X\left[\left(\frac{P_0}{P}\right)-1\right]}=\frac{C-1}{X_{mono}C}\left(\frac{P}{P_0}\right)+\frac{1}{X_{mono}C} \quad \text{(I-11)}$$

Where P_0 and P is the saturated gas pressure and the gas pressure at equilibrium of adsorption for a given temperature, X is total adsorbed gas quantity which is always presented in volume or mass units and X_{mono} is the monolayer adsorbed gas quantity also in volume or mass units. C is the BET constant which can be derived from equation (I-12):

$$C=exp\left(\frac{E_1-E_L}{RT}\right) \quad \text{(I-12)}$$

Where E_1 is the heat of adsorption for the first layer, and E_L is the heat of adsorption for the second and higher layers, which is equal to the heat of liquefaction. R is the ideal gas constant and T is the absolute temperature during adsorption process.

The BET isotherm was the first attempt to find a wider theory of physical adsorption [101]. One of the most important contribution from BET isotherm is that it provides a method to determine the surface areas of solids by physical adsorption of gas molecules. It is discussed in details in the following section 2.4 BET surface.

2.3.3 Other adsorption isotherms

Besides Langmuir isotherm and BET isotherm, there are some other adsorption isotherms which are practical at certain conditions.

The linear portion of the isotherm, also known as Henry's adsorption isotherm can be presented in equation (I-13):

$$\theta=K_{eq}\,P \quad \text{(I-13)}$$

It can be used to characterized the adsorption at low gas concentration or low partial pressure [95, 101, 102]. As equation (I-13) indicates, the surface coverage linearly increases along the partial pressure of the gas under the relevant condition.

The Freundlich isotherm takes the interactions between adsorbates on the surface into consideration and can be represented by equation (I-14):

$$\theta=K\,P^{1/n} \quad \text{(I-14)}$$

It considers the enthalpy variation as a function of the surface coverage. K and n in Freundlich isotherm are dimensionless constants for a given adsorbate and adsorbent at a particular temperature. Freundlich isotherm is usually used for liquid-solid adsorption system.

2.4 BET surface of a solid

The BET surface of a solid is the specific surface area determined by means of the BET theory based on the phenomenon of physical adsorption of a probe gas on the surfaces of a material in $m^2\ g^{-1}$. The key step in the determination of specific area, is to estimate the area of adsorbates forming a monolayer on the adsorbent surface [92, 100].

Nitrogen is commonly used as the probe gas for BET determination because of its well-known molecular size, inert nature and low price. According to equation (I-11), a straight line should be obtained when plotting $\frac{1}{X\left[\left(\frac{P_0}{P}\right)-1\right]}$ as a function of $\frac{P_0}{P}$. This straight line can be obtained experimentally. Figure I-4 is a theoretical plot of the presentation of BET equation (I-11), where the slop of this line is $tan\phi$ and the intercept of the line is i. For nitrogen adsorption, this curve of is linear in the monolayer within the low concentration range, i.e. $0.05 \leq p/p_0 \leq 0.30$.

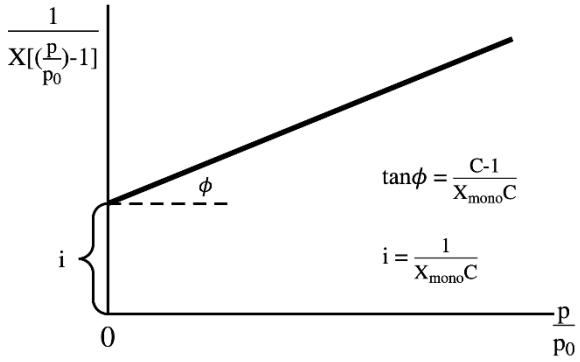

Figure I-4 Theoretical plot of the BET isotherm from equation (I-11).

The two important parameters in equation (I-11) X_{mono} and C can be calculated by equation (I-15) and (I-16):

$$X_{mono} = \frac{1}{tan\phi + i} \tag{I-15}$$

$$C = \frac{tan\phi}{i} + 1 \tag{I-16}$$

With these two parameters and the basic equation to calculate the specific surface S in m^2 from the adsorption data equation (I-17):

$$S = \frac{X_{mono}}{M} N A_m \tag{I-17}$$

where X_{mono} refers to the mass in g of the monolayer of the adsorbed gas species on the unit mass of adsorbent, M is the molecular weight in g/mol of the adsorbed gas species, N is the Avogadro's number, and A_m in m^2 is the area taken by one molecule of the adsorbed gas in the monolayer, the formula to calculate the specific surface area is given as:

$$S_{BET} = \frac{1}{tan\phi + i} \cdot \frac{N \cdot A_m}{M} \tag{I-18}$$

The Value of A_m, can be calculated from Equation (I-19):

$$A_m = 1.091 \left(\frac{M}{\varrho N}\right)^{2/3} \tag{I-19}$$

Where ϱ is the density of the adsorbate species with the assumption of close-packing of the adsorbate molecules [103].

2.5 Surface reactions and catalyst

Surface reactions involve adsorption process and occur on the surface of adsorbent. The mechanism of a surface reaction can be studied by monitoring the adsorbed phase during the surface reactions using electrical methods, i.e., inelastic electron tunneling spectroscopy [153, 154], or optical diagnostic methods, i.e., Raman or IR spectroscopy [87, 155, 163][146, 147][167].

There are two important surface reaction mechanisms: Langmuir-Hinshelwood mechanism and Eley-Rideal mechanism [92, 104, 105].

Langmuir-Hinshelwood mechanism. For Langmuir-Hinshelwood mechanism, two different molecules A and B are first adsorbed on the surface site in adsorbed phase forming AS and BS, then the adsorbed species AS and BS react with each other for further reactions. This pathway could be described with the following reactions:

$$A_g + S \rightleftharpoons AS \tag{RI-1}$$

$$B_g + S \rightleftharpoons BS \tag{RI-2}$$

$$AS + BS \longrightarrow products \tag{RI-3}$$

Eley-Rideal mechanism. Instead of being adsorbed first then reacting with each other, for Eley-Rideal mechanism the reactants A will be adsorbed first to form the adsorbed phase species AS, then AS will react directly with B in gas phase. The pathway could be described with the following reactions:

$$A_g + S \rightleftharpoons AS \quad \text{(RI-4)}$$

$$AS + B_g \longrightarrow products \quad \text{(RI-5)}$$

These two surface reaction mechanisms provide prototypes mechanism and inspirations for following studies, especially for heterogeneous interaction studies including the present work.

In some cases, the adsorbent involved in the surface reactions acts as a catalyst, providing catalytic active surface sites which accelerate the reaction rate, or triggers new reactions which will not occur without the catalyst.

The activation effect of a catalyst during the surface reactions is supposed to be constant since the catalytic active surface sites are not consumed during the reactions and only act as the intermediates. However, in reality, the catalysts are normally found to be deactivated partially or totally by side-processes during the reactions [106]. For example, the catalytic surface sites are blocked by side-productions resulting in less active sites available for the reactions.

2.6 Turnover frequency and turnover number

To determine the catalytic nature of reactions, turnover frequency (TOF) in s^{-1}, as well as turnover number (TON), is widely used [105]. They are essential to decide whether a heterogeneous reaction is catalytic or not, and allow the comparison of the intrinsic catalytic activity on different solid materials, e.g. metal oxides [107].

The definition of TOF and TON has been changed over time and may vary from one research field to another [108]. In our case, where heterogeneous interactions are studied between gas-phase molecules and surface, the TOF refers to the molecules converted per active surface site per second, and TON refers to the total number of molecules converted on one active surface site within the reaction timescale or until the surface sites lose reactivity.

$$TOF = \frac{The\ rate\ of\ molecules\ being\ converted}{N^{\circ}\ of\ active\ surface\ site}\ (s^{-1}) \quad \text{(I-20)}$$

$$TON = \frac{Total\ N^{\circ}\ of\ molecules\ converted}{N^{\circ}\ of\ active\ surface\ site} \quad \text{(I-21)}$$

If TON reaches a value higher than 1 before the surface loses its total activity, it suggests that more than one molecule has been converted by one active surface site, thus indicating that the nature of the reaction is catalytic. For a well-defined system, to determine whether a reaction is catalytic or not does not need the reactions proceed to the end. As long as the TON exceeds 1 and the reaction still continues, the conclusion of a catalytic reaction can still be obtained according to the definition of TON.

To determine the TOF or TON, it is necessary to quantify the number of active surface sites N_s in µmol m^{-2} on the surface. Several approaches have been proposed in literatures by different authors and groups to quantify the number of the active surface sites based on different probe molecules. Some common methods are listed below:

- O_2 chemisorption. This method involves reducing the surface with H_2 and reoxidation to determine the number of active surface sites by the amount of O_2 adsorbed. This is not a very accurate approach because over reduction of the metal oxide surface usually happens. It is unable to distinguish between surface acidic and redox sites [109-111].
- Adsorption of CO_2 and NH_3. In this approach, CO_2 and NH_3 do not measure all the surface sites. CO_2 only adsorbs on basic OH groups on the surface and NH_3 only adsorbs on Lewis and Bronsted acid sites. It cannot distinguish between surface acidic and redox sites either [112-114].
- Adsorption and oxidation of alcohol. This method normally uses methanol or isopropanol as the probe molecule which allows to determine the number of active surface site as well as the nature of these active surface sites, i.e., redox site/acid site [115-117].

The number of active surface sites on some commonly used metal oxides in catalyst are listed in Table I-2. These results are retrieved from the work by Deepak Kulkarni and Israel E. Wachs [115] where the active surface sites are determined by isopropanol chemisorption and oxidation. The active surface site density for surface isopropoxide species on metal oxides is expressed in µmol m^{-2}.

Table I-2 Number of active surface sites on oxide catalyst. The values are retrieved from [115].

Metal oxide	Number of active sites (µmol m^{-2})	Metal oxide	Number of active sites (µmol m^{-2})
MgO	8.9	Mn_2O_3	2.6
CaO	2.7	Fe_2O_3	7.9
BaO	0.7	Co_3O_4	3.9
TiO_2	3.2	CuO	3,9 – 4.3
ZrO_2	2.6	Ag_2O	5.2 – 5.8
CeO_2	2.5	Al_2O_3	2.8
V_2O_5	1.6	SiO_2	0.5
MoO_3	1.2		

According the values of number of active surface sites of different metal catalysts in Table I-2, the average active surface site density for isopropanol adsorption on metal oxide surface is found to be at the range of 2–4 μmol m^{-2}. SiO_2 is found to be unreactive and has a low number of active surface site, i.e., 0.5 μmol m^{-2} regardless a relatively high BET surface area, i.e. at the range of 400 m^2 g^{-1}.

2.7 Summary of uptake and adsorption theory of gases on solid surface

In this section, fundamental knowledge of uptake and adsorption theories of gases on solid surface is introduced. It discusses:

(i) The definition and characterization of uptake process of gas on solid surface.

(ii) The fundamental of adsorption theory of gas on solid surface.

(iii) Important adsorption isotherm theories, i.e., Langmuir and BET adsorption isotherms.

(iv) Surface reactions which may involve catalytic process.

Conceptions such as uptake, adsorption, adsorbent, catalyst, and parameters such as uptake coefficient, BET specific surface area, turnover number are clarified which are widely applied and discussed in this study. They are necessary for the understanding of the rest of this chapter and also the results and discussions presented in this study.

Based on the fundamental knowledge and conceptions introduced, studying the uptake of gas phase species on solid surface will provide gas-phase kinetics from the heterogeneous interaction such as the reaction order and the reaction rate related to gas phase species. Parallel with gas phase kinetics, adsorbed phase investigation provides understanding of the surface species formed and the reaction pathways during the heterogeneous interaction. These two approaches, from gas phase and adsorbed phase are essential for heterogeneous interaction studies. As a result, the literature review of the heterogeneous interaction between gas species and minerals, and also the investigation of the heterogeneous interaction between mineral dusts with ozone and acetic acid conducted in this study, are organized following gas phase approach and adsorbed phase approach.

3 Ozone uptake on mineral dusts

Ozone is a key atmospheric trace gases, which is a main component of upper atmosphere keeping Earth from the harm of UV-radiation [118] and also plays an essential role in atmospheric reaction chains [119]. The atmospheric abundance of the mineral dust makes the investigations of ozone uptake on single metal oxide essentials to understand the interaction of ozone with this geomaterial in the atmosphere. Moreover, ozone is also an important reactive species of great practical importance, such as in clinic and medicine [120, 121], plasma catalysis for VOC abatement [122, 123]. Due to the scientific significance, environmental importance as well as the wide range of applications of ozone,

special attention has payed to ozone as the model inorganic gas species in this study. As a result, in this section, a literature review of studies on the heterogeneous interactions of gas-phase ozone with natural mineral dust, as well as certain reference metal oxides is given.

The first part of this review focuses on the kinetics of gas-phase ozone and the ability of ozone uptake on the investigated materials: Which technologies and setups are used to measure the gas phase ozone? What is the gas phase profile during ozone decomposition on the surface of mineral dust? Which parameters are used to characterize the gas-phase kinetic of ozone uptake? What are the impacts of ozone exposure time, ozone concentration, humidity and the temperature on the interaction of ozone with mineral dust or metal oxides? What similarities and differences have been observed during ozone interacting with different material, such as different mineral dusts, silica, wood ash, Fe_2O_3, Fe_3O_4, Al_2O_3, TiO_2, and MnO_2? Which heterogeneous reaction mechanisms have been proposed to explain the experimental observations of ozone decomposition on mineral surface?

The second part goes into the adsorbed phase observations on the surface during ozone uptake: Which technologies and setups are used to monitor the adsorbed phase? Which IR absorption bands have been observed during ozone molecules interaction with the surface sites on various surfaces? Which surface molecular structures have been confirmed? What are the similarities and differences observed during ozone interaction with different material such as SiO_2, TiO_2, CaO, MnO_2? Which surface reaction pathways have been proposed based on the adsorbed phase investigation?

The state of the art of observations and conclusions, using different technologies, are the cornerstone of ozone uptake onto a solid surface which provide great inspirations for this PhD.

3.1 Gas phase approach

S. Suzuki et al., in 1979, studied ozone decomposition on natural sea sand, collected from the seashore in Futsu Cape, Japan, as well as reference materials such as commercially available silica, Fe_2O_3, Fe_3O_4, and Al_2O_3 using a flow setup and UV-absorption ozone analyzer [124]. Authors found out that the ozone decomposition rate was higher on the so called “iron sand” sample, which was subdivided by means of a magnet from the sea sand and compared with the “remainder sand” part. Although it does not provide much quantitative kinetic rate information, it evidenced the correlation that ozone decomposition rate decreased with the exposure time and increased in proportion with the amount of sand sample. For experiments with higher ozone concentration, the ozone decomposition rate was also higher at beginning and dropped to a lower steady-state value. They also pointed out that for silica, the ozone decomposition rates remained almost constant at a low value during the whole period of ozone exposure. For Fe_2O_3 and Fe_3O_4, authors evidenced more efficiency regarding ozone decomposition. S. Suzuki et al. concluded that the iron-containing compounds in the sea sand had higher ozone decomposition rate compared to Al_2O_3 and silica compounds.

In the study performed by A. O. Klimovskii et al. in 1982, the kinetics of ozone decomposition on γ-Al_2O_3 was measured using several devices and methods such as mass spectroscopy, thermal desorption spectroscopy, and luminescence measurement of surface species [125]. The uptake coefficient of ozone on alumina surface was measured to be 10^{-4} using the macroscopic geometric area of the sample at room temperature. They also observed that during ozone decomposition, the O_2 pressure within the system increased simultaneously. Based on their observation and also the early work by G. I. Golodets [126], they proposed a two-step mechanism for ozone decomposition:

$$O_3(g) + (\,) \xrightarrow{K_1} (O) + O_2 \qquad \text{(RI-6)}$$

$$O_3(g) + (O) \xrightarrow{K_2} 2O_2 + (\,) \qquad \text{(RI-7)}$$

where ( ) are the "active surface centers", which can be the anion vacancies according to authors. They pointed out that Reaction (RI-7) was the rate-determining reaction. Also, authors suggested that (O) were mobile enough to recombine, thus forming O_2 in gas phase through the reaction R3.

$$(O) + (O) \xrightarrow{K_3} O_2 + 2(\,) + h\nu \qquad \text{(RI-8)}$$

A. Alebic-Juretic et al. have investigated the ozone destruction efficiency on several powders including silica-gel, alumina, wood ash, Saharan sand, calcite and NaCl using a fluidized-bed reactor at room temperature and atmospheric pressure [127]. Results showing the gas-phase ozone concentration after passing through the different samples with initial ozone concentration of 100 ppb are displayed in Figure I-5. The experimental results have been taken into consideration by three points of view, according to authors:

- Considering the initial drop in ozone concentration right upon addition of the sample, the wood ash had the best performance that only 14% of the initial ozone could pass through. For Saharan sand, 30% of the gas ozone could pass through. NaCl had no effect on the gas phase ozone concentration. The efficiency of ozone destruction was listed as: wood ash > silica-gel = alumina > Saharan sand > calcite > NaCl.
- Considering the concentration of ozone which was passing through the sample layer after a certain time when a steady-state uptake regime was reached, this time the most efficient material is alumina, which would allow 58% of the initial ozone pass. Surprisingly, in their experiment, the Saharan sand, calcite and NaCl showed no sink effect of ozone after certain time of exposure. The efficiency here was: alumina > wood ash > silica-gel > Saharan sand = calcite = NaCl.
- Considering the time required to reach the steady-state ozone uptake regime for each material, silica-gel and alumina required 200 minutes which turned out to be the most effictive ozone

sink in this case. While Saharan sand took 50 minutes. The ranking of efficiency for this point of view was: silica-gel = alumina > wood ash > Saharan sand > calcite > NaCl.

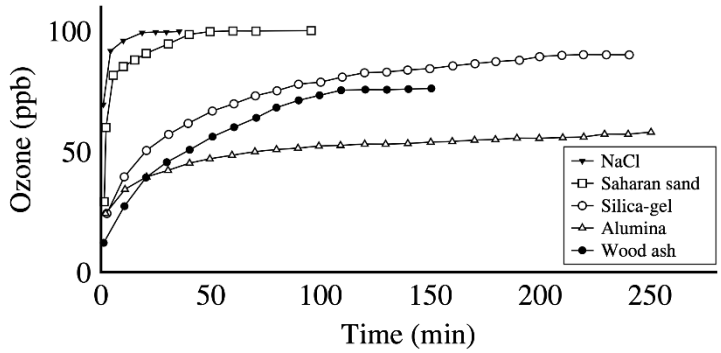

Figure I-5 Concentration profiles of gas phase ozone with initial concentration of 100 ppb as a function of time after passing through the samples: silica-gel, alumina, wood ash, Saharan sand, calcite and NaCl. The figure is reproduced based on the data retrieved from the work done by A. Alebic-Juretic et al. [127]. Copyright VCH verlagsgesellschaft mbH. W-6940 Weinheim 1992.

These results evidenced that various types of surface can uptake ozone with contrasted abilities. Based on these results and the abundance of particles in the atmosphere, it is suggested that these surfaces could serve as sinks of ozone in the atmosphere. They also investigated the impact of the surface area of the materials on ozone uptake and have observed that the time required to reach the steady-state uptake regime increased proportionally with the increase of surface area on SiO_2 [128]. In their later work in 2000, A. Alebic-Juretic et al. [129] considered the kinetics and mechanism of ozone decomposition on various surfaces. Authors pointed out that the removal process of ozone from air flow includes the adsorption of ozone onto the surface and the following chemical and/or catalytic reactions which occur on the surface active sites until the surface active sites are fully occupied or inactivated. Moreover, they evidenced that the process could not be simply described by first order kinetics. Also, their previous observation that the ozone uptake was faster at the beginning of the experiment, then the ozone uptake efficiency decreases gradually, was consistent with the mechanism proposed by A. O. Klimovskii et al. where the “active surface centers”, according to the authors, are consumed along ozone uptake [125].

A. E. Michel et al. have investigated the heterogeneous reactive uptake of ozone on mineral dust such as a mineral clay from Alfa Aesar, authentic natural China loess and Saharan dust, as well as some minerals and mineral oxides such as kaolinite from Alfa Aesar, α-Al_2O_3, α-Fe_2O_3, SiO_2 in a Knudsen cell reactor combined with a mass spectrometer [126, 130]. They observed that the mass signal for ozone (m/e = 48) dropped immediately when the surfaces of the materials were exposed to ozone, indicating that ozone molecules in gas phase were taken up by the surface of solids. Compared with α-Fe_2O_3 with whom the mass signal of ozone remained lower at a constant intensity, the mass signal of ozone with

Saharan dust and China loess displayed a slightly rising tendency towards the baseline but within the experimental time scale, it never returned back to baseline. Finally it reached a steady-state value with the presence of ozone. Figure I-6 shows the mass signal of ozone as a function of time during the ozone uptake on (a) 7.2 mg of α-Fe_2O_3 and (b) 37.3 mg of Saharan dust using a Knudsen cell from their experiments. The α-Fe_2O_3 and Saharan dust sample were exposed to 8 ppb and 11 ppb of ozone respectively when the sample holder lid was indicated as "open". They pointed out that the different between authentic mineral dust and pure metal oxides might be due to the organic compounds contained on the natural mineral dust surface, which might react greatly at the beginning of ozone uptake [131].

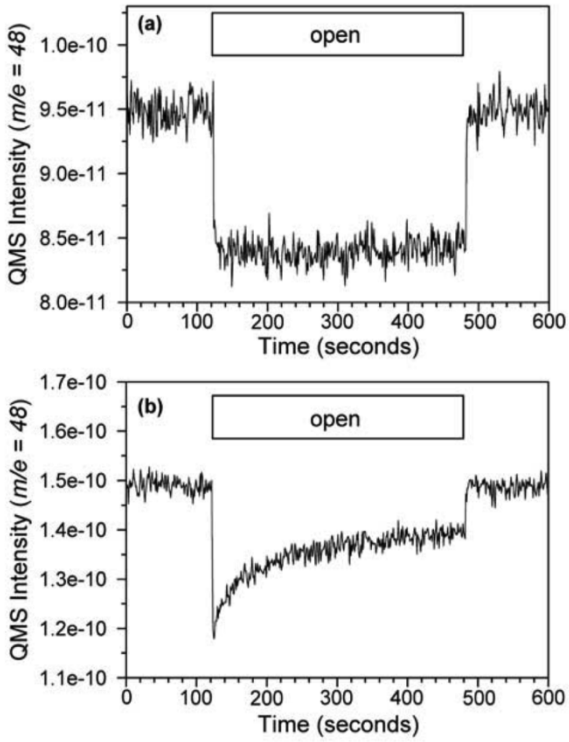

Figure I-6 Mass signal of ozone as a function of time during the ozone uptake on (a) 7.2 mg of α-Fe_2O_3 and (b) 37.3 mg of Saharan dust using a Knudsen cell. α-Fe_2O_3 and Saharan dust sample were exposed to 8 ppb and 11 ppb of ozone respectively during the period indicated as "open" in the figure. This figure is retrieved from [132].

A. E. Michel et al. also calculated the initial uptake coefficient of the solid samples using the BET surface area, which are $8 \pm 5 \times 10^{-5}$ for α-Al_2O_3, $1.8 \pm 0.7 \times 10^{-4}$ for α-Fe_2O_3, $5 \pm 3 \times 10^{-5}$ for SiO_2, $2.7 \pm 0.9 \times 10^{-5}$ for China loess, $6 \pm 3 \times 10^{-5}$ for ground Saharan dust and $4 \pm 2 \times 10^{-6}$ for sieved (< 50 mm) Saharan dust. The higher value observed with α-Fe_2O_3 was in agreement with the result from S. Suzuki et al. [124]. In their later study in 2003 [130], Michel et al. determined the steady-state uptake coefficient of ozone onto α-Al_2O_3, α-Fe_2O_3 and ground Saharan dust using the same protocol at the 4.5-h exposure time. The steady-state uptake coefficient is reported to be 7.6×10^{-6} for α-Al_2O_3, 2.2×10^{-5} for α-Fe_2O_3, and 6×10^{-6} for ground Saharan dust. The ozone uptake rate and the

total ozone uptake amount along time have been calculated. Figure I-7 displays their results of ozone uptake rate and total ozone uptake of 18 ppb of ozone onto 6.6 mg of α-Fe_2O_3 and 24 ppb of ozone onto 6 mg of α-Al_2O_3 as a function of time. They pointed out that although the ozone uptake rate on α-Al_2O_3 and α-Fe_2O_3 decreased significantly after a certain time of exposure, the samples still continued to consume ozone, with the order of 3×10^{14} molecules per minutes and total ozone uptake of $1 - 2.5 \times 10^{-5}$ molecules. This observation is in agreement with the report of Alebic-Juretic et al. [127-129] as well as the other studies focusing on the ozone uptake on metal oxides [133-135]. By taking the individual sample masses and surface areas into account, Michel et al. estimated that after 4.5 h of exposure, for both α-Fe_2O_3 and α-Al_2O_3, the surface coverages were greater than, or approaching 10^{15} molecules cm^{-2}, which exceeded the upper limit of the expected surface site number of 10^{15} site cm^{-2}. As a result, they suggested the catalytic nature of ozone uptake onto mineral particles and at the same time, pointed out the possible role of heterogeneous reactions on atmospheric chemistry for ozone loss.

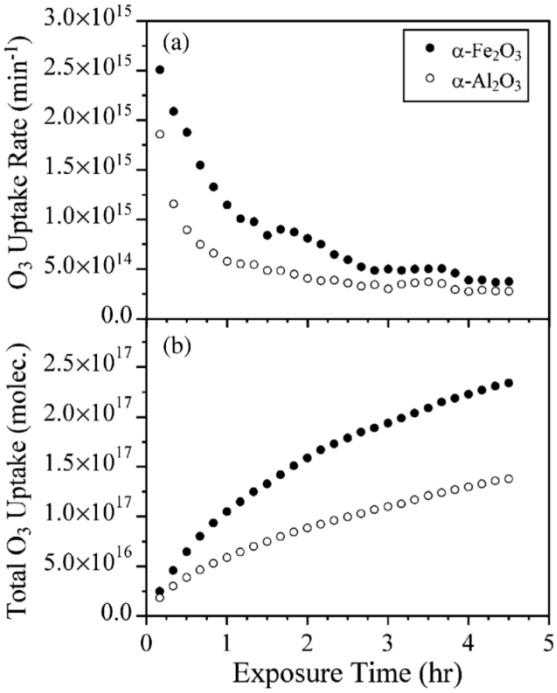

Figure I-7 (a) Ozone uptake rate (min^{-1}) and (b) total ozone uptake (molecules) of 18 ppb of ozone onto 6.6 mg of α-Fe_2O_3 and 24 ppb of ozone onto 6 mg of α-Al_2O_3 as a function of time. The figure is retrieved from [130].

F. Hanisch and J. N. Crowley have investigated the ozone uptake onto Saharan dust, which was collected from the Cape Verde Island in Knudsen reactor using mass spectrometer [136]. The kinetic of gas phase ozone uptake was determined under room temperature (296 K) with total pressure inferior to 1 mTorr and ozone number density of 3.1×10^{10} to 1.7×10^{13} cm^{-3}. The gas phase ozone concentration profile was observed: a fast initial drop followed by a rising tendency towards baseline and finally reached a

steady-state regime lower than initial level. It was consistent with the observations of A. E. Michel et al. [126, 130] in Knudsen reactor as well, also with the observations using other experimental setups by S. Suzuki et al. [124] and A. Alebic-Juretic et al. [129] as mentioned previously. In agreement with A. E. Michel et al. [126, 130], F. Hanisch and J. N. Crowley calculated the uptake coefficient of ozone onto Saharan dust using BET surface area to take the mass of the sample into consideration. Furthermore, they evidenced the dependence of uptake coefficient on ozone concentration: for lower ozone concentrations, the uptake coefficients were found to be one magnitude higher than those with higher ozone concentration. The range of value of ozone uptake coefficient within the experimental condition was from 2.2×10^{-6} to 4.8×10^{-5}, which was quite consistent with what Michel has determined using Knudsen reactor with similar ozone concentration on Saharan dust [130]. F. Hanisch and J. N. Crowley also made a test consisting in heating the dust sample and compared the ozone uptake on it with the unheated one. Greater ozone uptake was found on the heated Saharan dust sample than on the unheated sample, which was consistent with the conclusion made by L. Aldaz [137] that ozone is taken up much more efficiently on dry soils than on the wet soils. Additionally, several other kinds of mineral dust such as Arizona Test dust, Chinese dust from Taklamakan desert and the clay minerals kaolinite, illite, Ca-montmorillonite and palygorskite were examined, unfortunately only results of initial ozone uptake coefficient based on geometric surface were provided for these samples.

In a very recent study, J. Lasne et al. have experimentally examined ozone uptake onto clay dusts, more precisely montmorillonite and kaolinite using a horizontal double-wall flow-tube reactor interestingly operated under atmospheric pressure [138]. The influence of relative humidity (RH) has been investigated under different RH conditions at 296 K with initial gas ozone concentration of 40 ppb in the dark. A linear decrease of BET steady-state uptake coefficient of ozone on montmorillonite has been observed which was consistent with the observation from P. K. Mogili et al. [139] J. M. Roscoe et al. [140] on the surface of alumina and α-Fe_2O_3. Additionally, after comparing their kinetics results with those found in literature, authors highlighted the strong difference between experiments performed at atmospheric pressure, e.g., flow-tube reactor and environmental chamber experiments, and at low pressure, e.g., Knudsen cell experiments, as showed in Figure I-8 where the reference numbers should be referred in the original article by J. Lasne et al. [138]. As authors pointed out, the uptake coefficients obtained under low pressure were higher than those obtained under atmospheric pressure while similar partial pressures of ozone are used.

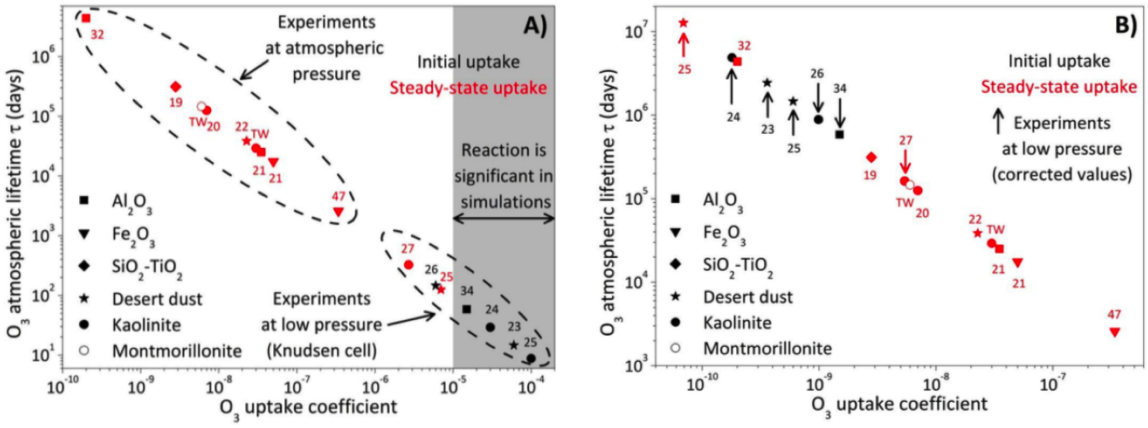

Figure I-8 (A) The atmospheric lifetime of ozone as a function of ozone uptake coefficient onto different minerals in literature. The reference number should be referred in the original article [138] and TW refers the original work. (B) The uptake coefficients and ozone atmospheric lifetimes have been corrected taking the pressure in the experimental setups into account. The figure is retrieved from [138].

Based on the work reported by G. I. Golodets [126], A. O. Klimovskii et al. [125], and A. Alebic-Juretic et al. [129], a possible mechanism of ozone uptake on the surface of metal oxides were discussed by the authors. Regardless of small nuances from one mechanism to another, authors all suggested that the first step of the decomposition of an ozone molecule was the attachment of the ozone molecule on the active surface site of the surface through a terminal oxygen atom. Then following surface reactions led to the decomposition of attached ozone molecules into O_2 molecules and some surface-bonded O species. These surface-bonded species might participate into the reactions of ozone decomposition too. As a result, experiments focusing on adsorbed phase ozone uptake on dusts were required to provide evidence and more details. To that regards, several experimental studies were conducted to investigate the mechanism of ozone uptake onto metal oxide surfaces.

3.2 Adsorbed phase approach

K. M. Bulanin et al. conducted the first detailed investigation of molecular ozone adsorption onto various metal oxides at very low temperature, i.e. 77 K, using FTIR spectroscopy [141-143]. The metal oxides examined are TiO_2, Al_2O_3, ZnO, SiO_2, ZrO_2, MgO, CeO_2 and CaO. Authors observed the IR spectra of adsorbed $^{16}O_3$, $^{18}O_3$ on SiO_2 and TiO_2, and also observed the isotopic modifications on adsorbed phase. K. M. Bulanin et al. evidenced the basic properties of ozone molecules. They noticed that ozone molecules formed hydrogen bonds with acidic surface OH groups through one of the terminal oxygen atoms during the uptake on SiO_2, as displayed in Figure I-9 (a). Authors also explained the orientation for strongly bonded ozone molecules based on the ozone uptake onto three types of the surfaces of TiO_2: completely hydroxylated, well-pumped at 300 K and evacuated at 773 K to control the strength of different Lewis acid sites. They suggested that ozone molecules attached to the surface sites via one of the terminal atoms, as showed in Figure I-9 (b). These results were consistent with their

preliminary experiments with rutile TiO_2, ZrO_2, MgO and CeO_2 where the same ozone adsorption form was found. K. M. Bulanin et al. also observed the acidic properties of ozone molecules concentrated at the central oxygen atoms with the OH group on the surface of CaO [142]. They observed an IR band at 812 cm^{-1} and suggested that this corresponds to the chemical adsorption of ozone molecules on basic sites forming a peroxide species. The central oxygen atom in this case, acts as an electron acceptor when interacting with the oxygen atom of a basic hydroxyl group as showed in Figure I-9 (c).

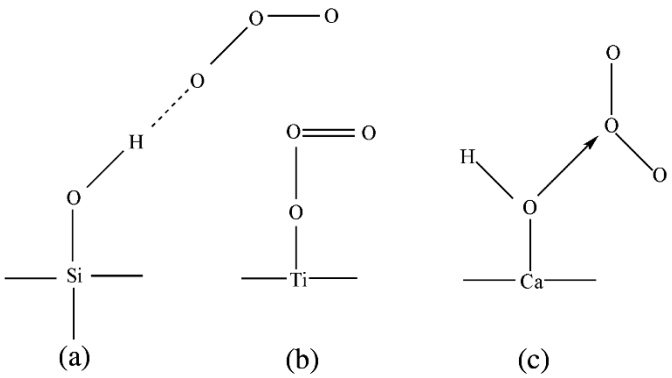

Figure I-9 Possible adsorption modes of ozone on the surface of (a) SiO_2, (b) TiO_2, and (c) CaO. Adapted from K. M. Bulanin et al. [142-144].

For the interaction of ozone with strong Lewis sites, K. M. Bulanin et al. suggested dissociative adsorption resulting in the formation of atomic oxygen atoms as intermediates during the ozone decomposition reactions. This mechanism proposed by authors could well explain why γ-Al_2O_3, which exhibits strong Lewis acidity on its surface, shows excellent property to decompose ozone at low temperature in the review of A. Klimovskii et al. [125]. Figure I-10 illustrates ozone decomposition mechanism. Even at 77 K, the physically adsorbed ozone molecules could not be evidenced due to the band-overlapping with the extensive hydrogen bonding of ozone molecules with the surface OH groups. As a result, authors made the conclusion that no molecular adsorption of ozone occurs on strong Lewis sites on the surface TiO_2, Al_2O_3, ZnO.

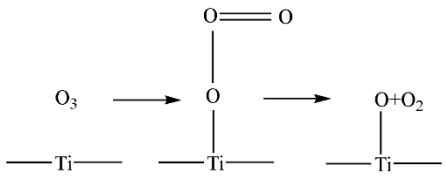

Figure I-10 Schematic diagram to illustrate the mechanism of ozone decomposition on the surface of TiO_2 adapted from the work of K. M. Bulanin et al. [143].

K. Thomas et al. studied the ozone adsorption on γ-Al_2O_3 using IR spectroscopy at low temperature, i.e. 77K [145]. Two important conclusions can be drawn from their work. One is that they proved that the

product of ozone decomposition is oxygen by the perfect match between the oxygen pressure rise measured inside the sample cell and the calculation based on the reaction pathway. Another one is that they proved that the strong Lewis acid sites on the surface played main role for ozone decomposition by the experimental observation that ozone decomposition stopped when these surface sites were poisoned by pyridine and the theoretical calculations. The essential role of active surface sites, mostly Lewis acid sites, was emphasized. Meanwhile, further investigation focusing on the surface species formed during the interactions of ozone molecules and surface sites was required.

In that regard, W. Li et al. investigated ozone decomposition on supported MnO_2 under room temperature and atmospheric pressure using in-situ Raman spectroscopy and the method of ab initio molecular orbital calculation [146]. They have observed an adsorbed species with a Raman signal at 884 cm^{-1} when the sample was exposed under ozone flow as reported in Figure I-11. Based on the Raman spectra information, and the comparison of isotope shift value $\nu(^{18}O)/\nu(^{16}O)$ compared with the calculated value, they assigned this Raman band at 884 cm^{-1} to surface peroxide species.

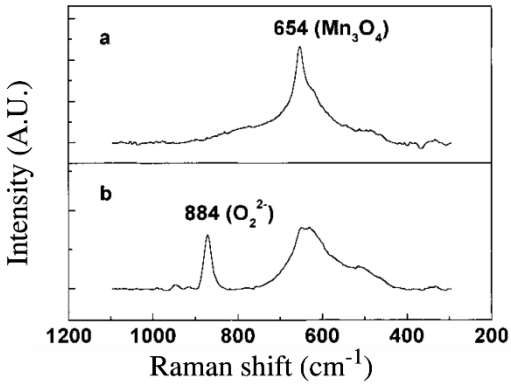

Figure I-11 In-situ Raman spectra of MnO_2 in (a) pure oxygen, (b) 2 mol % ozone/oxygen mixture at room temperature with flow rate of 1000 sccm. The figure is retrieved from W. Li et al. [146].

Carefully designed experiments by means of ^{18}O isotopic substitution measurement were also carried out to elucidated the reaction mechanism, which was described as the following reactions where * represented an active surface site.

$$O_3 + * \rightarrow (O*) + O_2 \quad \text{(RI-9)}$$

$$O_3 + (O*) \rightarrow (O_2*) + O_2 \quad \text{(RI-10)}$$

$$(O_2*) \rightarrow O_2 + * \quad \text{(RI-11)}$$

The reaction pathway proposed by W. Li et al is consistent with what proposed by A. O. Klimovskii et al. [125] in the previous section, where "( )" which refers to the "surface active center" in Reactions (RI-6), (RI-7) and (RI-8), is the equivalence of the active surface site " * " above.

In the following investigation of the steady-state and transient kinetic of ozone decomposition on MnO_2 by W. Li et al, they confirmed the role of surface peroxide species as a reaction intermediate and the reaction products as oxygen molecules and an atomic oxygen species during ozone decomposition [134].

J. M. Roscoe and J. P. D. Abbatt studied the interaction of ozone with the surface of alumina using the diffuse reflectance FTIR (DRIFT) at ambient temperature [140]. They observed a new spectroscopic feature at 1380 cm^{-1} after exposing the dry surface of alumina to ozone and assigned it to a surface oxide species on alumina, most likely to be a M=O species, due to the interaction of ozone with the Lewis acid sites on the surface of alumina. Figure I-12 displayed the FTIR spectra retrieved from the original work where on the FTIR spectrum of ozone uptake on dry alumina, besides the peak at 1380 cm^{-1}, a much weaker peak at 1740 cm^{-1} was also assigned to surface oxide species by authors, can also be observed.

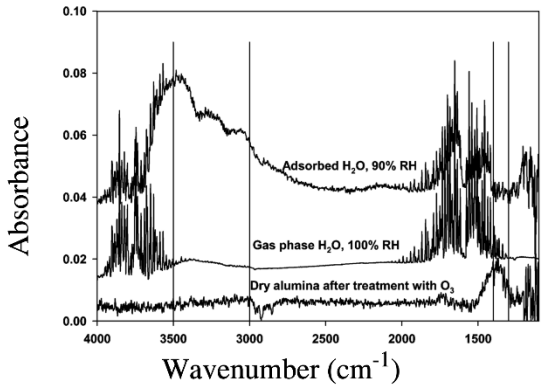

Figure I-12 FTIR spectra of ozone uptake onto dry alumina, water adsorbed on alumina, and gas phase water. The figure is retrieved from [140].

Additionally, J. M. Roscoe and J. P. D. Abbatt also investigated the impacts of water molecules on ozone decomposition with varying relative humidity. By measuring the growth of the DRIFT peak at 1380 cm^{-1}, they showed the competition of ozone molecules and water molecules for the surface sites on the surface of alumina with direct and quantitative kinetic information for the first time. Figure I-13 reports the profile of the peak area of the oxide peak at 1380 cm^{-1} along ozone uptake on the surface of alumina. The peak area was calculated by integrating the peak from 1300 to 1400 cm^{-1} under different conditions indicated in Figure I-12. Clearly with the presence of humidity, the oxide peak area growth is at a smaller extent.

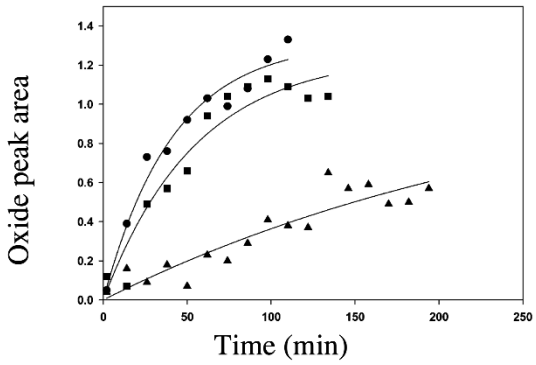

Figure I-13 Time evolution of the peak area of the oxide peak at 1380 cm^{-1} during ozone uptake on the surface of alumina. The peak area is calculated by integrating the peak from 1300 to 1400 cm^{-1} under: (●) dry O_2 as carrier gas, 13.0 mg of alumina and 2.5×10^{13} molecules cm^{-3} of ozone, (▲) equal amount of mixture of dry O_2 and dry N_2 as carrier gas, 14.1 mg of alumina and 1.3×10^{13} molecules cm^{-3} of ozone, (■) equal amount of mixture of dry O_2 and humid N_2 as carrier gas, 8 mg of alumina and 2×10^{13} molecules cm^{-3} of ozone. The lines are the first-order growth curve fitted to the individual data. The figure is retrieved from [140].

Recently, J. Jia et al. studied the decomposition of gaseous ozone on MnO_2 with different crystal structures using in-situ Raman spectroscopy to address the intermediate groups in the adsorbed phase during ozone uptake [147]. Among the three MnO_2, i.e. α-, β-, γ-MnO_2, authors found that α-MnO_2, with the largest specific surface area 80.7 m^2/g (13.8 m^2/g for β-MnO_2, and 74.6 m^2/g for γ-MnO_2) shows the highest activity for ozone decomposition. Moreover, when the samples were exposed to ozone/oxygen flow, peak at 835 cm^{-1} was observed which has been already assigned to O-O stretching mode of peroxide species (O_2^{2-}) by W. Li et al [146]. A new band at 1658 cm^{-1} is also observed and the authors suggest that this is the overtone of the O-O stretching vibration of the peroxide species since the wavenumber is almost twice than that of the peak at 835 cm^{-1}. Based on their observation, a similar ozone decomposition mechanism involving oxygen vacancy site, i.e. V_O according to authors, is proposed where ozone molecules could insert an O atom.

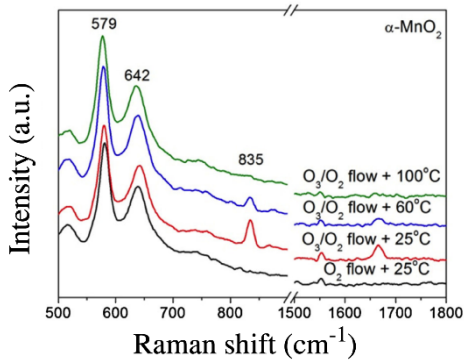

Figure I-14 In-situ Raman spectra of α-MnO_2 exposed under oxygen flow and oxygen/ozone flow mixture at different temperature. This figure is retrieved from [147].

J. Jia et al. also investigated the impact of temperature on the activity of ozone decomposition from 5 to 100˚C. No obvious impact of temperature is reported on α-MnO_2 since α-MnO_2 is an excellent ozone decomposer and the ozone removal efficiency remained 100% for all the temperature range tested. However, for β- and γ-MnO_2, a clear promoting effect of higher temperature is observed. They exhibit low reactivity for ozone decomposition at 5˚C but for both β- and γ-MnO_2, ozone removal efficiency reaches 100% when temperature exceeds 60˚C. Another conclusion is pointed out by authors according to the comparison among the three MnO_2 with different crystal structures: the specific surface reaction rate, i.e. the amount of ozone decomposed on unit specific surface area per time unit, is not the only factor which determines the overall ozone decomposition performance, since β-MnO_2 has the largest specific surface reaction rate, almost three times higher than those of the other two, but the lowest overall reaction rate due to the lowest specific surface area.

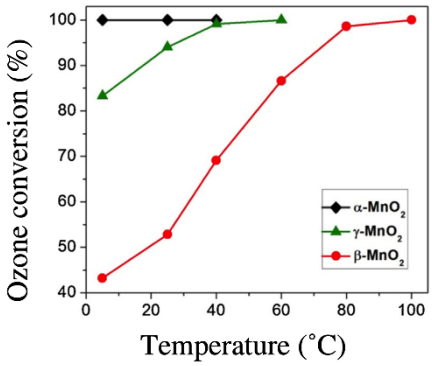

Figure I-15 Ozone conversion as a function of temperature over three different MnO_2, i.e. α-, β-, γ-MnO_2, with ozone inlet concentration of 14 ppm and weight space velocity of 660 L g^{-1} h^{-1}. This figure is retrieved from [147].

3.3 Conclusions and problematics

Based on previous literature review, important conclusions can be summarized:

- Knudsen cell has been widely used in literature [124, 126, 130, 136] to study the gas phase kinetics of ozone-solid interaction. Besides, some other reactors such as fluidized-bed reactor [127], flow-through reactor [125], double-wall flow-tube reactor [138] have also been used. The gas phase ozone concentration has been measured by devices based on various technologies such as UV-absorption ozone analyzer [124, 138], mass spectroscopy [125, 126, 130, 136], and FTIR spectroscopy [141-143]. The adsorbed phase has been measured by IR spectroscopy [145], in-situ Raman spectroscopy [146, 147], FTIR spectroscopy [141-143], diffuse reflectance FTIR (DRIFT) [140].
- Ozone is evidenced to decompose on the surface of the investigated metal oxides, such as Al_2O_3, Fe_2O_3, Fe_3O_4, SiO_2, TiO_2, MgO, CeO_2, CaO, MnO_2, and minerals and dusts, such as kaolinite,

Saharan dust and China loess with the observation of the loss of ozone from gas phase. For most investigated materials, the ozone decomposition rate has been evidenced to decrease with the exposure time for a given amount of material, suggesting the passivation of the surface by ozone. Steady-state ozone uptake regime has been observed during ozone uptake on SiO_2 [128, 129], Al_2O_3[129-131, 139, 145], Fe_2O_3 [130-132, 140], Saharan dust [136], TiO_2 [143] and MnO_2 [146, 147].

- Initial uptake coefficients of ozone uptake on the surface have been determined to be in the range of 10^{-6} – 10^{-4} using BET surface and Knudsen cell reactor [124, 126, 130, 136]. The uptake coefficient has found to decrease with the increase of the gas phase ozone concentration [136, 138-140]. For similar ozone concentration, the uptake coefficients obtained under low pressure with Knudsen cell are found to be higher (up to 5 orders of magnitudes) than those obtained under atmospheric pressure using flow-tube reactor or environmental chamber.
- The negative impact of water molecules on ozone uptake has been observed by M. Tang et al. [1], Y. Bedjanian et al. [78] and A.E. Zein et al. [80, 148]. Promoting effect of higher temperature on ozone uptake has been observed on β- and γ-MnO_2 [147].
- The strong Lewis acid sites on the surface played main role for ozone decomposition [141-143, 145]. No molecular adsorption of ozone molecules on the strong Lewis sites of the surface has been observed [141-144].
- Surface oxygenated groups are formed when ozone decomposes on surface sites (SS). J. M. Roscoe and J. P. D. Abbatt [140] have observed DRIFT band on Al_2O_3 at 1380 cm^{-1} attributed to oxygenated surface species designated as SS-O. W. Li et al [146] have observed Raman band at 884 cm^{-1} on MnO_2 and assigned this band to surface peroxide species, i.e. SS-O_2. J. Jia et al. [147] confirmed that the surface peroxide species denoted as SS-O_2 leads on α-MnO_2 to a peak at 1658 cm^{-1} corresponding to an overtone contribution of the peak at 835 cm^{-1}.
- Authors [125, 126, 129, 134, 140, 146, 147] agreed that the mechanism of ozone decomposition on the surface involves the interactions between ozone molecules and surface sites, during which surface oxygenated species, i.e. SS-O and SS-O_2, are formed and oxygen are produced.

The evidence of ozone decomposition properties of the investigated mineral particle suggests that the heterogeneous interaction of mineral particles in atmosphere with ozone may lead to ozone loss thus influencing the ozone budget in atmosphere.

However, most of the experiments dedicated to gas phase ozone kinetics determination have been conducted with Knudsen cell. The results reported in literature using Knudsen cells, in fact, are not directly relevant to real atmospheric processes since they have been carried out under non-relevant atmospheric conditions (i.e. several orders of magnitude lower pressure than in real atmosphere and

under dry conditions where in real atmosphere the relative humidity varies from 10 to 100 %). They reported higher uptake values than those determined under atmospheric pressure. The Knudsen cell is a low-pressure flow reactor operated under 10 mTorr total pressure, meaning 5 orders of magnitude lower than atmospheric pressure. This pressure difference can considerably impact the mechanism of ozone decomposition and bias the determination of uptake coefficient values. The latter has been precisely evidenced by Lasne et al.[138] as mentioned previously and also reported by Mogili et al [139] and Hanning-Lee, M. et al [149]. As a result, Knudsen cell data only represents an upper limit of the uptake coefficients which has been clearly emphasized in the latest IUPAC evaluation [88].

Besides the limits due to Knudsen cell, the ozone concentrations applied in literature are mostly at ppb level since most of the studies only focus on atmospheric chemistry. The reactivity of the materials toward ozone of high concentrations, i.e. ppm level, are poorly studied. Moreover, the studies of the impacts of water molecules on ozone uptake are limited as well.

Another limit is that the fundamentals of ozone decomposition are mostly investigated on single synthetic metal oxides. The surface states of single metal oxides are rather simple and homogeneous, compared with natural mineral dusts, of which the surface states are complex. The information from literature are not adequate for the understanding of ozone interacting with natural mineral dusts.

As a result, investigations of the interaction of ozone and authentic natural mineral dust under atmosphere-relevant conditions, i.e. relevant gas phase concentration range and relative humidity, are needed for both fundamental studies and applications.

4 VOCs uptake on mineral dusts

VOCs represent another important group of gas species extensively existing in atmosphere and human living space. They play an important role in atmospheric chemistry, e.g., as ozone precursors or intermediates in chemical oxidation cycles [80]. The interactions between some acidic VOCs with mineral dusts can influence the acidity of the surface of mineral dusts [87, 150], thus influencing the related chemical reactions. Among the group of VOCs, acetic acid, as one of the most abundant carboxylic acid in troposphere [87, 150], is rather representative. It is also a primary indoor air pollutant as well as one of most important intermediates and final degradation products during the oxidation process of other VOCs [151], e.g., in the application of plasma-catalysis for VOC abatement [150, 152]. Moreover, acetic acid can be strongly adsorbed on the surface of adsorbents changing their surface properties and performance [87]. As a result, special attention has been addressed on acetic acid in this study. Literature studies of the interactions of acetic acid, as well as other VOCs such as formic acid, formaldehyde and etc., with mineral particles are reviewed. The results from different groups concerning for the same or similar topics will be compared and discussed correspondingly. This section will also focus on both gas phase and adsorbed phase investigation on VOC uptake on the surface of minerals,

addressing the questions: What technologies and methods have been used? What about the adsorption properties of the minerals towards VOCs? What molecular structures of adsorbed VOC are formed on the surface? What about the reversible nature of VOC interaction with mineral surfaces? What are the influences of humidity and temperature on VOC uptake? What is known about the mechanisms of VOC interaction with mineral surface?

4.1 Gas phase approach

P. Li et al. investigated the surface reactions of acetaldehyde, acetone and propionaldehyde on metal oxide particles, i.e. SiO_2, Al_2O_3, Fe_2O_3, TiO_2 and CaO by FTIR monitoring and Knudsen cell experiments [155]. In the Knudsen cell measurement study coupled with mass spectrometry, P. Li et al. have observed of the drop of the QMS signal of tested VOCs during surface exposure which indicates the uptake of the carbonyl compounds by the surfaces. Compared with other minerals, SiO_2 is found less reactivity towards VOC adsorption. Besides, they also observed a small amount of the larger molecular weight unsaturated carbonyl in the gas phase by mass spectrometry attesting of the surface self-coupling reactions of the carbonyls. The product during the uptake of acetaldehyde on CaO is identified as crotonaldehyde. As a result, P. Li et al. suggested that the formation of the heavier carbonyls compounds occurs during the uptake of the test VOCs on the surfaces of minerals and also pointed out that this formation is also found to be pressure dependent according to authors.

P. Li et al. calculated the initial uptake coefficients under the relative experimental conditions and using BET surface area and the results are reported in Table I-3. The results show that the initial uptake coefficients of all the three VOCs, i.e., acetaldehyde, acetone and propionaldehyde on SiO_2 are smaller than the values on other metal oxides. It is consistent with the observation that the adsorption of VOCs on SiO_2 is weak and reversible.

Table I-3 Initial uptake coefficients of acetaldehyde, acetone and propionaldehyde on mineral oxide particles [155].

VOC	Initial uptake coefficient				
	SiO_2	α-Al_2O_3	α-Fe_2O_3	TiO_2	CaO
acetaldehyde	7.0×10^{-6}	3.2×10^{-5}	2.9×10^{-6}	9.4×10^{-5}	3.0×10^{-4}
acetone	6.2×10^{-6}	2.0×10^{-5}	1.6×10^{-4}	36×10^{-4}	1.2×10^{-4}
propionaldehyde	1.1×10^{-5}	4.7×10^{-5}	5.1×10^{-5}	1.5×10^{-4}	5.9×10^{-4}

S. Carlos-Cuellar et al. [87] reported the uptake of acetic acid, formaldehyde, and methanol on SiO_2, α-Al_2O_3, and α-Fe_2O_3 using the same method as P. Li et al. [155]. The initial uptake coefficients are determined and listed in Table I-4.

Table I-4 Initial uptake coefficients of acetic acid, methanol, and formaldehyde (6 μTor) on metal oxides [87].

VOC	Initial uptake coefficient		
	SiO_2	α-Al_2O_3	α-Fe_2O_3
acetic acid	$(2.4 \pm 0.4) \times 10^{-4}$	$(2 \pm 1) \times 10^{-3}$	$(1.9 \pm 0.3) \times 10^{-3}$
methanol	$(4 \pm 2) \times 10^{-6}$	$(1 \pm 0.7) \times 10^{-4}$	$(1.9 \pm 0.4) \times 10^{-4}$
formaldehyde	$(2.6 \pm 0.9) \times 10^{-7}$	$(7.7 \pm 0.3) \times 10^{-5}$	$(1.1 \pm 0.5) \times 10^{-4}$

According to S. Carlos-Cuellar et al., all the three VOC, i.e. acetic acid, formaldehyde, and methanol, are adsorbed on the surface of the metal oxides irreversibly. From the Knudsen cell investigation results in Table I-4, Acetic acid is found to be the most reactive one due to the carboxylic functional group in this compound, while SiO_2 is evidenced to be the less reactive metal oxide. This conclusion is consistent with the previous publication on acetaldehyde, acetone and propionaldehyde uptake on SiO_2, Al_2O_3, Fe_2O_3, TiO_2 and CaO by P. Li et al. [155] where SiO_2 also exhibits the lowest reactivity since the other metal oxides have surface sites of strong basic or acidic properties. Moreover, S. Carlos-Cuellar et al. also determined the surface coverages of these VOCs under a pressure of several μTorr when the uptake was no long observed. For α-Al_2O_3 and α-Fe_2O_3, the saturated surface coverages of acetic acid, formaldehyde, and methanol are all in the range of 10^{13} molecules cm^{-2}, meanwhile for SiO_2, the saturated surface coverage is two orders of magnitude lower, consistent with the their previous conclusion obtained from uptake coefficient as well as from P. Li et al. [155].

Focusing on the carboxylic acids, detailed investigations of heterogeneous interactions of formic acid, acetic acid as well as propionic acid on α-Al_2O_3 have been carried out by S. R. Tong et al. at ambient condition using DRIFT spectroscopy [167]. The reactive uptake coefficients, which refers to the rate of carboxylate ions formation on the surface divided by the total surface collision number per unit time according to authors, are calculated using geometric surface and BET surface respectively and listed in Table I-5.

Table I-5 Reactive uptake coefficients for the uptake of formic acid, acetic acid and propionic acid on α-Al_2O_3 based on DRIFT measurement [167].

VOC	Reactive uptake coefficients	
	Geometric	BET
formic acid	$(2.07 \pm 0.26) \times 10^{-3}$	$(2.37 \pm 0.30) \times 10^{-7}$
acetic acid	$(5.00 \pm 0.69) \times 10^{-3}$	$(5.99 \pm 0.78) \times 10^{-7}$
propionic acid	$(3.04 \pm 0.63) \times 10^{-3}$	$(3.03 \pm 0.52) \times 10^{-7}$

As pointed in Table I-5, the values of the uptake coefficients of the three carboxylic acids are close to each other, which addresses the contribution of the same function group, i.e., carboxylic functional group, to the reactivity to adsorb on the surface. The corresponding life time of these carboxylic acid with the interactions of the dust in the atmosphere is estimated to range from 50 min to 25 h for formic acid, from 23 min to 12 h for acetic acid, and from 43 min to 21 h for propionic acid. S. Carlos-Cuellar et al. pointed out that the heterogeneous interactions between acetic acid with mineral dust in the atmosphere is competitive with photolysis process of acetic acid, which leads to an atmospheric life time of 1.3 days for acetic acid.

4.2 Adsorbed phase approach

Besides the gas phase kinetics of VOC-mineral interaction, studies of the interaction between VOCs and mineral surfaces are focusing more on the adsorbed phase during VOCs molecules uptake on minerals, which provide details about the surface groups formed in adsorbed phase during the heterogeneous interaction and the mechanism underneath.

4.2.1 Molecular structures of adsorbed VOCs on mineral surfaces.

H. E. Evans and W. H. Weinberg studied the vibrational structures of adsorbed acetic acid, as well as adsorbed ethanol and acetaldehyde on the surface of alumina using inelastic electron tunneling spectroscopy (IETS) between 295 and 475 K (575 K for ethanol) [153, 154]. With a detailed IET spectra analysis and literature study with both IET and infrared/Raman studies, authors provided new insights regarding the adsorbed phase during the heterogeneous interactions. For the adsorption of ethanol on alumina, at low temperature (T < 470 K), ethoxide is formed on the surface with one O atom of ethanol bonded with Al atom of the surface as showed in Figure I-16 (a). While at higher temperatures (T > 470 K), acetate-like species are formed, as showed in Figure I-16 (b).

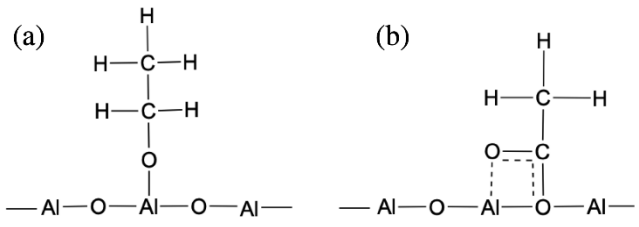

Figure I-16 Adsorption modes of adsorbed ethanol on alumina surface at (a) lower temperatures (T < 470 K), and (b) higher temperatures (T > 470 K).

For acetic acid, asymmetric and symmetric O-C-O stretching vibrations were observed. Based on the positions of asymmetric and symmetric O-C-O stretching bands and their difference, authors suggested that when adsorbed on the surface, acetic acid molecules were bound in bidentate structures on the surface. The bidentate structures can be either two oxygen atoms bounded to the same Al atom, or they

are bound to different Al atoms, as illustrated in Figure I-17. According to authors, the adsorbed acetic acid molecules have the bidentate symmetrical bridging structure. The similar peak positions and their differences in positions, especially for the O-C-O stretching peaks, of acetic acid and acetaldehyde suggested that acetaldehyde formed an acetate on the surface of alumina of the same structure, i.e. bidentate symmetrical bridging structure, as acetic acid does. Interestingly, during the adsorption of ethanol and acetic acid, authors observed the production of OH or H_2O groups and suggested that it might block the active surface sites of the surface. Not as ethanol and acetic acid, when acetaldehyde is adsorbed onto the surface of alumina, no production of hydroxide is observed. This observation, as well as previous experimental results, suggests that during the adsorption process, ethanol and acetic acid form surface O-H bonds with O from ethanol or acetic acid while acetaldehyde only forms H-H bonds with the H from acetaldehyde.

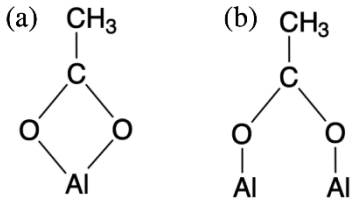

Figure I-17 Different bidentate structures of adsorbed acetic acid on alumina: (a) bidentate chelating species, (b) bidentate bridging species.

The adsorbed phase during acetic acid, formaldehyde, and methanol uptake on SiO_2, α-Al_2O_3, and α-Fe_2O_3 have been investigated by S. Carlos-Cuellar et al. [87] using transmission FTIR. Authors firstly pointed out that except acetic acid, which is found adsorbed irreversibly on the all the three metal oxides surface, formaldehyde and methanol are mostly irreversibly adsorbed on the surface of α-Al_2O_3 and α-Fe_2O_3 and completely reversibly adsorbed on the surface of SiO_2 based on the transmission FTIR observation. This observation again evidenced the high adsorbing property of acetic acid due to the carboxylic functional group [155][87][167], and also addressed the importance of the acidic-basic properties of the surface on adsorption reactivity of metal oxides.

For the adsorption of acetic acid and methanol on the surface of α-Al_2O_3 and α-Fe_2O_3, the transmission FTIR spectra suggested the formation of acetate (CH_3COO^-) and methoxide (CH_3O^-) respectively which is consistent with some previous observations [158-160]. As for the adsorption of formaldehyde on α-Al_2O_3 and α-Fe_2O_3, authors suggested the formation of certain irreversibly adsorbed surface species such as formate and methoxide [161]. The spectra are reported in Figure I-18.

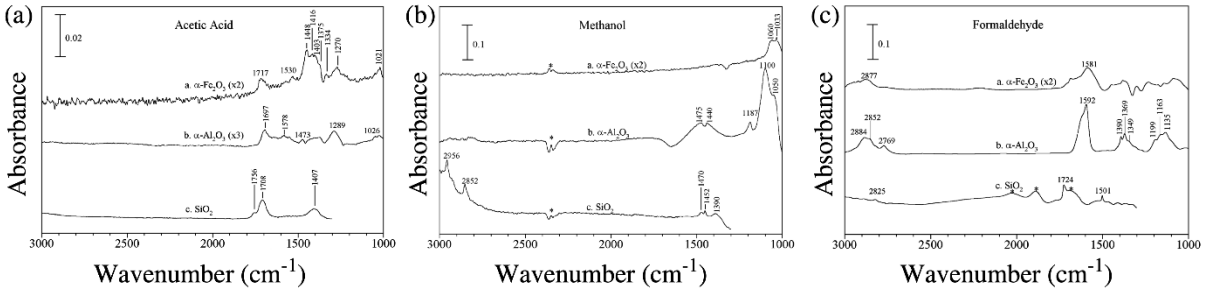

Figure I-18 Transmission FTIR spectra of (a) acetic acid, (b) methanol, and (c) formaldehyde adsorbed on the surface of SiO_2, α-Al_2O_3, and α-Fe_2O_3 with the presence of gas phase VOCs at a pressure of 30 m Torr, of which the gas-phase adsorptions have been subtracted from the spectra. Features indicated with * are due to (b) the dry-air purge and poor cancellation of CO_2 in the gas phase, (c) SiO_2 lattice which did not subtract out well. (The figure is retrieved from S. Carlos-Cuellar et al. [87].)

Besides the adsorption of acetic acid on the surface of SiO_2, α-Al_2O_3, and α-Fe_2O_3, the adsorption of acetic acid on TiO_2 powder is investigated by L. Liao et al. used FTIR spectroscopy at 35˚C [166]. After the adsorption of acetic acid and the evacuation of the acetic acid vapor, bands and peaks at 1027, 1049, 1296, 1341, 1415, 1453, 1535, 1675, 1736, 2936 cm^{-1} are observed on the FTIR spectra of TiO_2 which referred to the adsorbed surface species, as reported in Figure I-19.

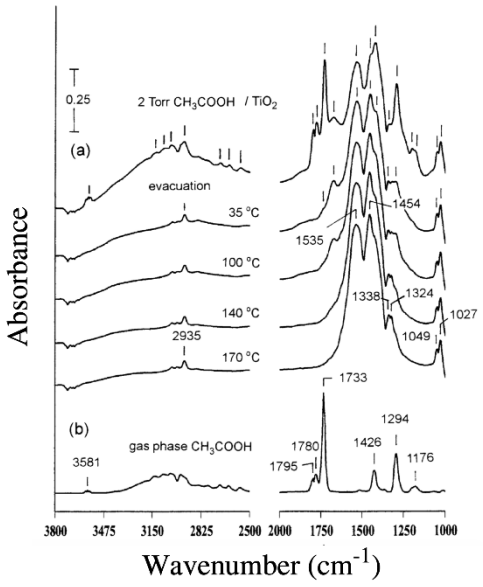

Figure I-19 FTIR spectra of acetic acid adsorbed on TiO_2 at 35˚C under 2 Torr. (The figure is adapted from L. Liao et al. [166].)

Among these peaks, authors suggest that peaks at 1296, 1415, 1675 and 1736 cm^{-1} are related to the same molecular structure on the surface since they all decrease with rising the temperature and all disappear beyond 170˚C. Authors assign peaks of 1675 and 1736 cm^{-1} to adsorbed carbonyl stretching. After the removal of adsorbed acetic acid by heating at 170˚C, bands and peaks at 1027, 1049, 1324,

1388, 1454, 1535 and 2935 cm^{-1} remain in the spectra and are assigned to adsorbed acetate species by authors. Particularly, authors suggest the chelating bidentate configuration of the acetate group bonding to the surface of TiO_2, i.e. $CH_3COO(a)$, as reported in Figure I-20.

According to L. Liao et al., molecularly adsorbed $CH_3COOH(a)$ and dissociatively adsorbed acetate species $CH_3COO(a)$ are formed during the adsorption of acetic acid on TiO_2, for which $CH_3COOH(a)$ is bounded to the surface of TiO_2 by hydrogen bonding and Lewis acid-basic interaction, and $CH_3COO(a)$ is bonded in a chelating bidentate configuration as reported in Figure I-20.

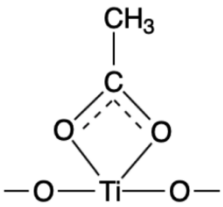

Figure I-20 Adsorption mode of acetate group on TiO_2 adapted from L. Liao et al. [166].

It is in contrast with the conclusions of H. E. Evans and W. H. Weinberg [153] for acetic acid uptake on alumina where the adsorbed acetic acid has the bidentate symmetrical bridging structure, as mentioned previously in Figure I-17. In the study of the adsorption of formic acid, acetic acid and propionic acid on α-Al_2O_3 by S. R. Tong et al. [167] suggested that the carboxylates formed on the surface of α-Al_2O_3 have bridging coordinated structures after comparing the calculated results with the experimentally observed DRIFT spectra, authors, which is consistent with the conclusion by H. E. Evans and W. H. Weinberg [153].

However, M. Tang et al. [162] supported the chelating bidentate configuration of the adsorbed acetate species based on the study of the interaction between acetic acid with γ-Al_2O_3. The same time, M. Tang et al. also suggested this controversy needs further investigation. Besides, M. Tang et al. found that molecularly adsorbed acetic acid is formed on the surface of γ-Al_2O_3, CaO and SiO_2, which is characterized by the FTIR bands at c.a., 1758, 1716 and 1273 cm^{-1}. Author also confirmed that dimers are the major form of molecularly adsorbed acetic acid on γ-Al_2O_3, and CaO, and especially on SiO_2 where there is only molecularly adsorbed acetic acid formed during acetic acid adsorption.

4.2.2 Influences of the surface properties of minerals on VOC adsorption

P. Li et al. [15] have addressed the importance of the surface properties of the mineral during VOC adsorption by monitoring the adsorbed phase of SiO_2, Al_2O_3, Fe_2O_3, TiO_2 and CaO during the interaction with acetaldehyde, acetone and propionaldehyde by FTIR. Authors pointed out that the adsorption of these carbonyl compounds on the surface of SiO_2 is weak and reversible, based on two facts: (i) the positions of the bands and peaks in the IR spectra of these carbonyl compounds adsorbed on the surface

obtained are very close to those in the gas or liquid phase. (ii) after the evacuation of the carbonyl vapor from the setup, the bands on SiO_2 disappeared as showed in Figure I-21 (a). This suggests that the adsorption of these carbonyl compounds on SiO_2 is mostly physical adsorption, consistent with the previous observation obtained using both gas phase and adsorbed phase approach [155][87][167][166][162].

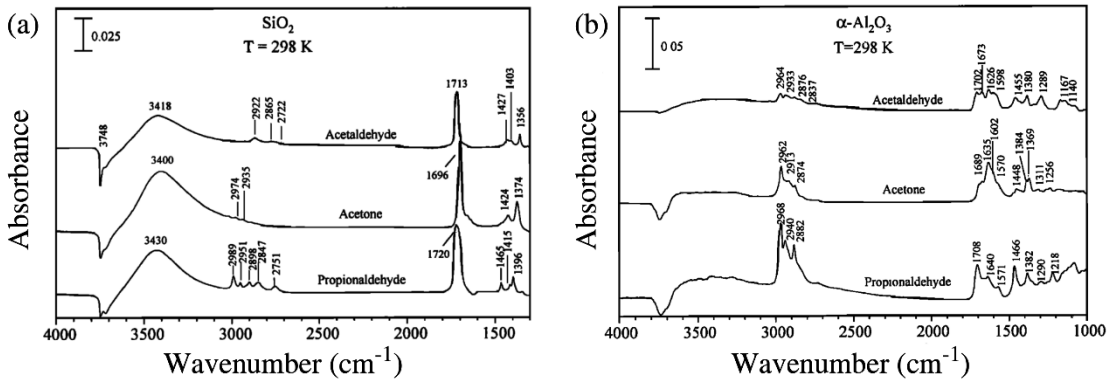

Figure I-21 Transmission FTIR spectra of acetaldehyde, acetone and propionaldehyde adsorbed on the surface of (a) SiO_2, (b) α-Al_2O_3. The pressure of the carbonyl compounds is 20 mtorr at 298 K. (The figure is retrieved from P. Li et al. [155].)

Unlike SiO_2, the adsorption of the carboxyl compounds on other metal oxides, i.e., Al_2O_3, Fe_2O_3, TiO_2 and CaO, examined by P. Li et al. is partially irreversible. After the evacuation of the carbonyl vapor, bands and peaks are still observed on the FTIR spectra of these metal oxides. Take α-Al_2O_3 as an example in Figure I-21 (b) where the bands and peaks are due to the strongly bounded surface groups. Compared with Figure I-21 (a), the FTIR spectra on α-Al_2O_3 exhibit more peaks and bands indicating that more than one molecular structures are on the surface. Authors suggested the molecular structures with higher molecular weight are formed on the surface of metal oxides which shows acidic or basic properties, consistent with the observation by M. Tang et al. [162] that dimer adsorbed acetic acid species is formed on the surface of γ-Al_2O_3, CaO and SiO_2.

For the other metal oxides examined by P. Li et al. [155], such as Fe_2O_3, TiO_2 and CaO, which exhibit either basic or acidic properties, the spectra evidenced that these carboxyl compounds were adsorbed on the surface after the evacuation of carbonyl vapors, which is similar to what is obtained with α-Al_2O_3. Also, the spectra suggest that these carbonyl compounds undergo heterogeneous reaction on the surfaces of these metal oxides, resulting in forming carbonyl compounds with higher molecular weight as observed through the bands in the region of 1500 to 1675 cm^{-1} as on the spectra of α-Al_2O_3.

4.2.3 Adsorbed phase during VOC adsorption on minerals under dry and wet conditions

S. Carlos-Cuellar et al. examined the uptake of formic acid on $CaCO_3$ particles using Knudsen cell, FTIR and SEM, under dry and wet conditions [163]. Formic acid is found adsorbed irreversibly on $CaCO_3$ under dry condition as revealed by the Knudsen cell experiments as well as the FTIR monitoring. Authors suggested the formation of adsorbed formates on the surface of $CaCO_3$ via reaction (RI-12) where adsorbed carbonic acid was also formed. The FTIR bands at 1686, 1249, 1023 and 830 cm^{-1} evidence the adsorbed carbonic acid as reported in Figure I-22.

$$Ca(OH)(HCO_3)\ (s) + HCOOH(g) \rightarrow Ca(OH)(HCOO)\ (a) + H_2CO_3\ (a) \qquad \text{(RI-12)}$$

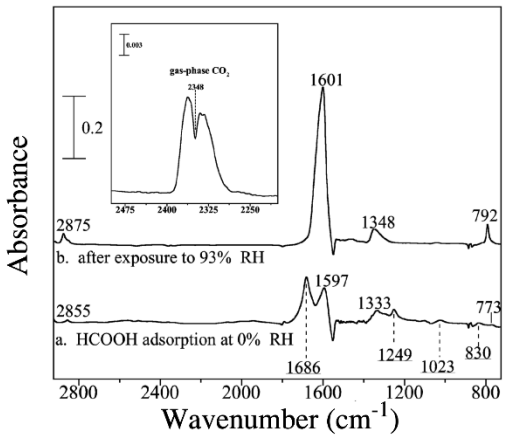

Figure I-22 a. Transmission FTIR spectra of adsorbed formic acid on $CaCO_3$ surface under dry condition, b. then the $CaCO_3$ is exposed to 94% RH. The underlined peaks are assigned to adsorbed carbonic acid in order to distinguish from formate peaks. (The figure is retrieved from H.A. Al-Hosney et al. [163].)

Under dry condition, the saturated surface coverage of formic acid is determined to be $3 \pm 1 \times 10^{14}$ [163]. When exposing the surface already saturated with formic acid to water (93% RH), changes of vibrational frequency, intensity of certain peaks, and disappearance of certain peaks are observed. It could be explained by the dissociation of carbonic acid to water and carbon dioxide, which was favored by water. Indeed, the presence of water can promote the uptake rate of formic acid on the surface by factors of 7 (62% RH compared to dry condition). Authors suggested that additional adsorption sites can be created in the presence of adsorbed water molecules. The net reaction could be described by reaction (RI-13):

$$CaCO_3(s) + 2HCOOH(g) \rightarrow Ca(HCOO)_2(s) + CO_2(g) + H_2O(a) \qquad \text{(RI-13)}$$

The same promoting effect of adsorbed water on the uptake of acetic acid molecules has been observed on $CaCO_3$ (calcite) by A. P. Prince et al. [164] and on ammonium nitrate film by J. E. Shilling and M.

A. Tolbert [165]. The adsorbed water molecules and the surface OH groups are suggested to have influences on the adsorption of VOCs on the surface.

S. R. Tong et al. [167] also studied the impact of water molecules on the uptake of carboxylic acids, i.e., formic acid, acetic acid as well as propionic acid, on α-Al_2O_3 particles. Water consumption has been observed in DRIFT spectra when the carboxylic acids are introduced on the surface of α-Al_2O_3 particles as reported in Figure I-23 (d-f). It is consistent with the observation by P. Li et al. [155] that acetaldehyde, acetone and propionaldehyde can interact with surface OH groups leading to the removal of initial surface OH groups. The same IR features has been observed by M. Tang et al. [17] by FTIR during acetic acid adsorption on the surface SiO_2.

Based on the analysis and comparison of DRIFT bands and peaks under dry and wet conditions, authors conclude that under wet conditions, the coordinated carboxylate and hydrated carboxylate can coexist on the surface of α-Al_2O_3. Below 20% RH, the presence of water promotes the uptake of carboxylic acids. However, S. R. Tong et al. observed a negative effect of water on the uptake of carboxylic acids on α-Al_2O_3 when the relative humidity exceeds 20%, which is in contrast with H. A. Al-Hosney et al [163] who have studied the uptake of formic acid on calcium carbonate particles, A. P. Prince et al. [164] who studied acetic acid on calcite and nitric acid reacted calcite aerosol, and J. E. Shilling and M. A. Tolbert [165] who studied the uptake of acetic acid on thin ammonium nitrate films. Not like other materials such as $CaCO_3$ and ammonium nitrate which are reactive soluble with high RH, the heterogeneous reaction of acid is not limited to the surface and both bulk oxygen atoms and surface oxygen atoms participate in the reaction [168]. S. R. Tong et al. pointed out that α-Al_2O_3 are reactive insoluble particles and the fact that uptake of carboxylic acid decreases at high RH condition suggests that the reactions occur only on the surface and the bulk oxygen atoms don't participate in the reaction. Water molecules, in this case, compete with the acid molecules for the surface sites. As a result, water molecules in this situation have three potential roles according to S. R. Tong et al.: (a) solvation of the carboxylate ion, (b) hydroxylation of the particle surface, and (c) competition for reactive sites.

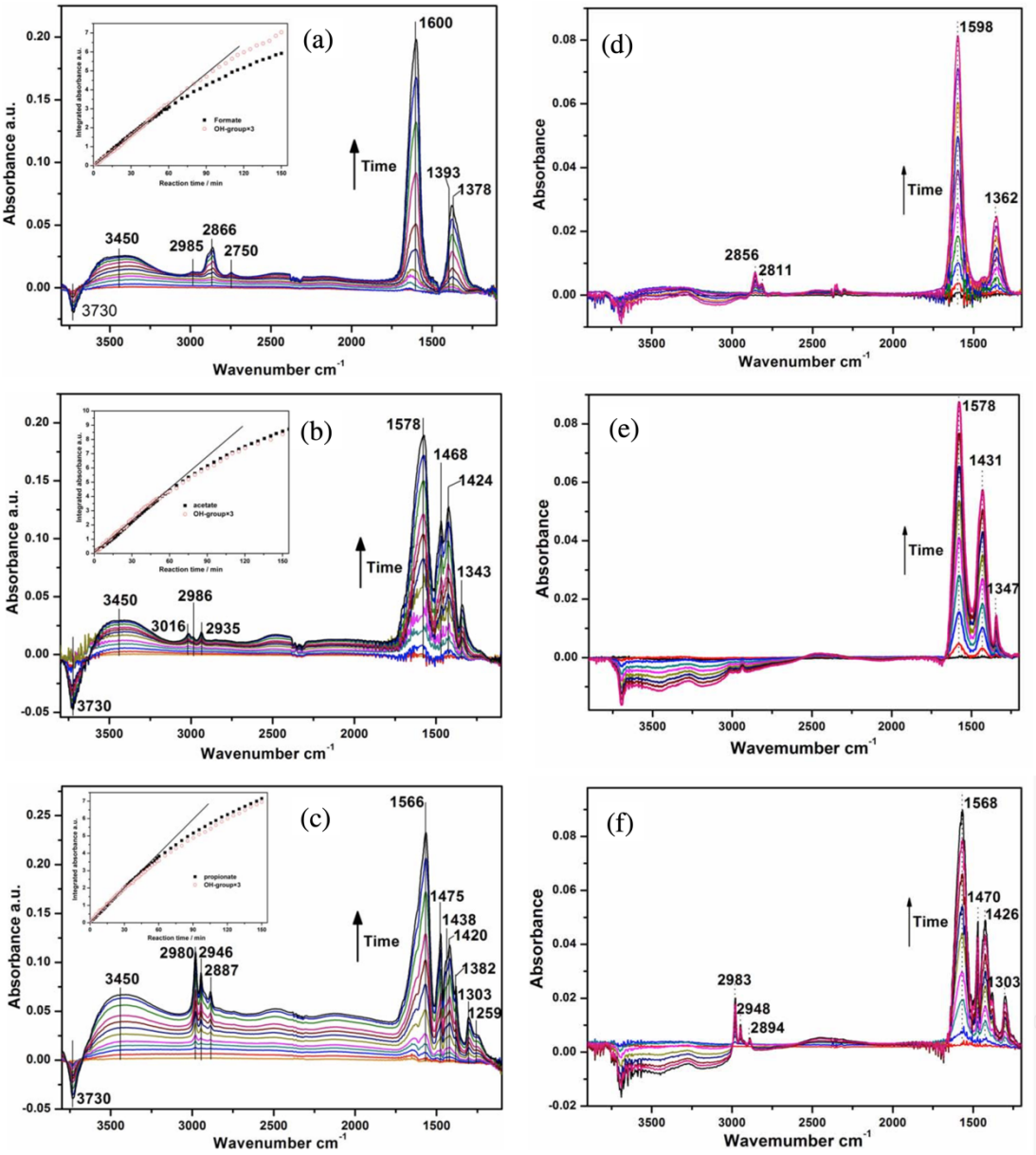

Figure I-23 DRIFT spectra recorded during the uptake of (a) formic acid at dry condition, (b) acetic acid at dry condition, (c) propionic acid at dry condition, (d) formic acid at 30% RH, (e) acetic acid at 30% RH and (f) propionic acid at 30% RH on α-Al_2O_3 particles. (Figures are adapted from [167].)

Mechanism for the reaction between carboxylic acids and α-Al_2O_3 is proposed where the surface-OH structures (Al-OH) are the most important reactive sites. The carboxylic acid molecules (RCOOH) interact with Al-OH to form adsorbed water molecules H_2O(a) via reaction (RI-14).

$$RCOOH(g) + Al\text{-}OH \rightarrow RCOO\text{-}Al + H_2O(a) \quad \text{(RI-14)}$$

With adsorbed water on the surface, the carboxylic acid can go through dissociation reaction with adsorbed water layer via reaction (RI-15).

$$RCOOH(g) + H_2O(a) \rightarrow H_3O^+_{(aq)} + RCOO^-_{(aq)} \quad \text{(RI-15)}$$

4.3 Conclusions and problematics

Based on previous literature review of VOC uptake on minerals, important conclusions can be summarized.

For experimental devices, Knudsen cell equipped with mass spectroscopy has been used for gas phase kinetic measurement of VOC adsorption on surface [87, 155, 163]. Inelastic electron tunneling spectroscopy (IETS) [153, 154], transmission FTIR [87, 155, 163], DRIFT spectroscopy [167] have been used to study the molecular structure of adsorbed VOC on the surface.

Using gas phase approach, the kinetic of adsorption addressed from the gas phase for VOCs such as acetic acid, methanol, acetaldehyde, and acetone are determined on various minerals. Among the investigated VOCs, carboxyl acids specifically acetic acid, are evidenced to be reactive, and strongly adsorbed compared to alcohols and aldehydes. This is due to the carboxylic functional group in this compound [87, 155, 167]. Among the investigated materials, the adsorption of VOCs on SiO_2 has been observed weak and reversible, unlike the adsorption of VOCs on Al_2O_3, Fe_2O_3, TiO_2 and CaO, as supported by the initial uptake coefficient [87, 155] and surface coverage [87] determined. The significance of the chemical properties of the surface sites on adsorption capacity of metal oxide is pointed out.

In the adsorbed phase investigation of VOC adsorption on minerals, molecularly adsorbed VOCs are monitored in-situ on Al_2O_3, Fe_2O_3, TiO_2, CaO, and SiO_2 and linked to surfaces either through weak hydrogen bonding or stronger acid-base interactions [155, 162, 166]. For acetic acid, dimers are the major form of adsorbed acetic acids [162]. Besides molecularly adsorbed VOC species, other surface structure are observed on the mineral surface depending on the VOC. They have been characterized by DRIFT or transmission FTIR:

- Acetic acid is observed to form bidentate bridging acetate on Al_2O_3 with two O atoms of acetic acid bound to different Al atoms of the surface [153, 154, 167], and chelating bidentate acetate on TiO_2 with two O atoms of acetic acid bound to the same Ti atom [166].
- Formic acid is found to form formate on $CaCO_3$ particles [163].
- Ethanol is found to form ethoxide on Al_2O_3 with one O atom of ethanol bonded with Al atom of the surface when temperature is below 470K [87, 153, 154].
- Acetaldehyde is found to form an acetate on the surface of Al_2O_3 of the same structure than acetic acid [153, 154].

- Formaldehyde is suggested form formate or methoxide on α-Al_2O_3 and α-Fe_2O_3 [87, 161].

During VOC adsorption on mineral surfaces, molecules are evidenced to interact with surface OH groups leading to the removal of initial surface OH groups characterized by the negative IR bands around 3700 cm^{-1} [155, 164, 167]. As for water molecules, the promoting effect of adsorbed water has been observed on the adsorption of acetic acid molecules on $CaCO_3$ (calcite) [164] and on ammonium nitrate film [165], and the adsorption of formic acid on $CaCO_3$ particles [163]. The competing effect of water molecules has been observed on the adsorption of acetic acid on α-Al_2O_3 [167]. A promoting or competing effect of adsorbed water molecules on VOC adsorption depends on the nature of the mineral.

The adsorption of VOCs on metal oxides suggests that the mineral particles in atmosphere may act as sink of VOCs, and possibly as secondary emission sources of VOCs due to the reversibly adsorption process. However, as previously mentioned for the literature review of ozone uptake on minerals (section *3.3*), the literature studies of VOC uptake on mineral surface have similar limitations:

- Most of the experiments for gas phase kinetics determination of VOC uptake have been performed with Knudsen cells, where the conditions are not relevant to real atmospheric conditions.
- The concentration of VOCs is mostly in the range of ppb which is not adequate to determine the mechanism under high VOC concentration range depending on the adsorption isotherm.
- The investigated materials are mostly single synthetic metal oxides which cannot represent the case of complex materials such as nature mineral dust.

As a result, investigations of the interaction of VOCs and authentic natural mineral dust under typical atmospheric conditions, i.e. relevant gas phase concentration range and relative humidity, are needed for both fundamental studies and applications.

5 The application of non-thermal plasma-catalysis for VOC treatment

Another potential outcome application of the study concerning the interactions of mineral dust with ozone and VOCs is indoor VOC removal by non-thermal plasma-catalysis (NTP-catalysis).

The method, historically named as NTP-catalysis, combines classical methods of adsorption and oxidation of VOCs, and provides good performance and synergetic effect [122, 169-172]. Regardless the scientific and technical aspects, the principle of NTP-catalysis for VOC oxidation involves two principle processes:

(i) Adsorption of the VOCs molecules by the couple material. During this process, the couple material acts as adsorbent and catalytic properties are not necessarily involved.

(ii) Oxidation of the adsorbed VOCs by the reactive species generated from NTP, i.e., radicals, NO_x, ozone and etc. During this process, ozone molecules catalytically decompose on the surface of the couple material and the oxidation process of VOCs is enhanced. As a result, the coupled materials used in NTP-catalysis are also referred as catalysts in literature.

In this application, ozone, VOCs and the coupled materials are the key elements. For a given VOC, there are three important factors which determine the performances of a NTP-catalysis system: NTP, coupled material, and their configurations. Following the three factors, the application of the present study in NTP-catalysis will be illustrated.

5.1 Indoor air issues

Indoor air pollution is always an important issue since we spend 80 to 90% of our lifetime in indoor environment. VOC (volatile organic compound) is a common kind of indoor air pollutant. According to the European Union, VOC is defined as an organic compound having a boiling point lower than 523 K at atmospheric pressure. Various sources of VOCs could be found inside buildings such as adhesives, carpeting, wood products and cleaning products, which emit gaseous pollutants such as formaldehyde, acetaldehyde and some organic acids [173]. Many different kinds of VOCs can be found indoor simultaneously in various concentrations with different physical, chemical and biological properties, having short- and long-term impacts on human health.

5.2 Non-thermal plasma (NTP)

5.2.1 Characteristics of NTP

Plasma is an ionized gaseous medium containing charged particles (electrons, ions), also known as the fourth state of matter. They can be found in nature, e.g., the aurora borealis, lightening, nebula et etc. or generated artificially by injecting energy into gaseous species. A part from NTP, there are high temperature plasma and thermal plasma, according to the different temperatures and densities of the charged particles of plasma [174, 175]:

- High temperature plasma: all electrons, ions and neutral species are in a thermal equilibrium state. The temperatures for electrons, ions and gas are equal and generally within 10^6 - 10^8 K. E.g., fusion plasmas, stars…
- Thermal plasma: the temperature of electrons, ions and gas are also equal or nearly equal but within a lower range of temperature, i.e., $\leq 2 \times 10^4$ K compared to the high temperature plasma. E.g., arc plasma.
- Non-thermal plasma: also called non-equilibrium plasma or less appropriately, cold plasma, where a large fraction of the energy is channeled to the electrons primarily at the same time the

ions and neutrals remain at or near room temperature. E.g., glow, corona, dielectric barrier discharges.

The specificity of NTP, compared with the other two, is that most of the energy put into the system to generate plasma will be transferred to the electrons to generate reactive species instead of heating the gas. As a result, the gas temperature remains near room temperature. And also because of this, NTP can be applied in a safer way and in some conditions where room temperature is required, such as treatment of biological tissues. These features of NTP, i.e., high energetic efficiency and low gas temperature, make NTP suitable for indoor air treatment by NTP-catalysis.

5.2.2 Generation of NTP

To obtain NTP at atmospheric pressure, ionization degree must be limited in order to maintain non-equilibrium state [174, 175]. Several approaches can be applied:

- The discharge power is maintained low to avoid overheating of the gas by putting a large resistor in series, e.g., stationary corona discharge [174].
- The pulse duration is limited to a short time, i.e. the range of ns to μs , to avoid the heating effect of the gas, e.g., pulsed corona discharge [174].
- A dielectric is imposed between the electrodes to stop the current thus limiting the heating effect of the gas, e.g., dielectric barrier discharge (DBD) [176].

Among these approaches, special attention is addressed to dielectric barrier discharge (DBD) due to its relative simplicity and flexibility. It is not complicated to build up a DBD reactor with various configurations, and it can operate with different gases, usually air, N_2, O_2, He et etc. Thus it is commonly used in laboratory experiments as well as in industrial applications [177]. Reactive gas phase species by NTP

The electric energy applied in the NTP reactor is initially transferred to the electrons to generate high-energetic electrons, usually with the energy of 1-20 eV for our DBD reactor, in-between the discharge zone. Then these high-energetic electrons collide with the gas molecules in the discharge gap and transform part of their energy to dissociate/excite/ionize the gas molecules. As a result, it will lead to the dissociative or ionization reactions of gas molecules to form primary radicals and charged species. These radicals may recombine and form other reactive species such as O_3 or nitrogen oxides. It may also result in the emission of photons by the excited gas molecules.

More precisely, the dissociative ionization reactions occurring in or between the plasma discharge region will produce short-lived ($1 < \tau < 100\ \mu s$) and long-lived ($\tau > hours$) reactive species. With different carrier gases, the short-lived reactive species can be: $O(^3P)$, $O(^1D)$, $N(^4S)$, $N(^2D)$, OH^-, HO_2^-,

O^+, O_2^+, N^+, O^- …, and the long-lived reactive species can be: O_3, H_2O_2, NO, NO_2… These reactive species can be used to further react with other stable species, for example, to decompose VOC molecules. One of the most important long-live reactive species produced by NTP is ozone, which is a strong oxidant agent widely used in sterilization, sewage treatment plant, and plasma assisted oxidation [120-123].

5.2.3 Problematic for VOC abatement by only NTP

However, when NTP works alone for VOC oxidation, the oxidation processes tend to be incomplete [178]. Because the interactions of plasma-generated reactive species and VOC molecules occurs mostly in gas phase, thus the probability of the interactions is not important enough considering the low concentration, i.e. 100 ppb or less, of VOC in indoor air. As a result, it could lead to poor performance of VOC removal and, sometimes the production of more harmful by-products.

5.3 Coupled materials used in NTP-catalysis

5.3.1 Advantages of using coupled materials with NTP for VOC abatement

Coupling NTP with solid materials is a good alternative for the problem of VOC abatement by NTP alone.

With the presence of the coupled materials acting as adsorbents, interactions between NTP-generated reactive species and VOC molecules occur not only in gas phase, but also on the surface of the materials. The concentration of the VOC molecules adsorbed by the materials on the surface can be several magnitudes higher than what in gas phase thus the interaction probability is promoted. The same time, coupled materials can expand the resident time of adsorbed VOC molecules to be treated by NTP-generated reactive species. If the materials are coupled with NTP in discharge region, it can enhance the electric field strength, extend the plasma region, enrich the gas-phase reactive species [179-183].

As a result, better performance of VOC abatement and synergy can be achieved by NTP-catalyst coupling compared with NTP working alone, which has been evidenced by studies and experiments.

Harling et al. investigated the destruction performance of toluene and benzene by NTP-catalysis using a packed-bed plasma reactor with TiO_2 and γ-Al_2O_3 supports, and Ag (0.5 wt.%) impregnated catalysts [184]. They experimentally evidenced the destruction rate of benzene by NTP-catalysis (TiO_2 and Ag/TiO_2 as coupled catalyst) is better than by catalyst alone at various temperatures. Also, they showed that the destruction ratio of toluene by NTP-catalysis (γ-Al_2O_3, $Ag/γ$-Al_2O_3, TiO_2 and Ag/TiO_2 as coupled catalysts) is much higher than NTP alone with no catalyst. The precise results are showed in Figure I-24 and Figure I-25 where clear synergy effects by NTP-catalysis for VOC removal can be observed.

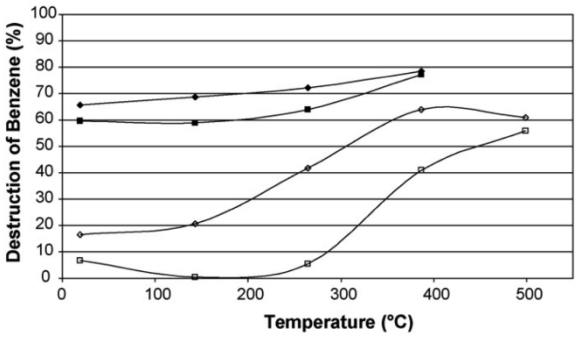

Figure I-24 Comparison of catalysis alone (open symbols) and plasma-catalysis (filled symbols) methods for the destruction of benzene at varying temperatures, using (◆) TiO_2 and (■) Ag/TiO_2 catalysts and supports, in a one-stage configuration. (The figure is retrieved directly from A. M. Harling et al. [184].)

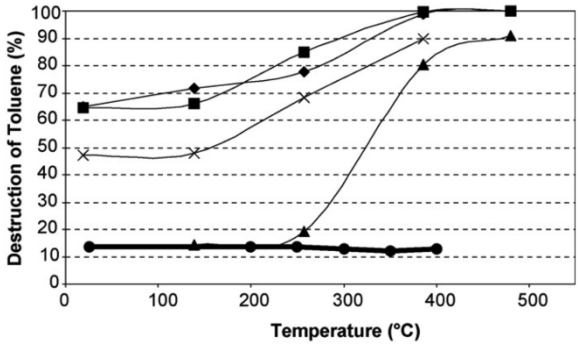

Figure I-25 Comparison of catalyst performance for the plasma-catalytic destruction of toluene at varying temperatures, using (◆) γ-Al_2O_3, (■) Ag/γ-Al_2O_3, (▲) TiO_2 and (×) Ag/TiO_2 catalysts and supports, in a one-stage configuration. The thick black line shows plasma alone results, with no catalyst. (The figure is retrieved directly from A. M. Harling et al. [184].)

5.3.2 Properties of the coupled materials used in NTP-catalysis

The adsorption properties and the catalytic ozone-decomposing properties of a solid material make a difference in the performance when it is coupled with NTP for VOC abatement.

The adsorption properties of the coupled materials play important roles in the adsorption process of VOC molecules. Generally speaking, a material with good adsorption properties used in NTP-catalysis is expected to be porous with big specific surface area and big adsorption capacity. As a result, it can adsorb more pollutant molecules and provide more surface for the interactions with NTP-generated reactive species. It has been evidenced that with the same NTP-catalyst setups for VOC oxidation, porous adsorbents provides higher CO_2 selectivity, which is one of the index regarding the performance of VOC removal, compared with non-porous adsorbents [185]. The specific results are showed in Figure I-26, where the porous adsorbents exhibit higher efficiency for VOC oxidation, compared with non-porous adsorbents of the same component. As a result, porous material is favored to be used for VOC abatement by NTP-catalysis.

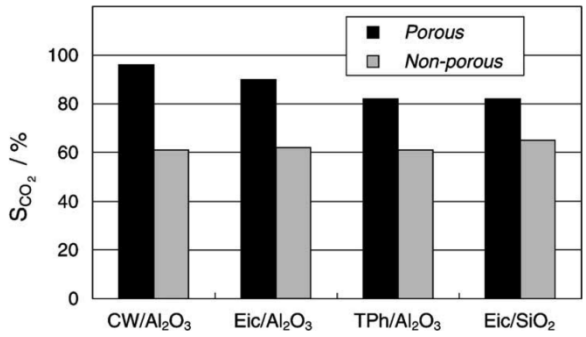

Figure I-26 CO_2 selectivities for the oxidation of Carbowax 400 (CW), *n*-eicosane (Eic), and *p*-terphenyl (TPh) immobilised on porous and non-porous materials with both a single-stage dielectric barrier discharge reactor and a two-stage plasma-catalysis system. (The figure is retrieved directly from F. Holzer et al [185].)

Another factor which influences NTP-catalysis performance of the coupled material is the ozone-decomposing properties. Because ozone as the key NTP-generated reactive species because of its powerful oxidant ability and long residual time of several hours, which is stable at room temperature and catalysts are necessary for ozone decomposition [133]. U. Roland et al. studied the correlation of ozone decomposition and VOC oxidation in NTP-alumina system [123]. In their study, Roland et al. evidenced that the capability of porous alumina for ozone decomposition is positively correlated with its activity for oxidation of carbon-containing compounds when used as coupled material in NTP-catalysis. Roland et al. suggested that since ozone decomposition and the subsequence consumption of atomic oxygen are the only relevant oxidation processes, the more ozone decomposes, the more intense the oxidation reactions are. This correlation between ozone decomposition and the VOC oxidation on the surface has been supported and evidenced by following investigations [186-188]. As a result, the capability of a material to decompose ozone is an important index for its performance in VOC abatement by NTP-catalysis.

Numerous materials have been tested and studied for VOC abatement using NTP-catalysis, among which many are metal oxides, such as Al_2O_3 [123, 169, 189, 190], MnO_2 [169, 191, 192], Fe_2O_3 [193, 194], SiO_2 [195, 196], TiO_2 [195, 197-200], MgO [201] and several combinations of these metal oxides [202-204], and noble metals such as Pt, Pd or Rh or the catalysts doped with these noble metals [169]. Many of them exhibit synergetic effects when coupled with NTP for VOC removal. However, the expensive price of noble metals boosts the use of metal oxides or metal oxide-based materials in industry. More attention is drawn to metal oxides or metal-oxide based materials.

5.4 NTP-catalysis configurations

5.4.1 In-situ and post-situ NTP-catalysis

Once the NTP and the adsorbent are settled, there are two kinds of configurations for NTP-catalysis system in general: in-plasma catalysis (also called in-situ NTP-catalysis) where the adsorbent is coupled

directly in the discharge region, and post-situ NTP-catalysis (also called two stage NTP-catalysis) where the adsorbent is placed downstream of the plasma. Figure I-27 gives the schematic to illustrate these two configurations of NTP-catalysis.

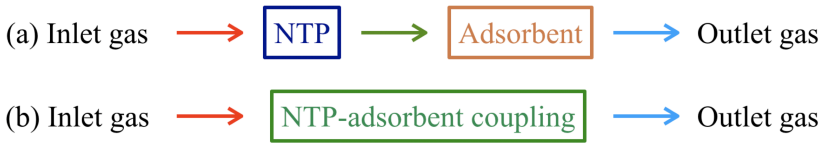

Figure I-27 Schematic of (a) post-situ and (b) in-situ plasma-catalysis configurations.

For in-situ NTP-catalysis configuration, when the plasma is turned on, all the NTP-generated long-lived and short-lived reactive species as well as electrons can interact with the surface of adsorbent since the adsorbent is right in the discharge region. For post-situ NTP-catalysis configuration, considering the fact that the NTP-generated short-lived species can generally exist for only several μs, only the long-lived species such as ozone and NO_x can finally reach the surface of adsorbent. The NTP-generated reactive species interacting with surface for in-situ and post-situ NTP-catalysis configurations respectively are summarized in Figure I-28.

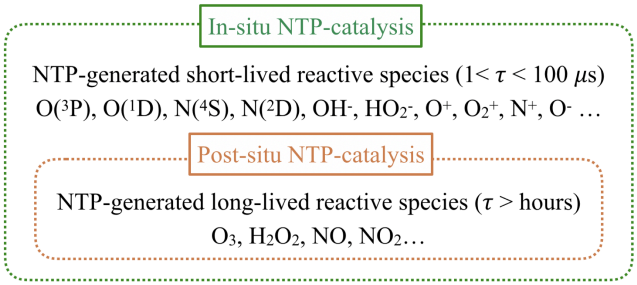

Figure I-28 NTP-generated reactive species interacting with surface for in-situ and post-situ NTP-catalysis configurations.

5.4.2 Continuous and sequential operation modes for NTP-catalysis

Regardless the different configurations of NTP-catalysis for VOC abatement, there are two different operation modes for a given NTP-catalysis system: continuous and sequential operation mode. For example, in continuous mode, the air flow containing VOCs is sent to NTP-catalysis system to be treated with NTP always active, and the adsorption and oxidation of the VOCs are synchronous. In sequential operation mode, the air flow containing VOCs is first sent to NTP-catalysis system with NTP off to let the VOCs adsorbed by the adsorbent, then the VOC is cut off and NTP is turned on to oxidize the adsorbed VOCs. The features of continuous and sequential operation modes for NTP-catalysis for VOC abatement are schematized by Figure I-29.

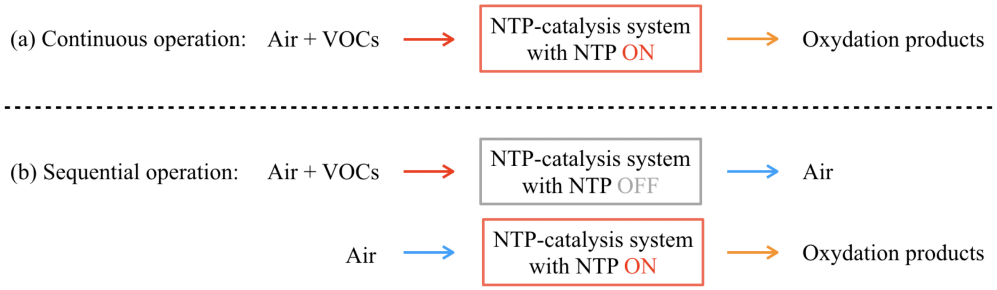

Figure I-29 Schematic of (a) continuous operation and (b) sequential operation of plasma-catalysis for VOC abatement.

L. Sivachandiran et al. [205] compared the performance between continuous and sequential operation modes for isopropanol removal using a Mn_xO_y packed bed NTP reactor, showing that different operation modes lead to different VOC removal performances with pros and cons.

C. Barakat et al. [200] have emphasized the advantages of using sequential operation mode of NTP-catalysis for VOC oxidation during research as well as in practice. Authors pointed out that by sequential operation mode where adsorption and oxidation process are separated, studies can focus onto the VOC oxidation process by NTP-generated species occurring on the surface of adsorbent, thus distinguishing the real synergetic effect between coupled adsorbent/catalyst and NTP. In this way, it is easier to understand the contribution of the reactive NTP-generated species to the NTP-catalysis system. Moreover, C. Barakat et al. also suggests that since in sequential operation mode the NTP is not continuously turned on, it is only turned on after the VOC is adsorbed on the surface of couple adsorbent or catalyst thus saving the energy consumed [200]. During their studies, C. Barakat et al. used sequential NTP-TiO_2 system to investigated the oxidation of IPA and acetone by ozone flow generated from NTP on the surface of TiO_2 in both gas phase and adsorbed phase, which evidences the reliability and advantage of using sequential NTP-catalysis for heterogeneous interaction studies and provides inspiration for this study present in this thesis.

5.5 Conclusions and remarks

NTP-catalysis exhibits advantages, such as high efficiency and synergetic effect, for indoor air VOC abatement. The couple materials used in NTP-catalysis play an important role in the performance of VOC removal regarding their adsorption properties and ozone-decomposing properties.

The study of the surface properties of natural mineral dust towards ozone and VOC presented in this manuscript could contribute generally in three aspects concerning the materials used in NTP-catalysis:

- The study concerning the interaction of mineral dust with VOCs will evaluate the adsorption properties of the mineral dust.

- The study concerning the interaction of mineral dust with ozone will evaluate the ozone-decomposing properties of the mineral dust.
- The study concerning the interaction of ozone with the adsorbed VOC on mineral dust will provide specific evaluation of the mineral dust in NTP-catalysis especially in post-situ configuration using sequential operation mode.

All the three aspects are key factors in the performance of VOC abatement by NTP-catalysis as mentioned in this section. The potential of the natural mineral dust, as a mixture of metal oxides, used as coupled material in NTP-catalysis for VOC abatement could be addressed by this study.

6 Objectives of this thesis

In this chapter, a general introduction of natural mineral dusts in atmosphere is first presented, highlighting the impacts of natural mineral dusts on atmospheric chemistry which is closely related to the reactivity of the geomaterials towards gas species. It is followed by the introduction of the fundamental knowledge and concepts of uptake and adsorption theory of gases on solid surfaces which are essential to understand the results and discussions in this study, addressing the individual contribution of gas phase approach and adsorbed phase approach in heterogeneous interaction studies.

Then, the literature review of the heterogeneous interactions of mineral dust with ozone and VOCs is discussed, pointing out some limitations and indicating the future direction of the current study. The potential application related to the current study, i.e., NTP-catalysis for VOC abatement, is also introduced at the end of this chapter, showing the practical value of this studies related to the reactivity of natural mineral dusts.

As a result, the principle objective of the present study focusing on the **Interactions of ozone and acetic acid with natural Gobi dust** is to provide a comprehensive evaluation of the heterogeneous surface properties of this geomaterial towards ozone and acetic acid under atmospheric-relevant conditions. This evaluation should contribute to the understanding of the fundamentals of the heterogeneous reactions on natural mineral dust with ozone and acetic acid, and also the applications of the studies in atmospheric chemistry and NTP-catalysis. In this regard, two sub-objectives have been defined:

- Investigating the interaction of mineral dust with ozone using gas phase approach and adsorbed phase approach under atmosphere-relevant condition.
- Investigating the interaction of mineral dust with acetic acid using gas phase approach and adsorbed phase approach under atmospheric relevant condition.

To reach this aim, Gobi dust is selected as a natural mineral dust of interest. Acetic acid is selected as the model VOC. Fourier transform infrared spectroscopy (FTIR) and ozone analyzer are used in gas

phase approach, and diffuse reflectance infrared Fourier transform spectroscopy (DRIFT) is used in adsorbed phase approach.

Chapter 2 presents the materials and methods used in this study. It first provides the descriptions and characterizations of the dust samples, gas preparations, synthetic materials used in this study. Then it moves to a detailed description for the experimental setups and protocols applied to study the heterogeneous interaction by gas phase approach and adsorbed phase approach respectively.

Chapter 3 and chapter 4 discuss the results obtained during the study of the interactions of Gobi dust with ozone, and acetic acid respectively. Both chapters start with the results obtained by gas phase approach, characterizing the gas phase kinetics and discussing the influence of different experimental conditions such as initial gas concentration and relative humidity. Then the results obtained by adsorbed phase approach using DRIFT are discussed, providing information on surface species formed during the heterogeneous interaction and the understanding of the reaction pathways. Gobi dust is also compared with its single components to address their individual reactivity towards ozone and acetic acid and provide a deeper understanding of the material behavior. Mechanisms of the heterogeneous interaction of Gobi dust with ozone/acetic acid is subsequently proposed at the end of each chapter. At the end of chapter 4, the ozonation of the adsorbed acetic acid on the surface of Gobi dust is also investigated. In this way, chapter 3 and chapter 4 provide a comprehensive evaluation of the surface properties of Gobi dust towards ozone and acetic acid respectively.

The general conclusion summarizes the main outcomes of this study.

References

[1] M. Tang, D.J. Cziczo, V.H. Grassian, Interactions of water with mineral dust aerosol: water adsorption, hygroscopicity, cloud condensation, and ice nucleation, Chemical reviews, 116 (2016) 4205-4259.

[2] C.R. Usher, A.E. Michel, V.H. Grassian, Reactions on mineral dust, Chemical reviews, 103 (2003) 4883-4940.

[3] P. Ginoux, M. Chin, I. Tegen, J.M. Prospero, B. Holben, O. Dubovik, S.J. Lin, Sources and distributions of dust aerosols simulated with the GOCART model, Journal of Geophysical Research: Atmospheres, 106 (2001) 20255-20273.

[4] I. Tegen, I. Fung, Modeling of mineral dust in the atmosphere: Sources, transport, and optical thickness, Journal of Geophysical Research: Atmospheres, 99 (1994) 22897-22914.

[5] I.N. Sokolik, O.B. Toon, Direct radiative forcing by anthropogenic airborne mineral aerosols, Nature, 381 (1996) 681.

[6] A. Goudie, N. Middleton, Saharan dust storms: nature and consequences, Earth-Science Reviews, 56 (2001) 179-204.

[7] G. Zhuang, J. Guo, H. Yuan, C. Zhao, The compositions, sources, and size distribution of the dust storm from China in spring of 2000 and its impact on the global environment, Chinese Science Bulletin, 46 (2001) 895-900.

[8] J. Sun, M. Zhang, T. Liu, Spatial and temporal characteristics of dust storms in China and its surrounding regions, 1960–1999: Relations to source area and climate, Journal of Geophysical Research: Atmospheres, 106 (2001) 10325-10333.

[9] X. Wang, Z. Dong, J. Zhang, L. Liu, Modern dust storms in China: an overview, Journal of Arid Environments, 58 (2004) 559-574.

[10] S. Guerzoni, R. Chester, The impact of desert dust across the Mediterranean, Springer Science & Business Media1996.

[11] J.M. Prospero, Long-range transport of mineral dust in the global atmosphere: Impact of African dust on the environment of the southeastern United States, Proceedings of the National Academy of Sciences, 96 (1999) 3396-3403.

[12] K.D. Perry, T.A. Cahill, R.A. Eldred, D.D. Dutcher, T.E. Gill, Long-range transport of North African dust to the eastern United States, Journal of Geophysical Research: Atmospheres, 102 (1997) 11225-11238.

[13] P. Formenti, M. Andreae, L. Lange, G. Roberts, J. Cafmeyer, I. Rajta, W. Maenhaut, B. Holben, P. Artaxo, J. Lelieveld, Saharan dust in Brazil and Suriname during the Large-Scale Biosphere-Atmosphere Experiment in Amazonia (LBA)-Cooperative LBA Regional Experiment (CLAIRE) in March 1998, Journal of Geophysical Research: Atmospheres, 106 (2001) 14919-14934.

[14] J. Prospero, R. Glaccum, R. Nees, Atmospheric transport of soil dust from Africa to South America, Nature, 289 (1981) 570.

[15] R. Talbot, M. Andreae, H. Berresheim, P. Artaxo, M. Garstang, R. Harriss, K. Beecher, S. Li, Aerosol chemistry during the wet season in central Amazonia: The influence of long-range transport, Journal of Geophysical Research: Atmospheres, 95 (1990) 16955-16969.

[16] L.G. Franzén, M. Hjelmroos, P. Kållberg, E. Brorström-Lunden, S. Juntto, A.-L. Savolainen, The 'yellow snowepisode'of northern Fennoscandia, march 1991—A case study of long-distance transport of soil, pollen and stable organic compounds, Atmospheric environment, 28 (1994) 3587-3604.

[17] L.G. Franzén, M. Hjelmroos, P. Kållberg, A. Rapp, J.O. Mattsson, E. Brorström-Lundén, The Saharan dust episode of south and central Europe, and northern Scandinavia, March 1991, Weather, 50 (1995) 313-318.

[18] E. Ganor, H. Foner, S. Brenner, E. Neeman, N. Lavi, The chemical composition of aerosols settling in Israel following dust storms, Atmospheric Environment. Part A. General Topics, 25 (1991) 2665-2670.

[19] P. Alpert, E. Ganor, Sahara mineral dust measurements from TOMS: Comparison to surface observations over the Middle East for the extreme dust storm, March 14–17, 1998, Journal of Geophysical Research: Atmospheres, 106 (2001) 18275-18286.

[20] D. Jaffe, T. Anderson, D. Covert, R. Kotchenruther, B. Trost, J. Danielson, W. Simpson, T. Berntsen, S. Karlsdottir, D. Blake, Transport of Asian air pollution to North America, Geophysical Research Letters, 26 (1999) 711-714.

[21] R.B. Husar, D. Tratt, B.A. Schichtel, S. Falke, F. Li, D. Jaffe, S. Gasso, T. Gill, N.S. Laulainen, F. Lu, Asian dust events of April 1998, Journal of Geophysical Research: Atmospheres, 106 (2001) 18317-18330.

[22] I. McKendry, J. Hacker, R. Stull, S. Sakiyama, D. Mignacca, K. Reid, Long-range transport of Asian dust to the lower Fraser Valley, British Columbia, Canada, Journal of Geophysical Research: Atmospheres, 106 (2001) 18361-18370.

[23] M.R.R.T. Jacques Descloitres, NASA/GSFC, A graceful arc of Saharan dust is streaming off the coast of northwest Africa and sweeping out over the Atlantic Ocean and the Canary Islands, Visible Earth, 2004.

[24] K. Pye, Aeolian dust and dust deposits, Elsevier2015.

[25] B. Marticorena, G. Bergametti, Modeling the atmospheric dust cycle: 1. Design of a soil-derived dust emission scheme, Journal of Geophysical Research: Atmospheres, 100 (1995) 16415-16430.

[26] S.C. Alfaro, A. Gaudichet, L. Gomes, M. Maillé, Modeling the size distribution of a soil aerosol produced by sandblasting, Journal of Geophysical Research: Atmospheres, 102 (1997) 11239-11249.

[27] E. Journet, Y. Balkanski, S.P. Harrison, A new data set of soil mineralogy for dust-cycle modeling, Atmospheric Chemistry and Physics, 14 (2014) 3801-3816.

[28] C. Bueno-Ferrer, S. Parres-Esclapez, D. Lozano-Castelló, A. Bueno-López, Relationship between surface area and crystal size of pure and doped cerium oxides, Journal of Rare Earths, 28 (2010) 647-653.

[29] K.H. Wedepohl, The composition of the continental crust, Geochimica et cosmochimica Acta, 59 (1995) 1217-1232.

[30] B. Mason, Principles of geochemistry, LWW1952.

[31] L. Gomes, D.A. Gillette, A comparison of characteristics of aerosol from dust storms in central Asia with soil-derived dust from other regions, Atmospheric Environment. Part A. General Topics, 27 (1993) 2539-2544.

[32] L. Gomes, G. Bergametti, F. Dulac, U. Ezat, Assessing the actual size distribution of atmospheric aerosols collected with a cascade impactor, Journal of Aerosol Science, 21 (1990) 47-59.

[33] T. Cahill, R. Eldred, P. Feeney, Particulate monitoring and data analysis for the National Park Service, 1982–1985, University of California, Davis, (1986).

[34] A. El Zein, M.N. Romanias, Y.J.E.s. Bedjanian, technology, Kinetics and products of heterogeneous reaction of HONO with Fe_2O_3 and Arizona Test Dust, 47 (2013) 6325-6331.

[35] M.N. Zeineddine, M.N. Romanias, V. Riffault, F. Thévenet, Heterogeneous Interaction of Various Natural Dust Samples with Isopropanol as a Probe VOC, The Journal of Physical Chemistry A, (2018).

[36] M.N. Romanias, H. Ourrad, F. Thevenet, V. Riffault, Investigating the Heterogeneous Interaction of VOCs with Natural Atmospheric Particles: Adsorption of Limonene and Toluene on Saharan Mineral Dusts, Journal of Physical Chemistry A, 120 (2016) 1197-1212.

[37] A.E. Zein, M.N. Romanias, Y. Bedjanian, Heterogeneous interaction of H_2O_2 with Arizona test dust, The Journal of Physical Chemistry A, 118 (2013) 441-448.

[38] J.W. Anthony, R.A. Bideaux, K.W. Bladh, M.C. Nichols, Handbook of mineralogy, Mineral Data Publ. Tucson1990.

[39] H. Liao, J.H. Seinfeld, Global impacts of gas-phase chemistry-aerosol interactions on direct radiative forcing by anthropogenic aerosols and ozone, Journal of Geophysical Research: Atmospheres, 110 (2005).

[40] T.D. Fairlie, D.J. Jacob, R.J. Park, The impact of transpacific transport of mineral dust in the United States, Atmospheric Environment, 41 (2007) 1251-1266.

[41] T.D. Fairlie, D.J. Jacob, J.E. Dibb, B. Alexander, M.A. Avery, A.v. Donkelaar, L. Zhang, Impact of mineral dust on nitrate, sulfate, and ozone in transpacific Asian pollution plumes, Atmospheric Chemistry and Physics, 10 (2010) 3999-4012.

[42] K. Koehler, S. Kreidenweis, P. DeMott, M. Petters, A. Prenni, O. Möhler, Laboratory investigations of the impact of mineral dust aerosol on cold cloud formation, Atmospheric Chemistry and Physics, 10 (2010) 11955-11968.

[43] X. Li, H. Maring, D. Savoie, K. Voss, J. Prospero, Dominance of mineral dust in aerosol light-scattering in the North Atlantic trade winds, Nature, 380 (1996) 416.

[44] I. Tegen, A.A. Lacis, I. Fung, The influence on climate forcing of mineral aerosols from disturbed soils, Nature, 380 (1996) 419.

[45] C. Moulin, C.E. Lambert, F. Dulac, U. Dayan, Control of atmospheric export of dust from North Africa by the North Atlantic Oscillation, Nature, 387 (1997) 691.

[46] P.a. Alpert, Y. Kaufman, Y. Shay-El, D. Tanre, A. Da Silva, S. Schubert, J. Joseph, Quantification of dust-forced heating of the lower troposphere, Nature, 395 (1998) 367.

[47] R. Miller, I. Tegen, Climate response to soil dust aerosols, Journal of climate, 11 (1998) 3247-3267.

[48] A.L. Quijano, I.N. Sokolik, O.B. Toon, Radiative heating rates and direct radiative forcing by mineral dust in cloudy atmospheric conditions, Journal of Geophysical Research: Atmospheres, 105 (2000) 12207-12219.

[49] D. Rosenfeld, R. Lahav, A. Khain, M. Pinsky, The role of sea spray in cleansing air pollution over ocean via cloud processes, Science, 297 (2002) 1667-1670.

[50] Y. Yin, S. Wurzler, Z. Levin, T.G. Reisin, Interactions of mineral dust particles and clouds: Effects on precipitation and cloud optical properties, Journal of Geophysical Research: Atmospheres, 107 (2002) AAC 19-11-AAC 19-14.

[51] P.J. DeMott, D.C. Rogers, S.M. Kreidenweis, The susceptibility of ice formation in upper tropospheric clouds to insoluble aerosol components, Journal of Geophysical Research: Atmospheres, 102 (1997) 19575-19584.

[52] H.-M. Hung, A. Malinowski, S.T. Martin, Kinetics of heterogeneous ice nucleation on the surfaces of mineral dust cores inserted into aqueous ammonium sulfate particles, The Journal of Physical Chemistry A, 107 (2003) 1296-1306.

[53] G.D. Clayton, F.E. Clayton, Patty's industrial hygiene and toxicology. Vol. 2A. Toxicology, John Wiley & Sons, Inc., Baffins Lane, Chichester, Sussex PO19 1DU1981.

[54] M. Doğan, Environmental pulmonary health problems related to mineral dusts: Examples from central Anatolia, Turkey, Environmental Geology, 41 (2002) 571-578.

[55] R. Richards, What effects do mineral particles have in the lung?, Mineralogical Magazine, 67 (2003) 129-139.

[56] A. Parker, J.E. Rae, Environmental interactions of clays: clays and the environment, Springer Science & Business Media1998.

[57] A.C. Kurtz, L.A. Derry, O.A. Chadwick, Accretion of Asian dust to Hawaiian soils: isotopic, elemental, and mineral mass balances, Geochimica et Cosmochimica acta, 65 (2001) 1971-1983.

[58] G. Zhuang, R.A. Duce, D.R. Kester, The dissolution of atmospheric iron in surface seawater of the open ocean, Journal of Geophysical Research: Oceans, 95 (1990) 16207-16216.

[59] X. Zhu, J.M. Prospero, D.L. Savoie, F.J. Millero, R.G. Zika, E.S. Saltzman, Photoreduction of iron (III) in marine mineral aerosol solutions, Journal of Geophysical Research: Atmospheres, 98 (1993) 9039-9046.

[60] X. Zhu, J. Prospero, F. Millero, Diel variability of soluble Fe (II) and soluble total Fe in North African dust in the trade winds at Barbados, Journal of Geophysical Research: Atmospheres, 102 (1997) 21297-21305.

[61] J.J. Walsh, K.A. Steidinger, Saharan dust and Florida red tides: the cyanophyte connection, Journal of geophysical research: Oceans, 106 (2001) 11597-11612.

[62] I.Y. Fung, S.K. Meyn, I. Tegen, S.C. Doney, J.G. John, J.K. Bishop, Iron supply and demand in the upper ocean, Global Biogeochemical Cycles, 14 (2000) 281-295.

[63] S. Liu, M. Trainer, M. Carroll, G. Hübler, D. Montzka, R. Norton, B. Ridley, J. Walega, E. Atlas, B. Heikes, A study of the photochemistry and ozone budget during the Mauna Loa Observatory Photochemistry Experiment, Journal of Geophysical Research: Atmospheres, 97 (1992) 10463-10471.

[64] R.B. Chatfield, Anomalous HNO_3/NOx ratio of remote tropospheric air: Conversion of nitric acid to formic acid and NOx?, Geophysical Research Letters, 21 (1994) 2705-2708.

[65] S.M. Fan, D.J. Jacob, D. Mauzerall, J. Bradshaw, S. Sandholm, D. Blake, H. Singh, R. Talbot, G. Gregory, G. Sachse, Origin of tropospheric NOx over subarctic eastern Canada in summer, Journal of Geophysical Research: Atmospheres, 99 (1994) 16867-16877.

[66] H. Singh, D. Herlth, R. Kolyer, L. Salas, J. Bradshaw, S. Sandholm, D. Davis, J. Crawford, Y. Kondo, M. Koike, Reactive nitrogen and ozone over the western Pacific: Distribution, partitioning, and sources, Journal of Geophysical Research: Atmospheres, 101 (1996) 1793-1808.

[67] N. Joshi, M.N. Romanias, V. Riffault, F. Thevenet, Investigating water adsorption onto natural mineral dust particles: Linking DRIFTS experiments and BET theory, Aeolian Research, 27 (2017) 35-45.

[68] S. Ibrahim, M.N. Romanias, L.Y. Alleman, M.N. Zeineddine, G.K. Angeli, P.N. Trikalitis, F. Thevenet, Water Interaction with Mineral Dust Aerosol: Particle Size and Hygroscopic Properties of Dust, ACS Earth and Space Chemistry, 2 (2018) 376-386.

[69] C. Usher, A. Michel, D. Stec, V. Grassian, Laboratory studies of ozone uptake on processed mineral dust, Atmospheric Environment, 37 (2003) 5337-5347.

[70] F. Karagulian, M.J.J.I.j.o.c.k. Rossi, The heterogeneous decomposition of ozone on atmospheric mineral dust surrogates at ambient temperature, 38 (2006) 407-419.

[71] X. Wang, M.N. Romanias, F. Thévenet, A.J.C. Rousseau, Geocatalytic Uptake of Ozone onto Natural Mineral Dust, 8 (2018) 263.

[72] M. Ullerstam, M.S. Johnson, R. Vogt, E. Ljungström, DRIFTS and Knudsen cell study of the heterogeneous reactivity of SO_2 and NO_2 on mineral dust, Atmospheric Chemistry and Physics, 3 (2003) 2043-2051.

[73] H. He, Y. Wang, Q. Ma, J. Ma, B. Chu, D. Ji, G. Tang, C. Liu, H. Zhang, J. Hao, Mineral dust and NOx promote the conversion of SO_2 to sulfate in heavy pollution days, Scientific reports, 4 (2014) 4172.

[74] M. Ndour, B. D'Anna, C. George, O. Ka, Y. Balkanski, J. Kleffmann, K. Stemmler, M. Ammann, Photoenhanced uptake of NO_2 on mineral dust: Laboratory experiments and model simulations, Geophysical Research Letters, 35 (2008).

[75] Y. Dupart, S.M. King, B. Nekat, A. Nowak, A. Wiedensohler, H. Herrmann, G. David, B. Thomas, A. Miffre, P. Rairoux, Mineral dust photochemistry induces nucleation events in the presence of SO_2, Proceedings of the National Academy of Sciences, 109 (2012) 20842-20847.

[76] C. Usher, H. Al-Hosney, S. Carlos-Cuellar, V. Grassian, A laboratory study of the heterogeneous uptake and oxidation of sulfur dioxide on mineral dust particles, Journal of Geophysical Research: Atmospheres, 107 (2002) ACH 16-11-ACH 16-19.

[77] Y. Bedjanian, M.N. Romanias, A. El Zein, Interaction of OH radicals with Arizona test dust: uptake and products, 117 (2013) 393-400.

[78] Y. Bedjanian, M. Romanias, A.E. Zein, Uptake of HO_2 radicals on arizona test dust, Atmospheric Chemistry and Physics, 13 (2013) 6461-6471.

[79] M.N. Zeineddine, M.N. Romanias, V. Gaudion, V. Riffault, F. Thévenet, Heterogeneous Interaction of Isoprene with Natural Gobi Dust, ACS Earth and Space Chemistry, 1 (2017) 236-243.

[80] M.N. Romanias, M.N. Zeineddine, V. Gaudion, X. Lun, F. Thevenet, V. Riffault, Heterogeneous Interaction of Isopropanol with Natural Gobi Dust, Environmental science & technology, 50 (2016) 11714-11722.

[81] R. Scanza, N. Mahowald, S. Ghan, C. Zender, J. Kok, X. Liu, Y. Zhang, S. Albani, Modeling dust as component minerals in the Community Atmosphere Model: development of framework and impact on radiative forcing, Atmospheric Chemistry & Physics, 15 (2015).

[82] F.J. Dentener, G.R. Carmichael, Y. Zhang, J. Lelieveld, P.J. Crutzen, Role of mineral aerosol as a reactive surface in the global troposphere, Journal of Geophysical Research: Atmospheres, 101 (1996) 22869-22889.

[83] Y. Mamane, J. Gottlieb, Heterogeneous reactions of minerals with sulfur and nitrogen oxides, Journal of aerosol science, 20 (1989) 303-311.

[84] Z. Levin, C. Price, E. Ganor, The contribution of sulfate and desert aerosols to the acidification of clouds and rain in Israel, Atmospheric Environment. Part A. General Topics, 24 (1990) 1143-1151.

[85] J.W. Winchester, M.X. WANG, Acid-base balance in aerosol components of the Asia-Pacific region, Tellus B, 41 (1989) 323-337.

[86] F. Parungo, Z. Li, X. Li, D. Yang, J. Harris, Gobi dust storms and the Great Green Wall, Geophysical Research Letters, 21 (1994) 999-1002.

[87] S. Carlos-Cuellar, P. Li, A. Christensen, B. Krueger, C. Burrichter, V. Grassian, Heterogeneous uptake kinetics of volatile organic compounds on oxide surfaces using a Knudsen cell reactor: Adsorption of acetic acid, formaldehyde, and methanol on α-Fe_2O_3, α-Al_2O_3, and SiO_2, The Journal of Physical Chemistry A, 107 (2003) 4250-4261.

[88] J. Crowley, M. Ammann, R. Cox, R. Hynes, M.E. Jenkin, A. Mellouki, M. Rossi, J. Troe, T. Wallington, Evaluated kinetic and photochemical data for atmospheric chemistry: Volume V–heterogeneous reactions on solid substrates, Atmospheric Chemistry and Physics, 10 (2010) 9059-9223.

[89] C. Kolb, R. Cox, J. Abbatt, M. Ammann, E. Davis, D. Donaldson, B.C. Garrett, C. George, P. Griffiths, D. Hanson, An overview of current issues in the uptake of atmospheric trace gases by aerosols and clouds, Atmospheric Chemistry and Physics, 10 (2010) 10561-10605.

[90] M. Tang, X. Huang, K. Lu, M. Ge, Y. Li, P. Cheng, T. Zhu, A. Ding, Y. Zhang, S. Gligorovski, Heterogeneous reactions of mineral dust aerosol: implications for tropospheric oxidation capacity, Atmospheric Chemistry and Physics, 17 (2017) 11727-11777.

[91] H.H. Kung, Transition Metal Oxides - Surface Chemistry and Catalysis, Elsevier1989.

[92] A.W. Adamson, A.P. Gast, Physical chemistry of surfaces, (1967).

[93] R.I. Masel, Principles of adsorption and reaction on solid surfaces, John Wiley & Sons1996.

[94] E. Koller, Aide-mémoire de génie chimique-4e éd, Dunod2013.

[95] A. Dąbrowski, Adsorption—from theory to practice, Advances in colloid and interface science, 93 (2001) 135-224.

[96] I. Langmuir, The adsorption of gases on plane surfaces of glass, mica and platinum, Journal of the American Chemical society, 40 (1918) 1361-1403.

[97] P. Atkins, J. De Paula, Atkins' physical chemistry | Clc, 2006.

[98] S. Brunauer, P.H. Emmett, E. Teller, Adsorption of gases in multimolecular layers, Journal of the American chemical society, 60 (1938) 309-319.

[99] S. Brunauer, P.H. Emmett, The use of low temperature van der Waals adsorption isotherms in determining the surface areas of various adsorbents, Journal of the American Chemical Society, 59 (1937) 2682-2689.

[100] G. Fagerlund, Determination of specific surface by the BET method, Matériaux et Construction, 6 (1973) 239-245.

[101] J.P. Fraissard, C.W. Conner, Physical Adsorption: Experiment, Theory, and Applications, Springer Science & Business Media1997.

[102] W. Steele, G. Zgrablich, W. Rudzinski, Equilibria and dynamics of gas adsorption on heterogeneous solid surfaces, Elsevier1996.

[103] S.J. Gregg, K.S.W. Sing, H. Salzberg, Adsorption surface area and porosity, Journal of the Electrochemical Society, 114 (1967) 279C-279C.

[104] G.A. Somorjai, Y. Li, Introduction to surface chemistry and catalysis, John Wiley & Sons2010.

[105] M. Heitbaum, F. Glorius, I. Escher, Asymmetric heterogeneous catalysis, Angewandte Chemie International Edition, 45 (2006) 4732-4762.

[106] P. Forzatti, L. Lietti, Catalyst deactivation, Catalysis today, 52 (1999) 165-181.

[107] J.M. Thomas, W.J. Thomas, Principles and practice of heterogeneous catalysis, John Wiley & Sons2014.

[108] M. Boudart, Turnover rates in heterogeneous catalysis, Chemical reviews, 95 (1995) 661-666.

[109] K.V. Chary, V. Vijayakumar, P.K. Rao, Characterization of molybdenum oxide catalysts supported on anatase and rutile polymorphs of titania by low-temperature oxygen chemisorption, Langmuir, 6 (1990) 1549-1550.

[110] B.M. Reddy, B. Manohar, E.P. Reddy, Oxygen chemisorption on titania-zirconia mixed oxide supported vanadium oxide catalysts, Langmuir, 9 (1993) 1781-1785.

[111] F. Arena, F. Frusteri, A. Parmaliana, Structure and dispersion of supported-vanadia catalysts. Influence of the oxide carrier, Applied Catalysis A: General, 176 (1999) 189-199.

[112] K. Tomishige, Y. Ikeda, T. Sakaihori, K. Fujimoto, Catalytic properties and structure of zirconia catalysts for direct synthesis of dimethyl carbonate from methanol and carbon dioxide, Journal of Catalysis, 192 (2000) 355-362.

[113] S. Bordawekar, E. Doskocil, R. Davis, Microcalorimetric study of CO_2 and NH_3 adsorption on Rb-and Sr-modified catalyst supports, Langmuir, 14 (1998) 1734-1738.

[114] F. Yin, A. Blumenfeld, V. Gruver, J. Fripiat, NH3 as a probe molecule for NMR and IR study of zeolite catalyst acidity, The Journal of Physical Chemistry B, 101 (1997) 1824-1830.

[115] D. Kulkarni, I.E. Wachs, Isopropanol oxidation by pure metal oxide catalysts: number of active surface sites and turnover frequencies, Applied Catalysis A: General, 237 (2002) 121-137.

[116] L.E. Briand, W.E. Farneth, I.E. Wachs, Quantitative determination of the number of active surface sites and the turnover frequencies for methanol oxidation over metal oxide catalysts: I. Fundamentals of the methanol chemisorption technique and application to monolayer supported molybdenum oxide catalysts, Catalysis Today, 62 (2000) 219-229.

[117] M. Badlani, I.E. Wachs, Methanol: a "smart" chemical probe molecule, Catalysis Letters, 75 (2001) 137-149.

[118] W.-C. Wang, J.P. Pinto, Y.L. Yung, Climatic effects due to halogenated compounds in the Earth's atmosphere, Journal of the Atmospheric sciences, 37 (1980) 333-338.

[119] F.K. Lutgens, E.J. Tarbuck, D. Tusa, The atmosphere, Prentice Hall Upper Saddle River, NJ2001.

[120] V. Bocci, Biological and clinical effects of ozone. Has ozone therapy a future in medicine?, British journal of biomedical science, 56 (1999) 270.

[121] A. Baysan, E. Lynch, The use of ozone in dentistry and medicine, Primary Dental Care, 12 (2005) 47-52.

[122] F. Thevenet, L. Sivachandiran, O. Guaitella, C. Barakat, A. Rousseau, Plasma-catalyst coupling for volatile organic compound removal and indoor air treatment: a review, Journal of Physics D-Applied Physics, 47 (2014).

[123] U. Roland, F. Holzer, F.-D. Kopinke, Combination of non-thermal plasma and heterogeneous catalysis for oxidation of volatile organic compounds: Part 2. Ozone decomposition and deactivation of γ-Al_2O_3, Applied catalysis B: environmental, 58 (2005) 217-226.

[124] S. Suzuki, Y. Hori, O. Koga, Decomposition of ozone on natural sand, Bulletin of the Chemical Society of Japan, 52 (1979) 3103-3104.

[125] A. Klimovskii, A. Bavin, V. Tkalich, A. Lisachenko, Interaction of ozone with γ-Al_2O_3 surface, Reaction Kinetics and Catalysis Letters, 23 (1983) 95-98.

[126] G.I. Golodets, Heterogeneous catalytic reactions involving molecular oxygen, (1983).

[127] A. Alebić - Juretić, T. Cvitaš, L. Klasinc, Ozone destruction on powders, Berichte der Bunsengesellschaft für physikalische Chemie, 96 (1992) 493-495.

[128] A. Alebic-Juretic, T. Cvitas, L. Klasinc, Ozone destruction on solid particles, Environmental monitoring and assessment, 44 (1997) 241-247.

[129] A. Alebić-Juretić, T. Cvitas, L. Klasinc, Kinetics of heterogeneous ozone reactions, Chemosphere, 41 (2000) 667-670.

[130] A. Michel, C. Usher, V. Grassian, Reactive uptake of ozone on mineral oxides and mineral dusts, Atmospheric Environment, 37 (2003) 3201-3211.

[131] T. Grøntoft, Dry deposition of ozone on building materials. Chamber measurements and modelling of the time-dependent deposition, Atmospheric environment, 36 (2002) 5661-5670.

[132] A. Michel, C. Usher, V. Grassian, Heterogeneous and catalytic uptake of ozone on mineral oxides and dusts: A Knudsen cell investigation, Geophysical research letters, 29 (2002) 10-11-10-14.

[133] B. Dhandapani, S.T. Oyama, Gas phase ozone decomposition catalysts, Applied Catalysis B: Environmental, 11 (1997) 129-166.

[134] W. Li, S.T. Oyama, Mechanism of ozone decomposition on a manganese oxide catalyst. 2. Steady-state and transient kinetic studies, Journal of the American Chemical Society, 120 (1998) 9047-9052.

[135] C. Heisig, W. Zhang, S.T. Oyama, Decomposition of ozone using carbon-supported metal oxide catalysts, Applied catalysis B: environmental, 14 (1997) 117-129.

[136] F. Hanisch, J. Crowley, Ozone decomposition on Saharan dust: an experimental investigation, Atmospheric Chemistry and physics, 3 (2003) 119-130.

[137] L. Aldaz, Flux measurements of atmospheric ozone over land and water, Journal of Geophysical Research, 74 (1969) 6943-6946.

[138] J. Lasne, M.N. Romanias, F. Thevenet, Ozone Uptake by Clay Dusts Under Environmental Conditions, (2018).

[139] P.K. Mogili, P.D. Kleiber, M.A. Young, V.H. Grassian, Heterogeneous uptake of ozone on reactive components of mineral dust aerosol: An environmental aerosol reaction chamber study, The Journal of Physical Chemistry A, 110 (2006) 13799-13807.

[140] J.M. Roscoe, J.P. Abbatt, Diffuse reflectance FTIR study of the interaction of alumina surfaces with ozone and water vapor, The Journal of Physical Chemistry A, 109 (2005) 9028-9034.

[141] K. Bulanin, J. Lavalley, A. Tsyganenko, IR spectra of adsorbed ozone, Colloids and Surfaces A: Physicochemical and Engineering Aspects, 101 (1995) 153-158.

[142] K. Bulanin, J. Lavalley, A. Tsyganenko, Infrared study of ozone adsorption on CaO, The Journal of Physical Chemistry B, 101 (1997) 2917-2922.

[143] K. Bulanin, J. Lavalley, A. Tsyganenko, Infrared study of ozone adsorption on TiO_2 (anatase), The Journal of Physical Chemistry, 99 (1995) 10294-10298.

[144] K. Bulanin, A. Alexeev, D. Bystrov, J. Lavalley, A. Tsyganenko, IR study of ozone adsorption On SiO2, The Journal of Physical Chemistry, 98 (1994) 5100-5103.

[145] K. Thomas, P. Hoggan, L. Mariey, J. Lamotte, J. Lavalley, Experimental and theoretical study of ozone adsorption on alumina, Catalysis Letters, 46 (1997) 77-82.

[146] W. Li, G. Gibbs, S.T. Oyama, Mechanism of ozone decomposition on a manganese oxide catalyst. 1. In situ Raman spectroscopy and ab initio molecular orbital calculations, Journal of the American Chemical Society, 120 (1998) 9041-9046.

[147] J. Jia, P. Zhang, L. Chen, Catalytic decomposition of gaseous ozone over manganese dioxides with different crystal structures, Applied Catalysis B: Environmental, 189 (2016) 210-218.

[148] A. El Zein, M.N. Romanias, Y. Bedjanian, Kinetics and products of heterogeneous reaction of HONO with Fe_2O_3 and Arizona Test Dust, Environmental science & technology, 47 (2013) 6325-6331.

[149] M. Hanning-Lee, B. Brady, L. Martin, J. Syage, Ozone decomposition on alumina: Implications for solid rocket motor exhaust, Geophysical research letters, 23 (1996) 1961-1964.

[150] P. Khare, N. Kumar, K. Kumari, S. Srivastava, Atmospheric formic and acetic acids: An overview, Reviews of Geophysics, 37 (1999) 227-248.

[151] L. Sivachandiran, F. Thevenet, P. Gravejat, A. Rousseau, Isopropanol saturated TiO_2 surface regeneration by non-thermal plasma: Influence of air relative humidity, Chemical Engineering Journal, 214 (2013) 17-26.

[152] A. Hodgson, H. Destaillats, D. Sullivan, W. Fisk, Performance of ultraviolet photocatalytic oxidation for indoor air cleaning applications, Indoor air, 17 (2007) 305-316.

[153] H. Evans, W. Weinberg, A comparison of the vibrational structures of ethanol, acetic acid, and acetaldehyde adsorbed on alumina, The Journal of Chemical Physics, 71 (1979) 4789-4798.

[154] H. Evans, W. Weinberg, The reaction of ethanol with an aluminum oxide surface studied by inelastic electron tunneling spectroscopy, The Journal of Chemical Physics, 71 (1979) 1537-1542.

[155] P. Li, K. Perreau, E. Covington, C. Song, G. Carmichael, V. Grassian, Heterogeneous reactions of volatile organic compounds on oxide particles of the most abundant crustal elements: Surface reactions of acetaldehyde, acetone, and propionaldehyde on SiO_2, Al_2O_3, Fe_2O_3, TiO_2, and CaO, Journal of Geophysical Research: Atmospheres, 106 (2001) 5517-5529.

[156] S.R. Morrison, The chemical physics of surfaces, Springer Science & Business Media2013.

[157] J.E. Rekoske, M.A. Barteau, Competition between acetaldehyde and crotonaldehyde during adsorption and reaction on anatase and rutile titanium dioxide, Langmuir, 15 (1999) 2061-2070.

[158] E. Finocchio, R.J. Willey, V. Lorenzelli, FTIR studies on the selective oxidation and combustion of light hydrocarbons at metal oxide surfaces Part 3.—Comparison of the oxidation of C3 organic compounds over Co_3O_4, $MgCr_2O_4$ and CuO, Journal of the Chemical Society, Faraday Transactions, 93 (1997) 175-180.

[159] K.-i. Shimizu, H. Kawabata, A. Satsuma, T. Hattori, Role of acetate and nitrates in the selective catalytic reduction of NO by propene over alumina catalyst as investigated by FTIR, The Journal of Physical Chemistry B, 103 (1999) 5240-5245.

[160] T. Wadayama, O. Suzuki, K. Takeuchi, H. Seki, T. Tanabe, Y. Suzuki, A. Hatta, IR absorption enhancement for physisorbed methanol on Ag island films deposited on the oxidized and H-terminated Si (111) surfaces: effect of the metal surface morphology, Applied Physics A, 69 (1999) 77-80.

[161] G. Busca, J. Lamotte, J.C. Lavalley, V. Lorenzelli, FT-IR study of the adsorption and transformation of formaldehyde on oxide surfaces, Journal of the American Chemical Society, 109 (1987) 5197-5202.

[162] M. Tang, W.A. Larish, Y. Fang, A. Gankanda, V.H. Grassian, Heterogeneous reactions of acetic acid with oxide surfaces: Effects of mineralogy and relative humidity, The Journal of Physical Chemistry A, 120 (2016) 5609-5616.

[163] H.A. Al-Hosney, S. Carlos-Cuellar, J. Baltrusaitis, V.H. Grassian, Heterogeneous uptake and reactivity of formic acid on calcium carbonate particles: a Knudsen cell reactor, FTIR and SEM study, Physical Chemistry Chemical Physics, 7 (2005) 3587-3595.

[164] A.P. Prince, P.D. Kleiber, V.H. Grassian, M.A. Young, Reactive uptake of acetic acid on calcite and nitric acid reacted calcite aerosol in an environmental reaction chamber, Physical Chemistry Chemical Physics, 10 (2008) 142-152.

[165] J.E. Shilling, M.A. Tolbert, Uptake of acetic acid on thin ammonium nitrate films as a function of temperature and relative humidity, The Journal of Physical Chemistry A, 108 (2004) 11314-11320.

[166] L.-F. Liao, C.-F. Lien, J.-L. Lin, FTIR study of adsorption and photoreactions of acetic acid on TiO 2, Physical Chemistry Chemical Physics, 3 (2001) 3831-3837.

[167] S. Tong, L. Wu, M. Ge, W. Wang, Z. Pu, Heterogeneous chemistry of monocarboxylic acids on α-Al_2O_3 at different relative humidities, Atmospheric Chemistry and Physics, 10 (2010) 7561-7574.

[168] A. Goodman, E. Bernard, V. Grassian, Spectroscopic study of nitric acid and water adsorption on oxide particles: Enhanced nitric acid uptake kinetics in the presence of adsorbed water, The Journal of Physical Chemistry A, 105 (2001) 6443-6457.

[169] V. Demidiouk, S.I. Moon, J.O. Chae, D.Y. Lee, Application of a plasma-catalytic system for decomposition of volatile organic compounds, Journal of the Korean Physical Society, 42 (2003) S966-S970.

[170] L. Wang, F. Zhao, G.X. Ying, Y. Xing, L. Du, An investigation of a new plasma-catalyst hybrid systems for indoor air pollution control, 2006.

[171] B.R. Raju, E.L. Reddy, J. Karuppiah, P.M.K. Reddy, C. Subrahmanyam, Catalytic non-thermal plasma reactor for the decomposition of a mixture of volatile organic compounds, Journal of Chemical Sciences, 125 (2013) 673-678.

[172] M. Bahri, F. Haghighat, Plasma-Based Indoor Air Cleaning Technologies: The State of the Art-Review, Clean-Soil Air Water, 42 (2014) 1667-1680.

[173] E. Gallego, X. Roca, J.F. Perales, X. Guardino, Determining indoor air quality and identifying the origin of odour episodes in indoor environments, Journal of Environmental Sciences, 21 (2009) 333-339.

[174] A. Fridman, A. Chirokov, A. Gutsol, Non-thermal atmospheric pressure discharges, Journal of Physics D: Applied Physics, 38 (2005) R1.

[175] M.A. Lieberman, A.J. Lichtenberg, Principles of plasma discharges and materials processing, John Wiley & Sons2005.

[176] A. Chirokov, A. Gutsol, A. Fridman, Atmospheric pressure plasma of dielectric barrier discharges, Pure and Applied Chemistry, 77 (2005) 487-495.

[177] U. Kogelschatz, Dielectric-Barrier Discharges: Their History, Discharge Physics, and Industrial Applications, Plasma Chemistry and Plasma Processing, 23 (2003) 1-46.

[178] P. Talebizadeh, M. Babaie, R. Brown, H. Rahimzadeh, Z. Ristovski, M. Arai, The role of non-thermal plasma technique in NOx treatment: A review, Renewable & Sustainable Energy Reviews, 40 (2014) 886-901.

[179] H.L. Chen, H.M. Lee, S.H. Chen, M.B. Chang, Review of packed-bed plasma reactor for ozone generation and air pollution control, Industrial & Engineering Chemistry Research, 47 (2008) 2122-2130.

[180] H.L. Chen, H.M. Lee, S.H. Chen, M.B. Chang, S.J. Yu, S.N. Li, Removal of volatile organic compounds by single-stage and two-stage plasma catalysis systems: a review of the performance enhancement mechanisms, current status, and suitable applications, Environmental science & technology, 43 (2009) 2216-2227.

[181] J. Van Durme, J. Dewulf, C. Leys, H. Van Langenhove, Combining non-thermal plasma with heterogeneous catalysis in waste gas treatment: A review, Applied Catalysis B: Environmental, 78 (2008) 324-333.

[182] A.M. Vandenbroucke, R. Morent, N. De Geyter, C. Leys, Non-thermal plasmas for non-catalytic and catalytic VOC abatement, Journal of hazardous materials, 195 (2011) 30-54.

[183] A. Mizuno, H. Ito, Basic performance of an electrostatically augmented filter consisting of a packed ferroelectric pellet layer, Journal of electrostatics, 25 (1990) 97-107.

[184] A.M. Harling, V. Demidyuk, S.J. Fischer, J.C. Whitehead, Plasma-catalysis destruction of aromatics for environmental clean-up: Effect of temperature and configuration, Applied Catalysis B: Environmental, 82 (2008) 180-189.

[185] F. Holzer, U. Roland, F.-D. Kopinke, Combination of non-thermal plasma and heterogeneous catalysis for oxidation of volatile organic compounds: Part 1. Accessibility of the intra-particle volume, Applied Catalysis B: Environmental, 38 (2002) 163-181.

[186] R. Radhakrishnan, S.T. Oyama, J.G. Chen, K. Asakura, Electron transfer effects in ozone decomposition on supported manganese oxide, The Journal of Physical Chemistry B, 105 (2001) 4245-4253.

[187] H. Einaga, A. Ogata, Benzene oxidation with ozone over supported manganese oxide catalysts: effect of catalyst support and reaction conditions, Journal of hazardous materials, 164 (2009) 1236-1241.

[188] L. Sivachandiran, F. Thevenet, A. Rousseau, Regeneration of isopropyl alcohol saturated Mn_xO_Y surface: Comparison of thermal, ozonolysis and non-thermal plasma treatments, Chemical Engineering Journal, 246 (2014) 184-195.

[189] X.L. Zhang, A.M. Zhu, X.H. Li, W.M. Gong, Oxidative dehydrogenation of ethane with CO_2 over catalyst under pulse corona plasma, Catalysis Today, 89 (2004) 97-102.

[190] T. Zhu, R. Chen, N. Xia, X.Y. Li, X.X. He, W.J. Zhao, T. Carr, Volatile organic compounds emission control in industrial pollution source using plasma technology coupled with F-TiO_2/gamma-Al2O3, Environmental Technology, 36 (2015) 1405-1413.

[191] H. Einaga, T. Ibusuki, S. Futamura, Performance evaluation of a hybrid system comprising silent discharge plasma and manganese oxide catalysts for benzene decomposition, Ieee Transactions on Industry Applications, 37 (2001) 1476-1482.

[192] B. Lu, X. Zhang, X. Yu, T. Feng, S. Yao, Catalytic oxidation of benzene using DBD corona discharges, Journal of Hazardous Materials, 137 (2006) 633-637.

[193] K. Krawczyk, M. Mlotek, Combined plasma-catalytic processing of nitrous oxide, Applied Catalysis B-Environmental, 30 (2001) 233-245.

[194] J.L. Wu, Y.X. Huang, Q.B. Xia, Z. Li, Decomposition of Toluene in a Plasma Catalysis System with NiO, MnO_2, CeO_2, Fe_2O_3, and CuO Catalysts, Plasma Chemistry and Plasma Processing, 33 (2013) 1073-1082.

[195] S. Futamura, A. Gurusamy, Synergy of nonthermal plasma and catalysts in the decomposition of fluorinated hydrocarbons, Journal of Electrostatics, 63 (2005) 949-954.

[196] S. Sauce, A. Vega-Gonzalez, Z.X. Jia, S. Touchard, K. Hassouni, A. Kanaev, X. Duten, New insights in understanding plasma-catalysis reaction pathways: study of the catalytic ozonation of an acetaldehyde saturated Ag/TiO_2/SiO_2 catalyst, European Physical Journal-Applied Physics, 71 (2015).

[197] S. Futamura, H. Einaga, H. Kabashima, L.Y. Hwan, Synergistic effect of silent discharge plasma and catalysts on benzene decomposition, Catalysis Today, 89 (2004) 89-95.

[198] M. Sugasawa, S. Futamura, Ieee, Synergistic Effect of Nonthermal Plasma and Catalysts on the Decomposition of VOCs, Conference Record of the 2007 Ieee Industry Applications Conference Forty-Second Ias Annual Meeting, Vols. 1-52007, pp. 1485-1488.

[199] L. Sivachandiran, F. Thevenet, A. Rousseau, Non-Thermal Plasma Assisted Regeneration of Acetone Adsorbed TiO2 Surface, Plasma Chemistry and Plasma Processing, 33 (2013) 855-871.

[200] C. Barakat, P. Gravejat, O. Guaitella, F. Thevenet, A. Rousseau, Oxidation of isopropanol and acetone adsorbed on TiO_2 under plasma generated ozone flow: Gas phase and adsorbed species monitoring, Applied Catalysis B-Environmental, 147 (2014) 302-313.

[201] C. He, L. Cao, X. Liu, W. Fu, J. Zhao, Catalytic behavior and synergistic effect of nonthermal plasma and CuO/AC catalyst for benzene destruction, International Journal of Environmental Science and Technology, 12 (2015) 3531-3540.

[202] T. Zhang, Q.R. Li, Y. Liu, Y.L. Duan, W.Y. Zhang, Equilibrium and kinetics studies of fluoride ions adsorption on CeO2/Al2O3 composites pretreated with non-thermal plasma, Chemical Engineering Journal, 168 (2011) 665-671.

[203] X.B. Zhu, X. Tu, D.H. Mei, C.H. Zheng, J.S. Zhou, X. Gao, Z.Y. Luo, M.J. Ni, K.F. Cen, Investigation of hybrid plasma-catalytic removal of acetone over CuO/gamma-Al_2O_3 catalysts using response surface method, Chemosphere, 155 (2016) 9-17.

[204] C. Norsic, J.M. Tatibouet, C. Batiot-Dupeyrat, E. Fourre, Non thermal plasma assisted catalysis of methanol oxidation on Mn, Ce and Cu oxides supported on gamma-Al_2O_3, Chemical Engineering Journal, 304 (2016) 563-572.

[205] L. Sivachandiran, F. Thevenet, A. Rousseau, Isopropanol removal using Mn_xO_Y packed bed non-thermal plasma reactor: Comparison between continuous treatment and sequential sorption/regeneration, Chemical Engineering Journal, 270 (2015) 327-335.

[206] A.A. Assadi, A. Bouzaza, D. Wolbert, Study of synergetic effect by surface discharge plasma/TiO_2 combination for indoor air treatment: Sequential and continuous configurations at pilot scale, Journal of Photochemistry and Photobiology A: Chemistry, 310 (2015) 148-154.

Chapter II. Materials and methods

Table of contents

Table of Figures

In this section, the materials and methods used in the present study in order to achieve the objectives of this thesis are discussed. It starts with the descriptions of the materials such as mineral dust sample, synthetic minerals and gases. Then, it moves to the description of the experimental setups and methods applied to gas phase and adsorbed phase characterizations.

1 Materials

1.1 Natural Gobi dust sample

The natural mineral dust sample has been collected in Gobi desert of Ningxia Province in China. This area represents the second most important source of atmospheric mineral dust in the atmosphere after Sahara desert [1].

Several important reasons have been taken into consideration before choosing Gobi dust as the natural material of interest for this study. Firstly, as mentioned in Chapter 1, the Gobi dust is the most representative atmospheric mineral aerosols in Asia especially south Asia, which has already caused significant impacts for many Asian countries especially China [2-4]. Studying the reactivity of Gobi dust can help better understanding its impacts in Asia. Secondly, it has been noticed in the literature that the Al/Si and Fe/Si elemental ratios of natural mineral dusts are correlated with their uptake efficiency towards VOC, i.e. isopropanol (see Figure II-1), and also suggested for inorganic species such as ozone, NO_2 and SO_2, based on the investigation of the heterogeneous interaction of various natural dust samples with isopropanol by M. Zeineddine et al in 2018 [5]. Among the available natural mineral dust samples, Gobi dust has one of the highest Al/Si rations compared with dusts collected from other sources around world, e.g. Rawdat dust and Mbour dust from Sahara region in Africa, Arizona test dust from North America and etc. according to Table I-1. As a result, Gobi dust is potentially suggested to have specific surface properties, thus to be a material of more practical interests.

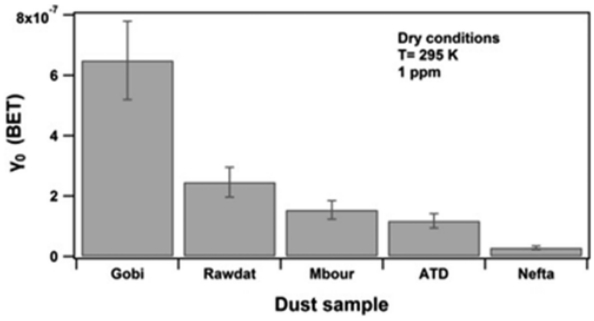

Figure II-1 Initial uptake coefficients of isopropanol onto Gobi dust and other mineral dusts. The figure is retrieved from [5].

The characterizations of Gobi dust sample regarding the particle size, specific surface area, morphology, composition, and the number of active surface sites of natural Gobi dust are summarized as followed.

Collected samples have been sieved to select the particle size, only the fraction below 100 μm is used. The specific surface area of the selected size fraction is comparable with typical surface areas of commercially available and synthetic metal oxides usually used in catalytic processes and plasma-catalysis [6, 7]. This aspect may promote gas surface interactions [8]. The BET specific surface area of the selected fraction of Gobi dust, measured by a laboratory sorption analyzer using nitrogen as adsorbate gas, is 10.5 ± 2.0 m^2 g^{-1}.

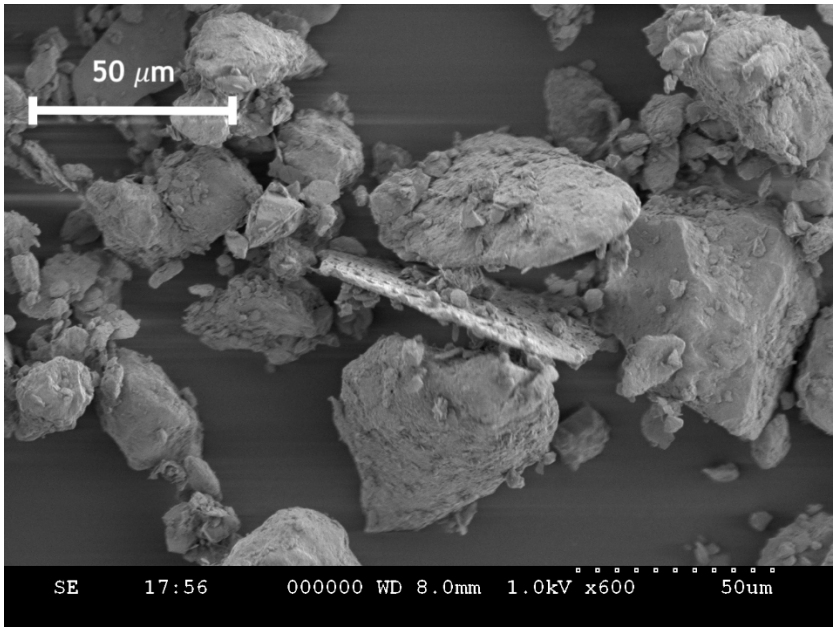

Figure II-2 SEM image of the sieved natural Gobi dust sample (< 100 µm).

The morphology of the sieved Gobi sample is evaluated using scanning electron microscopy (SEM). This technique reveals that particles are irregular in shape and exhibit contrasted sizes as shown in Figure II-2. Indeed, most of the particles are bulky in shape with mean diameters ranging from a few to 50 µm. However, flat particles are observed, suggesting the presence of distinct crystalline phases in the same sample.

The mineral phases and the elemental composition have been determined using X-ray diffraction (XRD; Bruker D2 phaser 2 theta analyzer) and X-ray fluorescence (XRF; Bruker AXS explorer S4 pioneer). Results related to the composition of natural Gobi dust are reported in Table II-1. It clearly shows that Gobi dust sample used in the present study contains various minerals as well as metal oxides, some of which are widely used in industry, such as SiO_2 [9], $Al_2Si_2O_5(OH)_4$, also known as kaolinite [10], and TiO_2 [11]. When compared with other natural dust samples such as Saharan dust and Arizona test dust (ATD) which have been used and characterized by A. E. Zein et al., A. Goudie et al., M.N. Zeineddine et al. and M.N. Romanias, Gobi dust contains the lowest fraction of SiO_2, i.e. only 33 wt % [5, 7, 12, 13]. This mineral is reported to be the less reactive mineral phase of natural dusts by several authors

[14-16]. Another important point is that Gobi dust has a relatively high content of $CaCO_3$, and this phase may markedly contribute to basic surface properties.

Table II-1 Composition of natural mineral Gobi dust determined by XRD and XRF

Name	Formula	wt %
Quartz	SiO_2	33.0 %
Calcite	$CaCO_3$	8.7 %
Albite	$NaAlSi_3O_8$	8.6 %
Muscovite	$KAl_3Si_3O_{10}(OH)_2$	25.8 %
Kaolinite	$Al_2Si_2O_5(OH)_4$	8.9 %
Rutile	TiO_2	4.4 %
Hedenbergite	$CaFeSi_2O_6$	6.2 %
Chromian pyrope	$Mg_3Al_2(SiO_4)_3$	4.1 %
Beaconite	$Mg_3Si_4O_{10}(OH)_2$	0.3 %

The number of active sites (μmol m^{-2}) on the surface of Gobi dust is estimated from the components of Gobi dust listed in Table II-1 and from the experimentally determined number of active sites of the main components in Gobi dust, such as SiO_2, TiO_2, as well as some other common metal oxides such as Al_2O_3, MgO, for which the detailed information can be found in Table I-2. As a result, an estimation of the number of active surface sites of Gobi dust is to be 2 μmol m^{-2}, within the average number of active surface site for usual metal oxides, i.e., from 2 to 4 μmol m^{-2}. Table II-2 lists the important physical and chemical characteristcis of natural Gobi dust used in this study.

Table II-2 Summary of the physical and chemical characterisctics of natural Gobi dust.

Particle size	≤ 100 μm
BET surface area	10.5 ± 2.0 m^2 g^{-1}
Density of active site	2 μmol m^{-2}

1.2 Synthetic minerals

Besides Gobi dust, some pure synthetic minerals are studied as reference materials to compare with Gobi dust. They are commercially available and detailed information can be found on the official website of SIGMA according to their reference numbers. Herein are the reference of these synthetic minerals.

Table II-3 characteristics of the synthetic minerals used.

SIGMA reference	Composition	Size fraction μm	BET surface $m^2 g^{-1}$
A2039	Al_2O_3	< 200	110 - 180
718467	TiO_2	< 0.05	35 – 65
C6763	$CaCO_3$	< 30	< 1
204358	SiO_2	< 200	200 – 400

For the aluminosilicates contained in Gobi dust, only $Al_2Si_2O_5(OH)_4$, which is also known as kaolinite, is available and is provided by SAGE IMT-Lille-Douai. The characterization is provided by J. Lasne et al. [17].

1.3 Gases

1.3.1 Carrier gases

Synthetic zero air, synthetic O_2 and N_2 were used as carrier gas for the kinetic and mechanistic studies. The synthetic air (Alphagaz 1, total purity: $N_2 + O_2 > 99.999$ %) and oxygen (Alphagaz 1, total purity: $O_2 > 99.995$ %) used as carrier gases are provided and certified by *Air Liquide* in cylinders. Their specifications provided by *Air Liquide* are listed in Table II-4. N_2 with high purity (> 99.99 %) is provided by l'Ecole Polytechnique which is produced by the evaporation of liquid nitrogen. Generally, N_2 is used to purge the gas line and maintain the experimental system dry and dynamic out of experiments.

Table II-4 specifications of the cylinder zero air and oxygen provided by *Air Liquide*.

Alphagaz 1 Air	Alphagaz 1 Oxygen
CO_2 < 1 ppm	C_nH_m < 500 ppb
CO < 1 ppm	H_2O < 3 ppm
C_nH_m < 100 ppb	
H_2O < 3 ppm	

To crosscheck the impurities specifications provided by the supplier for synthetic air and O_2, the gas flow has been analyzed with an infrared spectrometer FTIR (*Nicolet* 6700) with a gas cell of 2-L volume and 10-m optical path. Results show that the initial humidity in both zero air and oxygen is lower than 2 ppm and CO_2 concentration is lower than 1 ppm.

1.3.2 Ozone

Ozone is generated by flowing oxygen or zero air flow through either a laboratory dielectric barrier discharge (DBD) reactor for ppm-level ozone production (up to 500 ppm of ozone can be generated with input dry air flow of 500 sccm), or through a UV-light ozone generator (*Thermo Environment.* Model 165) for ppb to low ppm levels of ozone production (from 20 ppb to ca. 10 ppm).

The introduction and description of DBD reactor has been given in chapter 1. In this study, the DBD reactor is made of a Pyrex glass tube (0.8 mm of thickness with inner diameter of 1.7 mm) as dielectric, a tungsten wire (0.2 mm of thickness) placed in the middle of the Pyrex glass tube as high voltage electrode and a copper sheet (1.5 cm of length) wrapped around the outer surface of the tube as ground electrode. It is illustrated in Figure II-3 with a circuit scheme.

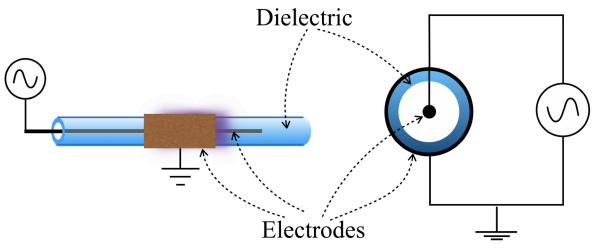

Figure II-3 Scheme of the DBD reactor used in this study.

The discharge is ignited by a laboratory high voltage power supply delivering up to 20 kV AC with maximum frequency of 1 kHz. The output voltage of the power supply is monitored by a high voltage

probe. Ozone production is regulated by tuning the input voltage, which in fact determines the specific input energy SIE, in J L^{-1}, during discharge. The specific input energy SIE is the ration between the power in Watts, injected into the discharge system, and the gas flow rate in sccm passing through the discharge region. The specific curve of this DBD reactor of ozone production as a function of SIE under dry condition is given in Figure II-4. This curve is calibrated with dry zero air flow of 250 sccm of flow rate. The flow rate, type of carrier gas as well as relative humidity all have influence on the behavior of the ozone production-SIE curve.

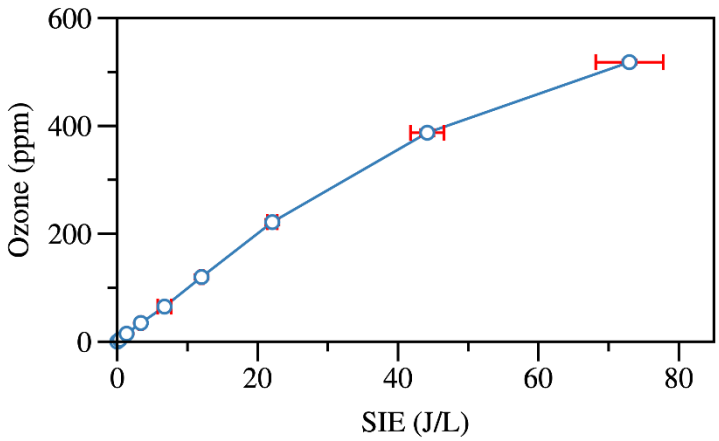

Figure II-4 Ozone production as a function of the SIE for the DBD reactor used in this study.

A typical IR spectrum obtained after ozone generation using the DBD reactor and oxygen as gas is shown in Figure 5. The gas phase ozone is characterized by the typical FTIR band centered at ca. 1050 cm^{-1} and its overtone band at 2100 cm^{-1} in Figure II-5. The band at 2300 – 2400 cm^{-1} is attributed to CO_2 which is present in the system. Note that oxygen was selected as carrier gas for O_3 production with the DBD instead of zero air to eliminate the possible formation of NOx in the gas flow. Indeed, it has been observed that using zero air as bath gas to produce relative high concentrations of O_3 (above 10 ppm) then NO_x is always formed.

On the contrary, this is not the case for the *Thermo 165* generator, where NO_x was not formed using zero air as bath gas. This is probably attributed to the most selective (but less efficient) production of ozone with the UV lamp.

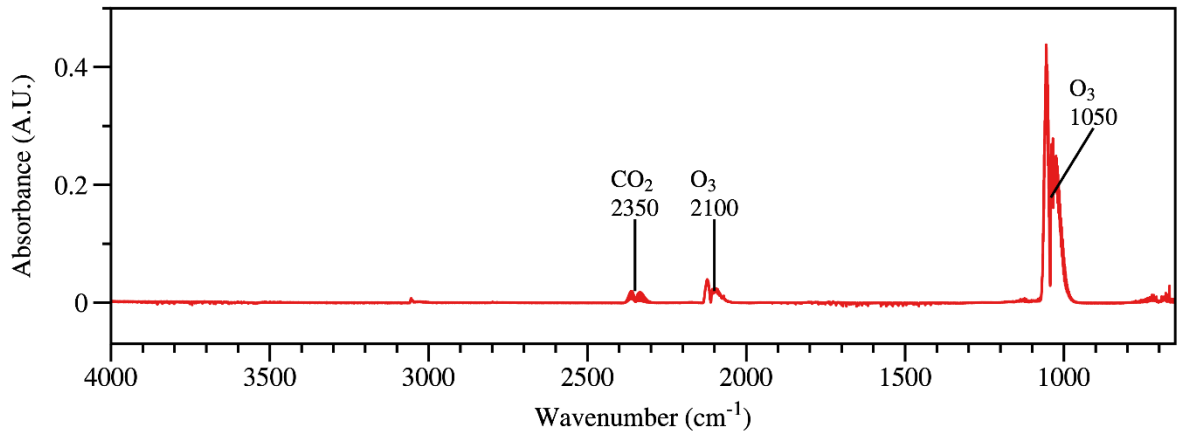

Figure II-5 FTIR spectrum of gas phase ozone of ca. 60 ppm acquired at atmospheric pressure under dry condition using oxygen as bath gas. The temperature of the FTIR gas cell is 50˚C.

1.3.3 Acetic Acid (AcA)

AcA vapor is generated by flowing carrier gas through a bubbler containing liquid acetic acid immersed in a cryostat. The liquid acetic acid used in this study is provided by *SIGMAL ALDRICH* with purity ≥ 99.7 % (reference number: 320099).

The concentration of AcA vapor can be calculated by Antoine Equation and is controlled by regulating the temperature of liquid AcA through the cryostat. Antoine Equation of AcA applicable from 290.3 K to 391 K is expressed in equation (II-1) [18]:

$$\log_{10}(P) = 4.682 - \left(\frac{1642.54}{T - 39.764}\right) \quad \text{(II-1)}$$

where P is the vapor pressure in bar, and T is the temperature in K.

The accessible range of AcA varies from several ppb with dilution to thousand ppm.

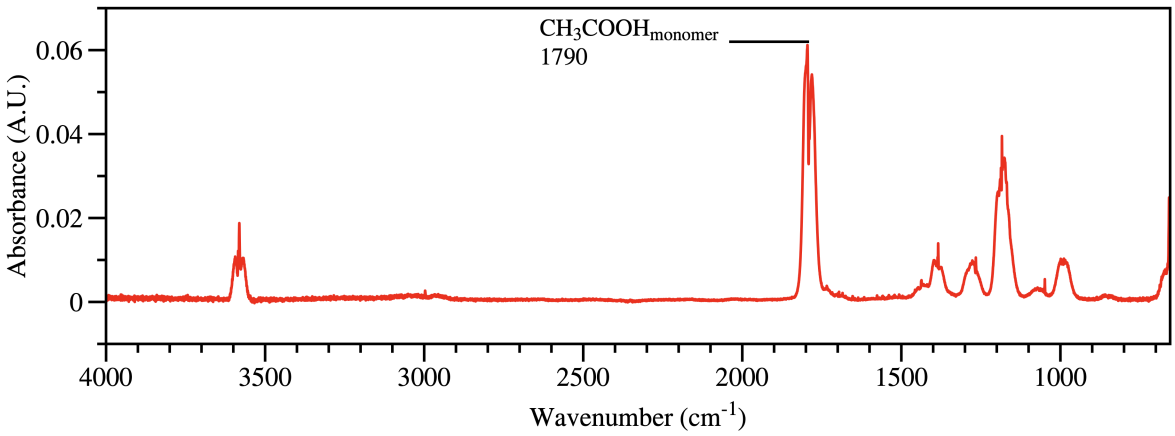

Figure II-6 FTIR spectrum of gas phase AcA of ca. 10 ppm acquired at atmospheric pressure under dry condition. The temperature of the FTIR gas cell is at room temperature.

The FTIR spectrum of 10 ppm of gaseousAcA acquired at atmospheric pressure under dry condition.is displayed in Figure II-6. The temperature of the FTIR gas cell is at room temperature. In this study, as indicated in Figure II-6, monomer is the main form of gas phase AcA, evidenced by the typical vibrational modes of ν(C=O) from monomers centered ca. 1790 cm^{-1} [19].

1.3.4 Water vapor

Water vapor is generated by flowing carrier gas through a bubbler containing deionized water immersed in a cryostat. Similarly, water vapor level is controlled by regulating the temperature of the cryostat and diluted with carrier gas. It can provide humid air flow ranging from 0 % to 100 % RH (relative humidity). Antoine equation applicable for water between 273K to 303 K is expressed as equation (II-2):

$$\log_{10}(P) = 5.402 - (\frac{1838.675}{T - 31.737}) \quad \text{(II-2)}$$

2 Methods

2.1 Gas phase approach

To monitor the gas-phase kinetics of gaseous species, i.e. ozone and AcA, during the interaction with Gobi dust sample, the experimental setup shown in Figure II-7 is used. It consists of three main parts:

(i) A gas flow preparation system which can provide zero air flow or air flow containing ozone, VOC, and water corresponding to different experimental requirements.

(ii) A U-shape flow-through reactor where the interactions of Gobi dust with gaseous species take place.

(iii) Diagnostic instruments connected to the outlet of the U-shape reactor to monitor the concentration of gas-phase species on-line.

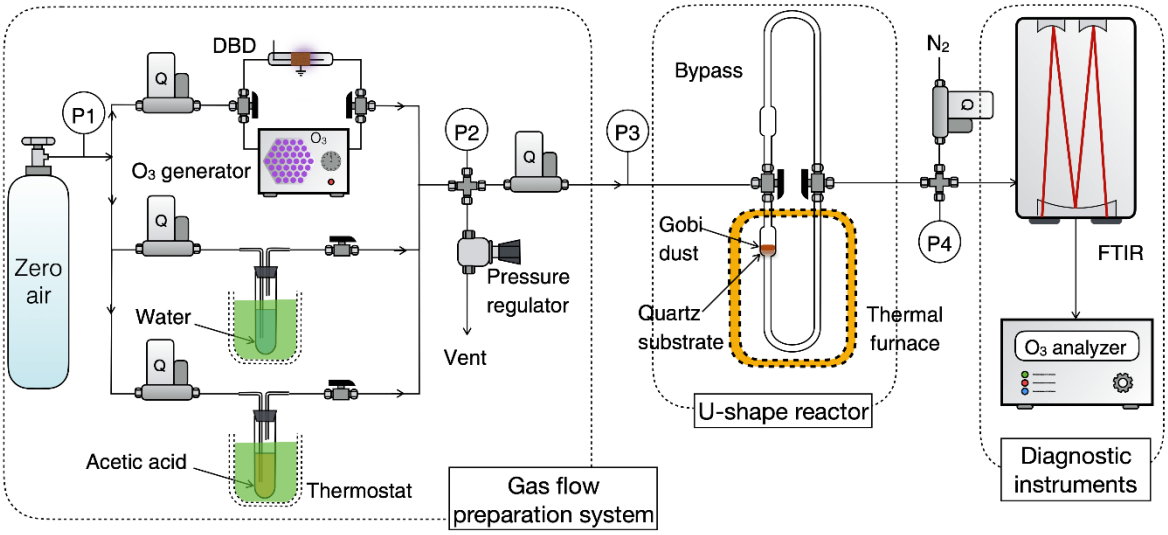

Figure II-7 Scheme of the experimental setup used in this study dedicated to gas phase investigation which consists of a gas flow preparation system, a U-shape reactor and diagnostic instruments.

This kind of experimental setup has been successfully used to investigate various heterogeneous systems [20-24]. Details of the specifications of each part of this setup, as well as typical protocol for gas-phase investigation will be given in the following sections.

2.1.1 Gas flow preparation system

Zero air is used as the main carrier gas in the gas phase approach. The main gas line is divided into three independent gas lines to provide different gas species, i.e. ozone, AcA and water vapor, as shown in Figure II-7. The generations of gaseous species have been described in *section 1.3* of the current chapter. Ozone level used in the gas phase approach is lower than 10 ppm, thus there is no co-generated NO_x from ozone generation.

The flow rates in all gas lines are controlled and monitored by using *Brooks (5800E series)* mass flow controllers. The pressure in the gas generation system is regulated to 1.3 ± 0.1 bar by a pressure regulator. There are two important reasons for maintaining the pressure inside gas preparation system a little higher than atmospheric pressure: (1) to provide enough pressure for gas flows to break through dust sample downstream, (2) to guarantee that the generation of ozone, water vapor as well as AcA during experiment remain stable and the concentrations of the gas phase species are not influenced by other operations.

2.1.2 U-shape reactor

A U-shape flow-through reactor made of quartz is connected downstream the gas preparation system. The volume of the U-shape reactor is 12 mL. A porous quartz sample holder with pore size of ca. 30 µm and diameter of ca.1 cm is placed inside the reactor to set the dust samples. From 10 mg to 200 mg

of dust sample can be placed inside the U-shape reactor. If the mass of dust sample is lower than 10 mg, the total surface of the sample holder cannot be covered thus causing too much interspace to bypass the gas species. If the mass of the dust sample is more than 200 mg, it can block the passage of gas due to the high packing density of the dust sample.

The residence time for gas flow is estimated to be ca. 3 s with flow rate of 150 sccm. The gas-dust contacting time is estimated to be ca. 20 – 100 ms varying with the mass of dust sample. The Reynold number is calculated based on the model for packed-bed reactor and flow-through reactor to be at the range from 4 to 10 which suggests that the flow is most likely in laminar state. This reactor is suggested have sufficant mass transfer process between gas species and dust sample by average mass transfer coefficients which are calculated at the range of 10^{-3} cm s^{-1}.

A bypass line of the same volume as the U-shape reactor is connected in parallel with the U-shape reactor as shown in Figure II-7. The U-shape reactor can be moved into a furnace (*Nabertherm* RT 50/250/11) to perform thermal treatment of the dust samples. The temperature inside of the furnace can be maintained stable at up to 800˚C.

2.1.3 Diagnostic instruments: transmission FTIR spectroscopy and ozone analyzer

2.1.3.1 FTIR spectroscopy

A FTIR spectrometer is connected at the outlet of the U-shape reactor to monitor the gas phase species during the heterogeneous interaction. It uses infrared light with wavelengths ranging from 2.5 to 25 μm to excite the atoms in a molecule to vibrate or rotate. Before reaching the sample, i.e. gaseous species, the infrared light is sent into an interferometer to generate interferogram within the infrared wavenumber range from 400 to 4000 cm^{-1}. When the frequency of the radiation corresponds to the frequency of the fundamental vibration mode of the molecules, this part of the energy from the radiation is absorbed by the molecule. The detector of the FTIR detects the absorption of the infrared signal with these certain frequencies after it passing through the gas, then sends it to computer for Fourier transformation to generate infrared spectrum.

In a FTIR spectrum, the light intensity is plotted as a function as wavenumber (cm^{-1}). Taking absorption spectrum as an example, the intensity of absorbance in the spectrum indicates the amount of light absorbed by the gas, and the wavenumber where the peak appears indicates the specific vibrational energy corresponding to certain functional molecular groups. The absorbance A with no unit, can be calculated from equation (II-3):

$$A = \log \frac{I}{I_0} \qquad \text{(II-3)}$$

Where I_0 is the intensity in the background spectrum, and I the intensity in the sample spectrum. According to Beer's Law, absorbance is also related to the concentration of molecules in a sample:

$$A = \varepsilon \, l \, C \quad \text{(II-4)}$$

where ε is the absorption coefficient (L mol^{-1} cm^{-1}), l the pathlength (cm) of the light, and C the concentration of the sample (mol L^{-1}). There is a linear relationship between the absorbance intensity and the concentration of the observed peaks. With calibration and spectrum analysis, we can get from the FTIR spectra what are the molecular functional group present and what are their concentrations in the sample.

In the study, a high-resolution Nicolet 6700 FTIR spectrometer is used. It is equipped with a 10 m optical-path gas cell with a volume of 2 L, and a mercury cadmium telluride (MCT) detector which is cooled at 77 K by liquid nitrogen. The gas cell is maintained at 50˚C to prevent from the adsorption of water as well as other gas species onto the mirrors inside the gas cell. The limit of detection of FTIR under dry condition is 10 ppb for N_2O, 10 ppb for NO, 15 ppb for ozone, 20 ppb for CO_2, 10 ppb for CO and 100 ppb for acetic acid.

OMNIC is the software used for spectrum acquisition. For each spectrum acquired, it takes around 32 seconds with 16 scans per spectrum and resolution of 0.5 cm^{-1}. TQ Analyst is used for calibration and spectrum analysis.

2.1.3.2 Ozone analyzer

A commercial ozone analyzer (*Environnement* S.A. O342e) is connected at the outlet of FTIR gas cell as a complementary measurement method to FTIR. It is based on the UV absorption of ozone and characterized by an accuracy of 0.1 ppb and a detection limit of 0.2 ppb based on the measurement in this study. It is dedicated for the measurement of ozone concentration in the gas phase with several advantages:

- It provides high resolution in ozone concentration measurement, i.e. 0.1 ppb.
- It provides a time resolution of 10 s.

There is a pump integrated inside of the ozone analyzer and the optimal flow for ozone analyzer is 1000 sccm. Since the flow rate through the U-shape reactor is 250 sccm, an extra N_2 flow of 750 sccm is added at the inlet of the FTIR gas cell as shown in Figure II-7. This flow can also accelerate the dynamic inside the FTIR gas cell. In this case it takes ca. 2 min to renew the total volume, i.e., 2 L, of the FTIR gas cell resulting to a delayed monitoring of 2 min which does not allow us to determine the gas phase kinetics at the initial stage during the heterogeneous interactions. The extra N_2 flow also dilutes the concentration of gas phase species by 4 times, lifting up the detection limits of the system 4 times. For

these reasons, at certain conditions, for example to determine the initial uptake coefficient of ozone uptake on Gobi dust, the ozone analyzer is directly connected at the outlet of the U-shape reactor with the extra N_2 flow, to avoid the buffer effect of the 2-L FTIR gas cell. Consequently, there is no delay of monitoring and initial stage kinetics and initial uptake coefficients can be determined.

2.1.4 Typical experimental protocol in gas phase approach

Gas phase approach is designed to obtain the gas phase concentration profiles of the tested gas species during their interactions with natural Gobi dust sample, aiming at the determination of uptake coefficients or numbers of molecules adsorbed. To achieve this purpose, typical experimental protocol in gas phase approach is the following.

Prior to any experiment, the dust samples are weighed using a high precision scale (± 0.1 mg), then set on the top of the sample holder of the U-shape reactor.

A typical experiment consists of five steps which are described as followed. To illustrate the protocol in a clearer way, a theoretical profile of concentration measurement of gas phase species named X, is provided as a specific example in Figure II-8.

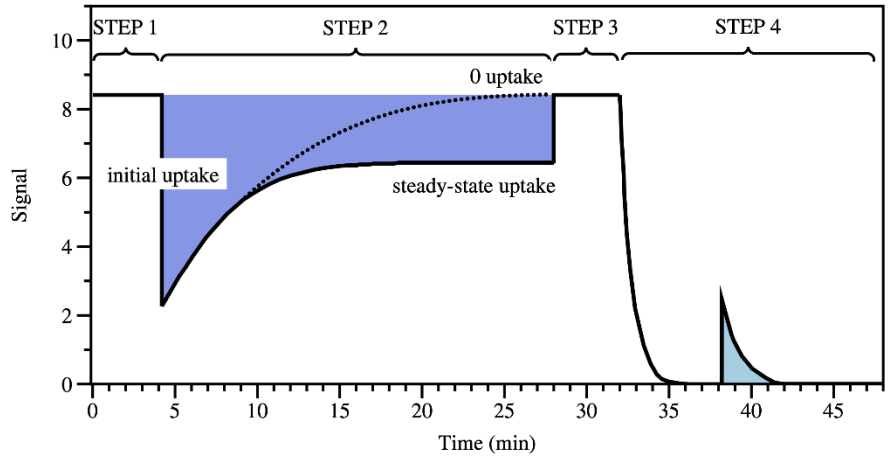

Figure II-8 Theoretical plot of gas-phase species concentration profile along the interaction with a solid substrate. SETP 1 corresponds to inlet gas-phase species concentration measurement; STEP 2 corresponds to dust surface exposure; STEP 3 corresponds to the final check of the stability of inlet initial gas-phase species concentration and STEP 4 corresponds to surface flushing with dry zero air flow. The solid and dashed lines correspond to two different uptake modes where for the solid line, the surface exhibits catalytic properties towards gas-phase species and for the dashed line, the surface is finally passivated. The filled area reveals the amount of the species of interest taken up or desorbed.

- **STEP 0 / Pretreatment of the dust sample.** The U-shape reactor is moved into the furnace and heated at 150 ˚C under a 250 sccm flow of dry zero air for 45 minutes to remove pre-adsorbed species, mostly water, from the dust sample surface. Then, it is moved out of the furnace to cool down the sample, still under zero air flow, for at least 1 hour. It has to be noted that the cooling

step is performed under targeted relative humidity if the following gas phase experiment is performed under humid condition in order to equilibrate the surface with water molecules.

- **STEP 1 / Initial gas phase concentration measurement.** The U-shape reactor is isolated and gas flow containing the species of interest (ozone or AcA) is driven through the bypass line to check the inlet concentration of the gas-phase species and evaluate its stability, as indicated by step (1) in Figure II-8.
- **STEP 2 / Dust surface exposure to the species of interest.** Once the steady concentration of the species of interest, i.e. ozone or acetic acid, is set in the bypass line, the gas flow is directed to the U-shape reactor, subsequently exposing the mineral dust sample to the species of interest. The exposure can be performed several hours or days long if necessary. If a decrease in gas phase concentration of the species of interest is observed at the outlet of the reactor, as depicted on the step (iii) in Figure II-8, it attests of the uptake of the species of interest by the dust surface.
- **STEP 3 / Verification of inlet concentration.** After a defined time of steady signal of the species of interest in the gas phase during step (iii), which could either totally restore to its initial value with 0 uptake of the species of interest as the dotted line in Figure II-8 indicates, or remain at a lower signal with a constant uptake of the species of interest as the solid line in Figure II-8 indicated, the flow containing the species of interest is re-directed to the bypass line to check the stability of the initial gas phase concentration of the species of interest (see (iv) in Figure II-8).
- **STEP 4 / Flushing the dust sample with zero air.** After verifying the initial inlet concentration of the species of interest, the gas flow is switched to zero air to purge the system. When the purge is done, indicated by the drop of the concentration signal of the species of interest to 0, the zero air flow is directed into the U-shape reactor to flush the sample.

2.1.5 Gas phase kinetic characterization

2.1.5.1 Calculations of the uptake coefficient and steady-state uptake rate

In the theoretical profile of the concentration of the species of interest depicted in Figure II-8, the solid curve shows a specific case where a transient uptake peak of the species of interest is initially observed and then followed by a steady-state uptake regime. These two uptake modes: initial uptake and steady-state uptake, can be distinguished clearly by the solid curve in Figure II-8.

According to Equation (I-2), uptake coefficient γ of a gas phase species X on the dust surface can be calculated based on the data from the X concentration profiles obtained experimentally. For accuracy, [X] in Equation (I-2) should be replaced by $\langle[X]\rangle$ which represents the average of the gas phase X concentration during the interaction and can be calculated from Equation (II-5):

$$\langle [X] \rangle = \frac{\int_0^d [X] dz}{\int_0^d dz} \tag{II-5}$$

where d is the thickness of the sample layer.

As a result, Equation (I-2) can be written in Equation (II-6):

$$\gamma = \frac{4|\mathrm{d}\{X\}/\mathrm{d}t|}{cA_{\mathrm{BET}}\langle [X] \rangle} \tag{II-6}$$

where $|\mathrm{d}\{X\}/\mathrm{d}t|$ is the absolute number of X molecules lost per second from the gas phase and expressed in molecule s^{-1}; $\{X\}$ denotes the number of X molecules; A_{BET} is the specific surface area determined by BET method expressed in cm^2 of the dust sample, which represents the upper limit of the effectively accessible surface area; c is the mean molecular speed of X molecules in cm s^{-1}. More precisely, $|\mathrm{d}\{X\}/\mathrm{d}t|$ can be calculated from Equation (II-7):

$$|\mathrm{d}\{X\}/\mathrm{d}t| = -\Gamma \cdot ([X]' - [X]_0) \tag{II-7}$$

where Γ is the gas flow rate in cm^3 s^{-1}, $[X]'$ is the gas phase X concentration of the gas flow right after the breakthrough of the sample. $|\mathrm{d}\{X\}/\mathrm{d}t|$ is assumed to remain constant inside all the sample layer. $c = 100 \times \sqrt{8kT/\pi M}$ (cm s^{-1}) with k the Boltzmann constant in J K^{-1}, T the operating temperature in K and M the molecular mass of X in kg.

By using the data corresponding to the first few seconds of the interaction between X and Gobi dust, i.e. the initial uptake peak, initial uptake coefficient γ_0 can be calculated using Equation (II-6) while the steady-state uptake coefficient γ_{ss} can be calculated the same way, based on the data from the steady-state uptake regime.

As mentioned in *section 2.1* in chapter 1, uptake coefficients are dimensionless parameters reflecting the probability of a molecule to be lost onto the solid surface. However, it should be noted that the initial uptake coefficient denotes the behavior of a previously unexposed surface, to that regard, it depicts the transient behavior of a fresh surface. Different with initial uptake coefficient, the steady-state uptake coefficient describes the behavior of the aged surface and is observed for longer time scales.

Complementarily, the steady state uptake rate r_{ss}, expressed in molecules cm^{-2} s^{-1} can be further retrieved from Equation (II-8) using the data of the steady-state uptake regime. It reveals the absolute number of X molecule taken up per specific surface area unit of Gobi dust and per time unit, during the steady-state uptake regime.

$$r_{ss} = \frac{\gamma_{ss} c \langle [X] \rangle}{4} = \frac{|\mathrm{d}\{X\}/\mathrm{d}t|}{A_{BET}} \quad \text{(II-8)}$$

2.1.5.2 Calculation of the amount of X molecules taken up and desorbed

The amount of X taken up onto the solid surface or desorbed, noted Q and expressed in molecules or mol, can be calculated by integrating the surface area of gas phase X concentration profile via equation (III-1).

$$Q = \int_{t_0}^{t} \Gamma \ \Delta[\mathrm{X}](\mathrm{t})\, dt \quad \text{(II-9)}$$

Where $\Delta[\mathrm{X}](\mathrm{t})$ in molecules cm^{-3}, is the difference between the X concentration measured and the baseline value, i.e., the value of the initial X concentration or 0. Γ is the flow rate in $cm^3\ s^{-1}$, and as a result, $\Gamma\ \Delta[\mathrm{X}](\mathrm{t})$ is the flow concentration of gas species X in molecules s^{-1}.

The adsorption capacity of the solid substrate q (molecules g^{-1} or mol g^{-1}) as well as the number of molecules adsorbed by per surface area unit of the solid, N (molecules cm^{-2}) could be further calculated by dividing Q with the mass of the solid, m (g) or the specific surface area A_{BET} (cm^{-2}) of the solid respectively, as indicated by Equation (II-10) and Equation (II-11):

$$q = \frac{Q}{m} \quad \text{(II-10)}$$

$$N = \frac{Q}{A_{BET}} \quad \text{(II-11)}$$

2.2 Adsorbed phase approach

To monitor the adsorbed phase of the surface of Gobi dust during the interaction with gas phase species, i.e. ozone and AcA, the experimental setup shown in Figure II-9 is used. It consists of two main parts:

(i) A gas flow preparation system similar to setup 1 which can provide zero air flow and gas flow containing ozone generated from oxygen, VOC, and water corresponding to different experimental requirements.

(ii) A Diffuse Reflectance Infrared Fourier Transform spectrometer (DRIFT) to monitor adsorbed phase of the sample surface which is equipped with an optical sample cell.

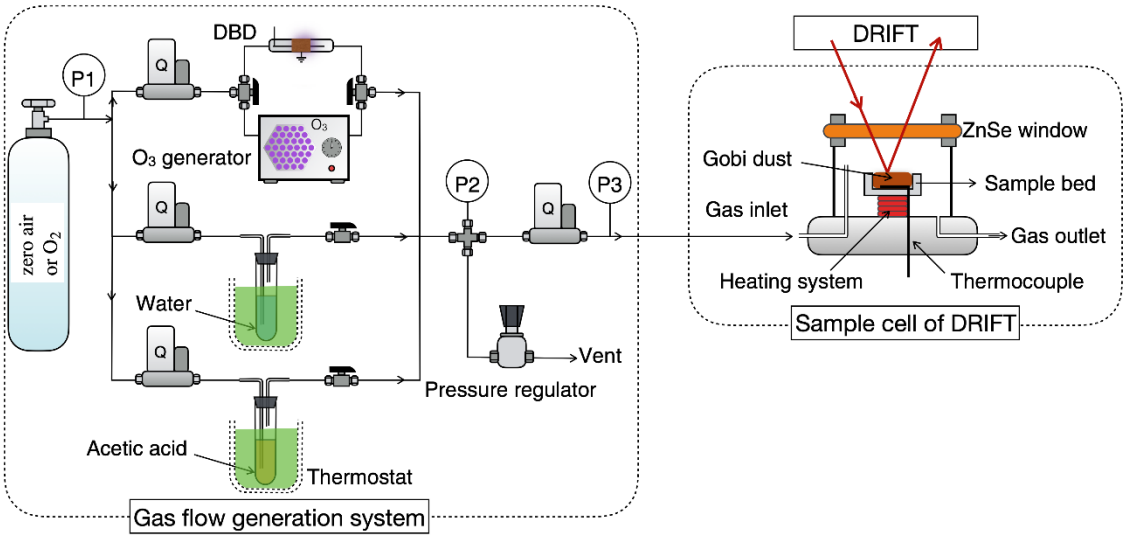

Figure II-9 Schematic of the experimental setup used in adsorbed phase approach which consists of a gas flow generation system and a DRIFT spectroscopy equipped with a sample cell.

Figure II-9 is the schematic of experimental setup used in adsorbed phase approach. Details of the specifications of each part of this setup, as well as typical protocol for adsorbed phase monitoring will be given in the following sections.

2.2.1 Gas flow preparation

The gas flow preparation system used in adsorbed phase characterization is similar to the one used for the gas phase investigation and the detailed specifications can be found in *2.1.1 Gas flow preparation*. The difference relied in the carrier gas used for ozone generation: oxygen is used instead of zero air. Since the ozone level used in adsorbed phase investigations can go up to 100 ppm, using oxygen to produce ozone allows avoiding the production of NO_x during the ozone production which could act as an interfering species in the heterogeneous processes. As a result, note that along the DRIFT investigations of the interactions between Gobi dust and ozone, the carrier gas is oxygen, and for the investigations of the interaction between Gobi dust and AcA, the carrier gas is zero air.

2.2.2 DRIFT cell

The adsorbed phase of Gobi dust is monitored inside the optical cell of the DRIFT spectrometer under atmospheric pressure and dynamic flow. The DRIFT cell consists of a ceramic crucible used as a sample holder, a heating resistor to perform thermal treatments of the samples, a thermocouple to monitor the temperature, a gas inlet and a gas outlet, and a ZnSe window to allow IR beam to enter and exit the cell as shown in Figure II-9. Few milligrams of dust sample are placed in the ceramic sample holder. The inlet gas flows over the surface of the dust sample. The total flow rate passing through the sample cell is regulated at ca. 250 sccm to avoid blowing away the sample.

2.2.3 Diagnostic instrument: DRIFT spectroscopy

DRIFT spectrometer (Nicolet 6700) with a sample cell and a mercury cadmium telluride (MCT) detector which needed to be cooled at 77 K by liquid nitrogen is used for the in-situ adsorbed phase monitoring of the surface in adsorbed phase approach.

The principle of DRIFT spectroscopy scientifically approximate with FTIR, as described in *section 2.1.3.1*. Different from FTIR which measures the gaseous species, DRIFT is dedicated for the monitoring of the surface of solid samples. The incident IR beam interact with the upper layers of the solid surface, and the total reflected light, including specular reflection and diffuse reflection, is collected by mirrors and sent to the detector (see Figure II-10) which detects the absorption of the infrared signal resulting from the interactions with the upper fraction of the sample place on the sample bed.

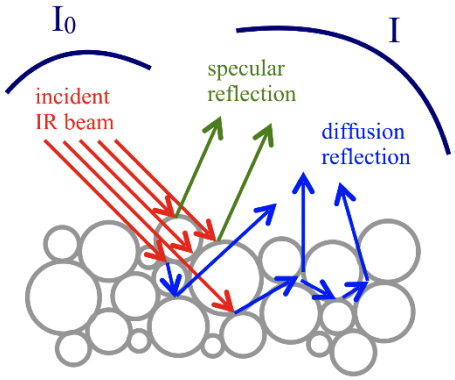

Figure II-10 The interactions between the incident IR beam with the surface of sample inside the DRIFT cell.

It has to be mentioned that DRIFT cannot provide absolute quantitative measurement of the surface species. Because the reflection light contains also specular reflection which cannot be separated from diffusion reflection technically thus the intensity of the total reflected light is not proportional to the concentration, according to Beer's law. However, by monitoring the evolution of the surface species using the normalized values of peak, DRIFT spectra can provide semi-quantitative measurement. For example, the temporal evolution of the surface coverage (θ) of a selected surface group can be determined by the ratio of the area of the corresponding peak over the maximal area obtained when equilibrated level is reached.

Besides semi-quantitative measurement, there are some other features concerning adsorbed phase investigation using DRIFT. The quality of the DRIFT spectrum acquired depends on the properties of the sample, such as the refractive index, the packing density, the particle size, the homogeneity of the surface. The sample-dependence of DRIFT measurement leads to another limitation that it is difficult to compare quantitatively the spectra acquired from two different experiments even with the same type

of sample. Also, DRIFT can only monitor the upper fraction of the sample placed in the sample bed instead of the entire thickness of the sample.

In this study, OMNIC is the software used for spectrum acquisition. For each spectrum acquired, it takes around 30 seconds with 32 scans per spectrum and resolution of 4 cm^{-1}. TQ Analyst is used spectrum analysis.

2.2.4 Typical experimental protocol in adsorbed phase approach

Adsorbed phase approach is designed to obtain the DRIFT spectra of the surface of Gobi dust sample during the interaction with the tested gas species, aiming to determine the surface groups formed in the adsorbed phase. To achieve this purpose, typical experimental protocol in adsorbed phase approach, which consists of four steps, is followed.

- **STEP 0 / Pretreatment of the dust sample.** The dust sample placed in the sample holder is heated at 150˚C for 2 hours under dry zero air flow. Then it is cooled down to room temperature (296 K) for at least 1 hours with the presence of zero air flow.
- **STEP 1 / Unexposed surface monitoring.** Once the sample is cooled down to room temperature (296 K), the spectrum of the unexposed surface of the dust sample is acquired by DRIFT prior to any exposure to target gas phase species.
- **STEP 2 / Dust surface exposure to the species of interest.** Once the spectra of fresh surface are acquired, the gas containing the species of interest will be generated and sent into the DRIFT cell. DRIFT spectra of the surface of the sample are regularly acquired to address the dynamic of surface groups along the interactions.
- **STEP 3 / Surface flushing with zero air flow.** Once the DRIFT spectra acquired during STEP 2 is considered as stable, the gas flow is switched to zero air flow to flush the sample surface.

2.3 Combination of gas phase approach and adsorbed phase approach

Gas phase approach and adsorbed phase approach can be combined experimentally by connecting the experimental setups of gas phase approach and adsorbed phase approach in series, as shown in Figure II-11. In this case, the gas first passes through the DRIFT sample cell to interact with the dust sample. Then the gas after the interaction goes through the gas cell of the FTIR to test the gaseous species. There is a bypass line connected in parallel to the DRIFT sample cell to let the gas bypass and be measured directly by FTIR without contacting dust sample.

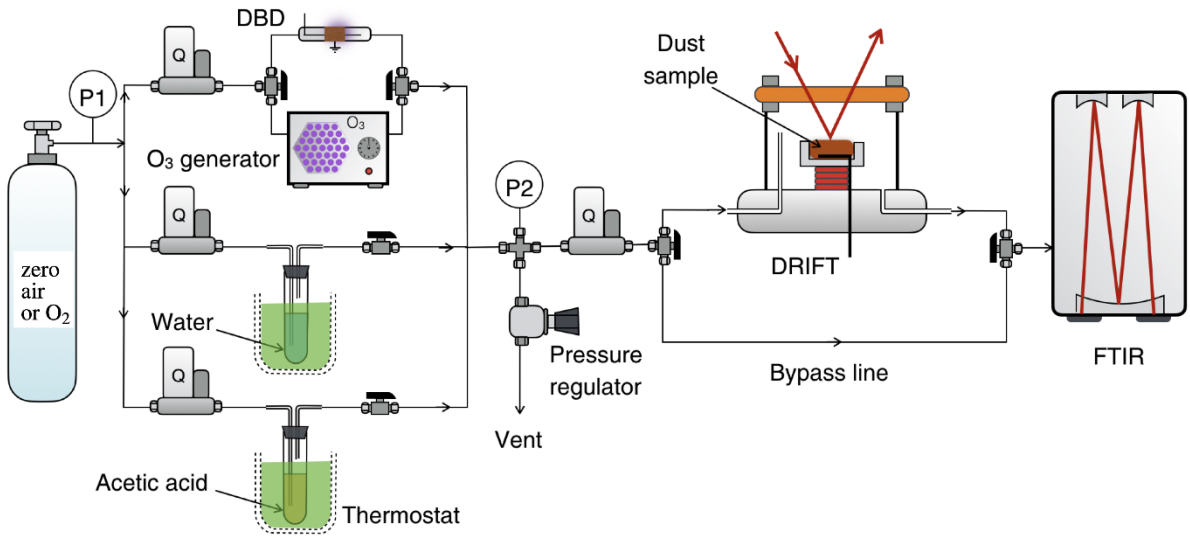

Figure II-11 Scheme of the combination of gas-phase and adsorbed-phase monitoring by connecting the DRFIT and FTIR in series.

This configuration allows us to check the gas phase species while monitoring the adsorbed phase in real time. However, there are some limitations:

- Only the upper fraction of the sample bed interacts with the gas phase species, which makes it impossible to know the exact mass of the sample involving in the reaction.
- The gas flow passes over the surface of the sample inside the DRIFT cell, making the extent of the interaction between gas-phase species and dust sample less effective than in the U-shape reactor where the gas flow breaks through the whole sample bed.
- The measurement becomes difficult with high concentration of the gas phase species. Considering the weak extent interaction degree inside the DRIFT cell, high initial concentration of gas phase species might cover the dynamic of gas phase concentration thus making the gas phase kinetic undetectable.

Under certain conditions where the gas-phase measurement and adsorbed phase monitoring cannot be connected experimentally, connections might still be made through the analysis of results obtained respectively by gas phase approach and adsorbed phase approach.

3 Summary

In this chapter, elements used for experiments in the context of this work are described, including the central materials, i.e. Gobi dust sample, synthetic metal oxides and gases, and the methods applied in gas phase approach, and adsorbed phase approach.

It explains how the experimental setups and protocols are designed in order to evaluate the surface properties of Gobi dust towards ozone and AcA. Gas phase approach aims at monitoring the dynamic of the gas phase species interacting with the dust sample, thus understanding the kinetics of the heterogeneous interaction between gas phase species with Gobi dust sample. Adsorbed phase approach aims at monitoring the dynamic of surface group formation, thus understanding the mechanism of the heterogeneous interaction occurring on the surface of Gobi dust. The main characteristics of the two approaches are gathered in Table II-5.

Table II-5 Main characteristics and operating conditions of gas phase approach and adsorbed phase approach.

	Gas phase approach	Adsorbed phase approach
Carrier gas	Zero air	Zero air / Oxygen
Reactor	U-shape catalytic reactor	Sample cell of DRIFT
Diagnostic devices	FTIR, ozone analyzer	DRIFT
Flow	Dynamic flow (250 – 500 sccm)	Dynamic flow (250 sccm)
Operating pressure	1100 mbar	1100 mbar
Temperature	Room temperature (296 K)	Room temperature (296 K)
Humidity range	0 – 20 % RH	0 – 20 % RH

Based on the materials and methods described in this chapter, the results obtained are introduced and discussed in the following chapters to provide a comprehensive evaluation of the surface properties of Gobi dust towards ozone and AcA.

References

[1] D.P. Sheehy, A perspective on desertification of grazingland ecosystems in north China, Ambio (Sweden), (1992).

[2] G. Zhuang, J. Guo, H. Yuan, C. Zhao, The compositions, sources, and size distribution of the dust storm from China in spring of 2000 and its impact on the global environment, Chinese Science Bulletin, 46 (2001) 895-900.

[3] J. Sun, M. Zhang, T. Liu, Spatial and temporal characteristics of dust storms in China and its surrounding regions, 1960–1999: Relations to source area and climate, Journal of Geophysical Research: Atmospheres, 106 (2001) 10325-10333.

[4] X. Wang, Z. Dong, J. Zhang, L. Liu, Modern dust storms in China: an overview, Journal of Arid Environments, 58 (2004) 559-574.

[5] M.N. Zeineddine, M.N. Romanias, V. Riffault, F. Thévenet, Heterogeneous Interaction of Various Natural Dust Samples with Isopropanol as a Probe VOC, The Journal of Physical Chemistry A, (2018).

[6] N. Joshi, M.N. Romanias, V. Riffault, F. Thevenet, Investigating water adsorption onto natural mineral dust particles: Linking DRIFTS experiments and BET theory, Aeolian Research, 27 (2017) 35-45.

[7] A.E. Zein, M.N. Romanias, Y. Bedjanian, Heterogeneous interaction of H_2O_2 with Arizona test dust, The Journal of Physical Chemistry A, 118 (2013) 441-448.

[8] C. Bueno-Ferrer, S. Parres-Esclapez, D. Lozano-Castelló, A. Bueno-López, Relationship between surface area and crystal size of pure and doped cerium oxides, Journal of Rare Earths, 28 (2010) 647-653.

[9] S. Pollard, G. Fowler, C. Sollars, R. Perry, Low-cost adsorbents for waste and wastewater treatment: a review, Science of the Total Environment, 116 (1992) 31-52.

[10] E. Johnson, S.E. Arshad, Hydrothermally synthesized zeolites based on kaolinite: a review, Applied Clay Science, 97 (2014) 215-221.

[11] S. Matsuda, A. Kato, Titanium oxide based catalysts-a review, Applied Catalysis, 8 (1983) 149-165.

[12] A. Goudie, N. Middleton, Saharan dust storms: nature and consequences, Earth-Science Reviews, 56 (2001) 179-204.

[13] M.N. Romanias, H. Ourrad, F. Thevenet, V. Riffault, Investigating the Heterogeneous Interaction of VOCs with Natural Atmospheric Particles: Adsorption of Limonene and Toluene on Saharan Mineral Dusts, Journal of Physical Chemistry A, 120 (2016) 1197-1212.

[14] Y. Zhao, Z. Chen, X. Shen, X. Zhang, Kinetics and mechanisms of heterogeneous reaction of gaseous hydrogen peroxide on mineral oxide particles, Environmental science & technology, 45 (2011) 3317-3324.

[15] P. Li, K. Perreau, E. Covington, C. Song, G. Carmichael, V. Grassian, Heterogeneous reactions of volatile organic compounds on oxide particles of the most abundant crustal elements: Surface reactions of acetaldehyde, acetone, and propionaldehyde on SiO_2, Al_2O_3, Fe_2O_3, TiO_2, and CaO, Journal of Geophysical Research: Atmospheres, 106 (2001) 5517-5529.

[16] S. Carlos-Cuellar, P. Li, A. Christensen, B. Krueger, C. Burrichter, V. Grassian, Heterogeneous uptake kinetics of volatile organic compounds on oxide surfaces using a Knudsen cell reactor: Adsorption of acetic acid, formaldehyde, and methanol on α-Fe_2O_3, α-Al_2O_3, and SiO_2, The Journal of Physical Chemistry A, 107 (2003) 4250-4261.

[17] J. Lasne, M.N. Romanias, F. Thevenet, Ozone Uptake by Clay Dusts Under Environmental Conditions, (2018).

[18] R. McDonald, S. Shrader, D. Stull, Vapor Pressures and Freezing Points of Thirty Pure Organic Compounds, Journal of Chemical and Engineering Data, 4 (1959) 311-313.

[19] M. Tang, W.A. Larish, Y. Fang, A. Gankanda, V.H. Grassian, Heterogeneous reactions of acetic acid with oxide surfaces: Effects of mineralogy and relative humidity, The Journal of Physical Chemistry A, 120 (2016) 5609-5616.

[20] M.N. Romanias, M.N. Zeineddine, V. Gaudion, X. Lun, F. Thevenet, V. Riffault, Heterogeneous Interaction of Isopropanol with Natural Gobi Dust, Environmental science & technology, 50 (2016) 11714-11722.

[21] M.N. Zeineddine, M.N. Romanias, V. Gaudion, V.r. Riffault, F.d.r. Thévenet, Heterogeneous Interaction of Isoprene with Natural Gobi Dust, ACS Earth and Space Chemistry, 1 (2017) 236-243.

[22] M.N. Romanias, M.N. Zeineddine, V. Riffault, F. Thevenet, Isoprene Heterogeneous Uptake and Reactivity on TiO_2: A Kinetic and Product Study, International Journal of Chemical Kinetics, 49 (2017) 773-788.

[23] F. Thevenet, L. Olivier, F. Batault, L. Sivachandiran, N. Locoge, Acetaldehyde adsorption on TiO_2: Influence of NO2 preliminary adsorption, Chemical Engineering Journal, 281 (2015) 126-133.

[24] F. Batault, F. Thevenet, V. Hequet, C. Rillard, L. Le Coq, N. Locoge, Acetaldehyde and acetic acid adsorption on TiO_2 under dry and humid conditions, Chemical Engineering Journal, 264 (2015) 197-210.

Chapter III. Interactions of ozone with natural Gobi dust

Table of contents

Table of Figures

In this section, results about the surface reactions between ozone and natural mineral dusts sampled from Gobi Desert are discussed, focusing on the ozone uptake properties of the proposed geomaterial. The chapter is divided in two sections: in the first section, the results of ozone decomposition on Gobi dust obtained by gas phase approach are presented. In particular, the initial and steady-state uptake coefficients of ozone onto Gobi dust are determined over a wide range of initial ozone concentrations, i.e., 0.02 to 10 ppm, under dry and 20% relative humidity (RH) conditions. In order to address the sustainability of ozone uptake onto Gobi sample, complementary cyclic and regeneration experiments are also presented. The second section concerns the adsorbed phase monitoring using DRIFT spectroscopy, in order to elucidate the mechanism of ozone decomposition and clarify the surface chemistry involved in the investigated process. Attempting to evaluate the contribution of the individual mineral components of Gobi dust to ozone decomposition, the results obtained on some individual minerals components of Gobi are also discussed. At the end of this chapter, the gas-phase and adsorbed-phase investigation will be combined to discuss and propose a general mechanistic scheme regarding the surface reaction pathway for ozone uptake onto Gobi dust.

1 Ozone decomposition on Gobi dust: gas phase approach

1.1 First insights to ozone breakthrough profile

1.1.1 Characterization of ozone decomposition behaviors on Gobi dust

Based on the gas-phase investigation protocol:

(i) Pretreatment of the dust sample: heating at 150˚C under dry zero air flow then cooling down to room temperature.

(ii) Initial ozone concentration measurement through bypass line.

(iii) Dust surface exposure to ozone flow.

(iv) Switch ozone flow to bypass line to verify initial ozone concentration.

(v) Flushing the dust sample with dry zero air

typical breakthrough profiles revealing the evolution of ozone concentration during the interaction with Gobi dust are obtained. The experimental breakthrough profiles recorded along ozone interaction with Gobi dust sample agree with the theoretical plot proposed by the solid line in Figure II-8. Figure III-1 shows the breakthrough profile of a specific case, where the initial inlet ozone concentration is 1.5 ± 0.1 ppm, the mass of the Gobi dust sample is 90 ± 1 mg and dry condition.

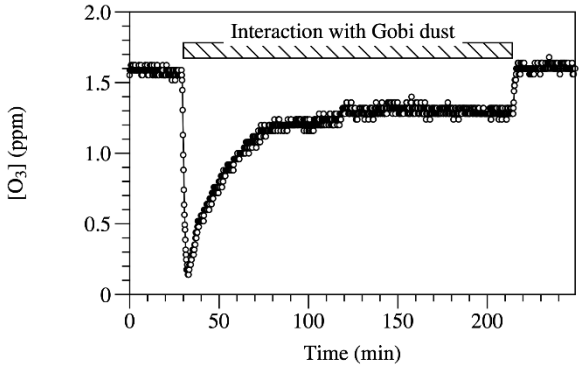

Figure III-1 Breakthrough profile during the interaction of ozone flow of 1.5 ± 0.1 ppm with 90 ± 1 mg Gobi dust (dry air, T = 296 K, P = 1013 mbar).

As displayed in Figure III-1, the heterogeneous system studied is experimentally characterized by (i) a significant and transient initial uptake peak and (ii) a steady-state uptake regime of ozone on Gobi dust surface.

Regardless the heterogeneous surface of Gobi dust, these two consecutive uptake modes with contrast suggest that on one hand, the behavior of the dust varies along the uptake process and the surface is modified by ozone molecules; on the other hand, these surface modifications, in turn, affect the decomposition process of ozone at later times. Particularly, in Figure III-1, at the beginning of the exposure of Gobi dust to ozone, the uptake reaches maximum on short time scale. This transient behavior could be associated to surface modifications and the formation of surface species that accumulates on Gobi dust surface. Interestingly, the gas phase concentrations of ozone do not recover to initial pre-exposure levels that could possibly indicate the existence of surface regeneration processes. As a result, the steady-state uptake regime might indicate an equilibrium between the accumulation of the surface species and the surface regeneration process.

The initial uptake coefficient, steady-state uptake coefficients as well as the steady-state uptake rate for the experiment in Figure III-1 are calculated to be $(4.6 \pm 0.6) \times 10^{-8}$, $(9.6 \pm 1.5) \times 10^{-9}$, and $(2.8 \pm 0.5) \times 10^{9}$ molecules cm^{-2} s^{-1}.

1.1.2 Steady-state uptake process of ozone on Gobi dust: catalytic or not?

The continuous steady-state uptake process of ozone on Gobi dust has been observed for long time scales, i.e., up to 30 h without surface deactivation under different experimental conditions. The latter, could probably indicate that O_3 decomposition could be of catalytic nature.

One method for determining whether a heterogeneous process is catalytic or not relies on the determination of the turn over number (TON). Such an approach was formerly proposed and applied in literature [1-3] as mentioned in chapter 1. According to the description in *section 2.1.5* of chapter 2, for

ozone decomposition on Gobi dust surface, the total number of the ozone molecule decomposing on the dust sample Q can be calculated by integrating the drop of the gas-phase ozone concentration compared with the initial ozone concentration and the exposure time by Equation (III-1), based on the breakthrough profiles of gas phase ozone concentration, as showed in Figure III-2.

$$Q = \int_{t_0}^{t} \Gamma \, \Delta[O_3](\mathrm{t}) \, dt \qquad \text{(III-1)}$$

Where $\Delta[O_3](\mathrm{t})$ in molecules cm^{-3}, is the difference between ozone concentration measured and the baseline value, i.e., the value of the initial ozone concentration or 0, $\Gamma \, \Delta[O_3](\mathrm{t})$ is the flow concentration of ozone in molecules s^{-1}.

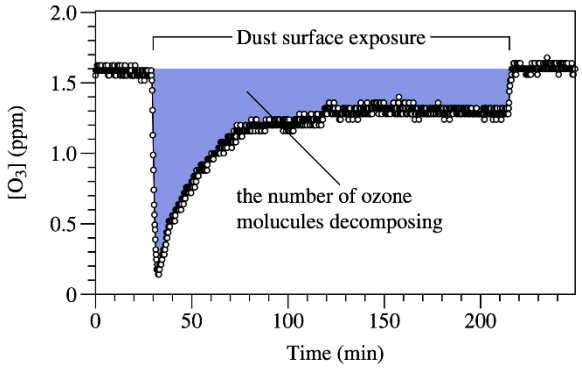

Figure III-2 Calculation of the total number of ozone molecules decomposing on Gobi dust according to breakthrough profile.

The total number of active sites of Gobi dust sample can be calculated from the mass of Gobi dust sample and the surface density of active sites. The surface density of active sites, which refers to the number of surface active site per specific surface area unit (μmol m^{-2}) of Gobi dust surface is estimated to be 2 μmol m^{-2} as described in chapter 2.

Dedicated experiments have been carried out on long time scale, up to 30 hours, to address the stability of the steady state uptake regime and determine the corresponding TON. Observed ozone concentration profiles were similar to the one reported on Figure III-1, i.e. no deactivation of the steady state regime was noticed after 30 hours of surface exposure to ozone. The TON number calculated under these experimental conditions, was always greater than 1 and thus the decomposition of ozone onto the Gobi dust exceeds the expected stoichiometry of the surface sites. As a result, the decomposition of ozone on Gobi dust surface could be characterized as catalytic. Michel et al [3] reported similar catalytic properties on synthetic metal oxides, namely α-Al_2O_3 and α-Fe_2O_3 with TON exceeding 1. As a result, the present work evidences a catalytic behavior regarding ozone decomposition on a natural mineral dust with a TON equivalent to those obtained on synthetic oxides.

1.1.3 Summary

Based on the observations from the breakthrough profile of ozone decomposition on Gobi dust, two different ozone decomposing modes have been observed during initial uptake stage and steady-state uptake regime respectively, of which the latter process is determined as catalytic based on TON exceeding 1. The kinetics of gas phase ozone during ozone-dust interaction can be characterized by: (i) initial uptake coefficient, (ii) steady-state uptake coefficient and (iii) uptake rate during the steady-state uptake regime of ozone molecules on Gobi dust.

In order to investigate the impact of different experimental conditions to the decomposition performance of Gobi dust, series of experiments were carried out as a function of the mass of Gobi dust sample, ozone concentrations and relative humidity. The obtained results are presented in the following sections.

1.2 Dependence of the uptake coefficients on the mass of dust sample

In this series of experiments the initial and steady state uptake coefficients of ozone are measured as a function of the mass of Gobi dust. The objective is to investigate the effective mass of the Gobi dust that participates to ozone decomposition. Consequently, different masses of the geomaterial, varied from 15 to 120 mg, are exposed to 2.5 ± 0.5 ppm under dry conditions, and the results are presented in Figure III-3.

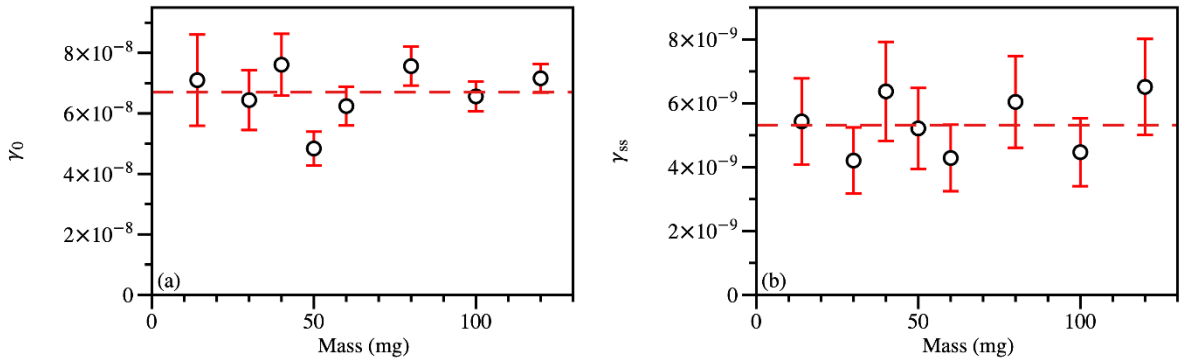

Figure III-3 (a) Initial uptake coefficients γ_0 and (b) steady-state uptake coefficient γ_{ss} of ozone uptake on Gobi dust as a function of sample mass. ($[O_3]_0$ = 2.5 ± 0.5 ppm, dry air, T = 296 K, P = 1013 mbar.) the error bar is determined from the error in the individual variables needed for calculation.

Figure III-3 clearly shows no dependence of the BET uptake coefficients on the sample mass. Since the total specific surface area of dust sample is proportional to the mass of dust sample, based on Equation (II-6), non-mass dependence indicates a linear positive correlation between ozone uptake rate, i.e. $d\{O_3\}/dt$ and the mass of the sample [3, 4]. Therefore, it is evidenced that in the range of Gobi dust masses used, all the surface sites of the sample remain fully accessible for ozone molecules. Thus, the BET surface area should be used for the calculation of the uptake coefficient.

In the present study, all experiments are performed in the considered mass range of dust.

1.3 Influences of initial ozone concentration on ozone uptake

The impact of gas phase ozone initial concentration on the uptake coefficients is studied in a wide concentration range, 5.0×10^{11} to 2.5×10^{14} molecule cm^{-3} (i.e. from 20 ppb to 10 ppm), under dry conditions. In Figure III-4 are displayed typical ozone breakthrough profiles recorded after exposing 100mg of Gobi dust to 0.5, 1.6 and 2.5 ppm of ozone. For clarity, the breakthrough curves are normalized in order to emphasize the differences.

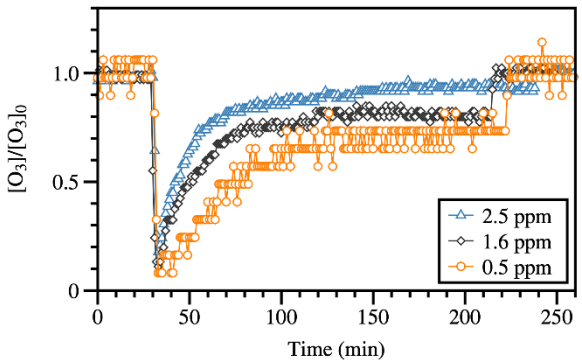

Figure III-4 Normalized breakthrough profiles recorded during exposure of 100 mg Gobi dust to 0.5 ppm, 1.6 ppm and 2.5 ppm ozone at room temperature and atmospheric pressure.

Regardless of the different extend of ozone uptake, the initial transient uptake and steady-state uptake regime can be observed clearly in all the three breakthrough profiles. It means that for all the initial ozone concentrations, the initial uptake coefficients (γ_0), the steady-state uptake coefficients (γ_{ss}) and the steady-state uptake rates (r_{ss}) can be calculated. In Figure III-5 are summarized the γ_0, γ_{ss} and r_{ss} values as a function of initial ozone concentrations.

The initial and steady-state uptake coefficient reported in Figure III-5 (a) and (b) represent the probabilities for an ozone molecule to be removed from one collision with the surface at the two different uptake state: initial uptake peak and stead-state uptake regime. Uncertainties quoted on data reported in Figure III-5 are retrieved from the errors associated to individual variables needed for uptake coefficient calculations.

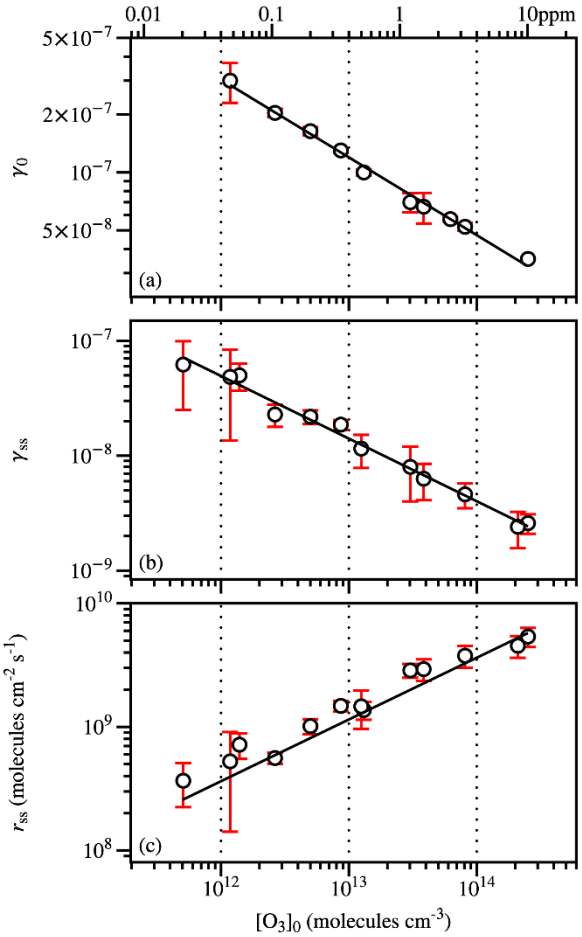

Figure III-5 (a) Initial uptake coefficients, (b) steady-state uptake coefficients and (c) steady-state uptake rates r_{ss} of ozone on Gobi dust versus different initial ozone concentrations at room temperature and atmospheric pressure. The error bar is determined from the error in the individual variables needed for calculation.

As showed in Figure III-5, γ_0 decreases with initial ozone concentration in the entire concentration range where experiments were performed. This behavior is somewhat unexpected since the number of surface sites of fresh Gobi dust, range from $10^{15} – 10^{16}$, and thus always exceeds the number of ozone molecules introduced in the reactor in the unit of time, i.e., $10^{12} – 10^{13}$ molecules s^{-1} within this ozone concentration range. This observation can be attributed either to the to (i) time resolution of the system that is not fast enough to record the true initial interaction process between ozone and Gobi dust and reveal the true initial uptake coefficient or (ii) a complicated reaction mechanism including multistep processes as it has already been revealed in literature. For steady-state uptake coefficient γ_{ss}, the surface has already reached the equilibrium with ozone molecules in gas phase. Since a define sample surface has a finite ability to decompose ozone in terms of molecule processed per time unit, as initial ozone concentration increases, the probability for a single molecule of ozone to decompose on the surface is decreased. Similar behavior for γ_{ss} is noticed under dry air as ozone inlet concentration increases by R. Sullivan et al. [6] as well as by S. Stephens et al. [7] for ozone decomposing respectively onto alumina and carbonaceous surfaces during steady-state ozone uptake regime. The experimental determined initial

and steady state coefficients are fitted using empirical power expressions: equations (III-2) and (III-3), to simulate their dependence on ozone initial concentration (molecules cm^{-3}).

$$\gamma_0 = 0.02[O_3]_0^{-0.4} \quad \text{(III-2)}$$

$$\gamma_{ss} = 0.17[O_3]_0^{-0.5} \quad \text{(III-3)}$$

Unlike uptake coefficients, r_{ss} increases with ozone initial concentration. This behavior indicates that the rate of the ozone decomposition process positively varies with the reactant concentration on the investigated concentration range. Based on experimental data reported on Figure III-5 (c), the kinetic of ozone uptake process onto Gobi dust is characterized by fractional reaction order, Equation (III-4), suggesting the existence of pre-equilibrium state in the decomposition process and/or a multiple step mechanism underlying the observed reaction.

$$r_{ss\,(dry\ air)} = 363\,[O_3]_0^{0.5} \quad \text{(III-4)}$$

where $[O_3]_0$ is expressed in molecules cm^{-3}.

1.4 Influences of relative humidity on ozone uptake

To evaluate the impact of relative humidity to the ozone decomposition, the γ_0, γ_{ss}, and r_{ss}, are determined at various ozone initial concentrations at 20% of RH. The corresponding data retrieved are plotted and compared with the results under dry condition in Figure III-6.

For γ_0 under 20% RH, no significant impact of water molecules can be pointed out in Figure III-6 (a). It could be explained by the reason discussed previously that the time resolution of the system is not fast enough to reveal the true initial ozone decomposing process. R. C. Sullivan et al. [6] have also observed no significant impact from water molecules for initial ozone uptake coefficient on the surface of alumina. They left the question open and suggested that it might due to the pre-adsorbed water molecules on the surface which could not be removed, or the experimental method they applied. However, in the case of γ_{ss}, it evidenced a significant negative impact of moisture on the steady state uptake coefficients (Figure III-6 (b)). The fit of steady-state uptake coefficient with initial ozone concentration can be described by power function Equation (III-5).

$$\gamma_{ss\,(20\%\,RH)} = 349[O_3]_0^{-0.8} \quad \text{(III-5)}$$

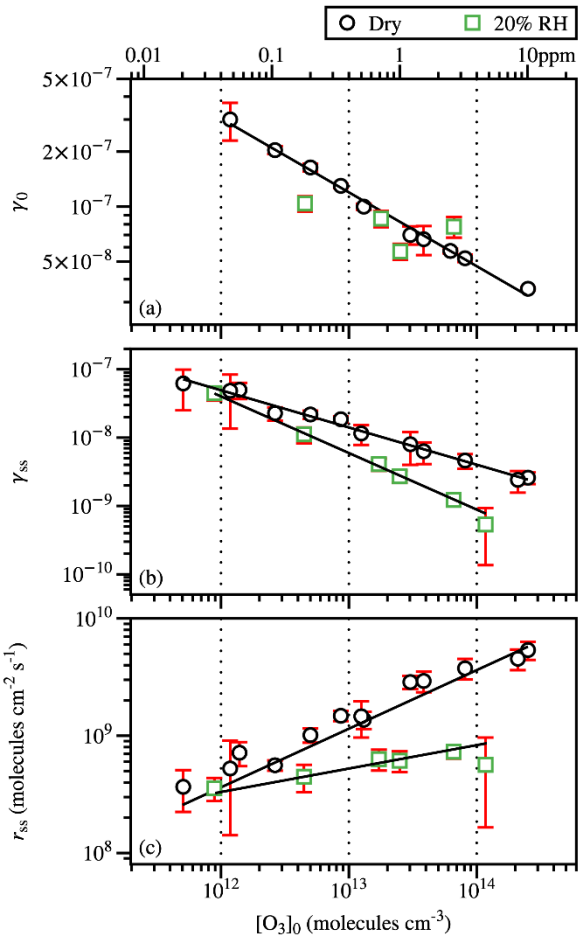

Figure III-6 (a) Initial uptake coefficients γ_0, (b) steady-state uptake coefficients γ_{ss} and (c) steady-state uptake rates r_{ss} of ozone on Gobi dust as function of initial ozone concentrations at room temperature and under atmospheric pressure. ○ represents the results in dry conditions and □ represents the results under 20 % RH condition. The error bar is determined from the error in the individual variables needed for calculation.

Indeed, when ozone initial concentration exceeds 1×10^{14} molecules cm^{-3}, corresponding to 4 ppm, the steady state uptake coefficient of ozone onto Gobi dust under 20 % RH is decreased by one order of magnitude compared to dry conditions. Similar negative impact of water molecules have been reported by M. Tang et al. [8], Y. Bedjanian et al. [9] and A.E. Zein et al. [10, 11] on the uptake of gas species such as HO_2, VOC (isopropanol) and HONO. These authors suggest that the adsorbed water molecules occupy available sites of the surface inhibiting the uptake of pollutants. In the present study, under 20% of RH, the surface of Gobi dust, is expected to be covered with a monolayer of water [12, 13], and thus water molecules seem to block the access of ozone molecules to the reactive surface sites. As a result, the probability for an ozone molecule to be taken up/decompose decreases. Note that the effect of blocking is expected to be more significant at long exposure times, i.e., where the γ_{ss} of ozone is measured, since the water uptake process is long-lasting and several hours are required to create an equilibrium between adsorbed and gas phase water.

Similar to dry condition, r_{ss} increases with ozone initial concentration under 20 % RH, however, the reaction rate under humid condition is lower compared to dry. It it consistent with the previous discussion that water molecules occupy the surface sites on Gobi dust sample competeing with ozone moleucles. Based on r_{ss} data reported on Figure III-6 (c), experimental kinetic laws can be proposed, that is reported in Equation (III-6) with $[O_3]_0$ in molecules cm^{-3}.

$$r_{ss\,(20\%\,RH)} = 1.32 \times 10^6\ [O_3]_0^{\,0.2} \qquad \text{(III-6)}$$

1.5 Atmosphere implementation

The determination of the uptake coefficient of ozone uptake on Gobi dust surface allows evaluating the atmospheric impact of ozone-dust heterogeneous processes and providing values and reference to the modeling study of atmospheric chemistry.

In this regard, the atmospheric lifetime of ozone due to the heterogeneous interaction with Gobi dust can be calculated via Equation (III-7) with the values of uptake coefficients determined in this study.

$$\tau_{het} = \frac{4}{\gamma c D} \qquad \text{(III-7)}$$

where γ is the uptake coefficient of the ozone onto Gobi dust, c is the mean molecular speed of ozone in cm s^{-1}, and D is the surface area density (cm^2 cm^{-3}) of Gobi dust in atmosphere.

The surface density of Gobi dust can be estimated from the concentrations of Gobi dust in atmosphere and the specific surface area of Gobi dust. According to the report of Japanese ministry of environment in 2008 [14], the atmospheric concentration of Gobi dust is determined to be 1400 μg m^{-3} when the dust is transported to forested regions. Taking the BET surface of Gobi dust as the specific surface area, which is 10.5 ± 2.0 m^2 g^{-1}, the surface area density D of Gobi dust is the multiplication of the concentration in atmosphere and the BET surface which is found to be 1.5 × 10^{-4} cm^2 cm^{-3}. Considering the fact that the natural amount of ozone in troposphere is normally around 0.04 ppm according to the Air quality fact sheet issued by Australian government in 2005 [15], the steady-state uptake coefficient of tropospheric ozone on Gobi dust under 20% RH and atmospheric condition can be extrapolated from Equation (III-5) as 8.8 × 10^{-8}. Since the BET surface is used to calculated uptake coefficients, this value of steady-state uptake coefficient should be regarded as the lower limit. As a result, the life time of ozone calculated in this way should be considered as the upper limit, which is around 100 days. However, if the uptake coefficient is calculated using the geometric surface area of Gobi dust sample, i.e. 0.8 cm^2 in our case, which represents the upper limit of the specific surface area of Gobi dust, the steady-state uptake coefficient of ozone is therefore estimated as 1.1 × 10^{-3}. Consequently, the life time of ozone is in the range of 12 minutes which represents the lower limit of ozone life time.

Based on the calculation, the life time of ozone due the gas-phase oxidation processes which is 22 hours based on literature study [14] is in the middle of the lower limit and upper limit value of ozone life time due to heterogeneous interaction with Gobi dust. As a result, the ozone loss due to the heterogeneous interaction with Gobi dust should not be ignored when it comes to atmospheric chemistry study.

1.6 Comparison of Gobi dust and its single mineral components

The steady-state uptake coefficients γ_{ss} of ozone uptake on Gobi dust and its major mineral components are compared to address the individual property of each component towards ozone.

However, as discussed in chapter 1.3.2, and also shown from the results presented above, the uptake of O_3 on mineral surfaces strongly depends on the experimental conditions, i.e. concentration, relative humidity, etc. [16]. Therefore, for a thorough comparison of the results of the current study and those reported in literature, solely studies conducted under close experimental conditions, are considered. With a limited number of investigations in literature, the value of γ_{ss} of 100 ppb of ozone on natural Gobi dust is compared with those of 100 ppb of ozone on SiO_2, $CaCO_3$, Al_2O_3 determined under atmospheric pressure, room temperature and dry condition using a flow-tube reactor for $Al_2Si_2O_5(OH)_4$ [17] and fluidized bed reactor for the rest [18], and 130 ppb of ozone on TiO_2/SiO_2 (3 wt %) under atmospheric pressure, room temperature and dry condition using a coated-wall flow-tube reactor in dark conditions [19] in Table III-1. The γ_{ss} value of Al_2O_3 is also listed for its reference value since it is the important mineral components in many other mineral dusts such as Saharan dust from Harmattan [20], Rawdat dust [21], as well as Arizona dust [22, 23].

Table III-1 Comparison of γ_{ss} of ozone on Gobi dust and its major mineral components under atmospheric pressure and room temperature. For Gobi dust, SiO_2, $Al_2Si_2O_5(OH)_4$ (kaolinite), $CaCO_3$ and Al_2O_3, the ozone concentration is 100 ppb and 130 ppb for TiO_2/SiO_2 (3 wt %).

Materials	Type of reactor	γ_{ss}
Gobi dust	flow-through U-shape reactor	2.28×10^{-8}
SiO_2 [18]	fluidized bed reactor	3.74×10^{-10}
$CaCO_3$ [18]	fluidized bed reactor	$<< 10^{-10}$
$Al_2Si_2O_5(OH)_4$ [17]	flow-tube reactor	1.49×10^{-8}
Al_2O_3 [18]	fluidized bed reactor	3.79×10^{-9}
TiO_2/SiO_2 (3 wt %) dark condition [19]	flow-tube reactor	$1.1 \pm 0.2 \times 10^{-9}$

As listed in Table III-1, among all the minerals, Gobi dust exhibits the highest value of γ_{ss}, i.e. 2.28×10^{-8}, towards ozone uptake. It suggests higher decomposition efficiency of this geomaterial over its

single mineral components i.e. SiO_2, $CaCO_3$, $Al_2Si_2O_5(OH)_4$, and TiO_2/SiO_2 (3 wt %) under dark conditions.

From Table 1, by adding together the value of γ_{ss} of all the single minerals in proportion found in natural Gobi dusts and assuming that all the aluminosilicates in Gobi dust behave as kaolinite, we can estimate the value γ_{ss} of an "equivalent" Gobi dust by equation (III-8).

$$\gamma_{ss,calculated} = \sum \gamma_{ss\ of\ x} \times relative\ abundance\ of\ x \quad \text{(III-8)}$$

The resulting value of γ_{ss} of Gobi dust is calculated to be 9.6×10^{-9}, which is by a factor of two lower than the γ_{ss} value determined on the natural Gobi dust experimentally.

Many of these minerals listed in Table III-1 are commonly used as catalysts or supports especially in NTP-catalysis for VOC abatement [24-32]. From a practical point of view, the better ozone-decomposing efficiency found in Gobi dust also points out the potential economic benefits of using natural Gobi dust for the industry, considering the low cost and energy saved compared with individual single mineral catalyst that need to be synthesized and purified.

1.7 Cyclic experiments and surface regeneration of Gobi dust

1.7.1 Surface generation by flushing and thermal treatment under dry condition

In order to investigate the stability of the steady-state surface properties of Gobi dust towards ozone decomposition, and the subsequent long-term behavior of the surface properties, a series of cyclic experiments have been performed.

During these experiments, the same natural Gobi dust sample is exposed to consecutive ozone flows characterized by the same initial ozone concentrations. An example is given in Figure III-7 which reports the gas-phase ozone concentration profile along one cyclic experiment.

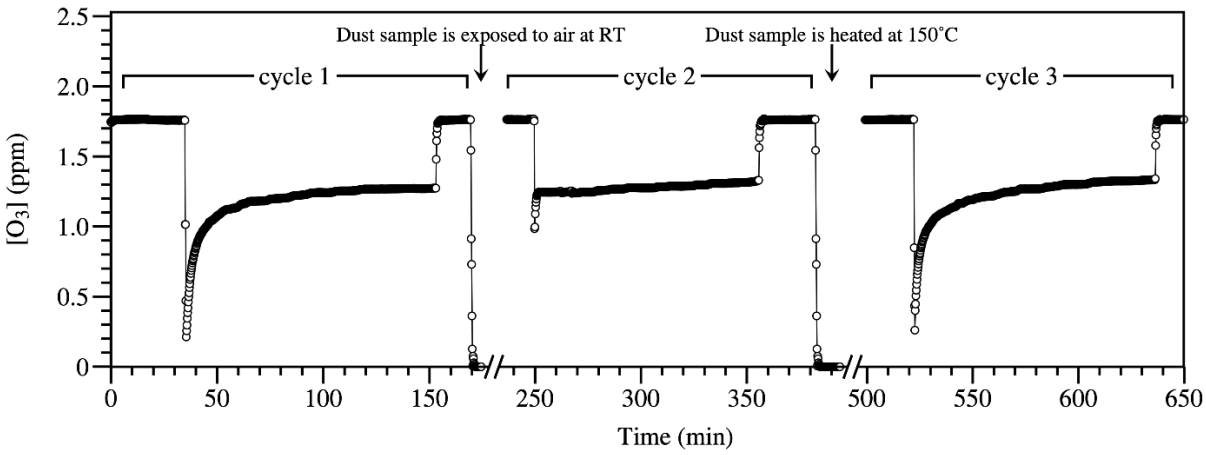

Figure III-7 Profiles of gas phase ozone concentration monitored along cyclic experiments of uptake onto 90 ± 1 mg of Gobi dust ($[O_3]_0$ = 1.7 ± 0.1 ppm, dry air, T = 296 K, P = 1013 mbar).

As indicated in Figure III-7, the surface of the same Gobi dust sample has been consecutively exposed three times to ozone under dry condition with an initial ozone concentration of 1.7 ± 0.1 ppm. The mass of the dust sample is 90 ± 1 mg. For *cycle 1* (see in Figure III-7), the experimental protocol is described below:

(i) Pretreatment of the dust sample: heating at 150°C under dry zero air flow then cooling down to room temperature.

(ii) Initial ozone concentration measurement through bypass line.

(iii) Dust surface exposure to ozone flow.

(iv) Switch ozone flow to bypass line to verify initial ozone concentration.

The only modification regarding experimental protocol for *cycle 2* and *cycle 3*, is no pretreatment, i.e., step (i) mentioned above, of the dust sample is applied. In-between *cycle 1* and *cycle 2*, the surface of the Gobi dust sample is exposed to air flow for 60 minutes at room temperature (296 K); while in-between *cycle 2* and *cycle 3*, the dust surface is heated up to 150°C (446 K) under dry air for 45 minutes, then cooled down to room temperature (296 K) under dry air flow.

The ozone concentration profile monitored along the first exposure phase in *cycle 1*, is coherent with the typical profile observed and reported on Figure III-1 since both initial and steady state uptakes can be observed.

The ozone concentration profile observed during *cycle 2* shows two specificities: first, no transient initial uptake peak is observed at the beginning of surface exposure; second, the steady state uptake regime is reached relatively fast and is similar with that of *cycle 1*. This behavior indicates that flushing with dry air for an hour at room temperature does not restore the surface sites after ozone-dust interaction in *cycle*

1. The surface groups formed on the surface of Gobi dust is stable at room temperature and the equilibrium between the adsorbed phase and the gas phase ozone is not modified. As a result, when the surface is exposed to ozone again in *cycle 2*, the surface is still in the same equilibrium for ozone uptake process and the steady-state regime is achieved since the very beginning as displayed in Figure III-7 *cycle 2*.

Unlike flushing with dry air at room temperature, the thermal treatment at 150˚C acts as a complete reset of the surface. Indeed, after heating the Gobi surface at 150˚C (423 K), the ozone concentration profile in *cycle 3* is similar to that in *cycle 1* since it exhibits an intense and transient initial uptake peak before reaching the steady-state uptake regime again. It has to be noted that the values of γ_0 determined for *cycle 1* and *cycle 3* are respectively $(4.4 \pm 0.4) \times 10^{-8}$ and $(4.3 \pm 0.3) \times 10^{-8}$, confirming that the Gobi surface has been restored by the thermal treatment. It suggests that surface sites of Gobi dust are restored to the initial condition by thermal treatment from the condition in steady-state regime where the surface of Gobi dust is in equilibrium with gas phase ozone molecules.

1.7.2 Surface regeneration by flushing and thermal treatment under 20% RH condition

Similar cyclic experiments under humid condition, i.e., 20% RH condition, have been carried out to investigate the stability of the steady-state surface properties of Gobi dust towards ozone decomposition and the subsequent long-term behavior of the surface properties under humid condition. Figure III-8 reports the gas-phase ozone concentration profile along the humid cyclic experiment.

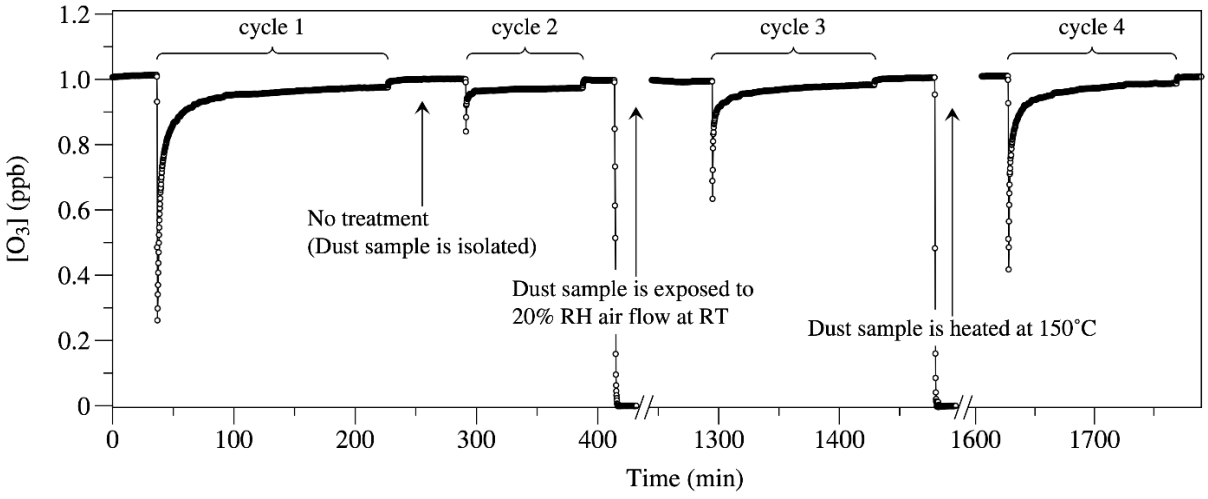

Figure III-8 Profile of gas phase ozone concentration measurement of a cyclic experiment of 1 ± 0.1 ppm of ozone onto 70 ± 1 mg Gobi dust under 20% relative humidity condition ($[O_3]_0$ = 1 ± 0.1 ppm, T = 296 K, P = 1013 mbar).

In this cyclic experiment, the surface of the same Gobi dust sample has been consecutively exposed four times to ozone under 20% RH condition with an initial ozone concentration of 1 ± 0.1 ppm. The mass of the dust sample is 70 ± 1 mg. The protocol for *cycle 1* is described as followed:

(i) Pretreatment of the dust sample: heating at 150˚C under dry zero air flow then cooling down to room temperature under 20% RH air flow.

(ii) Initial ozone concentration measurement through bypass line under 20% RH condition.

(iii) Dust surface exposure to ozone flow of 20% RH.

(iv) Switch ozone flow to bypass line to verify initial ozone concentration.

Between *cycle 1* and *cycle 2*, the ozone flow is first directed through the bypass line at 230 min (indicated in Figure III-8) for an hour then re-directed through the U-shape reactor at 290 min. In-between *cycle 2* and *cycle 3*, the surface of the Gobi dust sample is flushed by humid air flow without ozone for 10 hours at room temperature (296 K). While in-between *cycle 3* and *cycle 4*, the dust surface is heated up to 150°C (446 K) under dry air for 45 minutes, then cooled down to room temperature (296 K) under 20% RH air flow for c.a. 1 hour until the surface is saturated with humidity.

For *cycle 1*, the ozone concentration profile monitored is coherent with the typical profile observed and reported in Figure III-1 where both initial and steady state uptakes can be observed as showed in Figure III-8. For *cycle 2*, a slight transition behavior of ozone concentration profile is observed at c.a. 300 min when the ozone flow is switched to pass through Gobi dust. It is due to the pressure instability caused by changing the flow direction, which has been evidenced by blank experiment without dust sample. As a result, *cycle 2* can be regarded as the extension of *cycle 1* where the ozone uptake starts the way from the steady-state regime in *cycle 1* with the same surface properties toward ozone. It's consistent with the dry cyclic experiment and suggests that the surface state during steady-state uptake regime with ozone under 20% RH condition is stable.

For *cycle 3*, it shows two features concerning the ozone concentration profile: (i) a much smaller transient initial uptake peak compared with *cycle 1* is observed at the beginning of surface exposure; (ii) ozone concentration reaches the same steady state uptake regime as *cycles 1* and *2*. The latter, suggests that flushing the dust surface with humid flow at room temperature regenerates the surface of dust more efficiently than dry air. The regeneration effect by water molecules suggests the competition between ozone and water molecules; flushing with water liberates surface sites for ozone decomposition. Further information about the water regeneration effects are discussed in following sections.

For *cycle 4*, a significant initial uptake peak can be observed along the ozone concentration profile after the thermal treatment to the surface. The values of γ_0 determined for *cycles 1 4* in Figure III-8 are respectively $(5.8 \pm 0.5) \times 10^{-8}$ and $(4.5 \pm 0.5) \times 10^{-8}$ respectively. It shows similarity as the cyclic

experiment under dry condition, where Gobi surface has been greatly restored by the thermal treatment regarding ozone decomposition under the humid condition. However, the surface is not completely regenerated after thermal treatment compared to cyclic experiment under dry condition, which is probably due to the blocking effect of water molecules adsorbed on the surface. This suggestion is in accordance with the observation from the study of the influences of relative humidity on ozone decomposition on Gobi dust in *section 1.4*.

1.7.3 Conclusion from the cyclic experiments

The cyclic experiments address the surface stability and the surface regeneration process of Gobi dust towards ozone decomposition under dry and 20% RH condition through the kinetics of gas phase ozone.

It suggests that the surface modification due to ozone interacting when the dust sample reaches the steady-state ozone uptake regime is stable under room temperature for both dry and 20% RH condition. Thermal treatment is suggested to be able to restore the surface sites on Gobi dust surface thus regenerating the surface properties towards ozone decomposition significantly. Water molecules are suggested to have twofold effects during the interaction: On one hand, they can interact with the surface medications on Gobi dust by ozone molecules, reactivating surface sites on Gobi dust with limited surface regeneration effect. On the other hand, water molecules can also block the surface sites.

1.8 Conclusions of gas phase investigation

Conclusions are summarized as followed, based on the results presented during the investigation of ozone decomposition on Gobi dust by gas phase approach:

1. The surface properties of Gobi dust towards ozone decomposition varies along the heterogeneous interaction process: from a higher and transient surface properties to a lower and consistent surface properties. Correspondingly, initial uptake peak and steady-state uptake regime have been observed for ozone uptake onto Gobi dust.
2. For the range of ozone concentration from 20 ppb to 10 ppm, Gobi dust exhibits catalytic property towards ozone during the steady-state uptake regime. It is evidenced by the long exposure experiments with TON exceeding 1. Steady-state uptake coefficients of ozone on Gobi dust are determined to be from 2.6×10^{-9} to 6.2×10^{-8}. Within this ozone concentration range, data provided in the present work is applicable for both atmospheric chemistry and industrial applications.
3. Higher ozone concentration reduces the steady-state uptake coefficient but promotes the reaction rate during steady-state ozone uptake regime. The ozone decomposing reaction onto Gobi dust during steady-state uptake regime is characterized by a fractional reaction order, i.e.

0.5. It suggests the existence of pre-equilibrium state in the decomposition process and/or a multiple step mechanism underlying the observed reaction.

4. With the presence of water molecules, the ozone uptake is hindered during steady-state uptake regime. It suggests the competition between ozone molecules and water molecules for the same surface sites of Gobi dust.
5. The comparison of Gobi dust with its single mineral components shows synergetic effect regarding ozone decomposition. The potential and economic benefits of this geomaterial in NTP-catalysis for VOC abatement is suggested.
6. The cyclic experiments evidence the stability of the steady-state surface properties of Gobi dust towards ozone decomposition. The surface modifications due to the interaction with ozone molecules, which are involved into steady-state ozone decomposing process, are evidenced stable at room temperature under both dry and 20% RH condition. The initial surface properties of Gobi dust can be restored by thermal treatment at 150˚C, making Gobi dust recyclable. Water molecules can interact with the surface modification due to ozone interacting, resulting in limited surface regeneration effect in the time scale of 10 hours, and also can block the surface sites competing with ozone molecules.

The conclusions call for the investigation for adsorbed phase for further evidence, which will be discussed in next section.

2 Ozone decomposition on Gobi dust: adsorbed phase approach

The gas phase investigations call for further adsorbed phase investigation to understand the behavior of the natural Gobi dust regarding ozone decomposition, and clarify the surface chemistry involved. In this section, results of the adsorbed phase during the interaction of ozone and Gobi dust obtained by adsorbed phase approach are discussed. More precisely, the adsorbed phase of the surface of Gobi dust during the interaction with ozone as well as some other gas phase species relevant to this study such as water vapor and air plasma-generated species, characterized by DRIFT spectra are investigated and discussed. Moreover, the adsorbed phase of the individual minerals present in the Gobi dust are investigated in order to identify their respective surface properties towards ozone decomposition. These results and the discussions focus on the surface group formed during ozone-Gobi dust interaction thus helping understanding the mechanism of the reactions at the surface.

2.1 Adsorbed phase during ozone decomposition on Gobi dust under dry condition

DRIFT spectroscopy was employed for the in-situ monitoring of adsorbed phase species formed on Gobi dust after its exposure to 100 ± 5 ppm of ozone generated from oxygen at room temperature under dry condition. The experimental protocol is recalled briefly as followed:

(i) Pretreatment of the dust sample: heating at 150°C under oxygen flow and cooling down to room temperature under oxygen flow.

(ii) Unexposed surface monitoring: to acquire the initial adsorbed phase as background.

(iii) Dust surface exposure to ozone flow generated from oxygen.

(iv) Surface flushing by oxygen flow.

The chronological DRIFT spectra of one experiment are plotted in absorbance and reported in Figure III-9. These chronological DRIFT spectra reveal the evolution of the adsorbed phase of Gobi dust during ozone decomposition, where the positive bands suggest the formation of certain surface groups while negative bands indicate the removal of certain surface groups. For the absorbance bands with the same wavenumber from the spectra collected during the same experiment, which is the case in Figure III-9, the bigger the absorbance is, the higher the surface density of the corresponding surface group is. Several observations and remarks are pointed out according to Figure III-9.

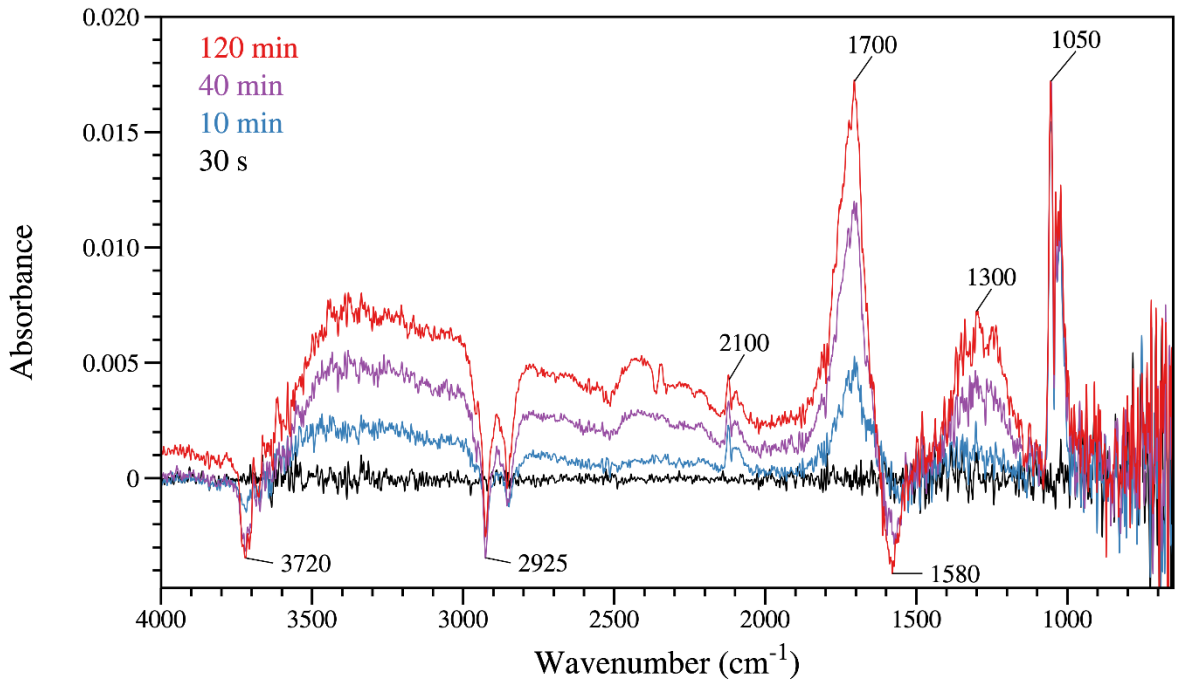

Figure III-9 Chronological DRIFT spectra of the surface of Gobi dust during the exposure to ozone ($[O_3]_0$ = 100 ± 5 ppm, dry condition, carrier gas is oxygen, T = 296 K, P = 1013 mbar).

When ozone is introduced into the system, bands around 1050 cm^{-1} and 2100 cm^{-1} appear immediately on the DRIFT spectra with constant intensities, which are identical to the IR absorbance bands of gas-phase ozone. Not related to adsorbed phase, these bands are assigned to gas-phase ozone based on two facts:

(i) They are identical to the IR absorbance bands of ozone in gas phase, as shown in Figure II-5.

(ii) They appear with constant intensities during ozone exposure and disappear immediately after the ozone flow is switched to oxygen flow during the surface flushing process.

Our results are consistent with the studies by K. M. Bulanin et al. who concluded that there is no molecular adsorption of ozone on various metal oxide at room temperature and even at 77 K [33-36], as mentioned in *section 3* of chapter 1.

Furthermore, broad bands are observed within the range of 2800 - 3800 cm^{-1} and 1500 - 1800 cm^{-1} that could be attributed to OH stretching vibration modes most likely from adsorbed water [12, 37, 38]. Interestingly, negative bands also appear during ozone decomposition within this region of wavenumber at around ca. 3720 cm^{-1}, 2925 cm^{-1} and 1580 cm^{-1}, probably due to surface OH group consumption [39]. The observation of these broad bands and negative bands suggests that surface OH groups are involved in ozone-Gobi dust interaction. The broad band noticed within the range of 2800 - 3800 cm^{-1}, could be attributed to adsorbed water [12, 37, 38] since it exists as impurity in the carrier gas flow, or water desorption from the glass tube of the DBD reactor during ozone production, which can be adsorbed and accumulate on the surface of Gobi dust. Additionally, pretreatment of the sample at 150°C cannot completely dehydrate the surface of sample. Remaining water molecules can lead to the presence of specific peaks or shoulders on the spectra [37]. It explains the broad OH stretching regions observed within the 2800 - 3800 cm^{-1} and 1500 - 1800 cm^{-1} [12, 37, 38] in Figure III-9. As for the negative bands at ca. 3720 cm^{-1}, 2925 cm^{-1} and 1580 cm^{-1}, it's suggested that ozone molecules can interact with the isolated OH groups terminated on the surface sites [39] leading the removal of these OH groups from the surface sites. This observation suggests that ozone molecules decompose on the same sites where surface isolated OH groups or adsorbed water molecules are attached.

Moreover, bands at ca. 1300 and 1700 cm^{-1} appear after few minutes of interaction along the uptake of ozone on Gobi surface and continuously increase till 120 min. This observation indicates that certain surface groups are formed on the surface of Gobi dust during ozone exposure. Peaks and bands within this wavenumber range have been observed during the interaction between ozone and mineral oxides in literature reviewed in *section 3* of chapter 1. Remarkably among the literature, Li et al. [40] have observed DRIFT band on Al_2O_3 at 1380 cm^{-1} attributed to oxygenated surface species designated as SS-O. Additionally, J. Jia et al. [41] confirmed that the surface peroxide species denoted as SS-O_2 leads on α-MnO_2 to a peak at 1658 cm^{-1} corresponding to an overtone contribution of the peak at 835 cm^{-1}.

Authors relate these peaks to surface groups formed from the interactions between ozone molecules and surface sites of the considered metal oxides. Interestingly, similar bands are observed by DRIFT on the natural Gobi dust surface. Considering a possible band shift due to different surface nature and properties of natural Gobi dust compared to single metal oxides, the band at 1300 cm^{-1} observed in Figure III-9 could be assigned to SS-O species and similarly the peak at 1700 cm^{-1} could be assigned to surface peroxide SS-O_2 species. These surface observations confirm the formation of different and specific surface groups during ozone uptake on Gobi dust surface.

2.2 Kinetics of the surface-group formation during ozone decomposing on Gobi dust under dry condition

DRIFT provides a semi-quantitative characterization of the adsorbed phase during ozone decomposition on Gobi dust surface, revealing specific molecular structures, i.e. SS-O and SS-O_2 on the surface. The absolute value or the surface density of SS-O and SS-O_2 cannot be retrieved from DRIFT spectra. As a result, it is not possible to directly compare SS-O with SS-O_2 quantitatively.

However, the integrated areas of the bands at 1300 and 1700 cm^{-1} still can reveal the evolution of the relative surface density of SS-O and SS-O_2 independently. In this regard, the normalized band areas of band at 1300 cm^{-1} and 1700 cm^{-1}, are calculated by integrating the band area for all the DRIFT spectra along time, from 1200 to 1400 cm^{-1} for the band at 1300 cm^{-1} and from 1650 to 1750 cm^{-1} for the band at 1700 cm^{-1}, then normalizing their maximum values to 1 for the purpose of comparison. Figure III-10 shows the temporal profiles of normalized band areas at 1300 and 1700 cm^{-1}.

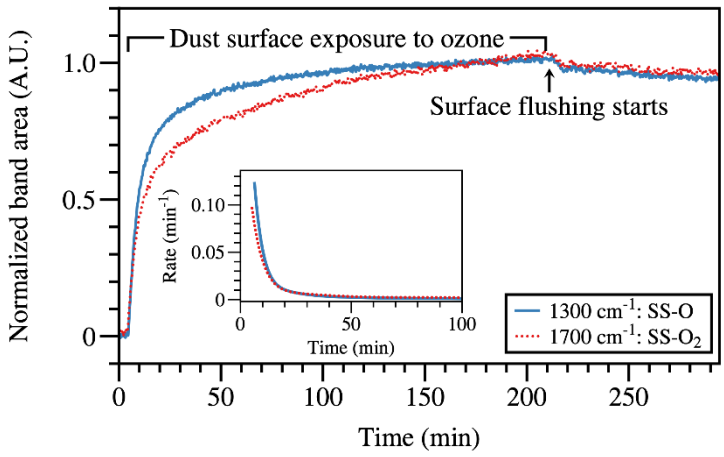

Figure III-10 Temporal profiles of the normalized DRIFT band area of SS-O and SS-O_2 formed on Gobi dust surface during ozone decomposition ($[O_3]_0$ = 100 ± 5 ppm, dry air, T = 296 K, P = 1013 mbar). The inserted figure is the rates of growth of the normalized band area of SS-O and SS-O_2 correspondingly.

The temporal profiles in Figure III-10 reveals the variation of the relative surface density of SS-O and SS-O_2 during surface exposure to ozone and surface flushing by oxygen without ozone. From Figure

III-10, several observations concerning the kinetic of the formation of SS-O and SS-O_2 can be determined:

(i) The temporal profiles of the normalized surface density of SS-O and SS-O_2 are not totally identical, which is an evidence of the formation of two different kinds of surface groups on the surface of Gobi dust during ozone decomposition.

(ii) The surface densities of both SS-O and SS-O_2 increase during surface exposure to ozone, and finally reach equilibrated values respectively. This observation supports the previous discussion in *section 1.1* which suggests that the transient initial ozone uptake behavior could be associated to surface modifications and the formation of surface species accumulating on Gobi dust surface and the steady-state uptake behavior indicates an equilibrium between the accumulation of the surface species and the surface regeneration process.

(iii) The surface densities of both SS-O and SS-O_2 remain relatively stable during surface flushing by dry oxygen flow with a slight decreasing tendency. This observation is consistent with the previous discussion of the stability of the surface groups at room temperature in *section 1.7*. Also, it supports the suggestion of the time-dependency of the regeneration process mentioned in the same section.

The inserted graph shows the corresponding rate of band areas growth within the first 100 minutes of surface exposure, and are the derivatives of the normalized band area curves. The rates of formation indicate that both SS-O and SS-O_2 are rapidly formed at the beginning of surface exposure to ozone. Comparing the formation rate of SS-O and SS-O_2, the inserted graph also indicates that SS-O is formed faster than SS-O_2 at the very beginning of surface exposure to ozone. It potentially suggests that SS-O might be formed before SS-O_2. Then, the rates of formation for both SS-O and SS-O_2 decrease and approach 0 after 50 minutes of surface exposure.

The kinetics of surface group formation and gas phase ozone concentration could not be experimentally determined in our case according to chapter 2, since there are several limitations to monitor the gas phase kinetics during adsorbed phase investigation:

- The range of ozone concentration applied in gas phase investigation is below 10 ppm while in adsorbed investigation is ca. 100 ppm.
- In gas phase approach, the ozone flow passes through the dust sample in U-shape reactor thus the whole dust sample is involved into ozone-dust interactions, while in adsorbed phase approach, the ozone flow passes above the dust sample in the DRIFT sample bed thus only the upper fraction of the sample is involved.

As a result, the initial ozone uptake peak and the steady-steady ozone uptake regime could not be pointed out from the temporal ozone concentration profile in gas phase during the experiments conducted in this section for adsorbed phase investigation. However, the gas phase ozone kinetics are suggested to develop faster considering the higher ozone concentration and lower amount of involved dust sample applied in adsorbed phase investigation.

As a result, in Figure III-10, the kinetics of the gas phase ozone, are suggested to have gone through the initial uptake stage and reached the steady-state uptake regime within the surface exposure process. In this way, the kinetics of the ozone concentration in gas phase and the surface densities of SS-O and SS-O_2 in adsorbed phase are connected. It is consistent with the previous discussion that the formation of the surface groups, i.e. SS-O and SS-O_2, starts at the initial uptake stage and their surface densities reach relatively stable values in steady-state uptake regime in equilibrium with gas phase ozone. Also, according to the inserted figure in Figure III-10, the formation of SS-O and SS-O_2 species is faster at the initial uptake stage and then continue to slow down until the overall rates of formation approach 0, where ozone decomposition is also suggested to have reached steady-state uptake regime.

2.3 Influences of water molecules on the adsorbed phase towards fresh Gobi dust and ozone-exposed Gobi dust

In order to address the mechanism for water molecules interacting with the surface of Gobi dust and the surface groups, i.e., SS-O and SS-O_2, formed during ozone-Gobi dust interaction, the adsorbed phase of Gobi dust is investigated under two experimental conditions in this section:

(i) Water molecules interact with fresh Gobi dust sample without exposure to ozone

(ii) Water molecules interact with the Gobi dust sample after exposed to ozone and flushed under dry condition.

2.3.1 Water molecules interact with fresh Gobi dust sample

To evaluate the surface modifications induced by water uptake on Gobi dust, the adsorbed phase of a pretreated Gobi dust sample is monitored following the experimental protocol as described:

(i) Pretreatment of the dust sample: heating at 150˚C under dry oxygen flow and cooling down to room temperature under dry oxygen flow.

(ii) Unexposed surface monitoring under dry oxygen flow.

(iii) Dust surface exposure to oxygen flow containing 50 ppm of water molecules.

(iv) Surface flushing by dry oxygen flow.

The chronological DRIFT spectra of the surface of Gobi dust during the exposure to water flow with water vapor concentration of 50 ppm, i.e., 0.15% RH, are plotted in absorbance and showed in Figure

III-11. This water concentration in gas phase allows to observe the surface groups formed during water-Gobi dust interaction from DRIFT spectra and the same time won't adsorb too much IR signal.

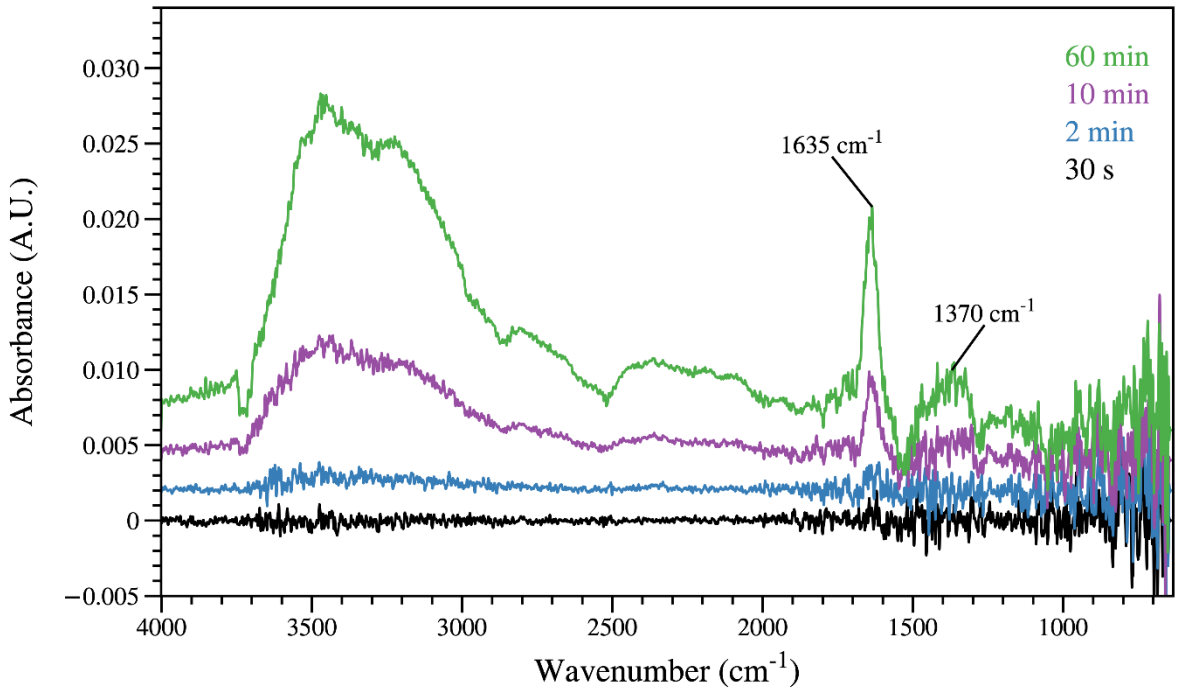

Figure III-11 Chronological DRIFT spectra of the surface of Gobi dust during the exposure to humid flow ($[H_2O]_0$ = 50 ± 2 ppm, T = 296 K, P = 1013 mbar). Water vapor is generated by flowing oxygen from cylinder through the bubbler containing deionized water. The spectra are showed with offset for clear display.

From Figure III-11, three principle observations are pointed out:

(i) No obvious negative absorbance peak is observed.

(ii) Broad bands over the wavenumber range of 2000 to 3700 cm^{-1} appear and increase during the water exposure. This is due to the stretching of the surface OH group, most probably from adsorbed water molecules according to literature [12, 37, 38, 42].

(iii) Two peaks at 1635 cm^{-1} and 1370 cm^{-1} appear and increase along the interaction of water molecules and the surface of Gobi dust. The Peak at 1635 cm^{-1} is the typical band assigned to water molecular bending vibration mode, i.e., H-O-H bending mode [39, 43]. The peak at 1370 cm^{-1} is suggested related to the vibrational mode of OH group as well.

DRIFT spectra of water uptake on Gobi dust are consistent with the observation by N. Joshi et al. [13] who investigated water uptake on Arizona Test Dusts (ATDs) by DRIFT at ambient temperature where they observed the DRIFT bands due to water adsorption at wavenumber range of 1600 – 1700 cm^{-1}, 2100 – 2300 cm^{-1} and 2600 – 3800 cm^{-1}. N. Joshi et al. didn't mention any peak observed around 1370 cm^{-1} but absorbance noise at 1300 – 1400 cm^{-1} can be observed from the DRIFT spectra of water

adsorption on ultrafine ATDs and a small absorbance peak at 1300 – 1400 cm^{-1} can be observed from the DRIFT spectra of water adsorption on SiO_2, based on their work [13]. Our observation is also consistent with the observation by J. M. Roscoe and J. P. D. Abbatt who studied the interaction of water vapor with the surface of alumina using DRIFT [44] where peaks and bands at similar wavenumber locations could be observed, as mentioned in Figure I-12. These observations provide evidence that water molecules can interact with the surface of Gobi dust, leading to the formation of surface groups, mostly adsorbed water molecules. The adsorbed water molecules formed on the surface of mineral dust during water adsorption have been observed by N. Joshi et al. [13] by DRIFT investigation.

During the interaction between water molecules and the surface of Gobi dust, the bands and peaks observed in the DRIFT spectra in Figure III-11 are all related to the vibrational modes of the surface OH group. During ozone decomposition on the surface of Gobi dust, DRIFT spectra of the adsorbed phase as showed in Figure III-9 also reveal some features related to surface OH groups, especially the broad bands at the range of 2800 – 3800 cm-1 which are suggested due to adsorbed water molecules. As a result, it is interesting to compared the DRIFT spectrum of the adsorbed phase during ozone-dust and water-dust interaction and they are compared in Figure III-12.

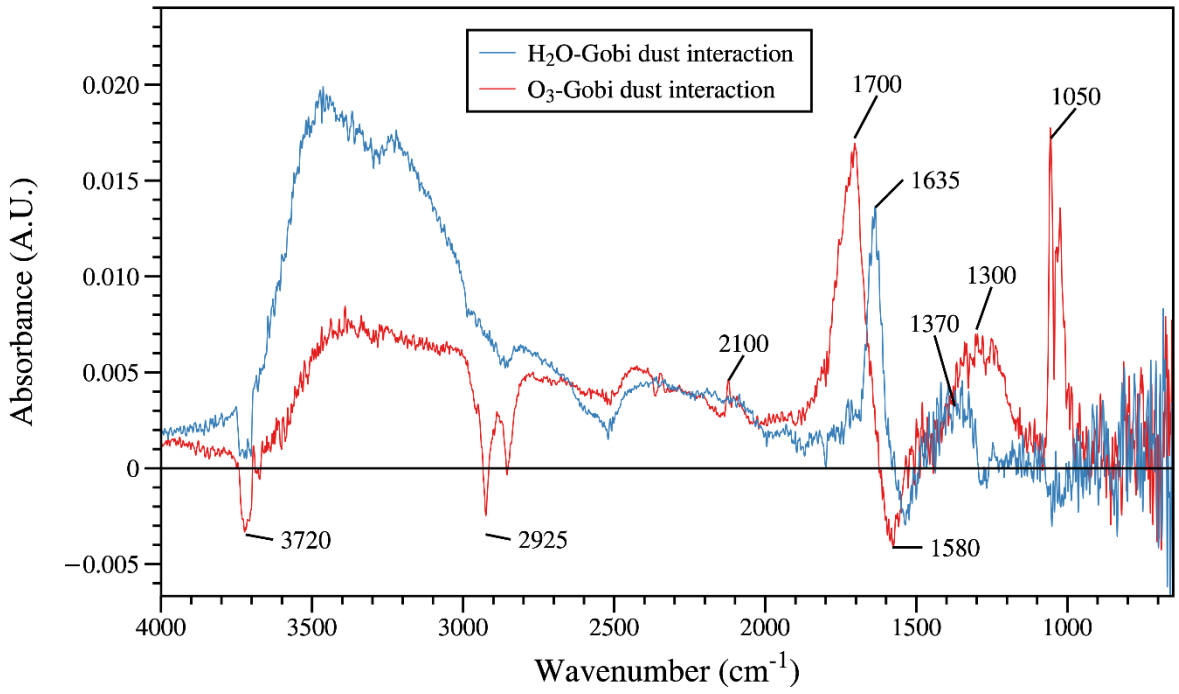

Figure III-12 DRIFT spectrum of (—) ozone decomposition on Gobi dust after 120 min and (—) water uptake on Gobi dust after 60 min. ($[O_3]_0$ = 100 ± 5 ppm, $[H_2O]_0$ = 50 ± 2 ppm, carrier gas is oxygen, T = 296 K, P = 1013 mbar).

As mentioned in *section 2.1*, broad bands within 2000 – 3700 cm^{-1} appear on the DRIFT spectra of ozone decomposition on pretreated Gobi dust surface, which also appear on the DRIFT spectra of water

uptake on Gobi dust surface. It confirms that these broad DRIFT bands are related to adsorbed water molecules on the surface. Besides, the negative peak at 3720 cm^{-1} is related to the stretching of the isolated surface OH groups terminated on the surface sites [39, 42], which confirms that ozone-dust interaction consumes these surface OH groups and also suggests that water molecules are taken up on these surface OH groups as well. It is in accordance with the competing effect of water molecules with ozone molecules for the same surface site in *section 1* of the current chapter.

The absorbance peaks with strong intensity within 1600 – 1700 cm^{-1}, caused by the interaction of ozone molecules and water molecules respectively with Gobi dust surface can be distinguished clearly from Figure III-12. The band at 1700 cm^{-1} attributed to SS-O_2 and the band at 1635 cm^{-1} attributed to H-O-H stretching have a small overlap for ca. 100 cm^{-1}. The weaker absorbance bands within 1300 – 1400 cm^{-1} from the two DRIFT spectrum in Figure III-12 are also in contrast, and the band at 1370 cm^{-1} caused by water-Gobi dust interaction is totally overlapped with the band at 1300 cm^{-1} caused by ozone-Gobi dust interaction. These observations support the conclusion in *section 2.1* of the current chapter, that the bands at 1300 and 1700 cm^{-1} in DRIFT spectra observed during ozone uptake onto Gobi dust surface, as showed in Figure III-9, are assigned to surface oxygenated groups, i.e., SS-O and SS-O_2, induced by the interaction of ozone molecules with surface sites of Gobi dust.

2.3.2 Water molecules interact ozone-exposed Gobi dust surface

In order to investigate the interaction of water molecules with ozone-exposed surface of Gobi dust, experiments are conducted following a typical protocol in section *2.1* of the current chapter with an extra step of flushing the surface with humid air flow, as described as followed:

(i) Pretreatment of the dust sample: heating at 150˚C under oxygen flow and cooling down to room temperature under oxygen flow.

(ii) Unexposed surface monitoring: to acquire the initial adsorbed phase as background.

(iii) Dust surface exposure to ozone flow generated from oxygen under dry condition.

(iv) Surface flushing by dry oxygen flow.

(v) **Surface flushing with oxygen flow containing water.** Once the DRIFT spectra acquired during step (iv) is considered stable, the oxygen flow will be switched to pass the bubbler containing deionized water to generate 30 ppm of water. The ozone-exposed Gobi dust surface is flushed with flow containing water vapor.

Figure III-13 shows the evolution of the adsorbed phase during the interaction of 30 ppm of water molecules with ozone-exposed Gobi dust surface, focusing on the wavenumber range of 800 to 2600 cm^{-1} where are the DRIFT bands attributed to SS-O and SS-O_2. The red spectrum (—) of the surface is acquired before flushing the surface by humid flow where a steady state has been achieved on the surface

after 1hour of ozone exposure and flushing under dry oxygen flow, the green spectrum (—) is after 20 min of flushing the surface with humid flow and the blue spectrum (—) is after 50 min of flushing with humid flow.

Concerning the band at 1300 cm^{-1} assigned to SS-O during ozone decomposition on Gobi dust, its intensity remains stable, pointing that the surface density of SS-O surface group remains constant during flushing with water thus suggesting a weak interaction between water molecules and SS-O.

For the band at 1700 cm^{-1} assigned to SS-O_2 in Figure III-13, the intensity of the band increases after 20 min of water-flushing. However, it is due to the overlapping with adsorbed water bands at 1635 cm^{-1} and baseline shifting. It is confirmed by the deconvolution of bands within 1500 – 1900 cm^{-1} on the DRIFT spectrum in blue (—) acquired after 50 min of water flushing, as indicated in Figure III-13, where the intensity of band at 1700 cm^{-1} has no significant change after interacting with water molecules for 50 min. This observation pointed out the weak interaction between water molecules and SS-O_2 on the surface.

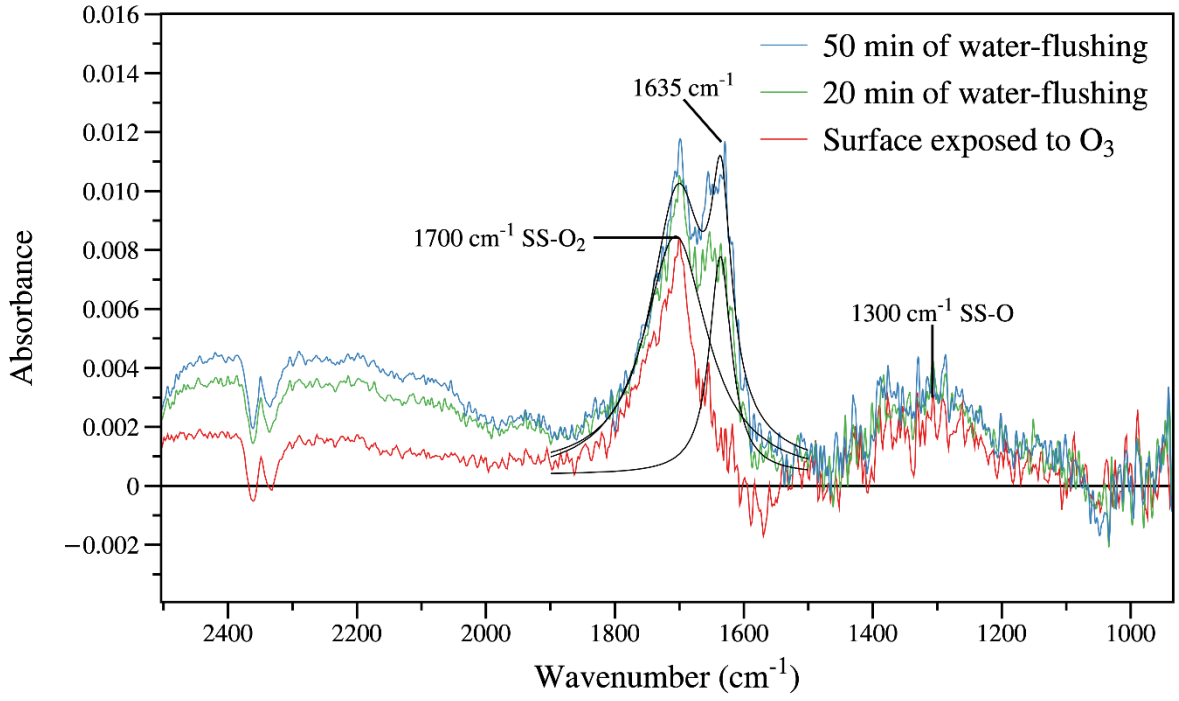

Figure III-13 DRIFT spectra during the interaction of water molecules with SS-O and SS-O_2 ($[O_3]_0$ = 100 ± 5 ppm, $[H_2O]$ = 30 ± 2 ppm, carrier gas is oxygen, T = 296 K, P = 1013 mbar). (—) is acquired at the end of Step (iv) Surface flushing with oxygen flow after the interaction between ozone and Gobi dust, (—) is the acquired after 20 min of water-flushing, while (—) is acquired after 50 min of water-flushing for which the deconvolution of bands within 1500 – 1900 cm^{-1} is indicated.

The observations that the band at 1300 cm^{-1} assigned to SS-O and the band at 1700 cm^{-1} assigned to SS-O_2 remain stable during 30 ppm of water interaction during this experiment suggest that water molecules

do not significantly interact with SS-O and SS-O_2 under this condition. However, considering the low water concentration applied to interact with SS-O and SS-O_2, which is 30 ppm equivalent to 0.1% RH condition, it does not exclude that with higher water concentration, the interaction between water molecules and SS-O or SS-O_2 will becomes more significant. This is consistent with the observation from the cyclic experiment under 20% RH condition discussed in *section 1.7.2*, for which the water concentration in gas phase is 200 times higher than 30 ppm. In the cyclic experiment under 20% RH condition, water molecules are suggested to interact with the ozone-induced surface modifications but to a limited degree, resulting in a slight regeneration effect on the surface properties of the surface towards ozone decomposition.

2.3.3 Conclusions and remarks

The interaction of water molecules with the fresh Gobi dust as well as ozone-exposed Gobi dust are investigated using adsorbed phase approach in this section. The adsorbed phase of a fresh Gobi dust sample during the interaction of 50 ppm of water flow is characterized with DRIFT spectrum by the broad bands at the wavenumber range of 2000 to 3700 cm^{-1} due to adsorbed water molecules on the surface and the typical peak at 1635 cm^{-1} assigned to water molecular bending vibration mode, i.e., H-O-H bending mode. The observations evidence the formation of surface groups, i.e., surface OH groups and adsorbed water molecules, on the surface during water-Gobi dust interaction. Water-dust interaction is suggested to compete for the same surface sites on Gobi dust with ozone decomposition on Gobi dust. For SS-O or SS-O_2 formed on the surface, they remain stable during the exposure to 30 ppm of water flow according to their corresponding DRIFT bands: no significant interaction with water molecules is observed under 30 ppm (0.1% RH) condition but interaction might be promoted with higher water concentration such as under 20% RH condition.

2.4 Adsorbed phase of Gobi dust exposed to air-generated ozone flow

For adsorbed phase investigation, the carrier gas used to produce ozone by the DBD reactor in this study is always oxygen in order to avoid the production of NO_x. However in literature, a large number of studies about the heterogeneous interactions concerning ozone were conducted with ozone produced from air, where the authors have highlighted the presence of the NO_x as the by-products and suggested the significant impacts of NO_x on the observations [45-47]. As a result, it would be interesting to examine the adsorbed phase of natural Gobi dust interacting with air-generated ozone, to evidence that the air-generated ozone by non-thermal plasma will results in different observations regarding adsorbed phase monitoring during the interactions with Gobi dust.

To start with, the chronological DRIFT spectra of the surface of Gobi dust during the exposure to ozone generated from zero air is showed in Figure III-14.

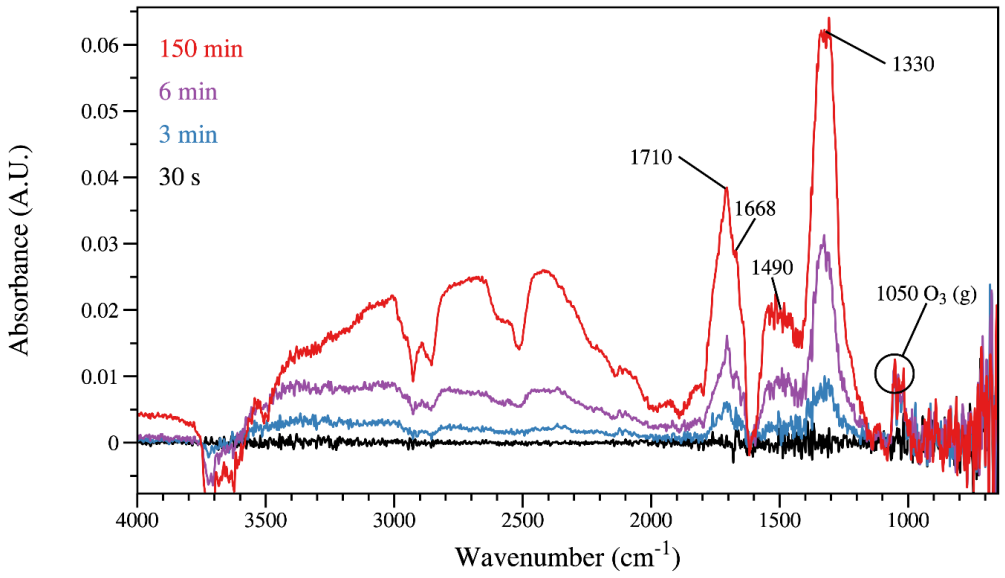

Figure III-14 Chronological DRIFT spectra of the surface of Gobi dust during the exposure to ozone generated from zero air ($[O_3]_0$ = 300 ± 10 ppm, dry condition, carrier gas is zero air, T = 296 K, P = 1013 mbar).

In Figure III-14, peaks and bands at 1050, 1330, 1490, 1668 and 1700 cm^{-1} appear after the Gobi dust exposed to air-generated ozone. Besides, the broad band over 2000 to 3500 cm^{-1} as well as the negative bands around 3700 cm^{-1} appears the same time. The gas phase species of the air-generated ozone flow using DBD reactor have been measured by FTIR, which shows that for 300 ppm of ozone generated from zero air under dry condition, besides ozone as the principle production, about 4.4 ppm of N_2O, 0.6 ppm of NO_2 and 1 ppm of NO are detected. To distribute the assignment of the bands in Figure III-14 and further characterize the DRIFT spectra of Gobi dust exposed to air-generated ozone, the DRIFT spectra of NO_2, NO and N_2O taken up on Gobi dust are compared with air-generated ozone in Figure III-15, to address the individual contribution of the NO_x to the adsorbed phase.

From Figure III-15, the peaks at 1050 and 2100 cm^{-1} assigned to gaseous ozone are only observed on the DRIFT spectrum of Gobi dust exposed to air-generated ozone flow.

The DRIFT spectra of adsorbed phase of Gobi dust during N_2O uptake is characterized only by the typical gas-phase N_2O band at 2223 cm^{-1}, which appears immediately when N_2O is introduced into the system and disappears right after N_2O flow is switched to zero air. It evidences that N_2O is barely adsorbed on the surface of Gobi dust under room temperature thus causing no significant surface modifications regarding DRIFT spectra observation.

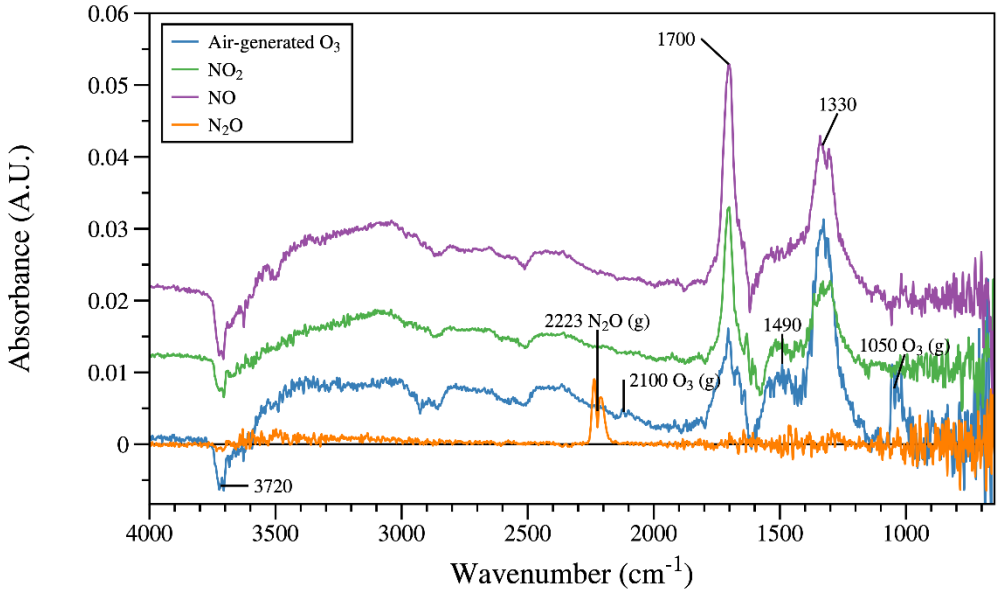

Figure III-15 DRIFT spectrum of (—) air-generated ozone uptake on Gobi dust after 120 min, (—) NO_2 uptake on Gobi dust after 60 min, (—) NO uptake on Gobi dust after 60 min and (—) N_2O uptake on Gobi dust after 60 min. ($[O_3]_0$ = 100 ± 5 ppm, ($[NO_x]_0$ = 100 ± 5 ppm, dry condition, carrier gas is zero air, T = 296 K, P = 1013 mbar).

The interaction between ozone and the surface, NO and the surface, and also NO_2 and the surface lead to the formation of bulk water, as evidenced by the broad bands over 2000 to 3500 cm^{-1} on all the DRIFT spectra. Moreover, the interaction between NO_x and surface can also lead to the removal of the isolated surface OH group, as the interaction between ozone and the surface. It is revealed by the negative peaks at 3720 cm^{-1} as showed in Figure III-15. These features are commonly found in literature of infrared studies for heterogeneous interactions and associated to the surface OH or water adsorption [12, 37-39, 43]. The same observation has been obtained by M. Angelini et al. during the study of HNO_3 and NO_2 on kaolinite surface using DRIFT [48].

The interaction of both NO and NO_2 with the surface of Gobi dust results in the appearance of the DRIFT bands at ca. 1330, 1490 and 1700 cm^{-1}. Bands and peaks within 1200 – 1700 cm^{-1} have been observed during the interaction of NO_2 with the surface, which are assigned to oxide-coordinated and water-solvated nitrate species, according to the authors [39, 49-51]. As a result, the peak at 1700 cm^{-1} on the DRIFT spectrum of air-generated ozone interacting with Gobi dust surface is the production of the interactions of both ozone and NO_x with the surface.

Although the DRIFT spectra during the NO_2-dust and NO-dust interaction are quiet similar, it has to be mentioned that the interaction of NO_2 with the surface is more important that the interaction of NO with the surface, according to the study by H. Judeikis and A. Wren [52]. In addition, in presence of ozone NO is readily oxidized to NO_2 and thus, the contribution of NO_2 impurities produced in air-generated ozone flow is expected to be the dominant.

Consequently, the presence of NOx in air-generated ozone has significant impacts on the DRIFT observations, which could be revealed in Figure III-16 where the spectrum of Gobi dust exposed to air-generated ozone flow after 100 min is compared with the spectrum of Gobi dust exposed to oxygen-generated ozone flow after 120 min.

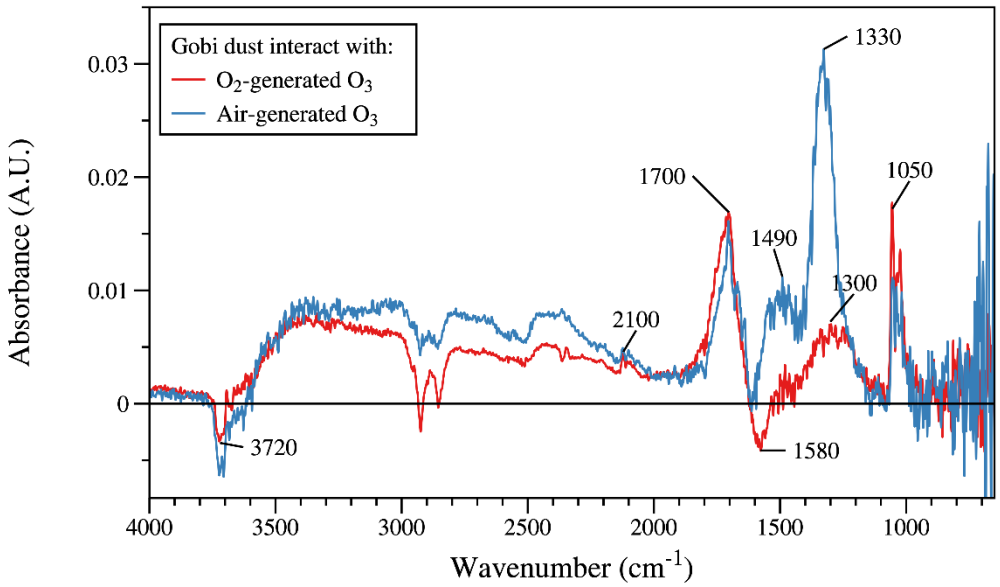

Figure III-16 DRIFT spectrum of (—) oxygen-generated ozone uptake on Gobi dust after 120 min and (—) air-generated ozone uptake on Gobi dust after 100 min. ($[O_3]_0$ = 100 ± 5 ppm, dry condition, T = 296 K, P = 1013 mbar).

Clearly from Figure III-16, the adsorbed phases of Gobi dust during air-generated ozone and oxygen-generated ozone share many similarities and quite some interesting differences. The negative peaks at 3720 cm^{-1} due to the removal of the isolated surface OH group and the broad band over 2000 to 3500 cm^{-1} due to the formation of bulk water are observed in both spectra. Besides, the bands assigned to gas-phase ozone at 1050 and 2100 cm^{-1} are also observed.

The differences between the two spectra are located around 1100 to 1800 cm^{-1}. The peak at 1330 cm^{-1} and the band at 1490 cm^{-1} appear in the DRIFT spectra of Gobi dust surface during the interaction of air-generated ozone with Gobi dust. They should be assigned to surface groups which are formed during the interaction of NO_x with Gobi dust instead of ozone, since NO_x are the extra gas phase species in air-generated ozone flow comparing to oxygen-generated ozone flow. Also, the peaks at 1700 cm^{-1} for air- and oxygen-generated ozone, even they are very close to each other on the two spectra, are not identical.

As a conclusion, the characteristics of the DRIFT spectra during the interaction of air-generated ozone flow with Gobi dust are due to combined interaction of ozone and NO_x. These spectra show some major differences with the DRIFT spectra obtained in oxygen-generated ozone flow. In particular, the 1300 cm^{-1} peak attributed to SS-O has a very different behavior depending upon the carrier gas. However, the

1700 cm^{-1} peak attributed to SS-O_2 can be used as a good marker of the ozone interaction with Gobi dusts in both cases as very little difference is observed between spectra resulting from oxygen and air generated ozone interaction. Attention should be paid by the scientific community about the NO_x impurities produced from air-generated ozone since they strongly interact with the surface thus influencing the performance of the surface, which might result in unexpected or unconsidered uncertainties in the measurements. This section also proves that using oxygen-generated ozone is an effective approach in order to avoid the interferences from NOx impurities.

2.5 Adsorbed phase of the single mineral components of Gobi dust during ozone decomposition under dry condition

Further understanding of the surface properties of Gobi dust surface can be retrieved from similar DRIFT investigations performed on major single minerals contained in Gobi dust. Based on the mineral phase composition of the Gobi dust sample (see Table II-1), the following minerals have been selected as main constituents: SiO_2, $Al_2Si_2O_5(OH)_4$, $CaCO_3$, and TiO_2. DRIFT experiments focusing on the adsorbed phase of these minerals have been performed to address their individual surfaces during their interactions with ozone. Al_2O_3 is also investigated and compared with Gobi dust as an important reference mineral which is found in many other types of mineral dust. These experiments have been performed at room temperature, under dry conditions, with an initial ozone concentration of 100 ± 5 ppm which is produced from oxygen as the carrier gas.

The DRIFT spectra of these single minerals and authentic Gobi dust after one hour of surface exposure to ozone have been acquired and compared in Figure III-17. By the time of the acquirements, the DRIFT spectra have already reached stable regime for all the samples.

From an overall point of view, bands and peaks are observed on the surfaces of $Al_2Si_2O_5(OH)_4$, Al_2O_3 and TiO_2 after one hour of interaction with ozone similar to Gobi dust, as showed in Figure III-17. For $Al_2Si_2O_5(OH)_4$, Al_2O_3 and TiO_2, the broad bands within 2000 –3700 cm^{-1} are observed related to the surface OH groups, which is consistent with the previous discussion. Comparing $Al_2Si_2O_5(OH)_4$ and Al_2O_3 with Gobi dust, no clear band at 1300 cm^{-1} has been observed on either of them, suggesting that this band observed on Gobi dust is due to the contribution from another mineral component. The peak at 1700 cm^{-1}, which is assigned to SS-O_2 on Gobi dust, has been observed on both $Al_2Si_2O_5(OH)_4$ and Al_2O_3.

Moreover, the overall shape of the DRIFT spectrum of $Al_2Si_2O_5(OH)_4$ within the ozone-induced bands range, i.e., from 1000 to 2000 cm^{-1}, is very close to that of Gobi dust, suggesting this aluminosilicate plays an important role in the surface properties of Gobi dust towards ozone and probably indicating that ozone decomposes mostly on aluminosilicates. Interestingly, Al_2O_3, which is the component of many other types of mineral dust and the reactive component in many metal-containing aluminosilicates,

also exhibits very similar features of DRIFT bands within this wavenumber range as Gobi dust. These observations suggest that the mechanism of ozone decomposition on the surface of $Al_2Si_2O_5(OH)_4$ and Al_2O_3 shares similarity with the mechanism of ozone decomposition on Gobi dust surface, thus making $Al_2Si_2O_5(OH)_4$ and Al_2O_3 important reference minerals regarding the investigation of the ozone decomposition on Gobi dust.

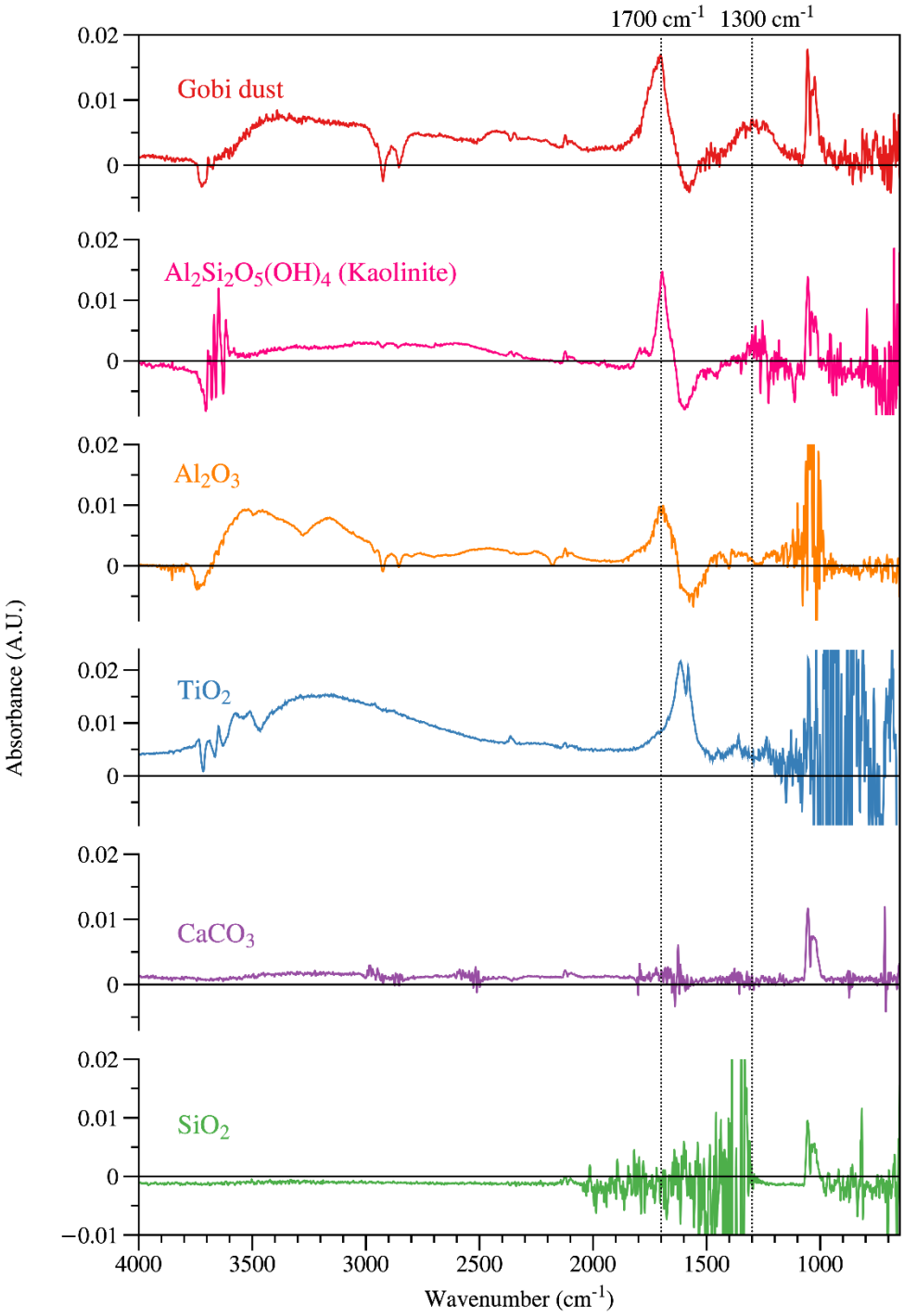

Figure III-17 DRIFT spectra of the surface of Gobi dust, synthetic $Al_2Si_2O_5(OH)_4$, Al_2O_3, TiO_2, $CaCO_3$ and SiO_2 after 1-hour surface exposure to ozone ($[O3]_0$ = 100 ± 5 ppm, dry condition, carrier gas is oxygen, T = 296 K, P = 1013 mbar).

For TiO_2, no band or peak at 1300 or 1700 cm^{-1} has been observed. However new peaks at 1620 and 1580 cm^{-1} have been observed, indicating the formation of surface groups on the surface of TiO_2 during the interaction with ozone. Even if these surface groups formed on TiO_2 have the same molecular structure as those formed on the surface of Gobi dust, i.e. SS-O or SS-O_2, the different surface property of Gobi dust and TiO_2 might lead to different vibration frequencies thus causing band shifting.

For $CaCO_3$ and SiO_2, except the bands assigned to gas phase ozone at 1050 cm^{-1} and 2100 cm^{-1}, their DRIFT spectra don't show other clear band or peak during ozone uptake. Same observation has been reported previously by L. Li et al. [53]. Not accidentally, the DRIFT spectra observations are also consistent with the values of steady-state uptake coefficient determined and reported in Table III-1, where the steady-state uptake coefficients of ozone on $CaCO_3$ and SiO_2 are one to two orders of magnitude smaller than what on Gobi dust, $Al_2Si_2O_5(OH)_4$ and Al_2O_3 under the same condition.

The comparison of DRIFT spectra shows both similarities and differences between natural Gobi dust and the single mineral compounds tested regarding the adsorbed phase during ozone uptake. It suggests the reference value of single minerals reported in literature regarding the mechanism of ozone decomposition on the surface, highlighting $Al_2Si_2O_5(OH)_4$ and Al_2O_3 as important reference minerals.

2.6 Conclusions of adsorbed phase investigation

Conclusions are summarized as followed, based on the DRIFT studies presented during the investigation of ozone decomposition on Gobi dust by adsorbed phase approach:

1. During the decomposition of ozone molecules on the surface of Gobi dust sample, surface oxygenated groups are formed from the interactions between ozone molecules and the surface sites, characterized by broad DRIFT band at 1700 cm^{-1} and band centered at 1300 cm^{-1}. The kinetics of the DRIFT bands formations are different, thus suggesting the presence of two different surface oxygenated groups. Based on literature, the DRIFT peak at 1700 cm^{-1} is assigned to SS-O_2 and band centered at 1300 cm^{-1} is assigned to SS-O.
2. The connections are built between the kinetics of SS-O and SS-O_2 formation and the gas phase ozone: SS-O and SS-O_2 are rapidly formed at the beginning of the ozone-dust interaction where the initial ozone uptake peak is observed by gas phase approach, and the surface densities of both SS-O and SS-O_2 remain stable during the steady-state ozone uptake regime.
3. Surface OH groups on Gobi dust are involved in the interaction of ozone molecules and the surface which are removed due to ozone-Gobi dust interaction.
4. Water molecules is suggested to compete for the same surface sites on Gobi dust with ozone molecules by forming adsorbed water on the same surface sites.

5. The interactions of water molecules are suggested to have no significant impact on SS-O and SS-O_2 on Gobi dust surface with water concentration of 30 ppm (0.1% RH). This interaction between water molecules and SS-O and SS-O_2 might be promoted with longer interacting time or higher water concentration such as under 20% RH condition.
6. The DRIFT spectra during the interaction of air-generated ozone flow with Gobi dust show major differences with the DRIFT spectra obtained in oxygen-generated ozone flow regarding the wavenumber range from 1100 to 1800 cm^{-1}. The interaction of NO_2 and NO contained in the air-generated ozone flow and Gobi dust results in the DRIFT peaks at 1700 cm^{-1} and 1330 cm^{-1}, which overlap with the DRIFT bands at 1700 cm^{-1} and at 1300 cm^{-1}obtained from ozone-dust interaction. As a result, using oxygen-generated ozone has proven to be an effective approach to avoid the overlapping of NO_2 produced bands with ozone produced bands.
7. DRIFT studies of the adsorbed phase during ozone decomposition on mineral components of Gobi dust as well as Al_2O_3 evidence the formation of surface oxygenated groups on the surface of $Al_2Si_2O_5(OH)_4$ (kaolinite), Al_2O_3, and TiO_2 during ozone decomposition. The similar features of DRIFT bands obtained on $Al_2Si_2O_5(OH)_4$ and Al_2O_3 as on Gobi dust suggest the similar mechanism of ozone decomposition on the surfaces of these materials, highlighting $Al_2Si_2O_5(OH)_4$ and Al_2O_3 as important reference minerals in literature regarding ozone decomposition. No DRIFT band corresponding to surface oxygenated groups has been observed on the surface of $CaCO_3$ and SiO_2 during ozone decomposition.

3 Mechanism for the surface reactions of ozone decomposition on Gobi dust

Based on the investigations of both gas phase and adsorbed phase during ozone decomposition on Gobi dust sample in the present study, a mechanism of surface reactions between surface sites on Gobi dust sample ([SS_{Gobi}]) and ozone molecules is proposed. The idea that the surface sites of Gobi dust participate to the decomposing reaction of ozone molecules, is consistent with the mechanism of ozone decomposition on Al_2O_3 proposed by R. C. Sullivan [6].

It has to be mentioned that the surface sites on the surface of Gobi dust are likely to be not homogeneous considering the complex nature of Gobi dust. However, this mechanism suggests that the surface reactions between all the surface sites on Gobi dust, regardless their nature, with ozone molecules are through the same pathway. As a result, they will be all represented as [SS_{Gobi}].

At room temperature in our study, consistent with the conclusion from K. M. Bulanin et al. [33-36], it has not been observed the molecular adsorption of ozone leading to the formation of SS-O_3 species. However, surface oxide species [SS_{Gobi}]-O and peroxide species [SS_{Gobi}]-O_2 are formed through the interaction with the strong Lewis sites on the surface as suggested by R. C. Sullivan A [6] and

Klimovskii et al. [54] in case of ozone decomposition on Al_2O_3, and by K. M. Bulanin et al. in case of ozone decomposition on TiO_2 [35] and has been also evidenced in the current study.

Ozone molecules decompose on Gobi dust through reactions RIII-1 and RIII-2 by Eley-Rideal mechanism for surface reactions with rate constants k_1 and k_2 respectively, forming surface oxygenated groups $[SS_{Gobi}]$-O and $[SS_{Gobi}]$-O_2:

$$O_3\ (g) + [SS_{Gobi}] \rightarrow [SS_{Gobi}]\text{–}O + O_2\ (g) \text{ with } k_1 \qquad \text{RIII-1}$$

$$[SS_{Gobi}]\text{–}O + O_3\ (g) \rightarrow [SS_{Gobi}]\text{–}O_2 + O_2\ (g) \text{ with } k_2 \qquad \text{RIII-2}$$

The rate of the second reaction RIII-2 depends on the surface concentration of $[SS_{Gobi}]$-O. At low concentration of $[SS_{Gobi}]$-O, the dominant reaction is RIII-1. At high concentration of $[SS_{Gobi}]$-O, RIII-2 starts to be important and lead to the formation of $[SS_{Gobi}]$-O_2. These two reactions can explain what was observed in the initial stage of the experiment of gas phase monitoring. Initially, exposing the pretreated surface to ozone, there are many free $[SS_{Gobi}]$ available to interact with ozone molecules thus leading the initial uptake peak on the gas phase ozone concentration profile as showed in Figure III-1. Then $[SS_{Gobi}]$ are consumed rapidly thus leading to a "passivation" of the surface, which means less available $[SS_{Gobi}]$ to be consumed by ozone. This is why the recovering of the gas phase ozone concentrations was observed. As a consequence, the concentration of $[SS_{Gobi}]$ decreases while those of $[SS_{Gobi}]$-O and $[SS_{Gobi}]$-O_2 increase.

At the same time, $[SS_{Gobi}]$-O and $[SS_{Gobi}]$-O_2 can self-decompose. Migrations of the atomic oxygen atoms of $[SS_{Gobi}]$-O are possible at room temperature [35] which leads to the recombination of two atoms and the regeneration of a new $[SS_{Gobi}]$ through RIII-3:

$$2[SS_{Gobi}]\text{–}O \rightarrow [SS_{Gobi}]\text{–}O_2 + [SS_{Gobi}] \text{ with } k_3 \qquad \text{RIII-3}$$

$[SS_{Gobi}]$-O_2 can decompose gradually that also regenerates the free surface sites, i.e. $[SS_{Gobi}]$ through the following reaction RIII-4:

$$[SS_{Gobi}]\text{–}O_2 \rightarrow [SS_{Gobi}] + O_2(g) \text{ with } k_4 \qquad \text{RIII-4}$$

Literature studies suggest that the dominant pathway is reaction RIII-4 [55]. However, RIII-3 could not be excluded.

As a mixture of minerals, Gobi dust exhibits the same behavior regarding ozone decomposition when compared with some synthetic single metal oxides reported in literature and referred above such as Al_2O_3, TiO_2, regardless of the complexity of the Gobi dust surface. The mechanism discussed herein is

in great agreement with the mechanism proposed by other authors [44, 55, 56], and similar mechanism approach could be applied on different mineral oxides with different rate constants k.

The surface site regeneration process RIII-3 and RIII-4 will gradually compete with ozone decomposition process RIII-1 and RIII-2 as the number of [SS_{Gobi}] decreases while that of [SS_{Gobi}]-O_2 increases. Finally, an equilibrium will reach among the 4 reactions, under which condition the steady-state uptake regime are observed, as showed in the gas phase ozone concentration profiles in Figure III-1 and Figure III-7.

When Gobi dust sample is exposed to high ozone concentrations, all the 4 reactions are accelerated regarding the reaction rate, which is supported by the fact that ozone uptake rates during steady-state increase with higher gas-phase ozone concentrations. Also, it has been observed in this study that the steady-state uptake stage comes faster when Gobi dust of a same mass is exposed to ozone flow of a higher concentration. In the cyclic experiments, flushing with air under room temperature does not restore the initial surface properties of the surface indicating that this process poorly impacts the [SS_{Gobi}]-O recombination or the [SS_{Gobi}]-O_2 decomposition. As a consequence, the number of available [SS_{Gobi}] remains almost constant and no significant changes are noticed after re-exposition of the surface (Figure III-7 cycle 2). However, the initial surface properties of the surface is recovered under thermal pretreatment of the surface in the absence of O_3 (cycle 3 of Figure III-7), pointing that at temperatures as high as 150˚C, a sufficient amount of energy is provided to the surface that favors the recombination of [SS_{Gobi}]-O and the decomposition of [SS_{Gobi}]-O_2 through reactions RIII-3 and RIII-4 leading to surface regeneration.

As for water molecules, they are involved into surface reactions with the same surface reactive sites as discussed previously through the follow reaction RIII-5:

$$[SS_{Gobi}] + H_2O(g) \rightarrow [SS_{Gobi}]\text{–}H_2O \text{ with k5} \qquad \text{RIII-5}$$

The interactions of water molecules are competitive with ozone decomposition in RIII-1 and RIII-2 for the same surface sites. This conclusion agrees with the negative effects on ozone decomposition with the presence of humidity. Moreover, the competition between ozone and water molecules for the same surface sites of Gobi dust is supported by the observation that isolated surface OH groups are removed during ozone decomposition according to the DRIFT spectra, as showed in Figure III-9.

Interestingly, since water molecules interact with the same surface site where the surface oxygenated species namely $[SS_{Gobi}]\text{–}O_2$ and $[SS_{Gobi}]\text{–}O$ terminate, the interactions of water molecules with surface sites of Gobi dust might also lead to the decomposition of $[SS_{Gobi}]\text{–}O_2$ and $[SS_{Gobi}]\text{–}O$ according to reaction RIII-5. It tends to promote the surface regeneration reactions RIII-3 and RIII-4. However, instead of free surface sites [SS_{Gobi}], the interactions of water molecules generate adsorbed water, i.e.,

$[SS_{Gobi}]$–H_2O which blocks the surface sites where ozone molecules decompose. It explains the observation in *section 1.7.2* that flushing the Gobi dust sample with humid air flow has a very limited regeneration effect towards ozone decomposition.

4 Conclusions and implementations

In this section, the surface properties of natural Gobi dust towards ozone is investigated in both gas phase and adsorbed phase. Gobi dust is evidenced experimentally to exhibit catalytic property for ozone decomposition over a large range of ozone concentration, i.e. 20 ppb to 10 ppm. The uptake coefficients and steady-state decomposition rates have been determined. Surface oxygenated groups, i.e. SS-O and SS-O_2, have been observed being formed during ozone-dust interaction by DRIFT spectra. A mechanism of ozone decomposition on Gobi dust has been proposed under dry condition, which describes the both processes of ozone composition and surface regeneration. It is summarized as follows:

O_3 decomposition		Surface regeneration
$O_3(g) + SS \rightarrow SS\text{-}O + O_2(g)$	⇄	$SS\text{-}O_2 \rightarrow SS + O_2(g)$
$SS\text{-}O + O_3(g) \rightarrow SS\text{-}O_2 + O_2(g)$		$2SS\text{-}O \rightarrow 2SS + O_2(g)$

Details are summarized in *1.8 Conclusions of gas phase investigation* and *1.8 Conclusions of gas phase investigation.*

Moreover, in the present study, the synergetic effect found in Gobi dust regarding ozone decomposition and the fact that Gobi dust exhibits better catalytic ozone-decomposing properties over Al_2O_3, SiO_2, $CaCO_3$, suggests the potential of using this geomaterial in catalyst industry.

For catalysts used in VOC removal by non-thermal plasma assisted oxidation, Al_2O_3 is one of the most commonly used porous catalysts. There are two properties especially important among the others when choosing the catalyst for NTP-catalysis: the ozone-decomposing property and the adsorption capacity of VOC, as mentioned in *section 1.5.* Comparing Gobi dust with Al_2O_3 in ozone decomposition, the steady-state uptake coefficient Gobi dust of 100 ppb ozone under dry condition is 2.28×10^{-8}, which is 6 times the steady-state uptake of Al_2O_3 with the same ozone concentration, i.e. 3.79×10^{-9}. As for the capacity of adsorption for VOC molecules, it's generally related to specific surface area. The BET surface of Al_2O_3 used in industry is generally in the range of 60 – 80 $m^2\ g^{-1}$ [57]. With finishing and specific processing, the BET surface area of Al_2O_3 can be in the range of 180 – 200 $m^2\ g^{-1}$ which is more dedicated for laboratory research. For Gobi dust, the BET surface area is around 10 $m^2\ g^{-1}$, significantly lower than Al_2O_3. However, BET surface area is not the only one parameter which determined the adsorption property. Further investigation for adsorption capacity of Gobi dust is needed. It will be investigated in the next chapter using acetic acid as model VOC.

Also, the surface properties of Gobi dust towards ozone decomposition can be restored by thermal treatment which makes Gobi dust a catalyst recyclable.

Besides, this geomaterial has one exclusive advantage over other synthetic catalysts: Gobi dust does not need to be synthesized and purged. Actually, for the production of Al_2O_3 with Bayer process as the most important method, the production of one ton of primary Al_2O_3 will cost energy around 9.6 GJ from pure gibbsite as raw material, and this number will be doubled if mixed gibbsite and boehmite are used as raw material [58]. Moreover, it will release emissions from smelter containing air pollutants and green gases such as SO_2, NO_x, CO_2, CO, HF, dusts, fluorides and etc [59, 60]. As a result, using natural Gobi dust as catalyst to replace traditional catalyst such as Al_2O_3 can save energy and reduce the emissions of air pollutants.

References

[1] J.M. Thomas, W.J. Thomas, Principles and practice of heterogeneous catalysis, John Wiley & Sons2014.

[2] M. Boudart, Turnover rates in heterogeneous catalysis, Chemical reviews, 95 (1995) 661-666.

[3] A. Michel, C. Usher, V. Grassian, Reactive uptake of ozone on mineral oxides and mineral dusts, Atmospheric Environment, 37 (2003) 3201-3211.

[4] C. Usher, A. Michel, D. Stec, V. Grassian, Laboratory studies of ozone uptake on processed mineral dust, Atmospheric Environment, 37 (2003) 5337-5347.

[5] B. Dhandapani, S.T. Oyama, Gas phase ozone decomposition catalysts, Applied Catalysis B: Environmental, 11 (1997) 129-166.

[6] R. Sullivan, T. Thornberry, J. Abbatt, Ozone decomposition kinetics on alumina: effects of ozone partial pressure, relative humidity and repeated oxidation cycles, Atmospheric Chemistry and Physics, 4 (2004) 1301-1310.

[7] S. Stephens, M.J. Rossi, D.M. Golden, The heterogeneous reaction of ozone on carbonaceous surfaces, International Journal of Chemical Kinetics, 18 (1986) 1133-1149.

[8] M. Tang, D.J. Cziczo, V.H. Grassian, Interactions of water with mineral dust aerosol: water adsorption, hygroscopicity, cloud condensation, and ice nucleation, Chemical reviews, 116 (2016) 4205-4259.

[9] Y. Bedjanian, M. Romanias, A.E. Zein, Uptake of HO_2 radicals on arizona test dust, Atmospheric Chemistry and Physics, 13 (2013) 6461-6471.

[10] M.N. Romanias, M.N. Zeineddine, V. Gaudion, X. Lun, F. Thevenet, V. Riffault, Heterogeneous Interaction of Isopropanol with Natural Gobi Dust, Environmental science & technology, 50 (2016) 11714-11722.

[11] A. El Zein, M.N. Romanias, Y. Bedjanian, Kinetics and products of heterogeneous reaction of HONO with Fe2O3 and Arizona Test Dust, Environmental science & technology, 47 (2013) 6325-6331.

[12] S. Ibrahim, M.N. Romanias, L.Y. Alleman, M.N. Zeineddine, G.K. Angeli, P.N. Trikalitis, F. Thevenet, Water Interaction with Mineral Dust Aerosol: Particle Size and Hygroscopic Properties of Dust, ACS Earth and Space Chemistry, 2 (2018) 376-386.

[13] N. Joshi, M.N. Romanias, V. Riffault, F. Thevenet, Investigating water adsorption onto natural mineral dust particles: Linking DRIFTS experiments and BET theory, Aeolian Research, 27 (2017) 35-45.

[14] M.N. Zeineddine, M.N. Romanias, V. Gaudion, V.r. Riffault, F.d.r. Thévenet, Heterogeneous Interaction of Isoprene with Natural Gobi Dust, ACS Earth and Space Chemistry, 1 (2017) 236-243.

[15] Ground-level ozone (O3), in: D.o.t.E.a. Energy (Ed.), Australian Government, 2005.

[16] J. Crowley, M. Ammann, R. Cox, R. Hynes, M.E. Jenkin, A. Mellouki, M. Rossi, J. Troe, T. Wallington, Evaluated kinetic and photochemical data for atmospheric chemistry: Volume V–heterogeneous reactions on solid substrates, Atmospheric Chemistry and Physics, 10 (2010) 9059-9223.

[17] J. Lasne, M.N. Romanias, F.J.A.E.a.S.C. Thevenet, Ozone Uptake by Clay Dusts Under Environmental Conditions, (2018).

[18] A. Alebić - Juretić, T. Cvitaš, L. Klasinc, Ozone destruction on powders, Berichte der Bunsengesellschaft für physikalische Chemie, 96 (1992) 493-495.

[19] M. Nicolas, M. Ndour, O. Ka, B. D'Anna, C. George, Photochemistry of atmospheric dust: ozone decomposition on illuminated titanium dioxide, Environmental science & technology, 43 (2009) 7437-7442.

[20] A. Goudie, N. Middleton, Saharan dust storms: nature and consequences, Earth-Science Reviews, 56 (2001) 179-204.

[21] M.N. Zeineddine, M.N. Romanias, V. Riffault, F. Thévenet, Heterogeneous Interaction of Various Natural Dust Samples with Isopropanol as a Probe VOC, The Journal of Physical Chemistry A, (2018).

[22] M.N. Romanias, H. Ourrad, F. Thevenet, V. Riffault, Investigating the Heterogeneous Interaction of VOCs with Natural Atmospheric Particles: Adsorption of Limonene and Toluene on Saharan Mineral Dusts, Journal of Physical Chemistry A, 120 (2016) 1197-1212.

[23] A.E. Zein, M.N. Romanias, Y. Bedjanian, Heterogeneous interaction of H_2O_2 with Arizona test dust, The Journal of Physical Chemistry A, 118 (2013) 441-448.

[24] S. Futamura, A. Gurusamy, Synergy of nonthermal plasma and catalysts in the decomposition of fluorinated hydrocarbons, Journal of Electrostatics, 63 (2005) 949-954.

[25] S. Sauce, A. Vega-Gonzalez, Z.X. Jia, S. Touchard, K. Hassouni, A. Kanaev, X. Duten, New insights in understanding plasma-catalysis reaction pathways: study of the catalytic ozonation of an acetaldehyde saturated $Ag/TiO_2/SiO_2$ catalyst, European Physical Journal-Applied Physics, 71 (2015).

[26] T. Zhang, Q.R. Li, Y. Liu, Y.L. Duan, W.Y. Zhang, Equilibrium and kinetics studies of fluoride ions adsorption on CeO_2/Al_2O_3 composites pretreated with non-thermal plasma, Chemical Engineering Journal, 168 (2011) 665-671.

[27] X.B. Zhu, X. Tu, D.H. Mei, C.H. Zheng, J.S. Zhou, X. Gao, Z.Y. Luo, M.J. Ni, K.F. Cen, Investigation of hybrid plasma-catalytic removal of acetone over CuO/gamma-Al_2O_3 catalysts using response surface method, Chemosphere, 155 (2016) 9-17.

[28] C. Norsic, J.M. Tatibouet, C. Batiot-Dupeyrat, E. Fourre, Non thermal plasma assisted catalysis of methanol oxidation on Mn, Ce and Cu oxides supported on gamma-Al_2O_3, Chemical Engineering Journal, 304 (2016) 563-572.

[29] V. Demidiouk, S.I. Moon, J.O. Chae, D.Y. Lee, Application of a plasma-catalytic system for decomposition of volatile organic compounds, Journal of the Korean Physical Society, 42 (2003) S966-S970.

[30] X.L. Zhang, A.M. Zhu, X.H. Li, W.M. Gong, Oxidative dehydrogenation of ethane with CO_2 over catalyst under pulse corona plasma, Catalysis Today, 89 (2004) 97-102.

[31] U. Roland, F. Holzer, F.-D. Kopinke, Combination of non-thermal plasma and heterogeneous catalysis for oxidation of volatile organic compounds: Part 2. Ozone decomposition and deactivation of γ-Al_2O_3, Applied catalysis B: environmental, 58 (2005) 217-226.

[32] T. Zhu, R. Chen, N. Xia, X.Y. Li, X.X. He, W.J. Zhao, T. Carr, Volatile organic compounds emission control in industrial pollution source using plasma technology coupled with F-TiO_2/gamma-Al2O3, Environmental Technology, 36 (2015) 1405-1413.

[33] K. Bulanin, J. Lavalley, A. Tsyganenko, IR spectra of adsorbed ozone, Colloids and Surfaces A: Physicochemical and Engineering Aspects, 101 (1995) 153-158.

[34] K. Bulanin, J. Lavalley, A. Tsyganenko, Infrared study of ozone adsorption on CaO, The Journal of Physical Chemistry B, 101 (1997) 2917-2922.

[35] K. Bulanin, J. Lavalley, A. Tsyganenko, Infrared study of ozone adsorption on TiO_2 (anatase), The Journal of Physical Chemistry, 99 (1995) 10294-10298.

[36] K. Bulanin, A. Alexeev, D. Bystrov, J. Lavalley, A. Tsyganenko, IR study of ozone adsorption On SiO2, The Journal of Physical Chemistry, 98 (1994) 5100-5103.

[37] I.E. Wachs, Raman and IR studies of surface metal oxide species on oxide supports: supported metal oxide catalysts, Catalysis Today, 27 (1996) 437-455.

[38] P.A. Connor, K.D. Dobson, A.J. McQuillan, Infrared spectroscopy of the TiO_2/aqueous solution interface, Langmuir, 15 (1999) 2402-2408.

[39] A. Goodman, E. Bernard, V. Grassian, Spectroscopic study of nitric acid and water adsorption on oxide particles: Enhanced nitric acid uptake kinetics in the presence of adsorbed water, The Journal of Physical Chemistry A, 105 (2001) 6443-6457.

[40] W. Li, G. Gibbs, S.T. Oyama, Mechanism of ozone decomposition on a manganese oxide catalyst. 1. In situ Raman spectroscopy and ab initio molecular orbital calculations, Journal of the American Chemical Society, 120 (1998) 9041-9046.

[41] J. Jia, P. Zhang, L. Chen, Catalytic decomposition of gaseous ozone over manganese dioxides with different crystal structures, Applied Catalysis B: Environmental, 189 (2016) 210-218.

[42] M.L. Hair, Hydroxyl groups on silica surface, Journal of Non-Crystalline Solids, 19 (1975) 299-309.

[43] Q. Ma, H. He, Y. Liu, In situ DRIFTS study of hygroscopic behavior of mineral aerosol, Journal of Environmental Sciences, 22 (2010) 555-560.

[44] J.M. Roscoe, J.P. Abbatt, Diffuse reflectance FTIR study of the interaction of alumina surfaces with ozone and water vapor, The Journal of Physical Chemistry A, 109 (2005) 9028-9034.

[45] L. Sivachandiran, F. Thevenet, P. Gravejat, A. Rousseau, Investigation of NO and NO_2 adsorption mechanisms on TiO_2 at room temperature, Applied Catalysis B-Environmental, 142 (2013) 196-204.

[46] F. Thevenet, L. Olivier, F. Batault, L. Sivachandiran, N. Locoge, Acetaldehyde adsorption on TiO_2: Influence of NO_2 preliminary adsorption, Chemical Engineering Journal, 281 (2015) 126-133.

[47] L. Sivachandiran, F. Thevenet, A. Rousseau, D. Bianchi, NO_2 adsorption mechanism on TiO_2: An in-situ transmission infrared spectroscopy study, Applied Catalysis B-Environmental, 198 (2016) 411-419.

[48] M.M. Angelini, R.J. Garrard, S.J. Rosen, R.Z. Hinrichs, Heterogeneous reactions of gaseous HNO_3 and NO_2 on the clay minerals kaolinite and pyrophyllite, The Journal of Physical Chemistry A, 111 (2007) 3326-3335.

[49] G. Underwood, T. Miller, V. Grassian, Transmission FT-IR and Knudsen cell study of the heterogeneous reactivity of gaseous nitrogen dioxide on mineral oxide particles, The Journal of Physical Chemistry A, 103 (1999) 6184-6190.

[50] C. Börensen, U. Kirchner, V. Scheer, R. Vogt, R. Zellner, Mechanism and kinetics of the reactions of NO_2 or HNO_3 with alumina as a mineral dust model compound, The Journal of Physical Chemistry A, 104 (2000) 5036-5045.

[51] A. Goodman, T. Miller, V. Grassian, Heterogeneous reactions of NO_2 on NaCl and Al_2O_3 particles, Journal of Vacuum Science & Technology A: Vacuum, Surfaces, and Films, 16 (1998) 2585-2590.

[52] H.S. Judeikis, A.G. Wren, Laboratory measurements of NO and NO_2 depositions onto soil and cement surfaces, Atmospheric Environment (1967), 12 (1978) 2315-2319.

[53] L. Li, Z. Chen, Y. Zhang, T. Zhu, J. Li, J. Ding, Kinetics and mechanism of heterogeneous oxidation of sulfur dioxide by ozone on surface of calcium carbonate, Atmospheric Chemistry and Physics, 6 (2006) 2453-2464.

[54] A. Klimovskii, A. Bavin, V. Tkalich, A. Lisachenko, Interaction of ozone with γ-Al_2O_3 surface, Reaction Kinetics and Catalysis Letters, 23 (1983) 95-98.

[55] W. Li, S.T. Oyama, Mechanism of ozone decomposition on a manganese oxide catalyst. 2. Steady-state and transient kinetic studies, Journal of the American Chemical Society, 120 (1998) 9047-9052.

[56] S.T. Oyama, Chemical and catalytic properties of ozone, Catalysis Reviews, 42 (2000) 279-322.

[57] J. Metson, Production of alumina, Fundamentals of Aluminium Metallurgy, Elsevier2011, pp. 23-48.

[58] L. Liu, L. Aye, Z. Lu, P. Zhang, Analysis of the overall energy intensity of alumina refinery process using unit process energy intensity and product ratio method, Energy, 31 (2006) 1167-1176.

[59] A. Gillespie, M. Hyland, J. Metson, Irreversible HF adsorption in the dry-scrubbing process, JOM, 51 (1999) 30-32.

[60] S.J. Hay, J.B. Metson, M.M. Hyland, Sulfur speciation in aluminum smelting anodes, Industrial & engineering chemistry research, 43 (2004) 1690-1700.

Chapter IV. Uptake and ozonation of acetic acid on natural Gobi dust

Table of contents

Table of Figures

The uptake and the ozonation of acetic acid (AcA) on natural Gobi dust are investigated in this chapter.

Regarding AcA uptake on Gobi dust, in the first section using the gas phase approach, the adsorption isotherms of AcA on Gobi dust under dry and 20% RH conditions at room temperature, the desorption profiles under dry air flushing, humid air flushing, as well as thermal treatment are discussed. The interactions of Gobi dust towards AcA are characterized by parameters such as the surface coverage and the adsorption capacity, and also compared with the main mineral components of Gobi dust. In the second section using adsorbed phase approach, the reactivity of Gobi dust towards AcA is characterized by studying the DRIFT spectra of the adsorbed phase during AcA interaction with Gobi dust under dry and 20% RH condition. The DRIFT spectra of the adsorbed phase of the main mineral components of Gobi dust during the interaction with AcA are also studied and compared with those of Gobi dust. Combining the results of gas phase and adsorbed phase approach, a mechanism explaining the interactions between Gobi dust and AcA molecules is proposed. At the end of this chapter, the results related to the gas phase investigation of the ozonation of AcA on Gobi dust is discussed.

1 AcA uptake on Gobi dust: gas phase approach

1.1 First insight to acetic acid concentration profile

Based on the gas-phase investigation protocol described in *section 2.1.4* of chapter 2 and following:

- STEP 0 / Pretreatment of the dust sample: heating at 150˚C under dry zero air flow then cooling down to room temperature.
- STEP 1 / Initial AcA concentration measurement through bypass line.
- STEP 2 / Dust surface exposure to AcA.
- STEP 3 / Switch AcA flow to bypass line to verify initial AcA concentration.
- STEP 4 / Flushing the dust sample with dry zero air

Typical AcA concentration profiles along the uptake and flushing processes of AcA on Gobi dust samples are obtained. Figure IV-1 shows an AcA concentration profile with initial inlet AcA concentration of 66 ± 1 ppm, the mass of the Gobi dust sample is 51 ± 1 mg and the experiment is performed under dry condition.

In Figure IV-1, the gas phase AcA concentration profile is divided in two parts: AcA uptake process which is indicated by STEP 1 to 3, and desorption process by flushing the surface indicated by STEP 4.

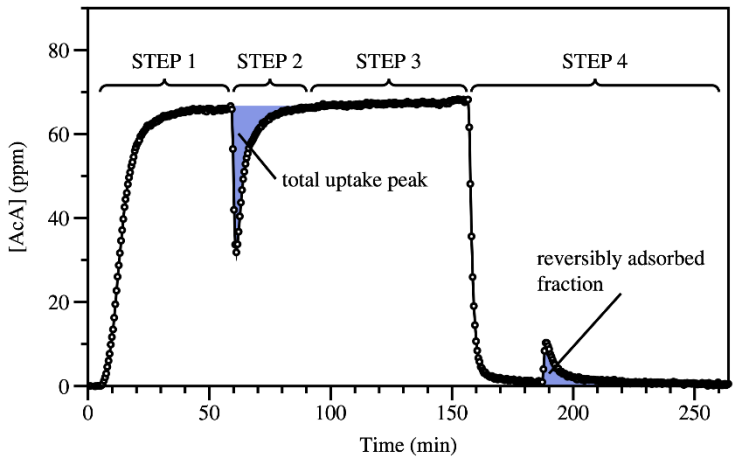

Figure IV-1 AcA concentration profile of 66 ± 1 ppm AcA taken up on 51 ± 1 mg Gobi dust (dry air, T = 296 K, P = 1013 mbar). STEP 1 to 4 correspond to the experimental protocol steps. The integrated areas represent the total amount of the taken up AcA and the reversibly adsorbed fraction of AcA.

During AcA adsorption: a significant and transient initial AcA uptake peak at the beginning of STEP 2 is observed, then the gas phase AcA concentration signal increases up to its inlet value as measured in STEP 1. The observation of the restoration of AcA gas phase concentration to its inlet value during the AcA adsorption suggests a finite capacity of Gobi dust sample regarding AcA adsorption for a given AcA concentration. The equilibrium between gas phase AcA and the surface is achieved at 100 min, as Figure IV-1 indicates.

During flushing process, when dry air flow is directed into the U-shape reactor to flush the Gobi dust sample after AcA adsorption, a peak of AcA concentration is observed in Figure IV-1. Then the AcA concentration decreases and returns to 0. The fact that AcA molecules are detected again in gas phase during flushing process suggests that a fraction of taken-up AcA is removed from the surface by simple zero air flushing under room temperature, which refers to the reversibly adsorbed fraction of AcA by Gobi dust under this condition. This observation is an evidence that a part of AcA molecules is physically and reversibly adsorbed on the surface of Gobi dust, which is in agreement with the observation by S. Carlos-Cuellar et al. [1] and S. R. Tong et al. [2]. As a consequence, a fraction of taken-up AcA molecules is physisorbed on the surface of the natural dust sample.

The total amount of AcA molecules taken up per specific surface area unit of Gobi dust, N_{total}, describes the surface concentration of AcA taken up on Gobi dust. It is calculated as 2.44×10^{14} molecules cm^{-2} based on the temporal AcA concentration profile in Figure IV-1 and Equations (II-9) - (II-11), and using BET surface area of Gobi dust. By the same method, the amount of the reversibly adsorbed AcA per specific surface area unit of Gobi dust, N_{re} is calculated to be 6.5×10^{13} molecules cm^{-2}. Results indicate that the fraction of reversibly adsorbed AcA in the total amount of taken-up AcA is 27 % in this case. Their difference is the irreversibly taken-up fraction of AcA, N_{ir}, estimated to be

1.79×10^{14} molecules cm^{-2} that corresponds to nearly 73% of the total uptake of the AcA. As a result, the irreversible uptake capacity of Gobi dust toward 66 ppm of AcA, is determined as 29.8 μmol g^{-1}.

In the following investigation using gas phase approach, AcA uptake process is characterized by the total uptake, the reversibly adsorbed fraction and the irreversible uptake. As a result, N_{total}, N_{re}, N_{ir} by AcA, as well as the irreversible uptake capacity of Gobi dust towards AcA are used for characterization or comparison purposes.

1.2 Uptake of AcA on Gobi dust under dry condition: gas phase investigation

1.2.1 Investigation of AcA adsorption isotherm on Gobi dust

The isotherms of AcA uptake on Gobi dust samples under dry condition are determined at atmospheric pressure and room temperature with AcA concentrations ranging from 6.2×10^{12} to 2.7×10^{15} molecules cm^{-3}, corresponding to 0.25 to 106 ppm. The results are displayed in Figure IV-2 where the isotherms of the total uptake, irreversibly taken up fraction and reversibly adsorbed fraction of AcA on Gobi dust are determined. The errors are calculated from the uncertainties of the individual variables needed for calculation.

Based on the adsorption isotherms in Figure IV-2, the N_{total}, N_{re} and N_{ir} increase with the increase of AcA concentration, approaching a saturation value when AcA concentration is beyond c.a. 10^{15} molecules cm^{-3}. Similar adsorption isotherms of VOCs such as isopropanol and isoprene on minerals have been obtained by M. Zeineddine et al. [3, 4] and M. Romanias et al. [5]. According to Figure IV-2, the value of N_{total} approaches towards the range of $(2.7 \pm 0.3) \times 10^{14}$ molecules cm^{-2}, while N_{ir} approaches $(1.9 \pm 0.3) \times 10^{14}$ molecules cm^{-2} and N_{re} approaches $(8 \pm 0.8) \times 10^{13}$ molecules cm^{-2}.

Comparing N_{ir} with N_{total}, it suggests that most of the AcA uptake on Gobi dust sample, i.e., c.a. 70 % to 90 % of the total adsorption at room temperature, is an irreversible uptake on the surface. The same observations have been evidenced during the investigation of AcA on metal oxides such as Al_2O_3, TiO_2, Fe_2O_3 by P. Li et al. [6], S. Carlos-Cuellar et al. [1] and S. R. Tong et al. [2]. It has to be mentioned that it is not always the case for VOCs uptake on SiO_2 [1, 6], where most of the total adsorption is reversible. In our study, the values of N_{ir} are 7 to 10 times the values of N_{re} when AcA concentration is below 3 ppm. With the increase of the AcA concentration, the differences between N_{re} and N_{ir} decrease, and finally N_{ir}/N_{re} reaches a value around 2 when AcA concentration approaches beyond c.a. 10^{15} molecules cm^{-3}.

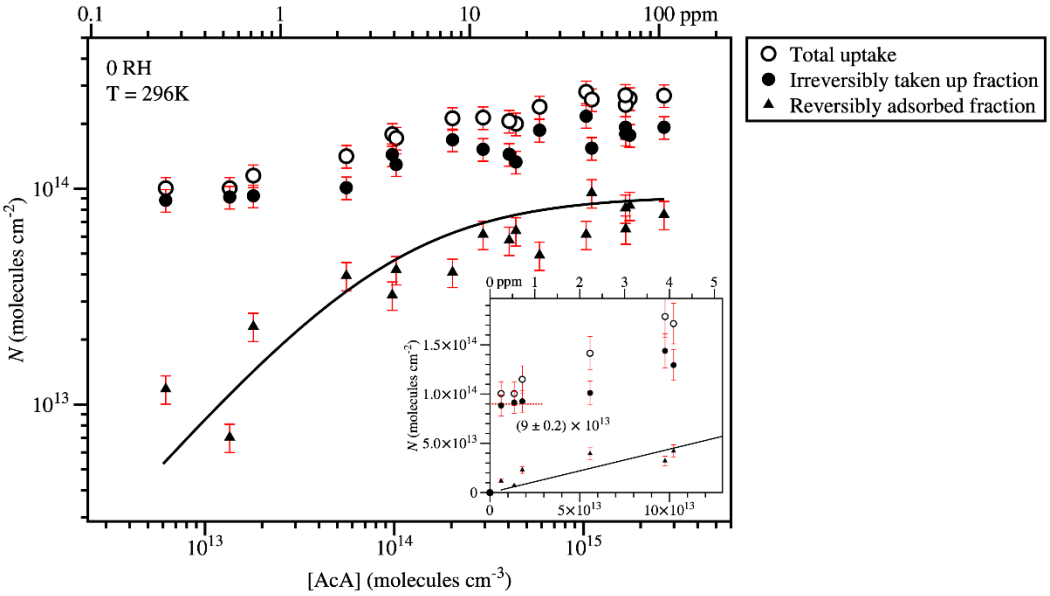

Figure IV-2 Isotherms of total uptake, irreversibly taken up fraction and reversibly adsorbed fraction of AcA on Gobi dust sample determined at room temperature (296 K) and dry condition. The solid line is the fit of the data of the adsorption isotherm of the reversibly adsorbed fraction, using Langmuir isotherm model. The insert figure displays the same isotherms in the range of [AcA] below 5 ppm with leaner type of both x-axis and y-axis for clarity where the straight line is only for guiding purpose and has no physical meaning. The errors are calculated from the error in the individual variables needed for calculation.

For clarity, the magnification of AcA adsorption isotherms focusing on the low AcA concentration below 5 ppm is shown as an insert in Figure IV-2. Along the adsorption isotherms of AcA within the investigated AcA concentration range, N_{ir} displays a stable value within the first data points, i.e. $(9 \pm 0.2) \times 10^{13}$ molecules cm^{-2} when AcA concentration is below 1 ppm as shown. Limited to the minimum AcA concentration applied for the experiments, i.e., 1.18×10^{13} molecules cm^{-3} (0.25 ppm), it is still not low enough to observe the gradual increase of the irreversibly taken up fraction of AcA as a function of AcA concentration. This observation suggests that the irreversibly uptake process of AcA occurs very fast and reaches a saturation level even at low AcA concentration range, i.e., below 1 ppm, which is the important characteristic of a chemisorption process [7, 8]. However, N_{ir} also increases when AcA concentration is beyond 1 ppm. This behavior of the N_{ir} as a function of AcA concentration might suggest the coexistence of at least two irreversible uptake processes:

(i) Chemisorption process which occurs fast and reaches saturation at very low concentration, which is independent on the investigated AcA concentrations.

(ii) An AcA concentration-dependent uptake process which are suggested to correspond to a physisorptive process but involving intense interactions [9, 10]. This aspect will be further investigated in this chapter.

Therefore, the irreversibly taken up fraction of AcA on Gobi dust seems to include chemisorbed AcA molecules and strongly physisorbed AcA molecules on the surface.

Regarding the N_{re} fraction of AcA a different behavior of is observed in the insert figure in Figure IV-2. In particular, N_{re} exhibits a linear increase as a function of AcA concentration which is characteristic of a physisorption process in accordance with Langmuir model. Based on Equation (I-10), the fraction of the surface coverage θ due to reversibly adsorbed AcA can be expressed by equation (IV-1):

$$\theta = \frac{N_{re}}{N_{re,Max}} = \frac{K_{Lang} \times [AcA]}{1 + K_{Lang} \times [AcA]} \quad \text{(IV-1)}$$

where $N_{re,Max}$ is the saturation surface coverage (molecules cm^{-2}) for reversibly adsorbed AcA, and K_{Lang} (cm^3 molecule^{-1}) is the Langmuir equilibrium constant, which describes the equilibrium between the adsorption and desorption processes within the gas and adsorbed phase. Equation (IV-1) can be further rearranged to obtain equation (IV-2):

$$\frac{[AcA]}{N_{re}} = \frac{1}{K_{Lang} \times N_{re,Max}} + \frac{1}{N_{re,Max}} \times [AcA] \quad \text{(IV-2)}$$

From equation (IV-2), the value of $N_{re,Max}$ and K_{Lang} could be determined if we linearly fit $[AcA]/N_{re}$ versus $[AcA]$ based on the data experimental obtained. The partition coefficient K_{Lin} (cm), defined as $K_{Lin} = K_{Lang} \times N_{re,Max}$, is more commonly used when it comes to the comparison among different materials, since the value of monolayer coverage varies among samples thus a direct comparison of K_{Lang} is not representative [11]. Consequently, $N_{re,Max}$ K_{Lang} and K_{Lin} are determined to be $(8.11 \pm 0.8) \times 10^{13}$ molecules cm^{-2} $(6.22 \pm 1.2) \times 10^{-15}$ cm^3 molecule^{-1}, and 0.5 ± 0.1 cm. the overall uncertainty for the determination of $N_{re,max}$, K_{Lang}, and K_{Lin} is at the range of 15 % to 25%. The fit of the adsorption isotherm for reversibly adsorbed AcA using Langmuir model is indicated by the solid line in Figure IV-2.

Comparing with literature, the value of N_{total} is retrieved as $(1.8 \pm 0.3) \times 10^{14}$ molecules cm^{-2} for 10 ppm of AcA uptake on Gobi dust under dry condition from the study by M. Zeineddine [9], which is consistence with the value obtained from the current study determined as $(2.1 \pm 0.2) \times 10^{14}$ molecules cm^{-2} with the same condition,.

Besides AcA, the value of N_{total} of other VOCs on Gobi dust from literature are also compared with the values obtained in this study on Gobi dust at room temperature (296K) and under dry condition in Table IV-1.

Table IV-1 Comparison of N_{total} of AcA, isopropanol and isoprene on Gobi dust sample at room temperature (296K) and under dry condition.

VOC	VOC concentration range (molecules cm^{-3})	Maximum N_{total} (molecules cm^{-2})
AcA	$(0.62 - 270) \times 10^{13}$	$(2.7 \pm 0.3) \times 10^{14}$
AcA [9]	25×10^{13}	$(1.8 \pm 0.3) \times 10^{14}$
Isopropanol [5]	$(1 - 194) \times 10^{13}$	$(1.8 \pm 0.2) \times 10^{14}$
Isoprene [4]	$(0.32 - 615) \times 10^{13}$	$(2.0 \pm 0.4) \times 10^{13}$

Based on Table IV-1, it is evidenced that AcA exhibits the highest value of N_{total} compared with isopropanol and isoprene. According to the recent study of M. Zeineddine [9] the presence of the carboxylic functional group in AcA favors its partitioning to the adsorbed phase compared with isoprene and isopropanol. The latter observation is also in accordance with the study of S. Carlos-Cuellar et al. [1] who investigated the uptake of acetic acid, formaldehyde, and methanol on mineral oxides surfaces, i.e. SiO_2, α-Al_2O_3, and α-Fe_2O_3.

1.2.2 Conclusions and remarks from AcA adsorption isotherm on Gobi dust

The AcA uptake on Gobi dust under dry condition is investigated atmospheric pressure and room temperature within AcA concentration ranging from 6.2×10^{12} to 2.7×10^{15} molecules cm^{-3} (0.25 – 106 ppm). AcA adsorption isotherms of total uptake, reversibly adsorbed fraction and irreversibly taken up fraction of AcA are obtained and discussed. Observations and conclusions are summarized as followed:

- The amounts of total uptake, reversibly adsorbed fraction and irreversibly taken up fraction of AcA increase with AcA concentration and approach to a plateau at high AcA concentrations. The fraction of AcA adsorbed irreversibly on Gobi dust is more significant than the reversible fraction within the entire AcA range studied. The values of N_{re}/N_{total} are determined to be in the range of 7 % – 35 %. The reversibly adsorbed fractions and the irreversibly taken up fractions determined under dry condition and room temperature (296 K) at ca. 0.5 ppm, 10 ppm, 100 ppm which represents the low, middle and high AcA concentration range are presented in Figure IV-3.

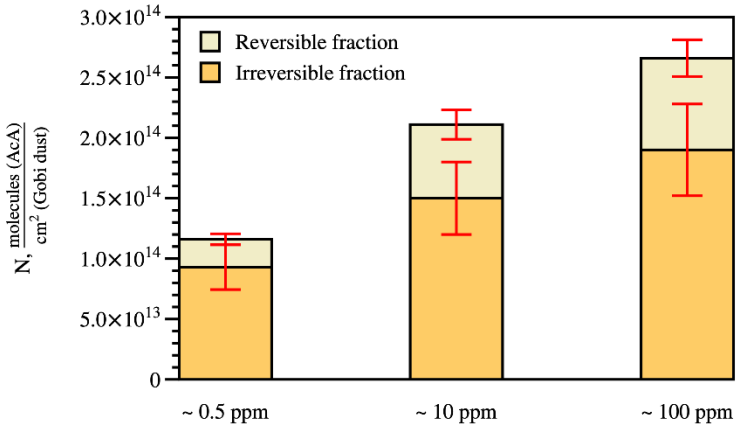

Figure IV-3 Reversibly adsorbed fractions and irreversibly taken up fractions of AcA on Gobi dust determined under dry condition and room temperature (296 K) at ca. 0.5 ppm, 10 ppm, 100 ppm which represents the low, middle and high AcA concentration range investigated. The errors are calculated from the error in the individual variables needed for calculation.

- The irreversibly taken up fraction of AcA on Gobi dust is suggested including chemisorbed AcA fraction and physisorbed AcA fraction, which is distinguished from the reversibly adsorbed AcA fraction where only physisorption process is involved. It further suggests the coexistence of at least two different sorption sites on the surface of Gobi dust for the uptake of AcA molecules.

1.3 Influence of water on AcA adsorption isotherms on Gobi dust: gas phase investigation

To address the influence of water molecules on AcA uptake on Gobi dust, experiments investigating AcA uptake on Gobi dust under 20% RH condition have been conducted. A typical experimental profile is illustrated in Figure IV-4 where the inlet AcA concentration is 52.8 ± 1 ppm and the mass of Gobi dust sample is 100 ± 1 mg.

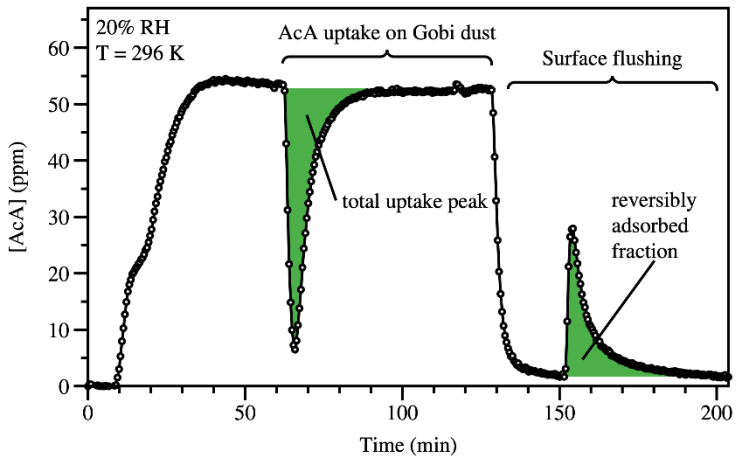

Figure IV-4 Temporal profile of AcA concentration during the uptake of 52.8 ± 1 ppm of AcA onto 100 ± 1 mg of Gobi dust and flushing process (20% RH, T = 296 K, P = 1013 mbar). The integrated areas represent the amount of the total uptake and the reversibly adsorbed fraction of AcA on Gobi dust respectively.

The N_{total} and N_{re} of AcA are calculated to be 1.99×10^{14} molecules cm^{-2} and 1.25×10^{14} molecules cm^{-2} respectively. Regardless the differences in the initial AcA concentrations and the mass of Gobi dust sample, the ratio between the reversibly adsorbed fraction of AcA, removed during surface flushing, and the total uptake of AcA, N_{re}/N_{total} is more important under 20% RH condition, i.e., 63 %, compared with the value obtained under dry condition, i.e., 27 % as shown in Figure IV-1. This preliminary observation suggests that the presence of water molecules influences the behavior of AcA uptake on Gobi dust and the same time, enhances the desorption process of AcA from the surface.

In order to address the influences of water molecules on N_{total}, N_{ir} and N_{re} the uptake of AcA on Gobi dust samples under 20 % RH are investigated at atmospheric pressure and room temperature with the AcA concentration from 1.02×10^{13} to 2.77×10^{15} molecules cm^{-3} (0.41 to 111 ppm). The results are shown in Figure IV-5 and compared with the corresponding fractions under dry condition. It should be noted that for clarity, results are displayed on both **linear scale** and **semi-log scale**, i.e., x-axis is logarithmic and y-axis is linear, side by side.

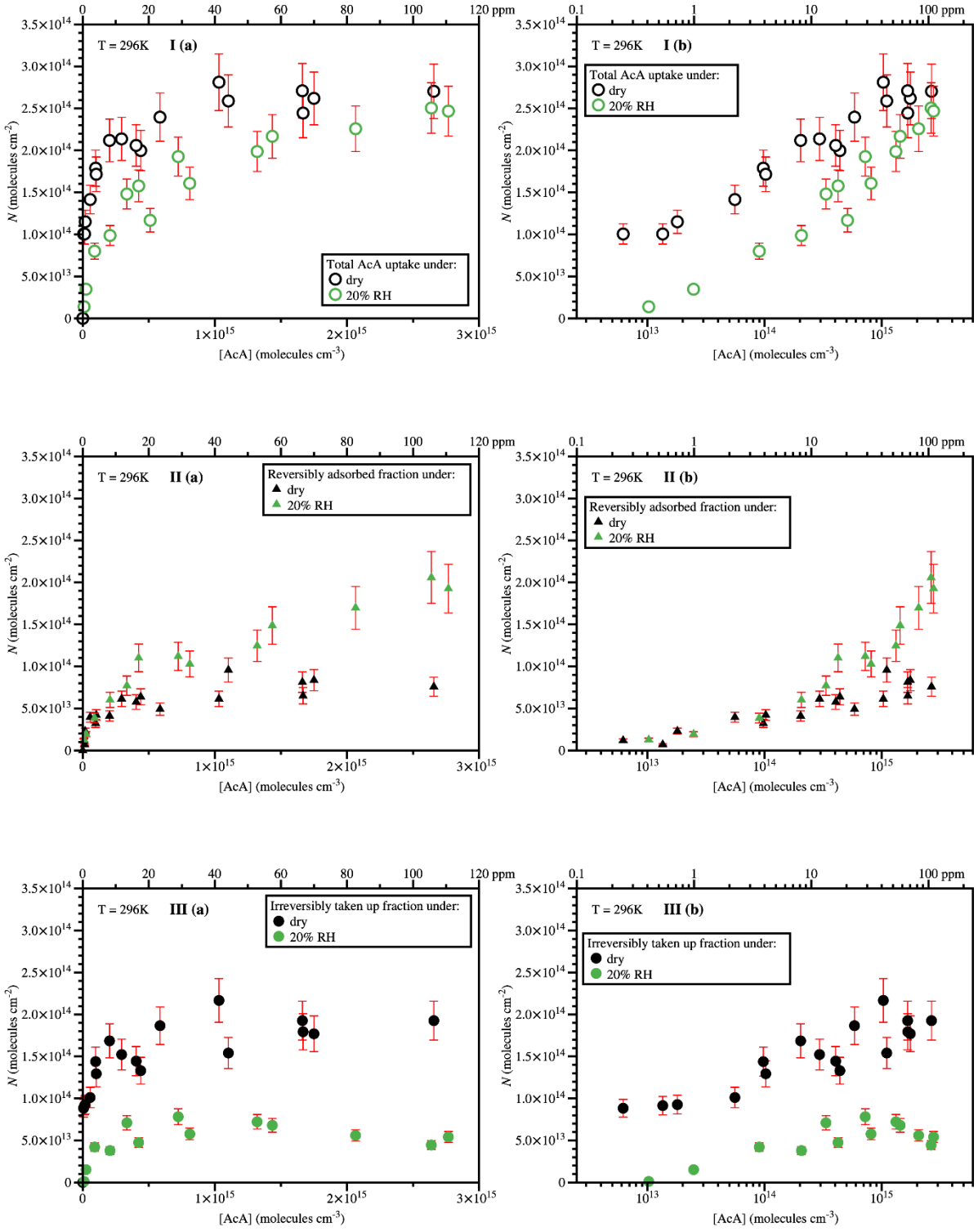

Figure IV-5 N of I (a) and (b) total uptake, II (a) and (b) reversibly adsorbed fraction, III (a) and (b) irreversibly taken up fraction of AcA on Gobi dust sample as a function of AcA concentration determined under dry and 20% RH condition at room temperature (296 K). The same comparison is displayed on (a) **linear scale** and (b) **semi-log scale**, i.e., x-axis is logarithmic and y-axis is linear, parallelly. The errors are calculated from the error in the individual variables needed for calculation.

1.3.1 Comparison of the total uptake of AcA on Gobi dust under dry and 20% RH

As displayed in Figure IV-5 I (a) and (b) the values of N_{total} of AcA on Gobi dust determined under 20% RH are generally lower than those measured under dry condition for the same AcA concentration, within the range of AcA concentration investigated. M. Zeineddine [9] have suggested the hindering effect of water molecules on AcA uptake on Gobi dust by the observation of a decrease of initial uptake coefficient and also observed that N_{total} decreases as the relative humidity increases. Moreover, for low AcA concentration, i.e. below 10 ppm, the difference between N_{total} under dry and 20% RH is more significant as shown in Figure IV-5 I. When AcA concentration increases, this difference in N_{total} between dry and 20% RH condition becomes less significant, according to Figure IV-5 I (a). In addition, interestingly, to achieve the saturation regime under humid higher concentrations of AcA are required compared with dry conditions.

The observations suggest that under 20% RH condition, the behavior of AcA uptake on Gobi dust surface has changed. In fact, above 20% of RH, the surface of Gobi dust sample is covered by a monolayer of water molecules, according to the study of water adsorption onto mineral dust particles conducted by N. Joshi et al. [12]. The number as well as the nature of the sorption sites on the surface might change, thus influencing AcA uptake process. S. R. Tong et al. [2] also suggested that the environment for AcA to uptake on the surface of Al_2O_3 is different under 30% RH condition compared with dry condition. During their study, S. R. Tong et al. pointed out that molecularly adsorbed water on the surface of Al_2O_3 suppresses the uptake of AcA and also observed the existence of hydrated acetate on the surface. As a result, S. R. Tong et al. suggested that the presence of water has two effects towards AcA uptake: hydroxylating the surface and dissolving acetate ion.

In order to identify more specifically the influence of water molecules on AcA uptake process on Gobi dust, the reversibly adsorbed fractions, as well as the irreversibly taken up fractions of AcA on Gobi dust under 20% RH condition and dry condition are respectively compared to address their individual contribution in the following sections.

1.3.2 Comparison of reversibly adsorbed fractions of AcA on Gobi dust under dry and 20% RH

From Figure IV-5 II, N_{re} obtained under 20% RH and dry condition together exhibit a different behavior than the total AcA uptake shown in Figure IV-5 I. For AcA concentrations below ca. 10 ppm, no significant difference between N_{re} under 20% RH and dry condition is observed. However, when AcA concentration exceed 10 ppm, N_{re} in 20% RH becomes clearly higher than N_{re} in dry condition. More precisely, unlike N_{re} determined under dry condition which gradually reaches a plateau with average value of $(8.0 \pm 0.8) \times 10^{13}$ molecules cm^{-2} indicating the saturation of the surface for reversibly physisorbed AcA, N_{re} determined under 20% RH exhibits an increasing trend and reaches a value of $(2.0 \pm 0.2) \times 10^{14}$ molecules cm^{-2} when AcA concentration is ca. 2.7×10^{14} molecules cm^{-3} (110 ppm)

which is more than twice the value under dry condition. The latter observations suggest that under 20% RH condition, the reversible physisorption process of AcA molecules is significantly promoted with the presence of adsorbed water molecules, which might further indicate the competition of water molecules with AcA molecules for the same surface sites on Gobi dust. S. R. Tong et al. [2] suggests that adsorbed water molecules on Al_2O_3 surface might provide adsorption sites for AcA molecules which are very likely to be reversibly adsorbed on Al_2O_3.

For N_{re}/N_{total}, the value determined under 20% RH is at a higher level, i.e., 48 – 88 %, compared with dry condition, i.e., 7 – 35 %.

1.3.3 Comparison of irreversibly taken up fractions of AcA on Gobi dust under dry and 20% RH

Under 20% RH condition, N_{ir} is significantly decreased compared with the value determined under dry condition within the entire range of AcA concentration. N_{ir} determined under 20% RH condition reaches a plateau with average value of ca. $(6.1 \pm 1) \times 10^{13}$ molecules cm^{-2}, which is smaller than one third of the average value of N_{ir} determined under dry condition, i.e., $(2.01 \pm 0.2) \times 10^{14}$ molecules cm^{-2} at the same AcA concentration range. Moreover, under 20% RH where the surface of Gobi dust is covered by a monolayer of adsorbed water molecules [12], the behavior of N_{ir} as a function of AcA concentration is modified. Indeed, instead of starting with a saturated value even at low AcA concentration as under dry condition shown in Figure IV-5 III, under 20% RH condition N_{ir} starts with a value approaching 0 and linearly increases within AcA concentration below 3 ppm, as clearly shown in Figure IV-5 III (b). It suggests that the sorption sites where AcA is irreversibly adsorbed under dry conditions are blocked by water molecules, and are not accessible for AcA molecules. This suggestion is also consistent with the previous conclusion that water molecules compete with AcA molecules for the same surface sites on Gobi dust.

1.3.4 Conclusions and remarks

In this section, the uptake of AcA on Gobi dust under 20% RH has been investigated and compared with dry condition. N_{total}, N_{re} and N_{ir} measured under dry and 20% RH condition are compared and discussed to address the influence of water molecules on AcA uptake on Gobi dust. Observations and conclusions are summarized as followed:

1. The presence of water molecules influences the total AcA uptake, reversibly adsorbed fraction and irreversibly taken up fraction of AcA on Gobi dust surface. N_{total}, N_{re} and N_{ir} determined under 20% RH at room temperature (296 K) at ca. 0.5 ppm, 10 ppm, 100 ppm which represents the low, middle and high AcA concentration range are presented and compared with dry condition in Figure IV-6.

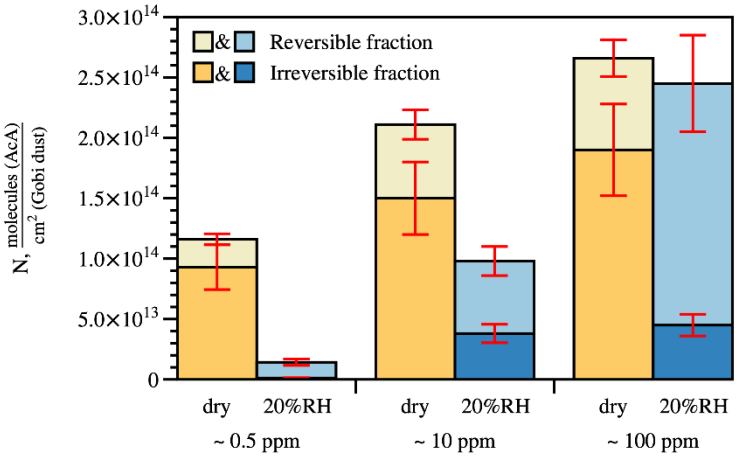

Figure IV-6 Reversibly adsorbed fractions and irreversibly taken up fractions of AcA on Gobi dust determined under dry and 20% RH condition at room temperature (296 K) at ca. 0.5 ppm, 10 ppm, 100 ppm which represents the low, middle and high AcA concentration range investigated. The errors are calculated from the error in the individual variables needed for calculation.

2. For total uptake of AcA on Gobi dust, negative impact of water molecules are observed, it is more significant for low AcA range, i.e., below 10 ppm. Under 20% RH condition, the surface state of Gobi dust is changed for AcA uptake process. The presence of water promotes the reversibly adsorbed fractions of AcA on Gobi dust due to the competition between water and AcA molecules for the same adsorption sites. For irreversibly taken up fraction of AcA on Gobi dust, the sorption sites for AcA on the surface are blocked or modified by adsorbed water molecules resulting in a decrease of irreversibly taken up fraction of AcA and the change of the mode of irreversible uptake process.

Further investigations, especially adsorbed phased monitoring, are needed to identify the nature of the new surface sites created by adsorbed water molecules, as well as the mechanism of the interaction between AcA molecules and surface with the presence of water molecules.

1.4 AcA uptake on Gobi dust with non-equilibrated uptake process

Experiments with non-equilibrated uptake of AcA on Gobi dust are designed, aiming at providing supplementary information about the priority between the reversibly and irreversibly adsorbed fraction of AcA on Gobi dust. Based on the typical experimental protocol for gas phase monitoring, the protocol for the experiment with non-equilibrated uptake process is described as followed:

- STEP 0 / Pretreatment of the dust sample: heating at 150˚C under dry zero air flow then cooling down to room temperature.
- STEP 1 / Initial gas phase concentration measurement under dry condition.
- STEP 2 / Dust surface exposure to AcA under dry condition.

- **STEP 3 / Switching AcA flow back to bypass line before AcA uptake process reaches equilibrium:** The AcA flow is directed back to bypass line before the signal of AcA concentration returns to the inlet value. The uptake process of AcA on Gobi dust surface is stopped before equilibrated.
- STEP 4 / Flushing the dust sample with dry air.

Figure IV-7 shows the AcA concentration profile of an experiment with non-equilibrated uptake process following the protocol above, where the initial inlet AcA concentration is 9.1 ± 0.2 ppm, the mass of the Gobi dust sample is 59 ± 1 mg.

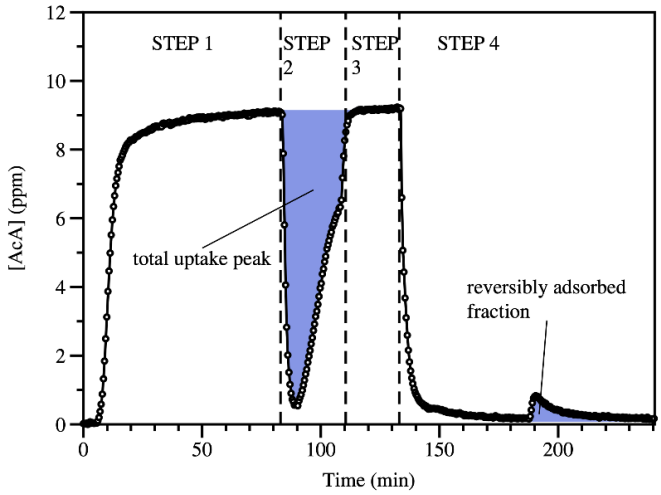

Figure IV-7 AcA concentration profile of an experiment with non-equilibrated uptake process under dry condition at room temperature (296 K) and atmospheric pressure. The inlet AcA concentration is 9.1 ± 0.2 ppm, the mass of the Gobi dust sample is 59 ± 1 mg. the integrated areas represent the amount of AcA.

As shown in Figure IV-7, the AcA flow is directed back to bypass at ca. 110 min before AcA uptake process is equilibrated, indicated by the abrupt rise of the AcA concentration. It has to be mentioned that the time to switch back the AcA flow is based on the objective judgement of author that the AcA concentration returns to ca. 2/3 of its inlet value, without specific criterion. Under this condition, the surface of Gobi dust sample is not equilibrated with gas phase AcA molecules. This can be deduced from the comparison with AcA concentration profile from experiments with equilibrated uptake process. The surface area integrated of the total uptake peak in Figure IV-7 refers the total amount of AcA taken up. During flushing process with dry air, a small peak of AcA concentration is observed indicating the reversibly adsorbed AcA fraction, for which the amount of AcA reversibly taken up can be calculated from the integrated area of the peak. Consequently, the irreversibly adsorbed fraction of AcA for this case can be obtained by subtracting the reversibly adsorbed fraction from the total AcA uptake.

Based on the temporal profile of AcA concentration shown in Figure IV-7, N_{total}, N_{re} and N_{ir} (molecules cm^{-2}) are determined for the experiment with non-equilibrated uptake process and presented in Table IV-2. For comparison, N (molecules cm^{-2}) of the experiment with an equilibrated uptake process with the same AcA concentration under dry condition, and the N ratio between experiments with non-equilibrated uptake process and equilibrated uptake process are also listed alongside in Table IV-2.

Table IV-2 Comparison of the number N (molecules cm^{-2}) of AcA molecules taken up per surface unit of Gobi dust determined under the experiments with non-equilibrated uptake process and equilibrated uptake process of 9.1 ± 0.2 ppm of AcA on Gobi dust under dry condition and 269 K.

N (10^{14} molecules cm^{-2})	Non-equilibrated uptake process	Equilibrated uptake process	Ratio Non-eq / Eq
N_{total}	1.4 ± 0.1	2.1 ± 0.2	67 %
N_{re}	0.13 ± 0.02	0.51 ± 0.05	25 %
N_{ir}	1.3 ± 0.1	1.4 ± 0.1	93 %

From Table IV-2, N_{total} only reaches 67 % of its equilibrated value during the experiment with non-equilibrated uptake process, among which the reversibly adsorbed fraction is only one quarter of its equilibrated value. However, for irreversibly taken up fraction, N_{ir} almost reaches its equilibrated value, i.e., 93% of the equilibrated value. As a result, the irreversibly taken up fraction of AcA on Gobi dust surface, which includes the chemisorbed fraction as well as strongly physisorbed fraction, is suggested to proceed faster than the reversibly adsorbed fraction.

1.5 Water-induced desorption process under dry condition by air flow of 20% RH

In order to provide information on the interactions of water molecules with the irreversibly taken up fraction of AcA molecules on the surface under dry condition, for the experiment discussed in the previous section, *section 1.4,* the surface of Gobi dust is flushed by humid air flow of 20% RH subsequently after flushing by dry air flow with an extra step STEP 5:

- **STEP 5 / Flushing the dust sample with air flow of 20% RH:** When flushing by dry air finishes, which is characterized by the observation that AcA concentration signal drops back to its baseline value, the dry air flow is switched to humid air flow of 20% RH to continue flushing the sample.

Figure IV-8 shows the AcA concentration profile during STEP 5, following the AcA profile in Figure IV-7.

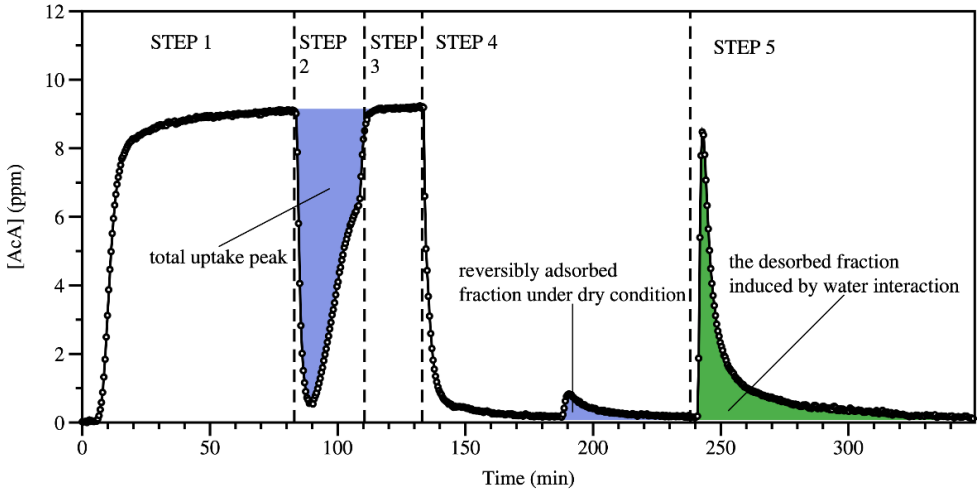

Figure IV-8 AcA concentration profile with non-equilibrated uptake process under dry condition at room temperature (296 K) and atmospheric pressure, followed by flushing process with humid flow of 20% RH. [AcA] = 9.1 ± 0.2 ppm, the mass of the Gobi dust sample is 59 ± 1 mg.

According to the discussion in the last section, after flushing the surface with dry air (STEP 4) under dry condition, the reversibly adsorbed fraction of AcA under dry condition is removed from the surface and only the irreversibly taken up fraction remains on the surface. As displayed in Figure IV-8 when flushing the surface with humid air flow of 20% RH, a significant water-induced desorption peak of AcA is observed. It indicates that water molecules interact with the irreversibly taken up fraction, resulting in a significant desorbed fraction of the irreversibly taken up fraction of AcA.

From the integrated surface area, the water-induced desorbed fraction of AcA is quantified to be (0.87 ± 0.06) × 10^{14} molecules cm^{-2}, which is the 67 % of the irreversibly taken up fraction of AcA on the surface under dry condition. It confirms that a fraction of AcA irreversibly taken under dry condition is removed due to interaction with water molecules and thus recovered in the gas phase (i.e. irreversible adsorbed fraction is turned to reversible). However, there is still ca. 33% of the irreversibly taken up fraction of AcA on the surface that cannot be removed by water interaction, which is suggested to include the chemisorbed fraction of AcA, consistent with the previous discussions in *section 1.3.*N determined during each step of the experiment is listed in Table IV-3.

Table IV-3 The number N (molecules cm^{-2}) of AcA molecules taken up per surface unit of Gobi dust determined during each step based on the AcA concentration profile in Figure IV-8.

AcA uptake Fractions	N (10^{14} molecules cm^{-2})	Ratio in total uptake
Total uptake	1.4 ± 0.1	100 %
Reversibly adsorbed fraction at RT	0.13 ± 0.02	9.3 %
Irreversibly adsorbed fraction at RT	1.3 ± 0.1	93 %
Water-induced desorbed fraction at RT	0.87 ± 0.06	62 %

As a result, the observations in Figure IV-8 confirm that the irreversibly taken up fraction of AcA under dry condition includes a fraction of molecularly adsorbed AcA which can be desorbed by water interaction and also includes a fraction of taken up AcA which is not influenced by water interaction. A few experimental investigations focusing on the interaction of water molecules with AcA molecules in adsorbed phase on dry surfaces have been conducted in literature [2, 13, 14]. However, they are mostly focusing on adsorbed phase characterization, which will be discussed in the later sections of this chapter.

1.6 Thermal-induced desorption process under dry condition by heating at 150˚C

Thermal-induced desorption process is investigated under dry condition following the protocols below:

- STEP 0 / Pretreatment of the dust sample: heating at 150˚C under dry zero air flow then cooling down to room temperature.
- STEP 1 / Initial gas phase concentration measurement under dry condition.
- STEP 2 / Dust surface exposure to AcA under dry condition.
- STEP 3 / Switch AcA flow to bypass line to verify initial AcA concentration.
- STEP 4 / Flushing the dust sample with dry air at room temperature (296 K).
- **STEP 5 / Flushing the dust sample at 150˚C (423 K) with dry air.**

By flushing Gobi dust sample with dry air flow at room temperature (296 K), the reversibly adsorbed fraction of AcA is determined to be 10 % - 30 % of the total AcA uptake, according to the discussion in *section 1.2*. However, a thermal-induced desorbed fraction of AcA is recovered during STEP 5 as shown in Figure IV-9.

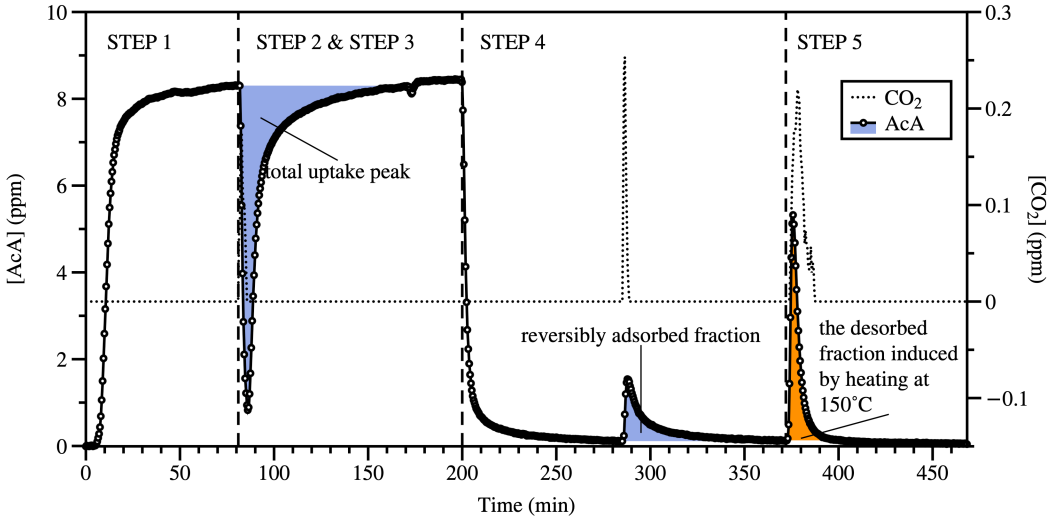

Figure IV-9 AcA concentration profile as well as the CO_2 level during AcA uptake, flushing the surface by dry air under room temperature (296 K), and thermal desorption by flushing with dry air at 150˚C (423 K). [AcA] = 8.3 ± 0.1 ppm, the mass of the Gobi dust sample is 32 ± 1 mg.

During STEP 5, the gas phase at the outlet of the U-shape reactor is monitored by the FTIR showing no significant production of CO_2 as shown in Figure IV-9. It suggests that the thermal-induced desorption process under 150 ˚C does not result in the advanced oxidation of AcA.

The number of total molecules taken up, the reversibly adsorbed, the irreversibly adsorbed and the thermally induced desorbed fractions of AcA in molecules cm^{-2} are calculated from Figure IV-9 and listed in Table IV-4.

Table IV-4 N of AcA in molecules cm^{-2} calculated for each fraction based on the AcA concentration profile in Figure IV-9.

AcA uptake Fractions	N (10^{14} molecules cm^{-2})	Ratio in total uptake
Total uptake	1.9 ± 0.2	100 %
Reversibly adsorbed fraction at RT	0.4 ± 0.01	22 %
Irreversibly adsorbed fraction at RT	1.5 ± 0.2	79 %
Thermal-induced desorbed fraction at 150˚C	0.6 ± 0.02	32 %

According to Figure IV-9 and Table IV-4, a significant amount of AcA molecules is recovered during STEP 5: thermal desorption process by flushing the surface at 150˚C. Indeed, ca. 22 % of the total uptake of AcA is desorbed after STEP 4, When flushing the surface at 150˚C with dry air flow, a fraction of ca. 32 % of the total AcA uptake is recovered, which equals 40 % of the irreversibly taken up fraction of AcA at room temperature. At the end of experiment, ca. 54 % of the total AcA uptake is recovered based

on the AcA balance. Interestingly, compared with last section, after flushing the surface with humid air flow of 20% RH, ca. 71 % of the total AcA uptake is recovered. It seems that flushing the surface with humide air flow has better surface regeneration efficiency regarding AcA uptake. However this aspect needs further investigations.

As a result, the thermal-induced desorption process at 150 ˚C under dry condition points out that AcA molecules are adsorbed on at least two different types of surface sites on the surface of Gobi dust with different adsorption enthalpies under dry condition. there is still a fraction of AcA irreversibly taken up on the surface of Gobi dust after thermal treatment at 150 ˚C.

1.7 Comparison of Gobi dust and its single mineral components regarding the irreversible uptake capacity

Irreversible uptake capacity of a material towards a certain gas phase species, q_{ir} in μmol g^{-1}, which corresponds to N_{ir} but is expressed in different units, is an important parameter for the sorbents used in industry since using the mass of the sorbent is convenient and intuitive for cost control and performance evaluation. The irreversible uptake capacity of Gobi dust towards AcA, is a good index to evaluate the potential of this geomaterial used in industry, e.g., in NTP-catalysis for VOC abatement. In this regard, the irreversible uptake capacity of Gobi dust, as well as its main components, i.e., SiO_2, $Al_2Si_2O_5(OH)_4$, $CaCO_3$, and TiO_2, towards AcA is determined with the AcA concentration range below 80 ppm under dry condition at room temperature. Within this AcA concentration range, the irreversible uptake capacities of all the materials towards AcA reach the saturation values correspondingly. As a result, the saturation values of the irreversible uptake capacity towards AcA of these materials are listed and compared in Table IV-5. For comparison, the total uptake capacity q_{total} in μmol g^{-1}, the BET surface area, S_{BET} in m^2 g^{-1} of each material as well as the value of q_{ir}/S_{BET} in μmol cm^{-2} of each material are listed.

Table IV-5 Comparison of the total uptake capacity q_{total} in μmol g^{-1}, the irreversible uptake capacity in μmol g^{-1}, BET surface area, S_{BET} in m^2 g^{-1} as well as the value of q_{ir}/S_{BET} in μmol cm^{-2} of Gobi dust and its major mineral components, i.e., SiO_2, $Al_2Si_2O_5(OH)_4$, $CaCO_3$, and TiO_2 toward AcA uptake. The irreversible uptake capacity is determined under atmospheric pressure and room temperature, with the AcA range below 80 ppm.

Materials	Total uptake capacity q_{total} (μmol g^{-1})	Irreversible uptake capacity q_{ir} (μmol g^{-1})	BET surface area, S_{BET} (m^2 g^{-1})	q_{ir}/S_{BET} (μmol cm^{-2})
Gobi dust	44.9 ± 5	31.6 ± 5	10.5 ± 0.2	(3.16 ± 5) × 10^{-4}
SiO_2 (quartz)	1.2 ± 0.2	0.4 ± 0.1	400 ± 40	(1.0 ± 0.3) × 10^{-7}
$CaCO_3$ (calcite)	3.4 ± 0.3	1.5 ± 0.2	0.6 ± 0.1	(2.5 ± 0.3) × 10^{-4}
$Al_2Si_2O_5(OH)_4$ (kaolinite)	35.5 ± 4	19.7 ± 4	12.9 ± 0.2	(1.5 ± 0.3) × 10^{-4}
TiO_2 (rutile)	169.2 ± 10	140.1 ± 10	52 ± 6.4	(2.8 ± 0.2) × 10^{-4}

From Table IV-5, TiO_2 exhibits the most significant total and irreversible uptake capacity towards AcA regarding the same mass, i.e., around 170 and 140 μmol g^{-1}. It might be connected with the high specific surface area of TiO_2. The value of irreversible uptake capacity is significantly smaller compared with the value retrieved from the study by F. Batault et al. [10], ca. 360 μmol g^{-1}. It might be due to the different types of TiO_2 samples that F. Batault used which is TiO_2 P25, a mixture of rutile and anatase.

Under dry condition, $CaCO_3$, shows poor irreversible uptake capacity towards AcA compared with Gobi dust but comparable value of N_{ir} with Gobi dust. Interestingly, Zeineddine et al. [9] observed that under 50% of RH, $CaCO_3$ exhibits the highest N_{ir} among other mineral components and even Gobi dust towards AcA. The latter observations clearly show that the role of water molecules on the AcA uptake process is dependent on the nature of the minerals. Indeed, instead of the negative impacts, the promoting effects on VOCs uptake have been observed on $CaCO_3$ particles by H. A. Al-Hosney et al [15], calcite and nitric acid reacted calcite aerosol by A. P. Prince et al. [16], and on thin ammonium nitrate films by J. E. Shilling and M. A. Tolbert [17]. Authors suggest that these materials such as calcium carbonate, are reactive soluble under high RH condition [14]. As a result, the bulk atoms and surface atoms can both participate in the interactions with VOC molecules under high RH condition and the heterogeneous interactions with VOC molecules may not be limited to the surface.

SiO_2 exhibits the lowest total and irreversible uptake capacity towards AcA. It is in good consistence with the observations by Zeineddine et al. [9], P. Li et al. [6], and S. Carlos-Cuellar et al. [1] where SiO_2 is found to have the lowest uptake ability towards VOCs due to its poor surface basic/acidic properties.

The total and irreversible uptake capacity of Gobi dust towards AcA under dry condition is significantly higher than its component except TiO_2, i.e., SiO_2, $Al_2Si_2O_5(OH)_4$, and $CaCO_3$. However, when taking the specific surface area into consideration, Gobi dust exhibits the highest value of q_{ir}/S_{BET} among other tested components including TiO_2.

Further comparison can be made through the estimation of the value q_{ir} of an "equivalent" Gobi dust by adding together the value of q_{ir} of all the single minerals in proportion of their relative abundance, assuming that all the aluminosilicates in Gobi dust behave as kaolinite, and also the relative abundance of Gobi dust is homogeneous in the bulk and the surface via equation (III-8).

$$q_{ir,calculated} = \sum q_{ir\ of\ x} \times relative\ abundance\ of\ x \qquad \text{(IV-3)}$$

The resulting value of q_{ir} of Gobi dust is 17.0 ± 5 μmol g^{-1}, which is approximately the half of the value determined experimentally, i.e., 31.6 ± 5 μmol g^{-1}. It indicates that Gobi dust exhibit a better AcA uptake performance than the simple mixture of its mineral components. As a result, from a practical point of view, the better AcA uptake performance found in Gobi dust highlights the possibility, and also the economic benefits underneath, of using natural Gobi dust for the industry as a VOC adsorbent, considering the low cost and energy saved compared with the synthetic materials that need to be synthesized and purified.

1.8 Conclusions of gas phase investigation of AcA uptake on Gobi dust

Based on the results and discussions presented from the investigation of AcA uptake on Gobi dust using gas phase approach, conclusions are summarized as followed:

1. Under dry condition and room temperature, the total uptake of AcA molecules on Gobi dust includes reversibly adsorbed fraction and irreversibly taken up fraction, for which the irreversibly taken up fraction takes ca. 70 % to 90 % of the total uptake. The irreversible uptake capacity of Gobi dust towards AcA is determined to be 31.6 ± 5 μmol g^{-1} within the investigated AcA concentration.
2. AcA is irreversibly adsorbed at room temperature on at least two different adsorption sites resulting to (i) a strongly adsorbed AcA fraction that is not removed under humid air flushing or thermal treatment of the surface, and (ii) a weaker adsorbed AcA fraction, where AcA can be removed after humid air flushing and thermal treatment.
3. Under 20% RH, the presence of water molecules significantly promotes the reversibly adsorbed fraction of AcA on Gobi dust by competing with AcA molecules for the same surface sites on Gobi dust. While the chemisorption sites for AcA molecules on Gobi dust surface are blocked

or modified by water molecules, resulting in the decrease of irreversibly taken up fraction and the change of the mode of irreversible uptake process.

4. The irreversibly uptake process of AcA on Gobi dust surface is suggested to proceed and reach equilibrated faster than the reversibly adsorption process.
5. Water molecules interact significantly with the irreversibly taken up fraction of AcA on Gobi dust under dry condition, resulting in the removal of ca. 67% of the irreversible taken up fraction of AcA and the desorption of molecular AcA in gas phase. It suggests that water molecules interact with the same surface sites of Gobi dust, on which AcA molecules are molecularly irreversibly adsorbed under dry condition.
6. By flushing the surface with dry air at 150˚C, ca. 63 % of the irreversibly taken up fraction of AcA on Gobi dust under dry condition is desorbed. The thermal-induced desorption process suggests that AcA molecules are adsorbed on at least two different types of surface sites on the surface of Gobi dust with different adsorption enthalpies.
7. The comparison of Gobi dust with its single mineral components regarding the irreversible uptake capacity towards AcA shows synergetic effect in Gobi dust. The potential and economic benefits of using this geomaterial in catalyst industry is addressed.

These conclusions call for the investigation for adsorbed phase for further evidence, which will be discussed in next section.

2 AcA uptake on Gobi dust: adsorbed phase approach

The adsorbed phase of Gobi dust during AcA uptake is investigated in this section. The DRIFT spectra of Gobi dust surface during different steps of AcA uptake under dry and humid conditions are obtained and discussed. The adsorbed phase during the interactions of water molecules with irreversibly taken up fraction of AcA under dry condition is also investigated. Moreover, the individual mineral components of Gobi dust, i.e., SiO_2, $Al_2Si_2O_5(OH)_4$ (kaolinite), $CaCO_3$, and TiO_2 are investigated under dry condition focusing on adsorbed phase in order to identify their respective surface properties towards AcA uptake.

2.1 AcA uptake on Gobi dust under dry condition: adsorbed phase investigation

The temporal DRIFT spectra during the uptake of AcA on the surface of Gobi dust are acquired with AcA concentration of 10 ± 0.5 ppm under dry condition following the protocol as developed in chapter 2:

- STEP 0 / Pretreatment of the dust sample: heating the dust sample at 150˚C under dry air flow and cooling down to room temperature under dry air flow.
- STEP 1 / Unexposed surface monitoring: to acquire the initial adsorbed phase as background.

- STEP 2 / Dust surface exposure to AcA.
- STEP 3 / Surface flushing by dry air flow.

The DRIFT spectra within the wavenumber range of 1000 – 3800 cm^{-1} of Gobi dust surface after 6 min, 8 min, 1.5 h of AcA exposure as well as after 1 h of flushing by dry air flow are plotted in absorbance and reported in Figure IV-10.

Positive peaks and bands suggest the formation of certain surface groups while negative ones indicate the removal of certain surface groups. For the absorbance bands at the same wavenumber from the spectra collected from the same experiment, which is the case for Figure IV-10, the bigger the absorbance, the higher the surface density of the corresponding surface group.

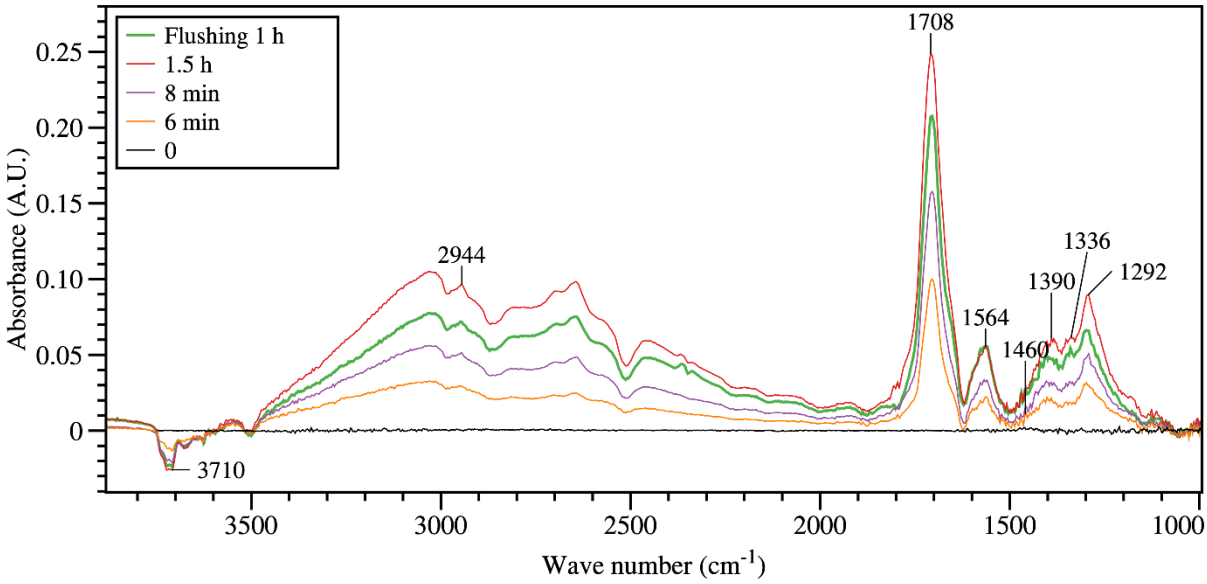

Figure IV-10 Chronological DRIFT spectra of the surface of Gobi dust during the exposure to AcA and after flushing by zero air flow for 1 hour ([AcA] = 10 ± 0.5 ppm, dry condition, T = 296 K, P = 1013 mbar).

The main features of DRIFT bands induced by the adsorbed AcA on Gobi dust are focused on the wave number range of 1000 – 2000 cm^{-1}. When AcA is introduced into the DRIFT sample cell, DRIFT bands are observed at 2944 cm^{-1}, 1708 cm^{-1}, 1564 cm^{-1}, 1460 cm^{-1}, 1390 cm^{-1}, 1336 cm^{-1}, and 1292 cm^{-1} as indicated in Figure IV-10. The intensities of all these bands increase during STEP 2 / Surface exposure to AcA, indicating that the corresponding surface groups are formed due to AcA uptake. Among them, the intensities of the bands at 2944 cm^{-1}, 1708 cm^{-1}, 1390 cm^{-1}, 1336 cm^{-1}, and 1292 cm^{-1} decrease during STEP 3 / Flushing the surface with dry air flow at room temperature, indicating the corresponding surface groups are partially reversibly adsorbed. The bands at 1564 and 1460 cm^{-1} remain stable during STEP 3, thus assigned to strongly bound surface species. More precisely based on the comparison and reference with literature studies, DRIFT band at 2944 cm^{-1} is attributed to $\nu_{as/s}(CH_3)$ of weakly bound

AcA, at 1292 cm^{-1} is attributed to ν(C-OH) or δ(OH) of weakly bound AcA, at 1336 cm^{-1} attributed to $\delta(CH_3)$ from weakly bound AcA, at 1390 cm^{-1} attributed to $\delta(CH_3)$ from weakly bound AcA, at 1708 cm^{-1} attributed to ν(C=O) of weakly adsorbed AcA dimers, and at 1564 cm^{-1} attributed to the asymmetric ν(O-C-O) and at 1460 cm^{-1} attributed to symmetric ν(O-C-O) of the strongly bound acetate species. The assignments of the vibrational mode as well as surface species for the DRIFT bands observed during the interactions of AcA with Gobi dust are summarized in Table IV-6.

Table IV-6 Surface species and vibrational mode assignments for DRIFT bands appearing during AcA uptake on Gobi dust surface at room temperature and dry condition.

DRIFT band	Surface species	Vibrational mode	References
1292	weakly bound AcA	ν(C-OH) or δ(OH)	1273 and 1295 [13], 1279 and 1302 [24], 1265 [25]
1336	weakly bound AcA	$\delta(CH_3)$	1329 and 1335 [13], 1331-1327 [26], 1343 [2], 1350 [25]
1390	weakly bound AcA	$\delta(CH_3)$	1385 and 1410 [13], 1420 [26]
1460	strongly bound acetate species	ν_a(O-C-O)	1479 [13], 1468 [2], 1470 [26], 1455 [16]
1564	strongly bound acetate species	ν_{as}(O-C-O)	1586 [13], 1583 [24], 1590 [26], 1578 [2], 1551 [16]
1708	weakly bound AcA	$\nu(C=O)_{dimer}$	1716 and 1711 [13], 1701 [24], 1714 [26]
2944	weakly bound AcA	$\nu_{as/s}(CH_3)$	2942 and 2936 [13], 2935 [27], 2937 [25]

Moreover according to Figure IV-10, broad bands within the range of wave number of 2000 - 3800 cm^{-1} appear along the interactions of AcA molecules with Gobi dust surface. This wavenumber range is due to vibrational mode of OH stretching [18-20]. Besides, the negative peak around 3710 cm^{-1}, which is assigned to isolated surface OH groups [18-20] is also observed, which are suggested to provide sorption sites for AcA molecules [10, 13, 21]. Thus, the negative peak at 3710 cm^{-1} attributed to these surface OH groups suggests either these surface OH groups are removed from the surface during the AcA-Gobi dust interactions, or they are modified probably due to the formation of hydrogen bonds with AcA molecules. It is in agreement with the observation by H. E. Evans and W. H. Weinberg [22, 23] that AcA molecules form hydrogen bonds to the surface of Al_2O_3 between O from AcA and H from the surface OH species. This fraction of adsorbed AcA molecules by hydrogen bonding contributes to the physisorbed fraction of AcA molecules on Gobi dust surface since the intensity of the bands decreases

after surface flushing. It is in accordance with F. Batault et al. [10] who suggested that AcA molecules physically adsorbed on the surface of TiO_2 by hydrogen bonding with Ti-OH.

Based on the DRIFT observation in Figure IV-10 and the surface species assignment in Table IV-6, several remarks are addressed:

1. Physisorbed AcA on Gobi dust, which includes reversibly adsorbed fraction and irreversibly adsorbed fraction are evidenced by the observations of:

   (i) The typical C=O stretching mode of physically adsorbed AcA in the wave number range of 1690 – 1790 cm^{-1} [27], i.e., ν(C=O) at 1708 cm^{-1} in Figure IV-10.

   (ii) The presence of all the vibrational modes of ν(C-OH) or δ(OH), $\delta(CH_3)$, $\nu_{as/s}(CH_3)$ and ν(C=O) which can be found in the gas phase spectrum of molecular AcA.

   (iii) The intensities of DRIFT bands assigned to vibrational modes of ν(C-OH) or δ(OH), $\delta(CH_3)$, $\nu_{as/s}(CH_3)$ and ν(C=O) decrease during surface flushing with dry air but do not totally disappear.

   It is supported by the observation obtained in gas phase investigation where a reversibly adsorbed fraction of AcA is recovered when flushing the surface with dry air under room temperature. It is also consistent with the discussions in *section 1.2* that the irreversibly taken up fraction of AcA includes physisorbed fraction.

   Although S. R. Tong et al. [2] suggested that no AcA molecules are physisorbed on the surface of α–Al_2O_3, since they did not observed any DRIFT bands within the wavenumber range of 1690 – 1790 cm^{-1}, the physisorbed AcA molecules have been observed and evidenced on γ-Al_2O_3 by M. Tang et al. [13], on TiO_2 by L. Liao et al. [28], and on γ- and δ-Al_2O_3 by M. Hasan et al. [26]. The authors also suggested the reversible property of the physisorbed AcA.

2. Dimer is the major form of the molecularly adsorbed AcA on adsorbed phase.

   The FTIR spectra of AcA in gas phase, which are acquired during gas phase investigation, confirm that the monomers of AcA molecules are dominant for gas-phase AcA within the AcA concentration range investigated in this study. However, when AcA molecules are physisorbed onto surface, only the DRIFT band at 1708 cm^{-1} attributed to ν(C=O) of dimmer AcA is observed, indicating that dimer is the major form for molecularly adsorbed AcA. It suggests that the formation of AcA dimers is favored by physisorption process of AcA on Gobi dust which is supported by analyzing the IR spectra obtained by M. Hasan et al. [26]. M. Tang et al. [13] who also observed that physisorbed AcA molecules on the surface of γ-Al_2O_3 are mostly in the form of dimer.

3. Surface acetate species is formed on the surface during AcA uptake on Gobi dust as the strongly bound surface species, which is suggested to coordinated to the surface in bidentate chelating structure with the two oxygen atoms from AcA bounded to the same metal center on the surface of Gobi dust.

4. The vibrational modes ν_a(O-C-O) and ν_{as}(O-C-O) indicate the formation of surface acetate species during AcA uptake [2, 22, 23, 28]. It has been suggested in literature that the surface acetate species are bounded to the metal centers by coordination bonds [13],. This can be evidenced by the stability of the DRFIT bands assigned to ν_a(O-C-O) and ν_{as}(O-C-O) during flushing process in Figure IV-10.

   As mentioned in *section 4.2* of chapter 1, the configuration of the coordinate bonded acetate species to the surface can be distinguished between bidentate chelating structure and bidentate bridging structure by Δ(COO), which is the wavenumber difference between ν_a(O-C-O) and ν_{as}(O-C-O). According to Figure IV-10, Δ(COO) of the surface acetate species formed during the interactions of AcA and Gobi dust is 104 cm^{-1}. There are arguments and debates in literature studies about the structure of the surface acetate species: H. E. Evans and W. H. Weinberg [22, 23] suggested the bidentate bridging structure of acetate species on Al_2O_3 with Δ(COO) of 125 cm^{-1}. S. R. Tong et al. [2] suggested the bidentate bridging structure of acetate on α–Al_2O_3 with Δ(COO) of 110 cm^{-1} after comparing the calculated and measured Δ(COO). However, L. Liao et al. [28] suggested the bidentate chelating structure of adsorbed acetate on TiO_2 with Δ(COO) of 81 cm^{-1}. And M. Tang et al. [13] compared the literature study then suggested the bidentate chelating structure of surface acetate species on γ–Al_2O_3 with Δ(COO) of 107 cm^{-1}. The value of Δ(COO) determined in this study, i.e., 104 cm^{-1}, is closer to the value of bidentate chelating structure of surface acetate species, for which the value of Δ(COO) is smaller than bidentate bridging structure. As a result, we suggest the bidentate chelating structure of the surface acetate species formed on Gobi dust during AcA uptake. Further experimental and theoretical works are needed to clarify this controversy.

Figure IV-11 is the schematic summary of the structures of the molecularly adsorbed AcA monomer and dimer as well as the acetate on Gobi dust under dry condition, where SS represents the metal center on the surface of Gobi dust.

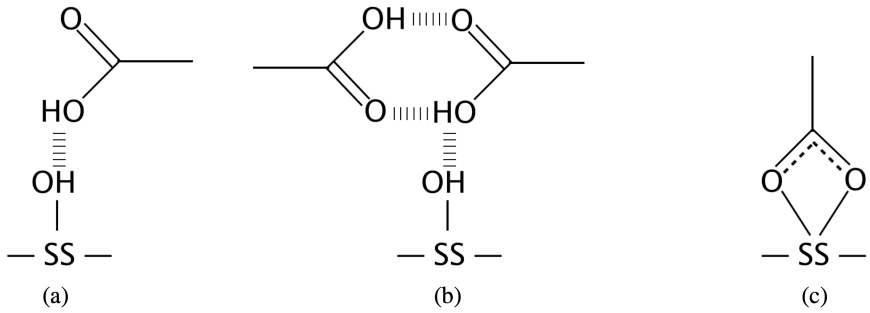

Figure IV-11 Scheme of the structures of (a) AcA monomer, (b) AcA dimer, and (c) acetate formed on the surface of Gobi dust during AcA uptake.

2.2 Kinetics of the formation of surface species during AcA uptake and surface flushing by dry air

The integrated areas of the DRIFT bands presented in Figure IV-10 versus time can reveal the evolution of the relative surface density of these surface species. In this regard, the normalized band areas of bands at 1708 cm^{-1}, 1564 cm^{-1}, 1460 cm^{-1}, 1390 cm^{-1}, 1336 cm^{-1}, and 1292 cm^{-1} are calculated by integrating the absorbance area with 30 cm^{-1} of wavenumber width from center of the bands for all the DRIFT spectra and then normalizing their maximum values to 1 for the purpose of comparison. The band at 2944 cm^{-1} is totally overlapped with bands of surface OH groups thus the band area at 2944 cm^{-1} is not compared with the rest. As a result, Figure IV-12 shows the temporal profiles of the normalized band areas of these bands during AcA uptake on Gobi dust surface and flushing process by dry air.

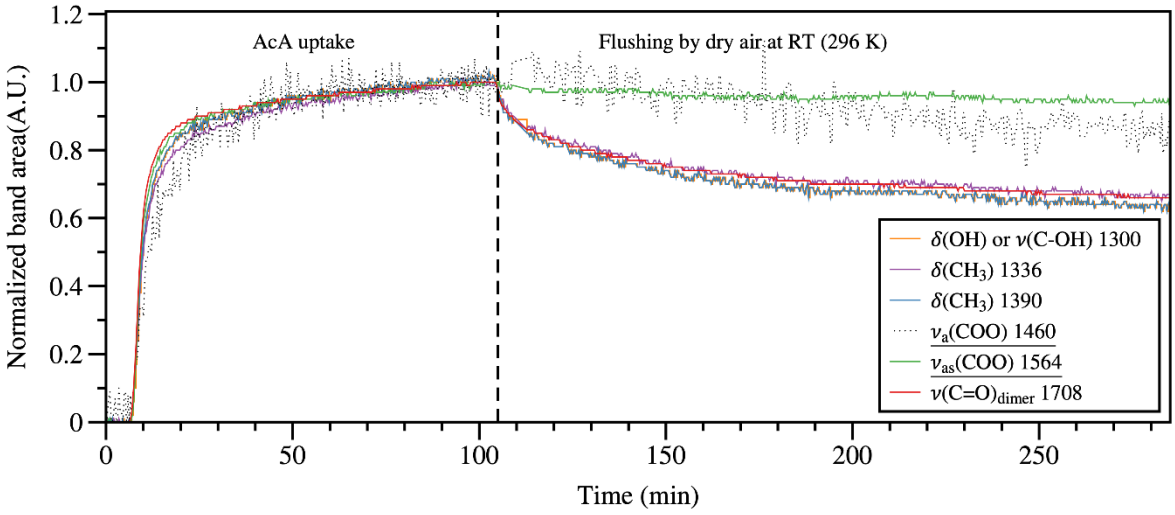

Figure IV-12 Temporal profiles of the normalized band areas of the DRIFT bands indicated in Figure IV-10 during AcA uptake on Gobi dust and flushing by dry air at room temperature. The legends underlined indicates the strongly bound surface species.

From Figure IV-12, several remarks related to the formation of the surface species on Gobi dust surface during AcA uptake and flushing by dry air are addressed:

1. During AcA uptake process, the normalized bands areas of all the DRIFT bands increase and approach to a stable value, due to AcA uptake. A plateau is reached after a period of time, i.e., c.a. 90 min in the case of Figure IV-12.
2. When flushing the surface by dry air, the normalized band areas at 1564 cm^{-1}, 1460 cm^{-1}, which assigned to ν_{as}(O-C-O) and ν_{a}(O-C-O) vibrational modes of the strongly bound acetate species on the surface correspondingly, remain relatively stable. The normalized band areas of bands at 1708 cm^{-1}, 1390 cm^{-1}, 1336 cm^{-1}, and 1292 cm^{-1}, which are assigned to the vibrational modes of ν(C=O)$_{dimer}$, δ(CH_3), δ(CH_3), and ν(C-OH) or δ(OH) respectively of the weakly bound AcA on the surface, decrease similarly but faster during surface flushing process. The later observation confirms the DRIFT band assignment mentioned above for strongly bound acetate species and weakly bound AcA.
3. According to the normalized band area values indicated in the temporal profile in Figure IV-12, approximately 30 % of the weakly bound AcA molecules are removed from the surface after flushing by dry air, which corresponds to the reversibly adsorbed fraction of AcA on the surface under dry condition. It is consistent with the results obtained during gas phase investigation of AcA uptake on Gobi dust under dry condition, where the reversibly adsorbed fraction of AcA is found to take 10 - 30 % of the total AcA uptake by the surface.

2.3 Influence of water molecules on adsorbed phase of Gobi dust regarding AcA uptake

The influence of water molecules on AcA uptake on Gobi dust are investigated by two series of experiments. In the first series of experiment, the adsorbed phase of Gobi dust surface during uptake of AcA molecules and surface flushing process are investigated under 20% RH condition to compare with the adsorbed phase investigation conducted under dry condition as discussed in *section 2.1*. In the second series, in order to investigate the adsorbed phase of Gobi dust during water-induced AcA desorption process, Gobi dust sample is first exposed to AcA then flushed by dry air at room temperature under dry condition, then air flow containing water is introduced into the DRIFT cell to interact with the AcA exposed Gobi dust.

2.3.1 Adsorbed phase of Gobi dust during AcA uptake under 20% RH condition

The adsorbed phase during AcA-dust interactions is investigated under 20% RH condition and the DRIFT spectra are acquired with AcA concentration of 10 ± 0.5 ppm following the protocol as mentioned in *section 2.1*:

- STEP 0 / Pretreatment of the dust sample: heating the dust sample at 150˚C under air flow and cooling down to room temperature under humid air flow of 20% RH.

- STEP 1 / Unexposed surface monitoring: to acquire the initial adsorbed phase as background under humid air flow.
- STEP 2 / Dust surface exposure to AcA under 20% RH condition.
- STEP 3 / Surface flushing by humid air flow of 20% RH.

Under this condition, the surface of Gobi dust is always equilibrated with water molecules under 20% RH during AcA uptake and surface flushing process by humid air flow. The DRIFT spectra within wavenumber range of 900 – 3800 cm^{-1} of Gobi dust surface after 1 h of AcA exposure and after 1.5 h of flushing with 20% RH humid air of are plotted in absorbance and reported in Figure IV-13.

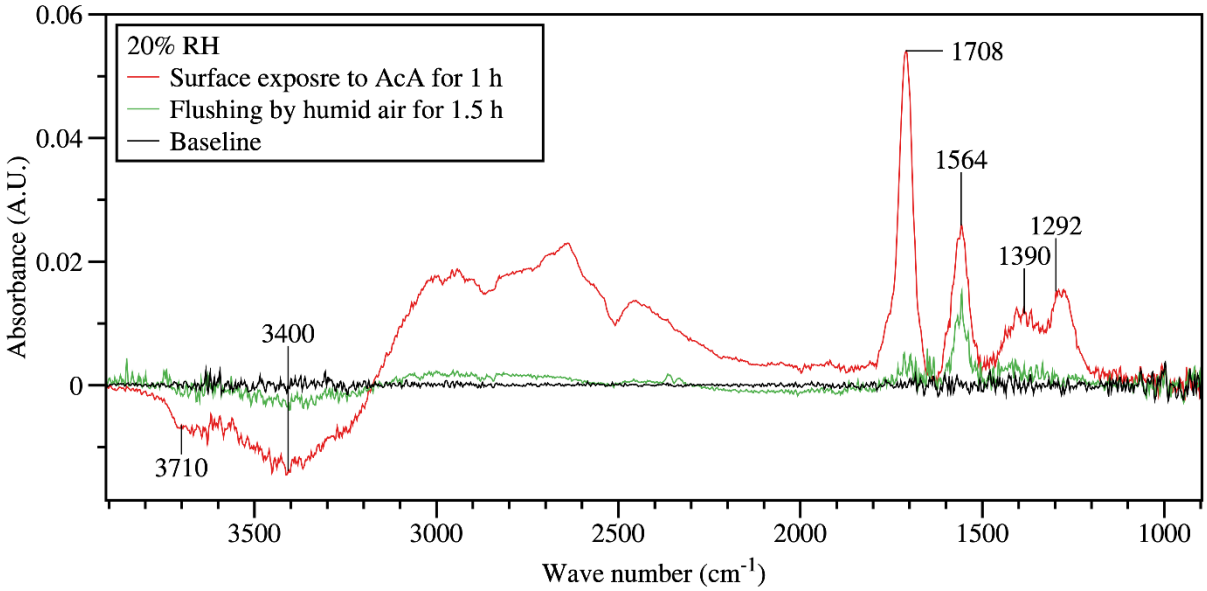

Figure IV-13 DRIFT spectra of (—) AcA adsorption on Gobi dust surface under 20% RH condition for 1 h and (—) after flushing by humid air flow of 20% RH for 1.5 h. The experiment was conducted under room temperature (296 K) 20% RH condition with AcA concentration of 10 ± 0.5 ppm.

During AcA uptake on Gobi dust under 20% RH condition, the negative band at 3710 cm^{-1} attributed to isolated surface OH group [18-20] and the negative broad band centered at 3400 cm^{-1}, which is characterized as the typical ν(OH) vibrational mode of adsorbed water molecules [10, 18-20] are observed. Similar DRIFT bands within the wave number range of 1200 – 1800 cm^{-1} after 1 h of AcA uptake under 20% RH condition are observed compared with the DRIFT spectra acquired during AcA-Gobi dust interactions under dry condition (see Figure IV-10): bands at 1708 cm^{-1} attributed to $\nu(C{=}O)_{dimer}$, 1390 cm^{-1} attributed to $\delta(CH_3)$ and 1292 cm^{-1} attributed to ν(C-OH) or δ(OH) of weakly bound AcA, and band at 1564 cm^{-1} attributed to asymmetric ν(O-C-O) of the strongly bound acetate species are observed. However, unlike dry conditions, under 20% RH the intensity of the band at 1564 cm^{-1} (attributed to asymmetric ν(O-C-O) of the strongly bound acetate species) is more intense compared with the bands at 1390 cm^{-1} and 1292 cm^{-1} assigned to weakly bound AcA.

In order to reveal the evolution of the relative surface densities of the surface species indicated by the DRIFT bands in Figure IV-13, the temporal profiles of the normalized band areas of the bands indicated in Figure IV-13 during AcA uptake on Gobi dust surface and flushing process under 20% RH condition are displayed Figure IV-14.

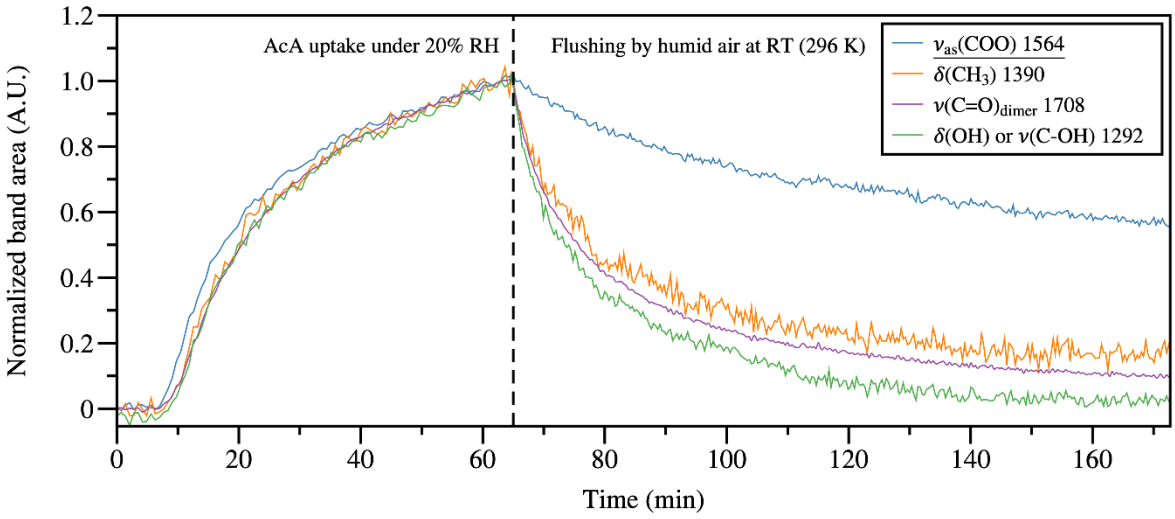

Figure IV-14 Temporal profiles of the normalized band areas of the DRIFT bands indicated in Figure IV-13 during AcA uptake on Gobi dust under 20% RH and surface flushing at room temperature under 20% RH. The legends underlined indicates the strongly bound surface species.

According to Figure IV-13 and Figure IV-14, during flushing by air flow of 20% RH, the bands assigned to weakly adsorbed AcA, i.e., 1708 cm^{-1}, 1390 cm^{-1} and 1292 cm^{-1} decrease to ca. 10 %, approaching the baseline level, indicating that ca. 90% of the corresponding weakly adsorbed AcA is restored in the gas phase . The band at 1564 cm^{-1}, which is attributed to the strongly bound acetate species, also decrease to ca. 60% but not disappear after 1.5 h of flushing. In addition, the negative bands at 3710 cm^{-1} and centered at 3400 cm^{-1} attributed to surface OH groups that has been removed due to AcA adsorption is now recovered almost to the baseline level, after surface flushing with 20% RH of humid air, as shown in Figure IV-13.

Based on the DRIFT observations of AcA on Gobi dust under 20% RH and the comparison with dry condition, conclusions are addressed as followed:

1. No new DRIFT bands are observed under 20% RH compared with dry condition indicating that the surface species formed are similar in both conditions.
2. Surface OH group and adsorbed water molecules are consumed during AcA-Gobi dust interactions, which further suggests that AcA compete with water molecules for the same surface sites, i.e., surface OH group, on Gobi dust.

Under 20% RH condition, the surface of Gobi dust is covered by a monolayer of water molecules [12]. When AcA molecules interact with the surface of Gobi dust under 20% RH, it results in the removal of adsorbed water molecules from the surface, as indicated by the negative broad band centered at 3400 cm^{-1} shown in Figure IV-13. S. R. Tong et al. [2] have observed the same features of DRIFT spectra during AcA uptake on the surface of α-Al_2O_3 under humid condition.

Since adsorbed water molecules are bound to the surface OH group through H-O-H bending mode, as suggested by A. L. Goodman et al [14] and also evidenced by the observation of the DRIFT peak at 1635 cm^{-1} assigned to H-O-H bending mode in Figure III-11, the adsorbed water molecules block the access of AcA to surface OH group which provides sorption sites for carboxylic acids [2, 10, 13, 21] thus suppressing the uptake of AcA on the surface OH group, which is in consistence with the previous conclusion in *section 2.1*.

3. Most of the weakly bound AcA on the surface are reversibly adsorbed on the surface of Gobi dust under 20% RH, which are suggested to bound to adsorbed water molecules through hydrogen bonding.

   The bands assigned to weakly adsorbed AcA, i.e., 1708 cm^{-1}, 1390 cm^{-1} and 1292 cm^{-1} decrease almost to the baseline level after flushing with 20% RH air flow as shown in Figure IV-13 and Figure IV-14. Therefore, the main fraction of the weakly adsorbed AcA is reversibly adsorbed on the surface under 20% RH condition. It is supported by the conclusion from gas phase investigation in s*ection 1.3*: the presence of water promotes the reversibly adsorbed fraction of AcA on Gobi dust. The ration of N_{re}/N_{total} under 20% RH is in the range of 48 – 88 %, higher than the ratio of N_{re}/N_{total} under dry condition, i.e., 7 – 35 %.

   Under 20% RH condition, the sorption sites, such as surface OH group, are significantly blocked by adsorbed water molecules, thus the amount of adsorbed AcA on surface OH group is expected to decrease significantly. The amount of reversibly adsorbed fraction of AcA increases, which might suggest that AcA molecules are reversibly adsorbed on other adsorption sites, i.e., adsorbed water molecules on Gobi dust surface.

4. Strongly bound acetate species are partially reversibly adsorbed under 20% RH.

   The band at 1564 cm^{-1} attributed to the strongly bound acetate species decrease when the surface is flushed by air flow of 20% RH, but does not totally disappear after 1.5 h of flushing as shown in Figure IV-13. It indicates that a fraction of the strong bound acetate species on the surface is reversibly adsorbed under 20% RH with the presence of water molecules. According to Figure IV-14, ca. 40% of the strongly bound acetate species is desorbed during the surface flushing process under 20% RH condition. On the contrary, under dry condition, the strongly bound

acetate species on the surface of Gobi dust is mostly irreversibly taken up. This conclusion suggests that under 20% RH condition, water molecules can interact with the surface acetate species on the surface, resulting in a partial removal of the strongly bound acetate species.

These conclusions are consistent regarding the corresponding gas-phase investigation under 20% RH, evidencing the competition of water molecules with AcA molecules for the same surface sites on the surface of Gobi dust and, at the same time, suggesting the creation of new surface sorption sites by water molecules.

2.3.2 Adsorbed phase of Gobi dust surface during water-induced desorption process

In order to investigate how water molecules interact with the irreversibly adsorbed fraction of AcA that has been adsorbed under dry condition on Gobi, an experiment with a water-induced desorption process is conducted following the protocol described as followed:

- STEP 0 / Pretreatment of the dust sample: heating the dust sample at 150˚C under air flow and cooling down to room temperature under dry air flow.
- STEP 1 / Unexposed surface monitoring: to acquire the initial adsorbed phase as background under dry condition.
- STEP 2 / Dust surface exposure to AcA of 10 ± 0.5 ppm under dry conditions.
- STEP 3 / Surface flushing by dry air flow.
- **STEP 4 / Surface flushing by air flow containing 250 ppm of water molecules (0.8% RH).**

With this water concentration of the gas flow, the DRIFT signal will not drop too much due to the strong absorption of water molecules, which is the case for 20% RH condition, and the interactions of water molecules are enough significant to be observed. As a result, the DRIFT spectrum acquired at the end of STEP 3 right before STEP 4, i.e., after flushing Gobi dust surface with dry air flow for 1.5 h, and the DRIFT spectrum acquired after introducing water molecules for 1 h are shown in Figure IV-15.

In Figure IV-15, the DRIFT bands at 1708, 1564, 1390, 1336 and 1292 cm^{-1} observed on the spectrum acquired at the end of STEP 3 (displayed in red) are all related to the irreversibly taken up fraction of AcA under dry condition. After water molecules are introduced into the system, the peak at 1640 cm^{-1} , the typical peak assigned to the H-O-H stretching of adsorbed water molecules [2, 14], is observed. The intensity of all the bands attributed to the irreversibly adsorbed fraction of the weakly bound AcA, i.e., bands at 1708, 1390, 1336 and 1292 cm^{-1}, decrease, as shown in Figure IV-15. It evidences that water molecules can interact with this fraction of the weakly bound AcA under dry condition, resulting in the partial removal of these surface species.

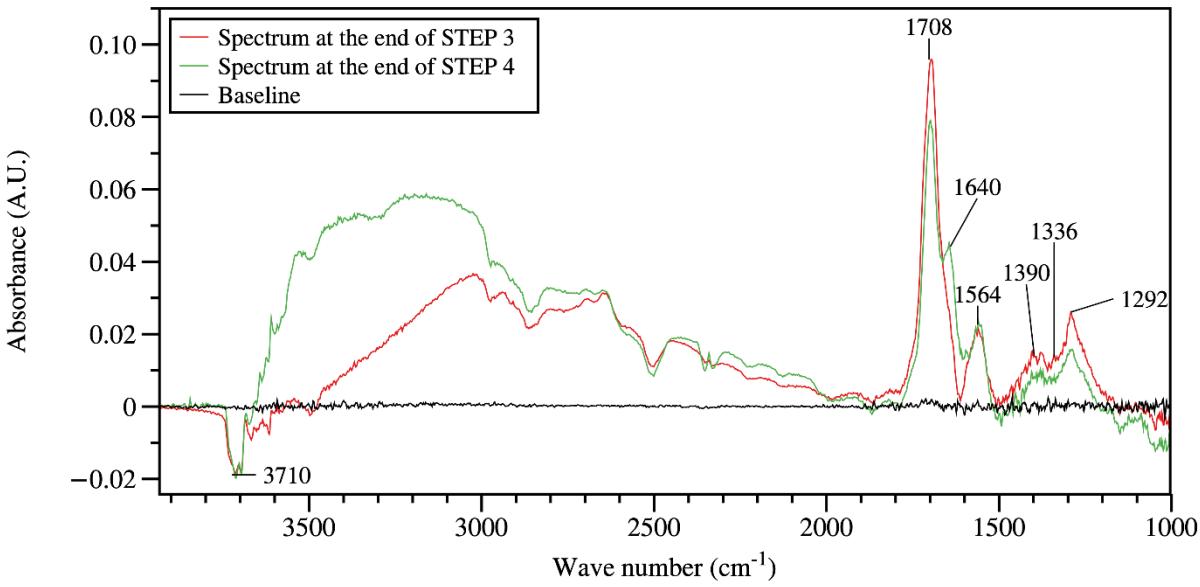

Figure IV-15 DRIFT spectra acquired (—) at the end of STEP 3: flushing the Gobi dust surface with dry air for 1.5 h after AcA uptake under dry condition, and (—) at the end of STEP 4: introducing water molecules to interact with the surface for 1.5 h. The experiment was conducted under room temperature (296 K) with AcA concentration of 10 ± 0.5 ppm.

Unlike the DRIFT band attributed to weakly bound AcA species, the band at 1564 cm^{-1} attributed to strongly bound acetate species is not influenced by the interactions with water molecules along wet flushing. This observation suggests that the water molecules, with the concentration of 250 ppm in gas phase (0.8% RH), do not impact strongly bound acetate species. However, in the previous section, the DRIFT spectra acquired under 20% RH condition indicates that water molecules interact with the strongly bound acetate species (as shown in Figure IV-13). Two possible reasons can explain the different observations: (i) In the experiment under 20% RH, the concentration of water molecules in gas phase equals ca. 5600 ppm, which is 22 times higher compared with the experiment discussed in this section, i.e., 250 ppm, suggesting that the competition of water molecules with adsorbed AcA molecules is more intense under 20% RH. (ii) Besides, in this experiment, the AcA molecules are adsorbed on the dry surface of Gobi dust, while the experiment under 20% RH, the surface of Gobi dust is covered by a monolayer of water molecules. The presence of the adsorbed water layer are suggested to provide medium for the dissociation reaction of AcA [2, 17].

The dynamics of the surface groups indicated in Figure IV-15 are revealed by the temporal profiles of the normalized band areas of the bands in Figure IV-15. The temporal profiles are calculated by integrating the absorbance of bands at 1708 cm^{-1}, 1564 cm^{-1}, 1390 cm^{-1}, 1636 cm^{-1} and 1292 cm^{-1} with 30 cm^{-1} of wavenumber width from the center of the bands for all the DRIFT spectra acquired along time respectively, then normalizing their maximum values to 1, which are shown in Figure IV-16. It is clearly shown in Figure IV-16 that the normalized areas of the band at 1564 cm^{-1} attributed to surface acetate species remain quite stable during the surface flushing by air flow containing 250 ppm of water

starting at ca. 190 min. The normalized areas of 1390, 1336 and 1292 cm^{-1} decrease by ca. 36% with the same behavior, which indicates that the corresponding vibrational modes might come from the same surface AcA species and they are desorbed during water interactions. However, the normalized areas of 1708 cm^{-1}, attributed to ν(C=O) of adsorbed AcA dimers, decrease by ca. 18% within the same time scale, not as significantly as the bands of 1390, 1336 and 1292 cm^{-1} do. It suggests that the bands at 1390, 1336 and 1292 cm^{-1} might be related to the adsorbed AcA monomers.

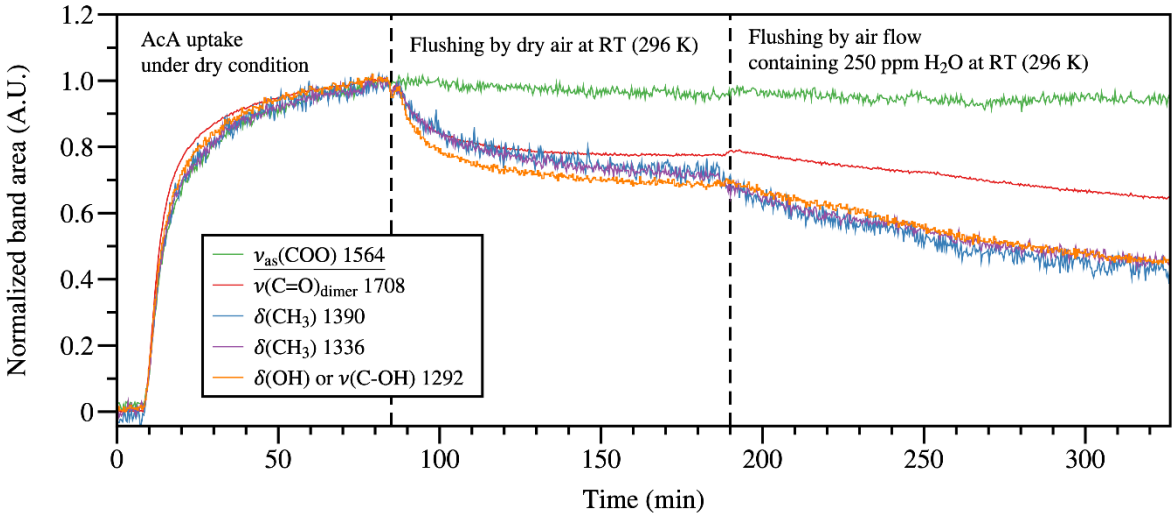

Figure IV-16 Temporal profiles of the normalized band areas of the DRIFT bands indicated in Figure IV-15 during AcA uptake on Gobi dust under dry condition, surface flushing at room temperature under dry condition and the water-induced desorption process by flushing the surface with air flow containing 250 ppm water. The legends underlined indicates the strongly bound surface species.

As a result, the following conclusions can be drawn:

1. Water molecules interact with the irreversibly adsorbed fraction of the weakly bound AcA species on Gobi dust under dry condition, resulting in the partial removal of these surface species, among which a lower fraction of the dimer adsorbed AcA species is desorbed.
2. For the given water concentration used, no significant interaction between water molecules and the surface acetate species formed under dry condition was noticed. Nevertheless, this trend could be highly dependent on the water concentration and thus possible removal of acetates at higher RH levels cannot be excluded.

2.3.3 Conclusion and remarks

Based on the investigations focusing on adsorbed phase of Gobi dust during AcA uptake under 20% RH condition, water molecules are evidenced to compete with AcA molecules for the same surface sites. Under 20% RH condition where the surface of Gobi dust is covered by a monolayer of adsorbed water, AcA molecules are suggested to bound to adsorbed water molecules through hydrogen bond which

represents the reversibly adsorbed fraction of AcA. Surface acetate species are also formed on the surface under 20% RH, which can be partially removed by flushing the surface with humid air flow.

During the investigation focusing on the interaction between water molecules with the irreversibly taken up fraction of AcA under dry condition on Gobi dust, water molecules are evidenced to interact with the irreversibly adsorbed fraction of the weakly bound AcA on the surface OH group, resulting in the partial removal of these surface species. Moreover, the interaction between water molecules of 250 ppm and the surface acetate species is suggested to be less significant compared with the interaction between water molecules and the weakly bound AcA on Gobi dust.

2.4 Adsorbed phase investigation of the mineral components of Gobi dust during AcA uptake under dry condition

To further address the individual adsorbed phase of the principle components of Gobi dust during AcA uptake, DRIFT investigations following the same protocol as applied in *section 2.1* have been performed on the main mineral components of Gobi dust, i.e., SiO_2, $Al_2Si_2O_5(OH)_4$ (kaolinite), $CaCO_3$, and TiO_2, at room temperature, under dry condition, with AcA concentration of 10 ± 0.5 ppm. Two DRIFT spectra for each mineral, i.e., one is acquired after 1.5 hour of AcA uptake, another one is acquired after 1 hour of flushing under dry air, are chosen to be displayed to show the adsorbed phase during AcA uptake before and flushing process. By the time of acquisition, the DRIFT spectra have already reached an equilibrated state for all the samples and both processes.

2.4.1 Adsorbed phase during AcA uptake on $Al_2Si_2O_5(OH)_4$ (kaolinite) under dry condition

Figure IV-17 shows the DRIFT spectra of the adsorbed phase of kaolinite acquired after 1.5 hour of AcA uptake and after 1 hour of surface flushing by air flow under dry condition respectively.

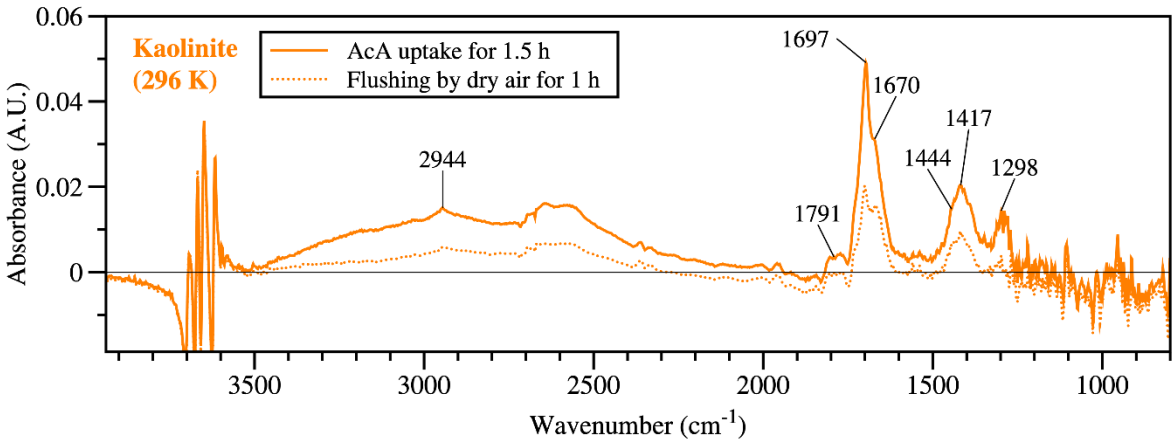

Figure IV-17 DRIFT spectra of the adsorbed phase of kaolinite acquired after (—) 1.5 hour of AcA uptake, and (·····) 1 hour of surface flushing by air flow under dry condition. The experiment was conducted under room temperature (296 K) dry condition with AcA concentration of 10 ± 0.5 ppm.

During AcA uptake on the surface of kaolinite, DRIFT bands at 2944, 1791, 1697, 1444, 1417, and 1298 cm^{-1} are observed as indicated in Figure IV-17. Among them, the band at 2499 cm^{-1} is attributed to $\nu_{as/s}(CH_3)$ of weakly bound AcA [13, 25, 27], the band at 1298 cm^{-1} is attributed to ν(C-OH) or δ(OH) of weakly bound AcA [13, 24, 25], the band at 1417 cm^{-1} is attributed to $\delta(CH_3)$ from weakly bound AcA [2, 13, 25, 26]. In the study conducted by J. Kubicki et al. [29], authors studied the ATR (attenuated total reflection) FTIR spectra of acetic acid in solution adsorbed on kaolinite and the bands at around 1280, 1400 and 1702 cm^{-1} have been observed without specific assignment for the vibrational mode which are close to the bands at 1298, 1417 and 1444, 1697 cm^{-1} observed in this study. However, J. Kubicki et al. suggested the AcA molecules are weakly adsorbed on kaolinite, which is consistent with the spectrum acquired after 1 h of flushing by dry air, where the intensity of all the bands decreases.

Compared with Gobi dust, the feature of the DRIFT spectrum of AcA uptake on kaolinite is very similar. Except the band at 1564 cm^{-1} which is observed on the DRIFT spectra of Gobi dust attributed to strongly bound acetate species is missing, the bands attributed to weakly bound AcA on Gobi dust during AcA uptake can be identified in the DRIFT spectrum of kaolinite with minor wavenumber shifting, as visible in Figure IV-10 and Figure IV-17. **It suggests that kaolinite may significantly contribute to the weakly bound AcA fraction.**

2.4.2 Adsorbed phase during AcA uptake on TiO_2 under dry condition

Figure IV-18 shows the DRIFT spectra of the adsorbed phase of TiO_2 acquired after 1.5 hour of AcA uptake and after 1 hour of surface flushing by air flow under dry condition respectively.

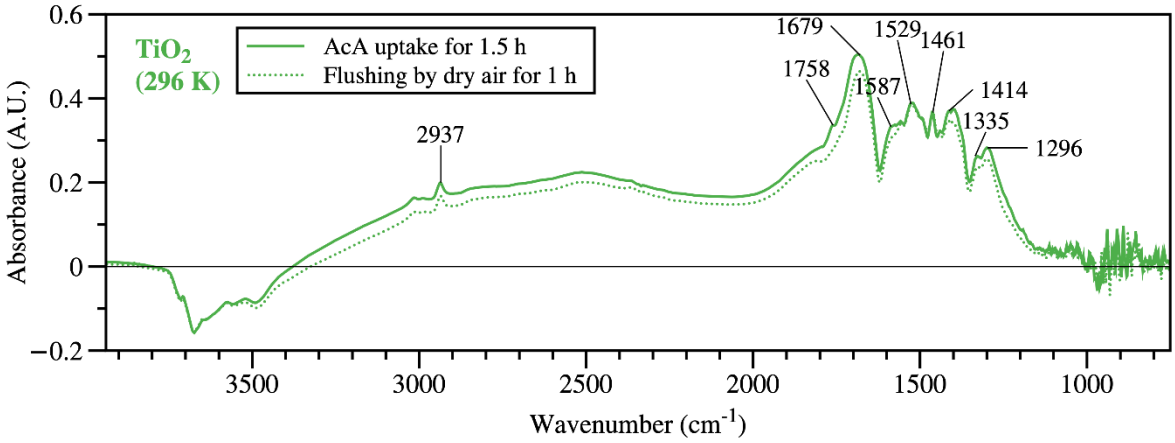

Figure IV-18 DRIFT spectra of the adsorbed phase of TiO_2 acquired after (—) 1.5 hour of AcA uptake, and (·····) 1 hour of surface flushing by air flow under dry condition. The experiment was conducted under room temperature (296 K) dry condition with AcA concentration of 10 ± 0.5 ppm.

During AcA uptake on the surface of TiO_2, DRIFT bands at 2937, 1758, 1679, 1587, 1529, 1461, 1414, 1335 and 1296 cm^{-1} are observed as indicated in Figure IV-18. This observation is in large consistence

with the FTIR study of AcA uptake on TiO_2 by L. Liao e al. [28] where authors have observed the IR peaks at 2936, 1736, 1675, 1535, 1453, 1415, 1341, and 1296 cm^{-1}. L. Liao e al. attributed the bands at 1296 and 1415 cm^{-1} to the molecularly adsorbed AcA on TiO_2 since they are close to the peaks of AcA adsorption in gas phase. The band at 1736 cm^{-1}, similar to the band of AcA dimer in gas phase, is assigned to the adsorbed AcA molecules through hydrogen bonding. According to L. Liao e al., the hydrogen bonding might be due to the interaction of AcA molecules with the Ti-OH group or another adsorbed AcA molecule. For the band at 1675 cm^{-1}, authors assigned it to the adsorbed AcA on Lewis acid sites on TiO_2 surface by hydrogen bond bonding with the oxygen atom from the carbonyl group (C=O) in AcA. After flushing the surface with dry air for 1 h, only the peak at 1758 cm^{-1} disappear which is assigned to the molecularly adsorbed AcA molecules through hydrogen bonding. It reveals that the adsorption of AcA on TiO_2 results in the formation of strongly bound surface species, which is consistent with the investigation by F. Batault et al. [10] that ca. 91% of the AcA molecules are irreversibly adsorbed on the surface of TiO_2 P25 (a mixture of rutile and anatase) under dry condition.

Compared with Gobi dust, regardless the fact that the overall feature of the DRIFT spectrum of TiO_2 during AcA uptake and surface flushing have significant contrasts due to the low fraction of TiO_2 in Gobi dust, i.e., 4.4 wt %, most of the DRIFT bands observed on Gobi dust during AcA uptake, i.e., the DRIFT bands at 2944 cm^{-1}, 1708 cm^{-1}, 1564 cm^{-1}, 1460 cm^{-1}, 1390 cm^{-1}, 1336 cm^{-1}, and 1292 cm^{-1}, can be identified on the DRIFT spectrum of TiO_2 during AcA uptake with minor wavenumber shifting, as visible in Figure IV-10 and Figure IV-18. **It highlights the possible contribution of TiO_2 in Gobi dust to AcA uptake, especially the irreversibly taken up fraction**.

2.4.3 Adsorbed phase during AcA uptake on SiO_2 under dry condition

Figure IV-19 shows the DRIFT spectra of the adsorbed phase of SiO_2 acquired after 1.5 hour of AcA uptake and after 10 min of surface flushing by air flow under dry condition respectively.

During AcA uptake on SiO_2 surface, only two DRIFT bands assigned to surface AcA species, i.e., the bands at 2948 cm^{-1} and 1716 cm^{-1}, are observed. The bands within 900 – 1300 cm^{-1}, at 1724, 1791, and 3582 cm^{-1} are characterized as the typical IR bands for gas phase AcA molecules, among which, the bands centered at 1791 cm^{-1} is assigned to ν(C=O) in monomer AcA and the band at 1724 cm^{-1} is assigned to ν(C=O) in dimer AcA from gas phase [13]. The bands assigned to gas phase AcA all disappear after flushing the surface within less than 10 min with dry air, which confirms the assignments of these bands to gas phase AcA instead of adsorbed AcA species. Considering that monomer is the main form of gas phase AcA molecules during this experiments, the observation of the significant DRIFT band of $(CH_3COOH)_{dimer}$ in Figure IV-19 suggests that the presence of SiO_2 favors the formation of $(CH_3COOH)_{dimer}$ in gas phase. It is in consistence with the observation by M. Tang et al. [13].

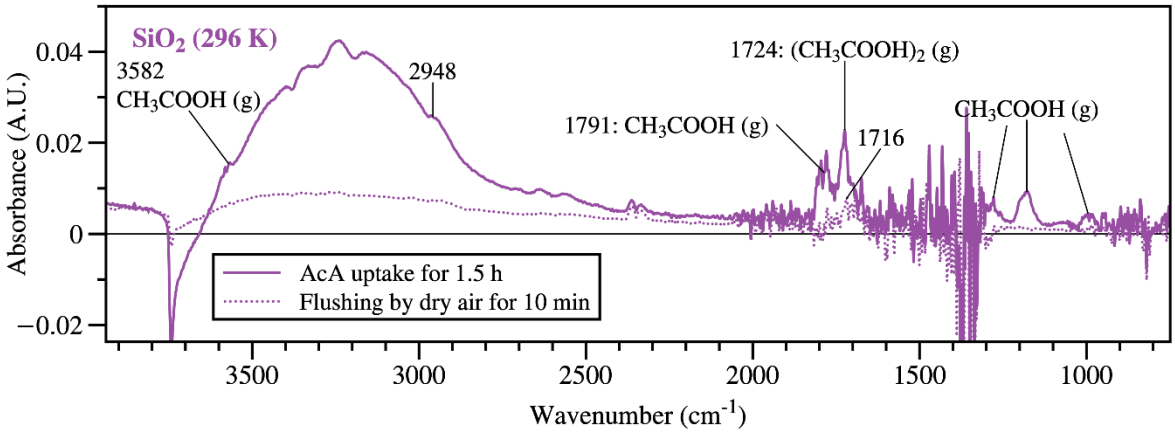

Figure IV-19 DRIFT spectra of the adsorbed phase of SiO_2 acquired after (—) 1.5 hour of AcA uptake, and (·····) 10 min of surface flushing by air flow under dry condition. The experiment was conducted under room temperature (296 K) dry condition with AcA concentration of 10 ± 0.5 ppm.

From the DRIFT spectrum acquire after 10 min of flushing, only the band at 1716 cm^{-1} remains, which is assigned to $\nu(C=O)_{dimer}$ of the weakly bound AcA [13, 24, 26]. It is consistent with the observation by M. Tang et al. [13] where the FITR band at 1716 cm^{-1} has been observed during AcA adsorption on SiO_2 surface. However, after evacuation of the gas from the reactor, M. Tang et al. [13] did not observed any band assigned to adsorbed AcA species on the surface of SiO_2. This might result from the experimental methods and conditions: M. Tang et al. have conducted the experiment under low AcA partial pressure, i.e., 5 – 110 mTorr, and they used vacuum pump for evacuation as the method for desorption which is possibly more impacting than only flushing with dry air under atmospheric pressure at room temperature. Nevertheless, the observation of the DRIFT band at 1716 cm^{-1} in this study is supported by S. Carlos-Cuellar et al. [1], who have observed transmission FTIR band at 1708 cm^{-1} which is assigned to $\nu(C=O)_{dimer}$ during AcA uptake on SiO_2 with the subtraction of gas phase AcA spectra.

The DRIFT observations during AcA uptake on SiO_2 are consistent with the observations in the gas phase investigations by S. Carlos-Cuellar et al. [1] where SiO_2 shows poor interactions towards AcA.. **As a conclusion, although SiO_2 is the most abundant mineral in Gobi dust, i.e., 33 wt %, it does not contribute significantly to AcA uptake process; when it does, it mostly contributes to the reversibly adsorbed fraction.** This is in accordance with the conclusion proposed by M. Zeineddine [9] who also investigated AcA uptake on Gobi dust surface.

2.4.4 Adsorbed phase during AcA uptake on $CaCO_3$ under dry condition

Figure IV-20 shows the DRIFT spectra of the adsorbed phase of $CaCO_3$ acquired after 1.5 hour of AcA uptake and after 10 min of surface flushing by air flow under dry condition respectively.

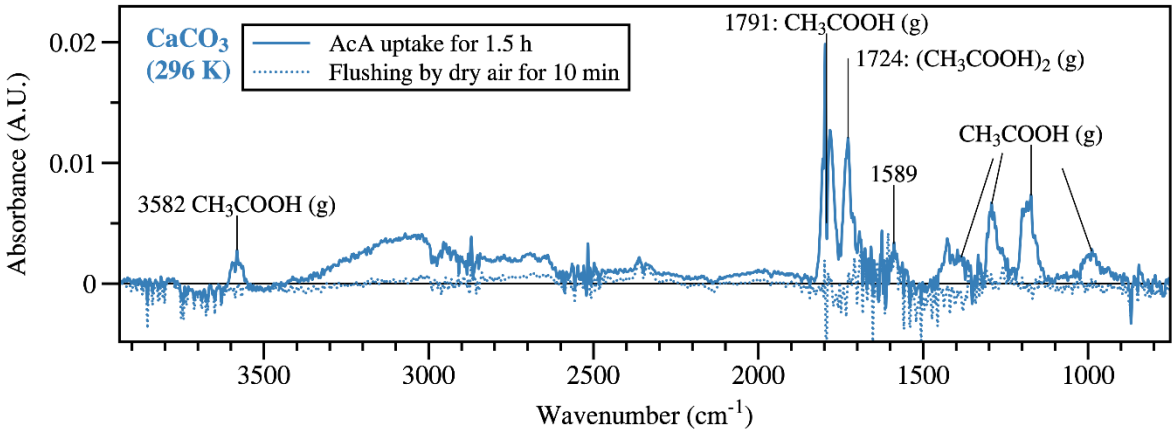

Figure IV-20 DRIFT spectra of the adsorbed phase of $CaCO_3$ acquired after (—) 1.5 hour of AcA uptake, and (·····) 10 min of surface flushing by air flow under dry condition. The experiment was conducted under room temperature (296 K) dry condition with AcA concentration of 10 ± 0.5 ppm.

The DRIFT spectrum during AcA uptake on $CaCO_3$ surface mostly exhibits the features characterized by gas phase AcA, i.e., observation of the bands at 3582, 1791, 1724, 1400, 1282, 1180 and 990 cm^{-1}, among which the bands centered at 1791 cm^{-1} is assigned to ν(C=O) in monomer AcA and the band at 1724 cm^{-1} is assigned to ν(C=O) in dimer AcA from gas phase as same as the spectrum of AcA adsorption on SiO_2 shown in Figure IV-19 [13]. Besides, the DRIFT band at 1589 cm^{-1} is assigned to ν_{as}(CO) in calcium acetate, based on the observation by O. Laskina et al. [30], and A. Prince et al. [16]. After flushing the surface for only 10 min with dry air, all the bands assigned to gas phase AcA disappear and only the band at 1589 cm^{-1} remains on the spectrum as shown in Figure IV-20. It suggests that no molecularly adsorbed AcA remains on the surface of $CaCO_3$ under dry condition after flushing with air, and only calcium acetate species are formed which corresponds to the irreversibly taken up fraction. The similar features of FTIR spectrum has been observed by A. Prince et al. [16] for AcA uptake on $CaCO_3$ under dry condition. A. Prince et al. also suggested the formation of carboxylate on the surface characterized by the band at 1445 cm^{-1} which cannot be identified in Figure IV-20.

Nevertheless, A. Prince et al. also pointed out that the uptake of AcA on $CaCO_3$ is less significant under dry condition compared with humid condition i.e. in the presence of adsorbed water molecules on the surface of $CaCO_3$. It is consistent with the observation by Q. Ma et al. [25] that the adsorbed water molecules on the surface of $CaCO_3$ have significant promoting effect regarding AcA uptake. It is consistent with the conclusion by M. Zeineddine [9] who evidenced that $CaCO_3$ contained in Gobi dust has the highest contribution to AcA take process under 50 % RH condition. Indeed, both A. Prince and Q. Ma suggested that the adsorbed water molecules provide another pathway for the interactions between AcA molecules and $CaCO_3$, extending the interactions from the surface to the bulk. It is consistence with the conclusion by A. L. Goodman et al. [14] that $CaCO_3$ is reactive soluble with

adsorbed water molecules. **As a result, $CaCO_3$ in Gobi dust is suggested to have minor contribution to AcA uptake process under dry condition, but have major contribution under humid condition.**

2.4.5 Conclusion and remarks

The DRIFT investigation of the adsorbed phase during AcA uptake on the principle mineral components of Gobi dust, i.e., SiO_2, $Al_2Si_2O_5(OH)_4$ (kaolinite), $CaCO_3$, and TiO_2, under dry condition with AcA concentration of 10 ± 0.5 ppm are discussed to address the individual adsorbed phase of these components during AcA uptake and their respective contributions.

Kaolinite, as an aluminosilicate, shows the most similar feature regarding DRIFT spectrum compared to Gobi dust. Most of the weakly bound AcA species on Gobi dust can be identified on kaolinite, except the absence of strongly adsorbed species. Thus, kaolinite is suggested to contribute mostly to the physisorbed AcA fraction which includes both reversibly adsorbed fraction and part of the irreversibly taken up fraction. The DIRFT investigation confirms the reactivity of TiO_2 towards AcA uptake and highlights its contribution to AcA uptake, especially regarding the irreversibly taken up fraction.

For SiO_2 and $CaCO_3$, the characterizations of DRIFT spectra are more related with the features of gas phase AcA, among which SiO_2 is suggested only to have a less significant contribution to reversibly adsorbed fraction of AcA and $CaCO_3$ is suggested to have no significant contribution to AcA uptake process under dry condition. However, the contribution of $CaCO_3$ regarding AcA uptake is suggested to be more significant under humid condition, e.g. under 50% RH as pointed out by M. Zeineddine [9].

2.5 Conclusion of adsorbed phase monitoring of AcA adsorption on Gobi dust

Conclusions based on DRIFT investigation of AcA uptake on Gobi dust using adsorbed approach are summarized as follows:

1. Physisorbed AcA on Gobi dust is evidenced in-situ, including reversibly adsorbed fraction and irreversibly adsorbed fraction. They are suggested to bound with surface OH group or another adsorbed AcA molecule through hydrogen bonding, forming adsorbed AcA monomer and mainly dimer species on the surface.
2. Surface acetate species are confirmed to be formed on the surface during AcA uptake on Gobi dust, they are irreversibly taken up on the surface at room temperature. They are suggested to coordinate in bidentate chelating structure with the two oxygen atoms from AcA bound to the same metal center on the surface of Gobi dust.
3. Water molecules are evidenced to compete with AcA molecules for the same surface sites, i.e., surface OH group, on Gobi dust, by forming adsorbed water molecules with surface OH group through hydrogen bonding. At the same time, AcA molecules can be bound to the adsorbed

water molecules through hydrogen bonding, forming reversibly adsorbed AcA. Besides, water molecules are also evidenced to interact with the irreversibly adsorbed fraction of the weakly bound AcA under dry condition, resulting in a partial removal of this fraction of weakly bound AcA. In contrast with weakly bound AcA species, the interaction of water molecules with strongly bound acetate species under dry condition is not significant.

4. Among the principle mineral components in Gobi dust, kaolinite and TiO_2 are found to have significant contribution to AcA uptake process compared with SiO_2 and $CaCO_3$. Kaolinite is found to mostly contribute to the weakly bound AcA species including a large fraction of reversibly adsorbed AcA, while TiO_2 is evidenced to mostly contribute to the irreversibly taken up fraction of AcA. The contribution of $CaCO_3$ to AcA uptake is suggested to depend significantly on relative humidity, Proposed mechanism for the interactions of AcA and Gobi dust.

3 Proposed mechanism for the interactions of AcA and Gobi dust

Based on the observations in both gas phase and adsorbed phase investigation during AcA uptake on Gobi dust, a mechanisms of AcA molecules interact with Gobi dust surface is proposed.

Surface sites with an OH group expressed as SS-OH where SS represents the metal center on the surface of Gobi dust, are potential candidates for AcA uptake even under dry conditions (note that the removal of surface OH groups requires strong thermal pretreatment methods). This proposed adsorption mechanism is also in agreement with the suggestions of A. L. Goodman et al. [14], H. E. Evans and W. H. Weinberg [22, 23], L. Liao et al. [28], and M. Tang et al. [13]. Through (RIV-1) AcA molecules from gas phase, i.e., CH_3COOH (g), are adsorbed on SS-OH by hydrogen bonding to form monomer adsorbed AcA:

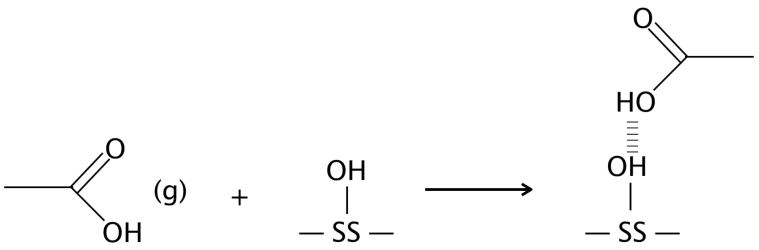

(RIV-1)

Meanwhile, the dimer form of the adsorbed AcA is also formed by hydrogen bonding between a gas phase AcA molecule, CH_3COOH (g) with $(CH_3COOH)(OH)SS$ (a) on the surface via Reaction (RIV-2):

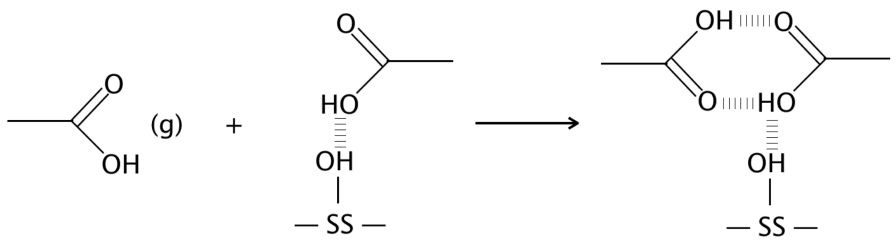

(RIV-2)

Dimer form of the adsorbed AcA species, i.e., $(CH_3COOH)_2(OH)SS$, is the main form of the molecularly adsorbed AcA in the adsorbed phase, as evidenced by the strong DRIFT band at 1708 cm^{-1} assigned to $\nu(C{=}O)_{dimer}$ in Figure IV-10.

This fraction of physisorbed AcA includes the reversibly adsorbed fraction and also the irreversibly adsorbed fraction. When the Gobi dust surface is flushed by dry air flow at room temperature, the reversibly adsorbed fraction of AcA is desorbed from surface to gas phase via the reverse reactions of (RIV-1) and (RIV-2). The enthalpies of (RIV-1) and (RIV-2) are suggested to be different.

For the formation of strongly bound acetate species on the surface of Gobi dust, as discussed in *section 2.1*, acetate with bidentate chelating coordination is formed via Reaction (RIV-3) and water molecules could be released to the gas phase or adsorbed phase:

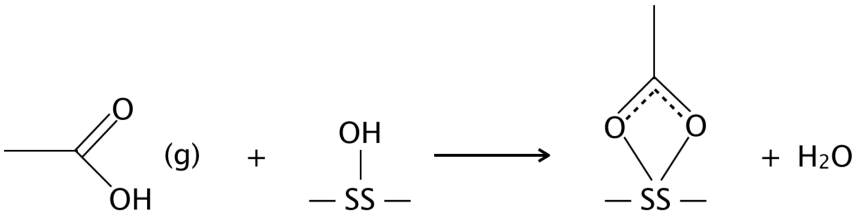

(RIV-3)

The structure of $CH_3COO(SS)$ is illustrated in Figure I-17 and Figure I-20, for which the two oxygen atoms for AcA is coordinated to the same metal center on Gobi dust. Reaction (RIV-3) has priority over reaction (RIV-1) and (RIV-2), meaning (RIV-3) occurs ahead of (RIV-1) and (RIV-2) and faster, as suggested by the experiment with unsaturated AcA adsorption in *section 1.4*. Also, the enthalpy of Reaction (RIV-3) is suggested to be more negative than Reaction (RIV-1) and (RIV-2).

Under 20% RH condition, the surface of Gobi dust is covered by a monolayer of water molecules and most of the SS-OH are occupied by water molecules according to Reaction (RIV-4):

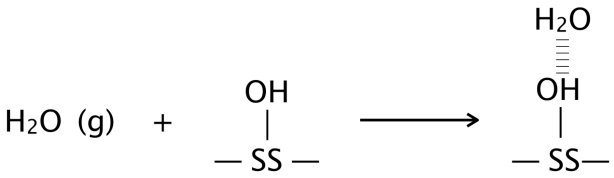

(RIV-4)

As a result, reactions (RIV-1), (RIV-2) as well as (RIV-4) are hindered, as observed in both gas phase and adsorbed phase. However, as discussed in *section 2.3*, AcA can still be molecularly adsorbed on adsorbed water molecules by hydrogen bonding via Reaction (RIV-5):

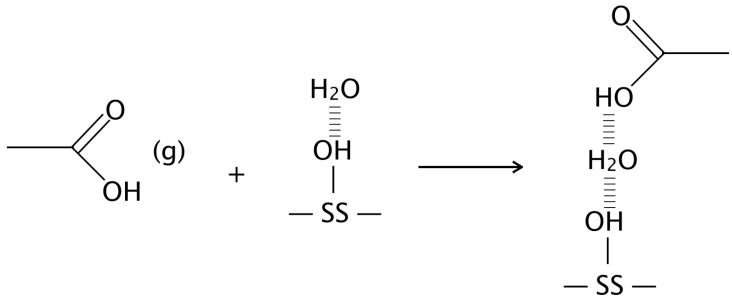

(RIV-5)

Dimer adsorbed AcA could also be formed under this condition, through Reaction (RIV-6)

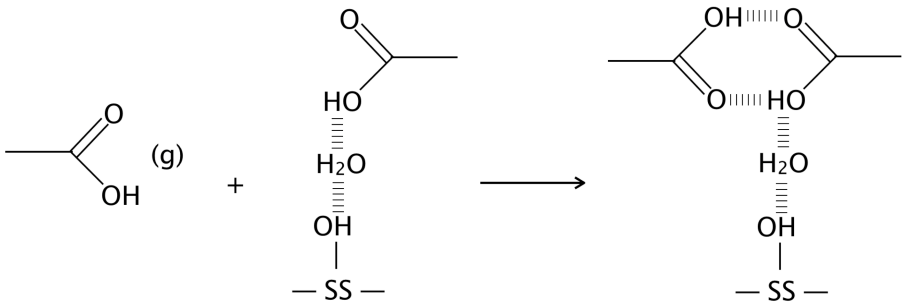

(RIV-6)

This adsorbed fraction of AcA species terminated through the adsorbed water molecules is weak and reversible, it is evidenced by the significant reversibly adsorbed fraction of AcA under 20% RH condition, i.e., up to 88 % of the total AcA uptake as indicated in *section 1.3*.

Acetate species, i.e., $CH_3COO(SS)$, is formed under 20% RH condition as discussed previously via Reaction (RIV-7) and water molecules could be released to gas phase or adsorbed phase:

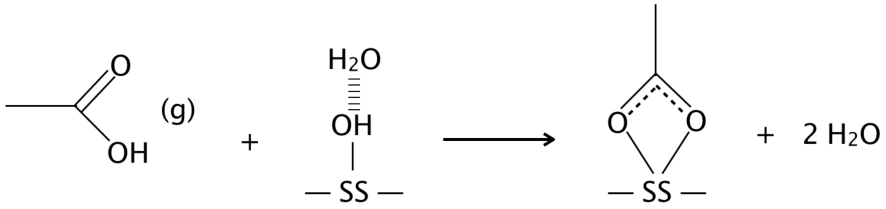

(RIV-7)

For the adsorbed AcA species under dry condition on the surface of Gobi dust, i.e., $(CH_3COOH)(OH)SS$ and $(CH_3COOH)_2(OH)SS$, water molecules can interact with these adsorbed AcA species, resulting in the partial removal of this fraction of adsorbed AcA into gas phase via Reaction (RIV-8) and (RIV-9), as discussed in *section 2.3*.

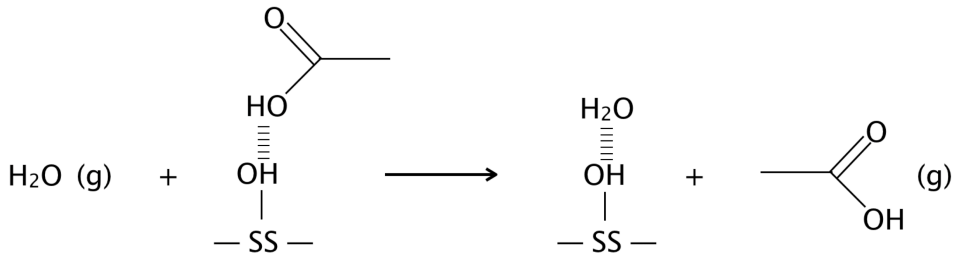

(RIV-8)

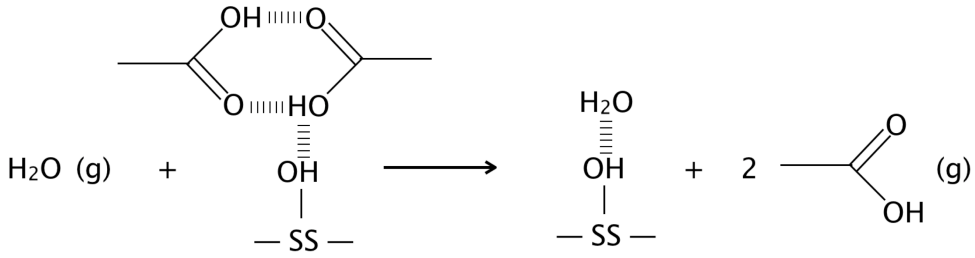

(RIV-9)

However, the interaction of water molecules has no significant impacts on the strongly bound acetate, i.e., $CH_3COO(SS)$, on the surface.

4 AcA ozonation on Gobi dust under dry condition

In order to evaluate the ozonation of AcA adsorbed on the surface of Gobi dust under dry condition, ozone is introduced into the system after AcA uptake on Gobi dust. The ozonation of AcA on Gobi dust is investigated using gas phase approach by following the protocol described below:

- STEP 0 / Pretreatment of the dust sample: heating at 150˚C under dry zero air flow then cooling down to room temperature.
- STEP 1 / Inlet AcA concentration monitoring through bypass line.
- STEP 2 / Dust surface exposure to AcA.
- STEP 3 / Switch AcA flow to bypass line to verify the stability of the inlet AcA concentration.
- STEP 4 / Flushing of the dust sample with dry zero air at room temperature, removal of the reversible adsorbed fraction of AcA.
- **STEP 5 / Dust surface exposure to ozone flow of 65 ± 2 ppm generated from oxygen at room temperature (296 K).**
- STEP 6 / Flushing the ozonated dust sample with dry zero air at 150˚C (423 K).

Figure IV-21 displays the AcA concentration profile of a complete experiment following the protocol described above. The mass of the Gobi dust is 30 ± 1 mg, the inlet AcA concentration is 8 ± 0.2 ppm and the ozone concentration in STEP 5 is 65 ± 2 ppm. The CO_2 level in gas phase is also monitored and indicated by the dotted line in Figure IV-21.

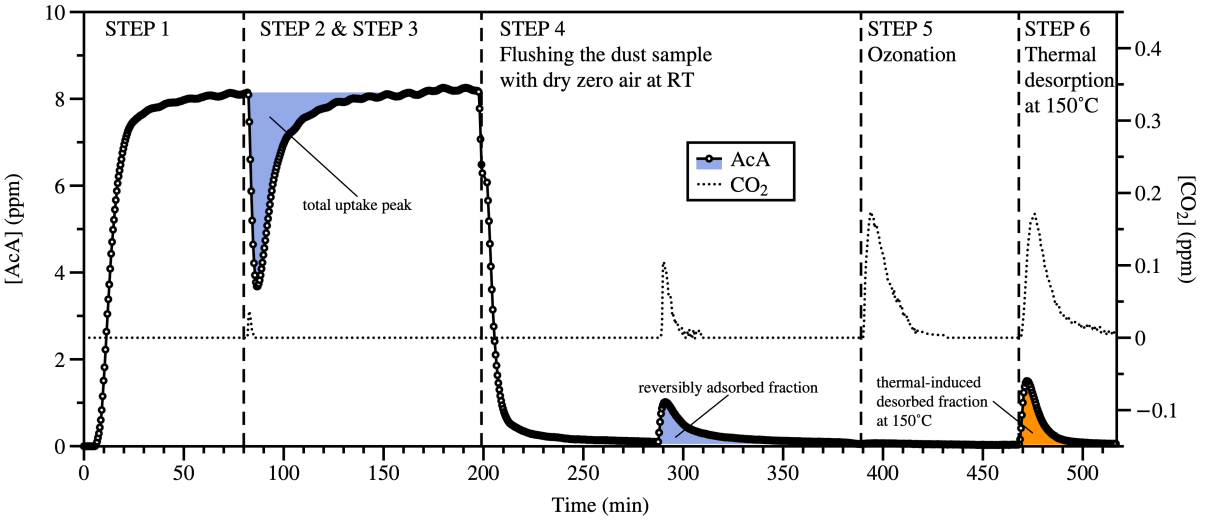

Figure IV-21 AcA concentration profile during AcA uptake, flushing the surface by dry air under room temperature (296 K), ozonation at room temperature (296 K) and thermal desorption by flushing with dry air at 150˚C (423 K). [AcA] = 8 ± 0.2 ppm, the mass of the Gobi dust sample is 30 ± 1 mg, [O_3] in STEP 5 is 65 ± 2 ppm.

At the end of STEP 4, only the irreversibly taken up fraction of AcA is present on the surface of Gobi dust. When the surface is exposed to ozone flow during STEP 5, no gas phase AcA is monitored as reported in Figure IV-21. It suggests that the interactions of ozone with the surface does not result in any desorption of the irreversibly adsorbed fraction of AcA on Gobi dust.

According to the CO_2 concentration profile reported in Figure IV-21, switching the gas line between bypass and U-shape reactor leads to a minor CO_2 peak as indicated at ca. 80 min. This CO_2 contribution might be associated to slight entering leaks of CO_2 from ambient air to the tubing of the experimental setup. When ozone flow is introduced into the U-shape reactor to interact with the surface covered by irreversibly adsorbed AcA, a CO_2 peak is clearly monitored in the gas phase as reported in Figure IV-21. The formation of CO_2 is induced during STEP 5 by the interactions of ozone with the AcA-exposed Gobi dust sample. By integrating the area of the CO_2 peak, the amount of CO_2 produced during the ozonation of STEP 5 is calculated to be ca. 0.033 μmol. It corresponds to ca. 1.6 % of the carbon mass balance regarding the carbon amount of the total AcA molecules taken up. Taking as a reference the irreversibly taken up fraction of CO_2, since only that fraction is exposed to ozone, the contribution of CO_2 resulting from the ozonation step is 2.0%.

After ca. 1 hour of ozone exposure, the ozone flow is stopped and the surface is heated at 150˚C under dry zero air flow. The fraction of thermally desorbed AcA is monitored and quantified. Also, CO_2 peak is monitored immediately upon the thermal treatment. It suggests that the thermal desorption of adsorbed species leads to the direct release of CO_2 in the gas phase. Compared to Figure IV-9, if no ozonation treatment of adsorbed AcA is performed, only a negligible amount of CO_2 is monitored in the gas phase

along the 150 °C thermal treatment. The presence of thermally induced CO_2 in Figure 21 suggests that the ozonation of irreversibly adsorbed AcA modifies the chemical nature of the organic adsorbed phase and may create other kinds of adsorbed species that are promptly thermally desorbed as CO_2. The direct emission of CO2 from adsorbed organic submitted to consecutive oxidation and thermal treatment has been reported by L. Sivachandiran et al. [31]. Authors evidenced that formates, chemisorbed on TiO_2 surface, are promptly thermally desorbed as CO_2 in the gas phase under a similar thermal treatment.

The amount of CO_2 emitted along the thermal treatment is calculated as 0.036 μmol, which corresponds to 1.7 % of the carbon mass balance based on the total taken up amount of AcA. It also corresponds to 2.2 % of the carbon mass balance calculated on the irreversibly taken up fraction of AcA, which is the only fraction exposed to ozone.

The amounts (μmol) of AcA and CO_2 monitored during each step and their respective percentages in the carbon mass balance (i) based on the total AcA molecules taken up and (ii) based on the irreversibly taken up AcA fraction, are calculated from Figure IV-21 and listed in Table IV-7.

Table IV-7 Amount of AcA and CO_2 calculated during each step and their percentages in carbon mass balance based on the AcA concentration profile in Figure IV-21.

	Amount (μmol)	Carbon mass balance / Based on total uptake fraction (%)	Carbon mass balance / Based on irreversibly taken up fraction (%)
Total uptake of AcA	1.04 ± 0.1	100	Ø
Reversibly adsorbed fraction of AcA at RT	0.22 ± 0.02	21	Ø
Ozone-induced desorbed fraction of AcA	0	0	0
Ozone-induced CO_2 production	0.033 ± 0.002	1.6	2.0
Thermal-induced desorbed fraction of AcA	0.31 ± 0.04	30	38
Thermal-induced CO2 production	0.036 ± 0.002	1.7	2.2

Table 6 indicates that 54.3% of the total carbon mass balance is recovered during the experiment, with 21 % of desorbed fraction of AcA induced by flushing at RT and 30 % recovered by the thermal treatment. It has to be noted that only 4.2 % of the carbon mass balance based on the irreversibly taken up fraction of AcA is recovered as CO_2. The latter suggests that AcA irreversibly adsorbed onto natural Gobi dust is weakly sensitive to ozone oxidation. Compared with thermal-induced desorption process

without ozonation discussed in *section 1.6* of this chapter, the carbon balance of thermal-induced desorbed fractions of AcA are the same, i.e., 30% with ozonation and 32% without ozonation. It suggests that the interactions of ozone molecules do not bring up significant difference for the adsorbed AcA on the surface, which supports the suggestion that the irreversibly adsorbed AcA on Gobi dust is weakly sensitive to ozone oxidation.

This result differs from the observations reported the study of the NTP oxidation and the thermal treatment of adsorbed acetone on TiO_2 reported by L. Sivachandiran et al. [31]. L. Sivachandiran et al. have monitored CO_2 productions corresponding to ca. 13% of the irreversibly adsorbed acetone during NTP oxidation and ca. 30% of the irreversibly adsorbed acetone during the following thermal treatment process. They also evidence that adsorbed formates are massively formed as surface intermediates during the oxidation process by NTP. The CO_2 production after NTP and thermal treatment of adsorbed acetone on TiO_2 represents 43% of the irreversibly adsorbed acetone, which is 10 times higher significant than the value obtained in this study for AcA. This difference could be explained by the fact that, due to its adsorption modes, acetone may be more sensitive to ozonation, and chemisorbed carboxylates result from an already initiated oxidation process. In the case of acetic acid, the VOC is already strongly bonded to the surface as a carboxylate. This configuration seems to offer a lower reactivity.

Interestingly, C. Barakat et al. [32] have investigated the NTP oxidation of another VOC, isopropanol, on the surface of TiO_2 and they observed that 2 % of the irreversibly taken up isopropanol is mineralized into CO_2 or CO by NTP. This result is close to our case with AcA, i.e., 4.2%. However, acetone has been monitored in the gas phase during NTP oxidation process by C. Barakat et al. as the major oxidation intermediate. It represents more than 22 % of the irreversibly taken up isopropanol. Besides, after thermal treatment, C. Barakat et al. reported a completed carbon mass balance, which is different in our case where 57.8% of carbon mass balance based on the irreversibly taken up AcA is missing. This aspect questions the formation of gas phase organic side-product along ozonation and their contribution to the carbon mass balance. Indeed, certain organic gas phase side-products of AcA ozonation may have been formed, this point would require more detailed investigation of the evolved gas phase species along ozonation and thermal treatment.

5 Summary and conclusions

The interactions of AcA with Gobi dust have been studied using gas phase approach and adsorbed phase approach at room temperature and atmospheric pressure under dry condition and humid (20% RH) condition.

AcA molecules are evidenced to be physisorbed and chemisorbed on the surface of Gobi dust under both dry and 20% RH condition. Under dry condition, the physisorbed fraction of AcA on Gobi dust

surface includes reversibly adsorbed fraction and irreversibly adsorbed fraction. Under 20% RH condition, the reversibly adsorbed fraction of AcA is promoted while the irreversibly adsorbed fraction is hindered. The irreversible uptake capacity of Gobi dust regarding AcA is determined to be 31.6 ± 5 μmol g^{-1} under dry condition and 13.8 ± 5 μmol g^{-1} under 20% RH condition within the investigated AcA concentration range.

The formation of molecularly adsorbed AcA and surface acetate species has been confirmed for both dry condition and 20% RH condition. The molecularly adsorbed AcA is suggested to bound with the surface OH group or another adsorbed AcA through hydrogen bonding, of which dimer is the major form. Adsorbed water molecules on the surface of Gobi dust surface are also evidenced to provide adsorption sites for molecularly adsorbed AcA molecules. The surface acetate species is suggested to be coordinated to the surface in bidentate chelating structure with two oxygen atoms from AcA bound to the same metal center on Gobi dust.

Water molecules compete with AcA molecules for the same adsorption site, i.e., surface OH group, on Gobi dust surface and also interact with the irreversibly adsorbed fraction of the molecularly adsorbed AcA under dry condition, resulting in the partial removal of this fraction of the molecularly adsorbed AcA from the surface. Water molecules are evidence to have no significant impact on the surface acetate species which are formed under dry condition during AcA uptake. However, under 20% RH condition where the surface of Gobi dust is covered by a monolayer of water molecules, the interactions between water molecules and surface acetate species is confirmed to be more significant.

The ozonation of the adsorbed AcA on Gobi dust is evidenced as a weak process under dry condition and room temperature. This behavior may be due to the stability of adsorbed AcA.

However, after the thermal treatment at 150˚C, more than half of the amount of the total AcA uptake is recovered, showing the possibility to regenerate the surface ability regarding AcA uptake of Gobi dust.

Compared with the principle mineral components of Gobi dust, i.e., SiO_2, $Al_2Si_2O_5(OH)_4$, $CaCO_3$, and TiO_2, Gobi dust is evidenced to have a higher AcA uptake regarding the irreversible uptake capacity towards AcA: Gobi dust exhibits twice higher the irreversible uptake capacity towards AcA than the calculated value based on the individual irreversible uptake capacity toward AcA of each component.

References

[1] S. Carlos-Cuellar, P. Li, A. Christensen, B. Krueger, C. Burrichter, V. Grassian, Heterogeneous uptake kinetics of volatile organic compounds on oxide surfaces using a Knudsen cell reactor: Adsorption of acetic acid, formaldehyde, and methanol on α-Fe_2O_3, α-Al_2O_3, and SiO_2, The Journal of Physical Chemistry A, 107 (2003) 4250-4261.

[2] S. Tong, L. Wu, M. Ge, W. Wang, Z. Pu, Heterogeneous chemistry of monocarboxylic acids on α-Al 2 O 3 at different relative humidities, Atmospheric Chemistry and Physics, 10 (2010) 7561-7574.

[3] M.N. Zeineddine, M.N. Romanias, V. Riffault, F. Thévenet, Heterogeneous Interaction of Various Natural Dust Samples with Isopropanol as a Probe VOC, The Journal of Physical Chemistry A, (2018).

[4] M.N. Zeineddine, M.N. Romanias, V. Gaudion, V. Riffault, F. Thévenet, Heterogeneous Interaction of Isoprene with Natural Gobi Dust, ACS Earth and Space Chemistry, 1 (2017) 236-243.

[5] M.N. Romanias, M.N. Zeineddine, V. Gaudion, X. Lun, F. Thevenet, V. Riffault, Heterogeneous Interaction of Isopropanol with Natural Gobi Dust, Environmental science & technology, 50 (2016) 11714-11722.

[6] P. Li, K. Perreau, E. Covington, C. Song, G. Carmichael, V. Grassian, Heterogeneous reactions of volatile organic compounds on oxide particles of the most abundant crustal elements: Surface reactions of acetaldehyde, acetone, and propionaldehyde on SiO_2, Al_2O_3, Fe_2O_3, TiO_2, and CaO, Journal of Geophysical Research: Atmospheres, 106 (2001) 5517-5529.

[7] R.I. Masel, Principles of adsorption and reaction on solid surfaces, John Wiley & Sons1996.

[8] V.F. Kiselev, O.V. Krylov, Adsorption and Catalysis on Transition Metals and Their Oxides, Springer Berlin Heidelberg, Berlin, Heidelberg, 1989.

[9] M.N. Zeineddine, Heterogeneous Interactions of Volatile Organic Compounds with Natural Mineral Dust Samples, Ecole nationale supérieure Mines-Télécom Lille Douai, 2018.

[10] F. Batault, F. Thevenet, V. Hequet, C. Rillard, L. Le Coq, N. Locoge, Acetaldehyde and acetic acid adsorption on TiO_2 under dry and humid conditions, Chemical Engineering Journal, 264 (2015) 197-210.

[11] J. Crowley, M. Ammann, R. Cox, R. Hynes, M.E. Jenkin, A. Mellouki, M. Rossi, J. Troe, T. Wallington, Evaluated kinetic and photochemical data for atmospheric chemistry: Volume V–heterogeneous reactions on solid substrates, Atmospheric Chemistry and Physics, 10 (2010) 9059-9223.

[12] N. Joshi, M.N. Romanias, V. Riffault, F. Thevenet, Investigating water adsorption onto natural mineral dust particles: Linking DRIFTS experiments and BET theory, Aeolian Research, 27 (2017) 35-45.

[13] M. Tang, W.A. Larish, Y. Fang, A. Gankanda, V.H. Grassian, Heterogeneous reactions of acetic acid with oxide surfaces: Effects of mineralogy and relative humidity, The Journal of Physical Chemistry A, 120 (2016) 5609-5616.

[14] A. Goodman, E. Bernard, V. Grassian, Spectroscopic study of nitric acid and water adsorption on oxide particles: Enhanced nitric acid uptake kinetics in the presence of adsorbed water, The Journal of Physical Chemistry A, 105 (2001) 6443-6457.

[15] H.A. Al-Hosney, S. Carlos-Cuellar, J. Baltrusaitis, V.H. Grassian, Heterogeneous uptake and reactivity of formic acid on calcium carbonate particles: a Knudsen cell reactor, FTIR and SEM study, Physical Chemistry Chemical Physics, 7 (2005) 3587-3595.

[16] A.P. Prince, P.D. Kleiber, V.H. Grassian, M.A. Young, Reactive uptake of acetic acid on calcite and nitric acid reacted calcite aerosol in an environmental reaction chamber, Physical Chemistry Chemical Physics, 10 (2008) 142-152.

[17] J.E. Shilling, M.A. Tolbert, Uptake of acetic acid on thin ammonium nitrate films as a function of temperature and relative humidity, The Journal of Physical Chemistry A, 108 (2004) 11314-11320.

[18] I.E. Wachs, Raman and IR studies of surface metal oxide species on oxide supports: supported metal oxide catalysts, Catalysis Today, 27 (1996) 437-455.

[19] P.A. Connor, K.D. Dobson, A.J. McQuillan, Infrared spectroscopy of the TiO_2/aqueous solution interface, Langmuir, 15 (1999) 2402-2408.

[20] S. Ibrahim, M.N. Romanias, L.Y. Alleman, M.N. Zeineddine, G.K. Angeli, P.N. Trikalitis, F. Thevenet, Water Interaction with Mineral Dust Aerosol: Particle Size and Hygroscopic Properties of Dust, ACS Earth and Space Chemistry, 2 (2018) 376-386.

[21] C. Börensen, U. Kirchner, V. Scheer, R. Vogt, R. Zellner, Mechanism and kinetics of the reactions of NO2 or HNO3 with alumina as a mineral dust model compound, The Journal of Physical Chemistry A, 104 (2000) 5036-5045.

[22] H. Evans, W. Weinberg, A comparison of the vibrational structures of ethanol, acetic acid, and acetaldehyde adsorbed on alumina, The Journal of Chemical Physics, 71 (1979) 4789-4798.

[23] H. Evans, W. Weinberg, The reaction of ethanol with an aluminum oxide surface studied by inelastic electron tunneling spectroscopy, The Journal of Chemical Physics, 71 (1979) 1537-1542.

[24] C. Xu, B.E. Koel, Adsorption and reaction of CH3COOH and CD3COOD on the MgO (100) surface: A Fourier transform infrared and temperature programmed desorption study, The Journal of chemical physics, 102 (1995) 8158-8166.

[25] Q. Ma, Y. Liu, C. Liu, H. He, Heterogeneous reaction of acetic acid on MgO, α-Al_2O_3, and CaCO 3 and the effect on the hygroscopic behaviour of these particles, Physical Chemistry Chemical Physics, 14 (2012) 8403-8409.

[26] M. Hasan, M. Zaki, L. Pasupulety, Oxide-catalyzed conversion of acetic acid into acetone: an FTIR spectroscopic investigation, Applied Catalysis A: General, 243 (2003) 81-92.

[27] Z.-F. Pei, V. Ponec, On the intermediates of the acetic acid reactions on oxides: an IR study, Applied surface science, 103 (1996) 171-182.

[28] L.-F. Liao, C.-F. Lien, J.-L. Lin, FTIR study of adsorption and photoreactions of acetic acid on TiO_2, Physical Chemistry Chemical Physics, 3 (2001) 3831-3837.

[29] J. Kubicki, L. Schroeter, M. Itoh, B. Nguyen, S. Apitz, Attenuated total reflectance Fourier-transform infrared spectroscopy of carboxylic acids adsorbed onto mineral surfaces, Geochimica et Cosmochimica Acta, 63 (1999) 2709-2725.

[30] O. Laskina, M.A. Young, P.D. Kleiber, V.H. Grassian, Infrared extinction spectroscopy and micro-Raman spectroscopy of select components of mineral dust mixed with organic compounds, Journal of Geophysical Research: Atmospheres, 118 (2013) 6593-6606.

[31] L. Sivachandiran, F. Thevenet, A. Rousseau, Non-Thermal Plasma Assisted Regeneration of Acetone Adsorbed TiO2 Surface, Plasma Chemistry and Plasma Processing, 33 (2013) 855-871.

[32] C. Barakat, P. Gravejat, O. Guaitella, F. Thevenet, A. Rousseau, Oxidation of isopropanol and acetone adsorbed on TiO_2 under plasma generated ozone flow: Gas phase and adsorbed species monitoring, Applied Catalysis B-Environmental, 147 (2014) 302-313.

General conclusion

The principle objective of this thesis is to investigate the surface properties of a natural mineral dust, namely Gobi dust towards ozone and acetic acid (AcA) through the characterization of their heterogeneous interactions with natural Gobi dust samples.

The main results, as well as the future perspectives, obtained from this thesis are summarized as followed in three sections:

1. Surface properties of natural Gobi dust towards ozone.
2. Surface properties of natural Gobi dust towards AcA.
3. Potential of using Gobi dust as a catalyst/adsorbent.

1. Surface properties of natural Gobi dust towards ozone

Gobi dust exhibits catalytic surface property towards ozone decomposition within the range of ozone inlet concentration from ca. 0.02 to 10 ppm, which has been studied in the present work. This behavior is characterized by a steady-state uptake regime and evidenced by the fact that the TON of ozone molecules on a single surface site of Gobi dust exceeds 1. Steady-state uptake coefficients of ozone on Gobi dust are determined from 2.6×10^{-9} to 6.2×10^{-8} depending on ozone concentration under dry condition.

Impacts of ozone concentration on ozone decomposition on Gobi dust

Higher ozone concentration reduces the probability of the decomposition of ozone molecules as revealed by the steady-state uptake coefficients, but promotes the reaction rate during steady-state ozone uptake regime, as revealed by the increase of the uptake rate (molecules s^{-1}) during steady-state uptake regime. The steady-state uptake coefficients of ozone on Gobi dust under 20% RH condition are determined from 4.5×10^{-8} to 5.4×10^{-10} to within ozone concentration range from 0.04 to 4.7 ppm.

Impacts of water molecules on ozone decomposition on Gobi dust

In the presence of water molecules, the ozone uptake is hindered during steady-state uptake regime. Water molecules is suggested to compete for the same surface sites on Gobi dust with ozone molecules and to form adsorbed water on the Gobi surface. The presence of water molecules is suggested to have no significant impact on SS-O and SS-O_2 surface groups resulting from O_3 decomposition on Gobi dust surface, assuming water concentration of 30 ppm (0.1% RH).

Regeneration of surface properties of Gobi dust regarding ozone decomposition

The initial surface properties of Gobi dust can be significantly restored by thermal treatment at 150˚C, ensuring the restorability of Gobi dust uptake properties. Water molecules are also found to positively interact with ozone-exposed Gobi dust surface, resulting in limited but noticeable surface regeneration on a 10-hour time scale.

Comparison of Gobi dust and its single mineral components regarding ozone decomposing efficiency

Gobi dust exhibits higher catalytic ozone-decomposing efficiency compared to its single mineral components such as SiO_2, $CaCO_3$, $Al_2Si_2O_5(OH)_4$, and TiO_2/SiO_2 (3 wt %) under dry condition. This behavior is revealed by higher steady-state ozone uptake coefficients obtained under equivalent condition. However, this result does not preclude the heterogeneous dispatching of the various mineral phases between the bulk and the surface of the sample.

Proposed mechanism of ozone decomposition on Gobi dust under dry condition

During ozone decomposition on Gobi dust, surface oxygenated groups are formed from the interactions between ozone molecules and the Gobi surface sites. These groups are characterized by DRIFT bands at 1700 cm^{-1} assigned to SS-O_2 and at 1300 cm^{-1} assigned to SS-O.

A mechanism of ozone decomposition on Gobi dust under dry condition has been proposed. It describes the processes of ozone composition, including the formation of surface oxygenated species and surface regeneration involved in the catalytic nature of the heterogeneous process:

O_3 decomposition		Surface regeneration
$O_3(g) + SS \rightarrow SS\text{-}O + O_2(g)$		$SS\text{-}O_2 \rightarrow SS + O_2(g)$
$SS\text{-}O + O_3(g) \rightarrow SS\text{-}O_2 + O_2(g)$		$2SS\text{-}O \rightarrow 2SS + O_2(g)$

2. Surface properties of natural Gobi dust towards Acetic Acid.

Acetic Acid molecules are evidenced to be physisorbed as well as chemisorbed on the surface of Gobi dust, forming molecularly adsorbed AcA as monomers and dimers, and surface acetate species. The physisorbed fraction of AcA on Gobi dust surface includes reversibly adsorbed fraction and irreversibly adsorbed fraction while the chemisorbed fraction is irreversibly adsorbed. The irreversible uptake capacity of Gobi dust regarding AcA under dry condition is determined to be 31.6 ± 5 μmol g^{-1} within the investigated AcA concentration range from 0.25 to 106 ppm.

Impacts of AcA concentration on AcA uptake on Gobi dust

Within the investigated AcA concentration range, the number of AcA molecules taken up per surface area unit of Gobi dust N (molecules cm^{-2}) of total uptake, reversibly adsorbed fraction and irreversibly taken up fraction of AcA firstly increase with AcA concentration then reach a plateau value.

Impacts of water molecules on AcA uptake on Gobi dust

Under 20% RH condition, the presence of water molecules significantly promotes the reversibly adsorbed fraction of AcA on Gobi dust and hinders the irreversibly adsorbed fraction by competing with AcA molecules for the same sorption sites. The irreversible uptake capacity of Gobi dust regarding AcA under 20% RH condition is determined to be 13.8 ± 5 μmol g^{-1} within the investigated AcA concentration range from ca. 0.41 to 111 ppm, which is less than half of the value determined under dry condition.

Water-induced and thermal-induced desorption process of AcA taken up on Gobi dust

Water molecules are proved to interact with the irreversibly taken up fraction of AcA on Gobi dust under dry condition. Flushing the AcA exposed Gobi dust sample with humid flow of 20 % RH results in significant removal of the irreversible taken up fraction of AcA: 67 % for the case where ca. 9 ppm of AcA is taken up on 60 mg Gobi dust under dry condition, evidencing the competition between water molecules and AcA molecules for the same surface sites.

A thermal treatment of the surface with dry air at 150 ˚C also results in the desorption of the irreversibly taken up fraction of AcA on Gobi dust: 63 % of the irreversibly taken up fraction of AcA on Gobi dust under dry condition is desorbed for the case where ca. 1.5 ppm of AcA is taken up on 24 mg Gobi dust under dry condition.

Comparison of Gobi dust with its single mineral components regarding the irreversible AcA uptake capacity

Gobi dust exhibits a higher AcA uptake capacity under dry condition, compared with its principle mineral components such as SiO_2, $Al_2Si_2O_5(OH)_4$ and $CaCO_3$, as revealed by higher values of the irreversible uptake capacity obtained under equivalent conditions.

Proposed mechanism of AcA uptake on Gobi dust under dry and humid condition

The formation of molecularly adsorbed AcA in both monomers and dimers, as well as surface acetate species with bidentate chelating structure has been confirmed during AcA uptake on Gobi dust surface for both dry and 20% RH conditions.

A possible mechanism to describe AcA uptake on Gobi dust under dry condition has been proposed as follows:

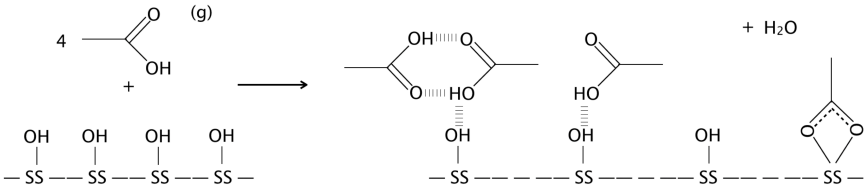

For 20% RH condition where the surface of Gobi dust is covered by a monolayer of water molecules, the mechanism of AcA uptake is proposed to be modified as follows:

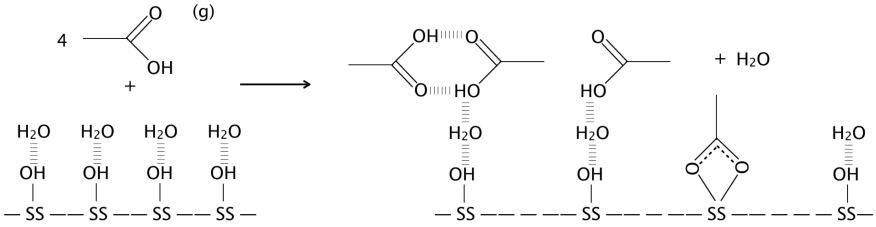

The reverse reaction pathways could describe the desorption process of molecularly adsorbed AcA monomer and dimer from the surface of Gobi dust.

Ozonation of adsorbed AcA on Gobi dust

The ozonation of the adsorbed AcA on Gobi dust is evidenced as minor mineralization pathway of adsorbed AcA under dry condition and room temperature.

3. Potential of using Gobi dust as a catalyst/adsorbent

This work experimentally evidenced that natural Gobi dust could potentially be used as a catalyst for ozone decomposition as well as an adsorbent for AcA uptake. The comparison between natural Gobi dust with its principle mineral components regarding the surface properties towards ozone-decomposition efficiency and AcA uptake ability highlights that the potential of this geomaterial is equivalent to usual synthetic single metal oxide. Noticeably, appears as a material of interest for NTP-catalysis. Natural Gobi dust does not need any synthesis or purification, leading to energy savings and reduction of the emissions. As a result, this work praises on the use of natural geomaterials instead of usual catalyst, which comes up with both environmental and economic benefits.

Abstract

This PhD thesis investigates the interactions of ozone and acetic acid with a natural mineral dust from Gobi Desert in China, under room temperature, atmospheric pressure, dry and wet conditions, using *post-situ* and *in-situ* characterization techniques to address gas phase and adsorbed phase species.

First, ozone uptake at the surface of Gobi dust is investigated over a large ozone concentration range (20 ppb – 10 ppm) to provide new insights on the heterogeneous processes of ozone with potential interest for both atmospheric chemistry and industrial frameworks. Gobi dust exhibits catalytic properties regarding ozone decomposition with a steady-state uptake coefficient ranging from 2.6×10^{-9} to 6.2×10^{-8} depending on ozone concentration. Water molecules compete with ozone for the same surface sites while thermal treatment at 150˚C can significantly regenerate the surface sites after surface exposure to ozone.

Second, the physisorptive and chemisorptive interaction modes of acetic acid on Gobi dust have been studied evidencing the formation of molecularly adsorbed acetic acid in monomer and dimer forms as well as bidentate chelating acetate. The amount and the partition of reversibly and irreversibly adsorbed fractions of acetic acid taken up on Gobi dust exhibit contrasted behaviors under dry and 20% RH conditions. Finally, the oxidation of adsorbed acetic acid by ozone at the surface of Gobi dust is investigated to typify the ability of that geo-material to act as a catalyst of interest.

Key words: mineral dust, geomaterial, ozone, acetic acid, adsorption, uptake coefficient

Résumé

Cette thèse de doctorat porte sur l'étude des interactions de l'ozone et de l'acide acétique avec des poussières minérales naturelles du désert de Gobi en Chine, à température ambiante, pression atmosphérique ainsi que dans des conditions sèches et humides. Les espèces en phase gazeuse et en phase adsorbée sont caractérisées par des techniques *post-situ* et *in-situ*.

La capture de l'ozone par les poussières de Gobi est étudiée sur une large gamme de concentrations (20 ppb – 10 ppm) afin de clarifier les processus hétérogènes impliquant l'ozone et évaluer leurs implications en chimie atmosphérique et dans les procédés. Les poussières de Gobi présentent des propriétés catalytiques de décomposition de l'ozone avec un coefficient de capture stationnaire variant entre 2.6×10^{-9} et 6.2×10^{-8} selon la concentration d'ozone. Les molécules d'eau rivalisent avec l'ozone pour l'accès aux sites de surface, tandis que le traitement thermique à 150 °C peut régénérer de manière significative certains sites de surface après une exposition à l'ozone.

Les modes d'interaction physisorptifs et chimisorptifs de l'acide acétique sur les poussières de Gobi sont ensuite étudiés: l'acide acétique s'adsorbe sous forme de monomère et dimère, ainsi que d'acétate bidentate. La quantité ainsi que la répartition des fractions réversibles et irréversibles d'acide acétique absorbées présentent des comportements différents entre conditions sèches et humides. Enfin, l'ozonation de l'acide acétique adsorbé sur les poussières de Gobi est étudiée pour évaluer l'aptitude de ce géo-matériau à être utilisé comme catalyseur d'intérêt.

Mots clés: poussières minérales, géomatériaux, ozone, acide acétique, adsorption, coefficient de capture